

PFC/RR-94-5

**Theory and Modelling of Quench in
Cable-In-Conduit Superconducting Magnets**

A. Shajii

April 1994

Plasma Fusion Center
Massachusetts Institute of Technology
Cambridge, MA 02139 USA

This work was supported by the US Department of Energy through the Idaho National Engineering Laboratory under contract C88-110982-TKP-154-87. Reproduction, translation, publication, use, and disposal, in whole or in part, by or for the US Government is permitted.

**Theory and Modelling of Quench in
Cable-In-Conduit Superconducting Magnets**

by

Ali Shajii

B.S. in Nuclear Engineering and Engineering Physics
University of Wisconsin-Madison (1990)

Submitted to the Department of Nuclear Engineering
in Partial Fulfillment of the Requirement for the Degree of


Doctor of Philosophy

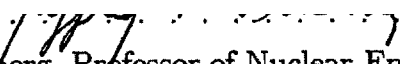
at the

MASSACHUSETTS INSTITUTE OF TECHNOLOGY

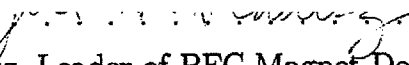
May 1994


© 1994 Massachusetts Institute of Technology. All Rights Reserved.

Signature of Author . . . 
Department of Nuclear Engineering, March 11, 1994

Certified by . . . 
Jeffrey P. Freidberg, Professor of Nuclear Engineering, Thesis Supervisor

Certified by . . . 
Richard J. Thome, Head of PFC Engineering Division, Thesis Supervisor

Certified by . . . 
Joel H. Schultz, Leader of PFC Magnet Design Group, Thesis Supervisor

Certified by . . . 
D. Bruce Montgomery, Associate Director of PFC, Thesis Reader

Accepted by
Allan F. Henry, Chairman, Departmental Committee on Graduate Students

Theory and Modelling of Quench in Cable-In-Conduit Superconducting Magnets

by

Ali Shajii

Submitted to the Department of Nuclear Engineering
on March 18, 1994 in Partial Fulfillment of
the Requirement for the Degree of Doctor of Philosophy

Abstract

A new simple, self consistent theoretical model is presented that describes the phenomena of quench propagation in Cable-In-Conduit superconducting magnets. The model (Quencher) circumvents many of the difficulties associated with obtaining numerical solutions in more general existing models. Specifically, a factor of 30-50 is gained in CPU time over the general, explicit time dependent codes used to study typical quench events. The corresponding numerical implementation of the new model is described and the numerical results are shown to agree very well with those of the more general models, as well as with experimental data.

Further, well justified approximations lead to the MacQuench model that is shown to be very accurate and considerably more efficient than the Quencher model. The MacQuench code is suitable for performing quench studies on a personal computer, requiring only several minutes of CPU time. In order to perform parametric studies on new conductor designs it is required to utilize a model such as MacQuench because of the high computational efficiency of this model.

Finally, a set of analytic solutions for the problem of quench propagation in Cable-In-Conduit Conductors (CICC) is presented. These analytic solutions represent the first such results that remain valid for the long time scales of interest during a quench process. The assumptions and the resulting simplifications that lead to the analytic solutions are discussed, and the regimes of validity of the various approximations are specified. The predictions of the analytic results

are shown to be in very good agreement with numerical as well as experimental results. Important analytic scaling relations are verified by such comparisons, and the consequences of some of these scalings on currently designed superconducting magnets are discussed.

Thesis Supervisor: Jeffrey P. Freidberg
Professor of Nuclear Engineering
Massachusetts Institute of Technology

Thesis Supervisor: Richard J. Thome
Head of Technology and Engineering Division
MIT Plasma Fusion Center

Thesis Supervisor: Joel H. Schultz
Leader of Magnet Design Group
MIT Plasma Fusion Center

Acknowledgments

I would like to thank the members of the Engineering Division at MIT's Plasma Fusion Center for many useful discussions during the course of this work. Several scientists are specifically acknowledged for their detailed and helpful suggestions: E. A. Chaniotakis, J. McCarrick, J. Minervini, D. B. Montgomery, and R. Pillsbury. Doctor J. Minervini has been kind enough to read and comment on the entire thesis and his input is very much appreciated. I would also like to thank Dr. R. Thome for his support during the past few years as my advisor. His insight lead me to this particular field in the area of superconducting magnets. I thank J. Schultz for his continuous support and his unbiased feedback about my work. I especially thank my other advisor Prof. J. Freidberg for his enormous help. He has been a friend, a mentor, and above all an inspiration for me. Finally, I thank my wife Dr. H. Azar, who has been with me through it all. Her support is always the primary reason for my progress.

Dedicated to my wife, Haleh

Table of Contents

Abstract	2
Chapter 1. Introduction	8
Chapter 2. Derivation of the Model	16
2.1 General 3-D Model	17
2.2 General 1-D Model	22
2.3 The Quench Model	36
Chapter 3. Numerical Solution	54
3.1 Numerical Procedure	57
3.2 Comparison With Computational Data	67
3.3 Comparison With Experimental Data	73
Chapter 4. Analytic Solution	113
4.1 The MacQuench Model	117
4.2 Analytic Solution	134
4.3 Discussion	151
Chapter 5. Dual-Channel CICC	177
5.1 Basic Model	179
5.2 Cross-Coupling Simplifications	183
5.3 Quench Simplifications	184
5.4 Discussion and Results	188
Chapter 6. Applications	196
6.1 TPX Conductor	200
6.2 ITER Conductor	202
6.3 ITER Model Coil	205
6.4 Sultan Conductor	208
Chapter 7. Conclusions	225
7.1 Future Directions	226

Appendix A. Simple Application of Multiple Scale Expansion . . .	229
Appendix B. Consequences of Neglecting Helium Inertia	237
Appendix C. Discussion of the BC's Used in Quencher	245
Appendix D. Thermal Hydraulic Quench Back in CICC	251

Chapter 1

Introduction

Chapter 1. Introduction

Superconducting magnets have many applications in large government and industrial projects. They are particularly useful in situations where high magnetic fields are required but economic or technological considerations limit the total steady state electrical power available. Such projects include the toroidal and poloidal field coils for magnetic fusion experiments, the detector magnets for high energy particle accelerators, and the coils for magnetically levitated public transportation (MAGLEV). Because of the high construction costs involved, magnet protection in the event of faults or abnormal conditions is one of the crucial design elements. One of the more serious abnormal conditions is that of quenching, a situation wherein a local section of the magnet, because of some local heat perturbation, returns to its normal state. If the perturbation is large enough, neighboring sections of the magnet are subsequently quenched because of heat convection by the coolant. If the quench is not detected quickly enough, the normal zone propagates along the entire length of the coil, quenching the entire magnet. Late detection of quench may cause irreversible damage to the magnet.

Cable-In-Conduit Conductors (CICC) consist of a superconducting cable surrounded by supercritical helium [1,2]. The helium is used to cool the superconductor during steady state operation. The system of helium and cable is surrounded by a conduit usually made of stainless steel (Incoloy and Titanium have also been used). Figure 1.1 shows a schematic diagram of the cross section of a CICC;¹ typically the conduit has an overall diameter of the order of a few centimeters, while the conductor has a length of a few hundred meters. The Cable-In-Conduit is wrapped with insulating material and then wound in the form of a pancake or in layers and the superconducting magnet usually contains a number of such pancakes or layers.

¹ A different CICC configuration, where a central hole is placed in the conduit (Dual-Channel CICC) is used in certain superconducting magnets. This important configuration is discussed in Chapter 5.

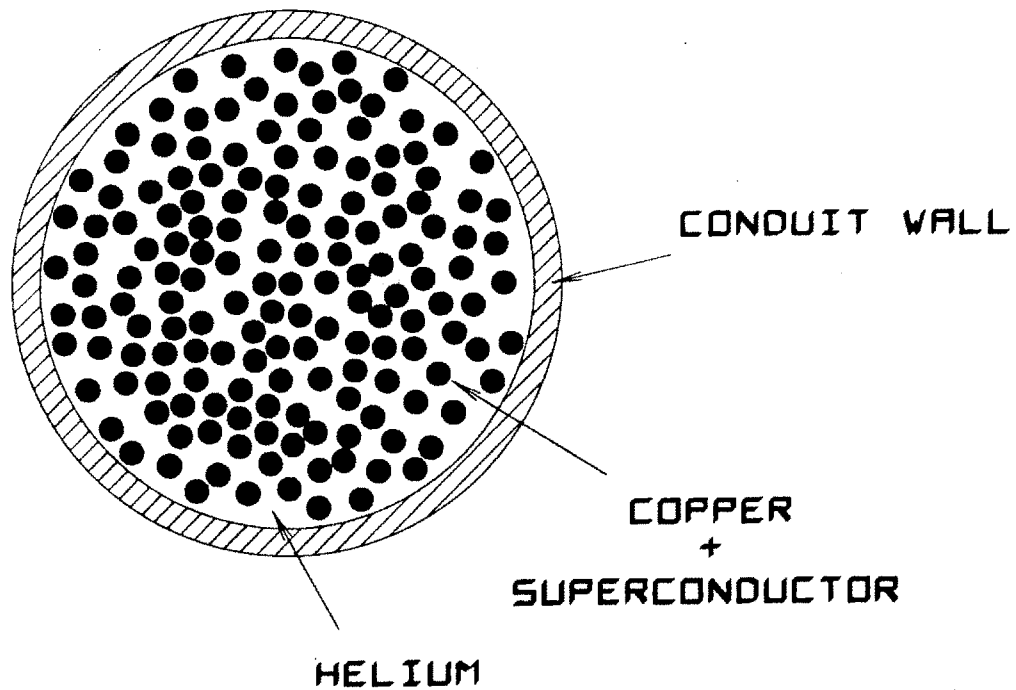


Figure 1.1: Schematic of the cross-sectional area of a CICC.

The superconducting cable consists of a large number of strands (10-1500) that enhance the heat transfer between the cable and the helium. These strands are made of a superconducting alloy embedded in a copper matrix. The alloy remains in its superconducting state when its temperature T lies below a critical value T_{cr} . Above T_{cr} , the alloy has a very high electrical resistivity. The copper matrix is used to carry the current in the event that the temperature in a section of the cable is raised above T_{cr} . In such a situation the current flows preferentially through the copper matrix which acts as a parallel resistor to the high resistivity, “quenched” section of the superconducting alloy. This allows for a large reduction of ohmic dissipation that would otherwise be present in the superconducting alloy. Even so, because of the high current flowing in the cable, it often takes only a few seconds for the quenched section of the cable to rise from its cryogenic temperature

$T \approx 5\text{K}$ and helium operating pressure $p \approx 5\text{ atm}$ to values of $T \approx 250\text{K}$ and $p \approx 25\text{ atm}$. Past this point, irreversible damage to the magnet can occur (e.g. thermal stresses become larger than the shear strength of the insulating material).

In designing the magnet it is of utmost importance to assure the safety of the magnet in the event of quench. The safety requirements consist of maintaining the temperatures below the melting point of any of the magnet components, and keeping the turn to turn and layer to layer voltages within the winding to acceptable levels to prevent arcing. In the event of a quench in the magnet, the voltage drop across the magnet (due to the resistive zone) can be monitored. When a certain critical voltage (V_{cr}) is observed across the magnet the current is dumped through an external parallel resistor. This resistor is chosen such that it provides the required discharge time constant.

The purpose of this thesis is to first present a new compact model that describes the process of quench in Cable-In-Conduit Superconducting Magnets, and a corresponding, efficient, numerical implementation. Secondly, this model is further simplified by means of several additional approximations valid for many superconducting magnets. This leads to a faster numerical procedure and an analytic solution. These analytic solutions represent the first such results that remain valid for the long time scales of interest during a quench process. Important analytic scalings are verified by direct comparisons with numerical as well as experimental data.

1.1 Existing Work

The process of quench propagation in CICC magnets has been known and qualitatively understood for many years [1,2,3]. Several excellent, sophisticated numerical codes have been developed to model quench events with sufficient accuracy for engineering design purposes [4,5]. These codes are fairly general in their engineering and physics content. Consequently, they have the advantage of being able to investigate not only quench propagation, but also other phenomena such

as stability. However, because of their generality (primarily to evaluate stability, a short time scale sequence of events) they often require large CPU time/run for quench simulation (typically several hours of CRAY time for a 3 second quench simulation), a disadvantage from the engineering design point of view. In fact this has been the primary motivation for the present work, and has led to a number of advances in the modelling of quench propagation.

In the past, a significant amount of the analytic work on the problem of quench propagation in CICC has been carried out by Dresner [3]. In fact, the quench propagation mechanism due to convection of helium, first considered by Dresner, is one of the central assumptions of the analytic work of this thesis. Other assumptions made here, however, differ greatly. Dresner's analysis makes use of an elegant similarity solution and is thus applicable to long coils. The specific assumptions introduced in his calculations result in a theory that is valid for relatively short times and low conductor temperatures ($T \lesssim 25$ K). As essentially the only existing analytic results treating the problem of quench in CICC magnets, Dresner's theory is used widely in the superconducting magnet community, although often in regimes where it is inapplicable [6] (i.e. the theoretical assumptions are not satisfied). In our analytic work we make use of some of the ideas of Dresner, but introduce an alternate set of approximations that make our solution valid over much longer periods of time (up to and including a full current dump) and higher temperatures ($T \lesssim 300$ K). Our analytic solutions are least accurate for very short times. The present theory is thus complementary to Dresner's theory. The main differences in modelling between the two theories of quench propagation are summarized in the main body of the thesis.

1.2 Present Work

This thesis is organized in seven chapters. In Chapter 2 a new simple, self consistent theoretical model is presented that describes the phenomena of quench propagation in Cable-In-Conduit superconducting magnets. The model circumvents many of the difficulties associated with obtaining numerical solutions in more general existing models. Specifically, a factor of 30-50 is gained in CPU time over the general, explicit time dependent codes used to study typical quench events. The corresponding numerical implementation of the new model (Quencher) is described in Chapter 3 where the numerical results are shown to agree very well with those of the more general models, as well as with experimental data.

In Chapter 4, the Quencher model presented in Chapter 3 is further simplified by considering a set of justified approximations. These simplifications first result in a faster quench model (MacQuench) that is suitable for studying quench on a personal computer (as opposed to powerful work-stations and CRAY supercomputers required by other codes). Secondly, a set of analytic solutions for the Quencher model is presented. The assumptions and the resulting simplifications that lead to the analytic solutions are discussed, and the regimes of validity of the various approximations are specified. The predictions of the analytic results are shown to be in very good agreement with numerical as well as experimental results. Important analytic scaling relations are verified by such comparisons, and the consequences of some of this scaling on currently designed superconducting magnets are discussed.

In Chapter 5, we present a theoretical model describing quench propagation in Cable-In-Conduit conductors with an additional central flow channel. The central channel is used to enhance the flow capabilities in the conduit during steady state operation as well as during quench events. Such a system is the proposed design for certain conductors in the International Thermonuclear Experimental Reactor (ITER). Here, the additional channel may be formed by a metal spring

or a porous tube located at the center of the conduit. We describe the separate thermal evolution in both the cable bundle and the central channel; in particular, the mass, momentum and heat transfer due to flow between the cable bundle and the central channel are included in the model. Several simplifications are introduced which greatly reduce the complexity of the model without sacrificing accuracy. The resulting reduced model is solved both numerically and approximately analytically.

In Chapter 6 we apply the tools developed in this thesis to study the quench behavior of certain conductors in their design phase. The numerical (Quencher and MacQuench) and analytic results are used and further compared in these studies. Important conclusions are drawn in regard to the quench behavior of the various conductors analyzed in this chapter. Finally, in Chapter 7 we summarize the important aspects of the thesis and discuss future directions for further research in the area of thermal-hydraulics in a CICC.

Chapter 1 References

- [1] Wilson, M. N., Superconducting Magnets, Oxford University Press, New York, 1983.
- [2] Dresner, L., *Superconducting stability, 1983: a review*, Cryogenics, Vol. 24, No. 6, 1984.
- [3] Dresner, L., *Protection Considerations for Forced-Cooled Superconductors*, 11th Symposium on Fusion Engineering, Proceedings Vol. 2, IEEE, New York, 1986.
- [4] Bottura, L., Zienkiewicz, O. C., *Quench Analysis of Large Superconducting Magnets Parts I and II*. Cryogenics, Vol. 32, No. 7, 1992.
- [5] Wong, R. L., *Program CICC Flow and Heat Transfer in Cable-In-Conduit Conductors – Equations & Verification*, Lawrence Livermore National Laboratory Internal Report, UCID 21733, May 1989.
- [6] Ando, T., Nishi, M., Kato, T., Yoshida, J., Itoh, N., Shimamoto, S., *Propagation Velocity of the Normal Zone in a Cable-In-Conduit Conductor*, Advances in Cryogenic Engineering, Vol. 35, Plenum Press, New York, 1990.

Chapter 2

Derivation of the Model

Chapter 2. Derivation of the Model

In this chapter we describe the quench model that forms the basis of the thesis. In order to derive this model we start with the three dimensional mass, momentum and energy conservation equations for the helium together with energy conservation relations for the conductor and the conduit wall (section 2.1). We first derive the general one dimensional model in section 2.2 and from this point we make certain approximations that are shown to be valid for the class of quench problems under consideration. This leads to the quench model presented in section 2.3 which is used in the remainder of the thesis.

2.1 General 3-D Model

The most general model that describes the thermal hydraulic behavior of the CICC consists of the three dimensional mass, momentum and energy conservation equations for the helium, together with the energy conservation equation of the conductor and that of the conduit wall. The detailed derivation of these equations from a macroscopic stand point is found in references [1,2], and the derivation of the helium equations based on kinetic models can be found in [3,4,5]. Below, we present the governing three dimensional equations for each of the CICC components.

The Conductor

The energy equation for the composite copper and superconductor material in each strand is given by

$$\left[\rho_c C_c(T_c) \frac{\partial T_c}{\partial t} = \nabla \cdot \kappa_c(T_c) \nabla T_c + Q_c(T_c, x, t) \right]_j \quad (2.1)$$

where the subscript c stands for the conductor, ρ denotes the density, T is the temperature, C is the specific heat, κ is the thermal conductivity, and S is the heat source in the conductor strands. The heat source Q_c represents the Joule heating that takes place in the copper, in regions where the conductor has become normal. This heat source is discussed in detail in section 2.3. Note that the subscript j is used to state that Eq. (2.1) is the governing equation of the j^{th} strand ($1 \leq j \leq N$, where N is the total number of strands). The ∇ operator is defined as $\nabla \equiv (\partial/\partial x)\mathbf{e}_x + (\partial/\partial y)\mathbf{e}_y + (\partial/\partial z)\mathbf{e}_z$, where we take the x and y directions to represent the cross-section of the CICC, and the z -axis to represent the axial length along the channel.

The conductor specific heat $\rho_c C_c$ and thermal conductivity κ_c comprise the copper and the superconductor contributions. These quantities are given by

$$\rho_c C_c = \frac{1}{A_c} [A_{cu} \rho_{cu} C_{cu} + A_{sc} \rho_{sc} C_{sc}] \quad (2.1a)$$

$$\kappa_c = \frac{A_{cu}}{A_c} \kappa_{cu} + \frac{A_{sc}}{A_c} \kappa_{sc} \quad (2.1b)$$

where the subscripts cu and sc are used to denote the copper and the superconductor, respectively. Also A represents the cross-sectional area, and $A_c = A_{cu} + A_{sc}$. The conductor properties are further discussed in Section 2.3, where we also discuss the properties of other material.

The Helium

The governing equations for the helium are the mass, momentum and energy conservation equations, together with the equation of state. These equations describe the turbulent (or laminar) flow of the helium in the conduit. In order to appropriately deal with the turbulent structure of the various quantities we use

the “Reynolds averaged” mass, momentum and energy equations [1,2,3]. These equations are given by

$$\frac{\partial \rho_h}{\partial t} + \nabla \cdot (\rho_h \mathbf{v}_h) = 0 \quad (2.2)$$

$$\rho_h \left(\frac{\partial}{\partial t} + \mathbf{v}_h \cdot \nabla \right) \mathbf{v}_h = -\nabla p_h - \nabla \cdot \boldsymbol{\tau}_h \quad (2.3)$$

$$\begin{aligned} \frac{\partial}{\partial t} \left[\rho_h \left(U_h + \frac{1}{2} v_h^2 \right) \right] + \nabla \cdot \left[\rho_h \mathbf{v}_h \left(U_h + \frac{1}{2} v_h^2 \right) \right] = \\ -\nabla \cdot \mathbf{q}_h - \nabla \cdot (p_h \mathbf{v}_h) - \nabla \cdot [\boldsymbol{\tau}_h \cdot \mathbf{v}_h] \end{aligned} \quad (2.4)$$

$$p_h = p_h(\rho_h, U_h) \quad (2.5)$$

where U_h is the internal energy of the helium.

Equations (2.2-2.4) evolve the fluid variables ρ_h , v_h , and U_h forward in time (the subscript h is used to denote the helium). Note that for turbulent flow in the conduit, all quantities correspond to “time averaged”, or “Reynolds averaged” variables [1,2,6-8]. (It is important to note that the averaging procedure for a compressible gas is defined differently than for an incompressible fluid [7,8].) The quantities $\boldsymbol{\tau}_h$ and \mathbf{q}_h include contributions from the Reynolds stress tensor (these quantities include the contribution of turbulent eddies which greatly influence both the stress and the heat distribution in the transverse (x,y) plane). The terms on the left-hand side of Eq. (2.3) describe the helium inertia, while the terms on the right-hand side represent the pressure gradient force and the friction force. In Eq. (2.4) the terms on the left-hand side represent convection of heat. The first term on the right-hand side involves the heat transfer due to turbulent convection in the cross-section as well as the heat conduction in the z-direction. The last two

terms are due to viscous dissipation, and the work done by pressure and viscous forces. Equation (2.5) is the equation of state for the helium.

The Conduit Wall

The energy equation of the conduit wall is similar to Eq. (2.1) and is given by

$$\rho_w C_w(T_w) \frac{\partial T_w}{\partial t} = \nabla \cdot \kappa_w(T_w) \nabla T_w \quad (2.6)$$

where we use the subscript w to denote the conduit wall. The quantities here are the obvious analogs to those in the conductor. Here, for simplicity of presentation, we ignore any heat sources that may be present in the conduit wall.

Before proceeding to obtain the relevant one dimensional equations (in the z -direction) we must specify the boundary conditions in the (x,y) plane. We delay discussing the initial condition and the boundary conditions in the z -direction until section 2.3. The boundary conditions in the (x,y) plane are as follows;

Conductor/Helium Interface

The heat flux boundary condition at the conductor/helium interface is taken to be the “Newton law of cooling” [1]. This boundary condition states that the heat flux leaving the surface of a single strand is proportional to $h_c(T_c - T_h)$. Here, h_c is the heat transfer coefficient, which for most cases, except laminar flow with a simple geometry, is determined experimentally. Thus we have

$$\mathbf{n} \cdot \mathbf{q}_c \Big|_{S_c} = -\mathbf{n} \cdot \mathbf{q}_h \Big|_{S_c} \quad (2.7a)$$

$$-\mathbf{n} \cdot \kappa_c \nabla T_c \Big|_{S_c} = h_c \left(T_c \Big|_{S_c} - \langle T_h \rangle \right) \quad (2.7b)$$

where the S_c denotes the conductor surface, and \mathbf{n} denotes the unit normal vector to S_c . Equation (2.7a) states that the jump in the heat flux is zero across the helium/conductor interface. The heat flux \mathbf{q}_c is defined as $\mathbf{q}_c \equiv -\kappa_c \nabla T_c$ (note that the helium heat flux \mathbf{q}_h is not defined in a similar manner since this flux includes the turbulent contribution in the (x,y)-direction). Also, note that the helium temperature in the last term of Eq. (2.7b) is not evaluated at the conductor/helium interface. This temperature (by definition) is taken to be the “bulk” temperature of the helium [1,8]. Equation (2.7b) is more of a definition for the heat transfer coefficient (h_c) than a “law”. The quantity h_c is measured experimentally and in general is a function of the average helium velocity in the z-direction as well as the helium temperature and density.

Each vector component of the helium velocity at the conductor/helium interface is zero. The perpendicular velocity is zero since no fluid crosses the interface, and the parallel velocity is taken to be zero in accord with the “no-slip” boundary condition. Thus we have

$$\mathbf{v} \Big|_{S_c} = 0 \quad (2.8)$$

Equations (2.7) and (2.8) are the required boundary conditions at the conductor/helium interface.

Conduit Wall/Helium Interface

The heat flux boundary condition at the wall/helium interface is similar to Eq. (2.7) and is given by

$$\mathbf{n} \cdot \mathbf{q}_w \Big|_{S_w} = -\mathbf{n} \cdot \mathbf{q}_h \Big|_{S_w} \quad (2.9a)$$

$$-\mathbf{n} \cdot \kappa_w \nabla T_w \Big|_{S_w} = h_w \left(T_w \Big|_{S_w} - \langle T_h \rangle \right) \quad (2.9b)$$

where S_w denotes the inner-wall surface, and \mathbf{n} is the unit normal vector to S_w . Note that the heat transfer coefficient h_w used in Eq. (2.9) is in general different than h_c used in Eq. (2.7). This is due to the different helium flow pattern within the conductor strands compared to the flow near the conduit wall. (The functional dependence of h_w is discussed in section 2.3).

The boundary condition for the helium velocity on the wall/helium interface is also similar to Eq. (2.8) and is given by

$$\mathbf{v} \Big|_{S_w} = 0 \quad (2.10)$$

Conduit Wall/Insulator Interface

The outer side of the conduit wall is taken to be well insulated such that

$$\mathbf{n} \cdot \mathbf{q}_w \Big|_{S_i} = -\mathbf{n} \cdot \kappa_w \nabla T_w \Big|_{S_i} = 0 \quad (2.11)$$

where S_i denotes the outer wall surface. This equation states that zero heat leaves the most outer radial-boundary of the CICC.

2.2 General 1-D Model

In this section, we derive the one dimensional equations (in the z-direction) that describe the thermal hydraulic behavior of a CICC. The use of 1-D equations in place of Eqs. (2.1–2.6) is the natural course to take when considering the large length to diameter ratio of the conduit. In the procedure that follows we use a multiple scale asymptotic expansion to derive the desired 1-D model. (For a simple illustrative example of the multiple scale expansion see appendix A.) We

define the expansion parameter $\epsilon \equiv d/L$, where L is the length of the conduit, and d represents the typical scale length in the (x,y) plane. Generally, for a CICC, $L \sim 100$ m and $d \sim 10^{-2}$ m, which results in $\epsilon \sim 10^{-4}$.

The Conductor

Following the procedure described in Appendix A, we expand the conductor temperature T_c as follows;

$$T_c(x, y, z, t) = T_{c0}(z, t) + T_{c2}(x, y, z, t) + \dots \quad (2.12)$$

where $T_{c2}/T_{c0} \sim \epsilon^2$ (here $\sim \epsilon$ indicates of the order of ϵ , or $O(\epsilon)$ [9]). Similarly, we expand the gradient operator as follows;

$$\nabla = \nabla_{\perp} + \frac{\partial}{\partial z} \mathbf{e}_z \quad (2.13)$$

where $(\partial/\partial z)/|\nabla_{\perp}| \sim \epsilon$. Using these expansions in Eq. (2.1) and keeping only the leading order terms (order ϵ^0) we find

$$\left[\rho_c C_{c0} \frac{\partial T_{c0}}{\partial t} = \frac{\partial}{\partial z} \kappa_{c0} \frac{\partial T_{c0}}{\partial z} + Q_{c0} + \nabla_{\perp} \cdot \kappa_{c0} \nabla T_{c2} \right]_j \quad (2.14)$$

Here $C_{c0} = C_c(T_{c0})$, and similarly for any other function of temperature $f(T)$, we have $f_0 \equiv f(T_0)$.

In a similar procedure as discussed in Appendix A, we integrate Eq. (2.14) over the cross-section of the j^{th} conductor strand. The result is given by

$$\left[\rho_c C_{c0} \frac{\partial T_{c0}}{\partial t} = \frac{\partial}{\partial z} \kappa_{c0} \frac{\partial T_{c0}}{\partial z} + Q_{c0} + \frac{1}{A_c} \int_{A_c} \nabla_{\perp} \cdot \kappa_{c0} \nabla_{\perp} T_{c2} dA \right]_j \quad (2.15)$$

where A denotes the cross-sectional area. This equation can be rewritten as

$$\left[\rho_c C_{c0} \frac{\partial T_{c0}}{\partial t} = \frac{\partial}{\partial z} \kappa_{c0} \frac{\partial T_{c0}}{\partial z} + Q_{c0} + \frac{1}{A_c} \oint_{S_c} [\mathbf{n} \cdot \kappa_{c0} \nabla_{\perp} T_{c2}] dS \right]_j \quad (2.16)$$

where we have used Gauss's theorem to manipulate the last term on the right-hand side of this relation. Equation (2.16) is the "solvability condition" (or the integrability condition) for T_{c2} . The last term on the right-hand side of this equation represents the heat loss from the radial boundary of a given strand. Using Eq. (2.7b) we write this term as follows;

$$\begin{aligned} \left[\oint_{S_c} [\mathbf{n} \cdot \kappa_{c0} \nabla_{\perp} T_{c2}] dS \right]_j &= - \left[\oint_{S_c} h_{c0} (T_{c0} - \langle T_h \rangle) dS \right]_j \\ &= - [h_{c0} (T_{c0} - \langle T_h \rangle) P_c]_j \end{aligned} \quad (2.17)$$

where $[P_c]_j$ is the perimeter of the j^{th} conductor strand. We now write Eq. (2.16) as follows

$$\left[\rho_c C_{c0} \frac{\partial T_{c0}}{\partial t} = \frac{\partial}{\partial z} \kappa_{c0} \frac{\partial T_{c0}}{\partial z} + Q_{c0} + \frac{h_{c0} P_c}{A_c} (\langle T_h \rangle - T_{c0}) \right]_j \quad (2.18)$$

This is the one-dimensional heat conduction equation for the j^{th} conductor strand.

The Helium

We follow a similar procedure as above to obtain the 1-D conservation equations for the helium. The appropriate expansion for the various quantities of interest are given by

$$U_h = U_{h0}(z, t) + U_{h2}(x, y, z, t) + \dots \quad (2.19a)$$

$$T_h = T_{h0}(z, t) + T_{h2}(x, y, z, t) + \dots \quad (2.19b)$$

$$\rho_h = \rho_{h0}(z, t) + \rho_{h2}(x, y, z, t) + \dots \quad (2.19c)$$

$$p_h = p_{h0}(z, t) + p_{h2}(x, y, z, t) + \dots \quad (2.19d)$$

$$\mathbf{v}_h = v_{h0}(x, y, z, t) \mathbf{e}_z + \mathbf{v}_{\perp 1}(x, y, z, t) + \dots \quad (2.19e)$$

where for any quantity f we have $f_n/f_0 \sim \epsilon^n$. Note that $\langle T_h \rangle = T_{h0}$. Using this expansion in Eq. (2.2) and keeping terms of order ϵ^0 , we find

$$\frac{\partial \rho_{h0}}{\partial t} + \frac{\partial}{\partial z}(\rho_{h0} v_{h0}) + \rho_{h0} \nabla_{\perp} \cdot \mathbf{v}_{\perp 1} = 0 \quad (2.20)$$

as the leading order mass conservation equation.

To eliminate the last term on the left-hand side of Eq. (2.20), we integrate this equation over the helium cross-sectional area. The result is given by

$$\frac{\partial \rho_{h0}}{\partial t} + \frac{\partial}{\partial z} \left(\rho_{h0} \frac{1}{A_h} \int_{A_h} v_{h0} dA \right) + \rho_{h0} \frac{1}{A_h} \oint_{S_c+S_w} [\mathbf{n} \cdot \mathbf{v}_{\perp 1}] dS = 0 \quad (2.21)$$

The last term on the left-hand side of this equation is zero by virtue of Eqs. (2.8) and (2.10). Therefore we find

$$\frac{\partial \rho_{h0}}{\partial t} + \frac{\partial}{\partial z}(\rho_{h0} \overline{v_{h0}}) = 0 \quad (2.22)$$

as the 1-D mass conservation equation for the helium. The area-averaged velocity (in the z -direction) is defined as

$$\overline{v_{h0}} \equiv \frac{1}{A_h} \int_{A_h} v_{h0} dA \quad (2.23)$$

Before proceeding to the momentum conservation relation we must discuss the stress tensor $\boldsymbol{\tau}_h$. This tensor is approximated by various different schemes [6]. In the discussions that follow we assume that

$$\boldsymbol{\tau}_h = -\mu_T \nabla \mathbf{v} \quad (2.24)$$

where the quantity μ_T is the eddy-viscosity which in general is much larger than the molecular viscosity μ_h . We assume $\mu_T \sim \epsilon^2$. It should be noted that this choice of representation for τ_h is solely for ease of notation. In principle for any given stress tensor we can consider a separate asymptotic expansion for τ_h . This leads to exactly the same results as presented below, with a much more tedious notation.

In view of the above discussion, the leading order momentum equation in the z-direction is given by

$$\rho_{h0} \left(\frac{\partial}{\partial t} + v_{h0} \frac{\partial}{\partial z} + \mathbf{v}_{\perp 1} \cdot \nabla_{\perp} \right) v_{h0} = -\frac{\partial p_{h0}}{\partial z} + \nabla_{\perp} \cdot \mu_T \nabla_{\perp} v_{h0} \quad (2.25)$$

The term $\nabla_{\perp} \cdot (\mu_T \nabla_{\perp} v_{h0})$, may appear to be a term of order $1/\epsilon^2$. However, for the class of problems under consideration, due to the small size of $\mu_T \sim \epsilon^2$, this term is balanced by the zeroth order equation.

Next, we integrate Eq. (2.25) over the helium cross-sectional area to obtain

$$\frac{\partial}{\partial t} (\rho_{h0} \overline{v_{h0}}) + \frac{\partial}{\partial z} (\rho_{h0} \overline{v_{h0}^2}) = -\frac{\partial p_{h0}}{\partial z} + \frac{1}{A_h} \oint_{S_c + S_w} [\mathbf{n} \cdot \mu_T \nabla_{\perp} v_{h0}] dS \quad (2.26)$$

The last term in this equation represents the friction force between the helium and the solid surfaces. This force is generally determined experimentally since the solution of the turbulent flow in the (x,y) plane is *not* known. In this regard it is customary to define the friction factor f as follows

$$\begin{aligned} -\frac{f \rho_{h0} \overline{|v_{h0}| v_{h0}}}{2d_h} &\equiv \frac{1}{A_h} \oint_{S_c + S_w} \mu_T [\mathbf{n} \cdot \nabla_{\perp} v_{h0}] dS \\ &= -\frac{1}{A_h} \oint_{S_c + S_w} [\mathbf{n} \cdot \boldsymbol{\tau}_h]_z dS \end{aligned} \quad (2.27)$$

(Note the analogy between this definition and the definition of the heat transfer coefficient given by Eq. (2.7).) The experimental measurements of the friction

force are presented in the form of curves of the dimensionless parameter f versus the Reynolds number R (here $R \equiv \rho_0 d_h \overline{v_{h0}} / \mu_h$, where μ_h is the physical viscosity of the helium and d_h is the hydraulic diameter). The hydraulic diameter is given by four times the helium area, divided by the total wetted surface in the conduit; $d_h = 4A_h / (P_c + P_w)$ where P_c is the perimeter of all of the conductor strands and P_w is the wetted-perimeter of the wall. The functional dependence of f is discussed in section 2.3.

Using Eqs. (2.26) and (2.27), we obtain

$$\frac{\partial}{\partial t}(\rho_{h0} \overline{v_{h0}}) + \frac{\partial}{\partial z}(\rho_{h0} \overline{v_{h0}^2}) = -\frac{\partial p_{h0}}{\partial z} - \frac{f \rho_{h0} |\overline{v_{h0}}| \overline{v_{h0}}}{2d_h} \quad (2.28)$$

Note that in this equation an additional unknown $\overline{v_{h0}^2}$ is introduced. In order to continue without requiring additional equations for determining $\overline{v_{h0}^2}$, we make the following approximation

$$\overline{v_{h0}^2} \approx \overline{v_{h0}}^2 \quad (2.29)$$

This approximation is generally satisfied for turbulent velocity profiles in a conduit, and to a lesser extent for a laminar velocity profile [2]. (Errors of up to $\sim 10\%$ may be introduced with this approximation, although for quench this whole term is unimportant.) Using Eq. (2.29), we have

$$\rho_{h0} \frac{\partial \overline{v_{h0}}}{\partial t} + \rho_{h0} \overline{v_{h0}} \frac{\partial \overline{v_{h0}}}{\partial z} = -\frac{\partial p_{h0}}{\partial z} - \frac{f \rho_{h0} |\overline{v_{h0}}| \overline{v_{h0}}}{2d_h} \quad (2.30)$$

This is the desired 1-D momentum conservation equation for the helium.

Before proceeding to the energy conservation relation we briefly discuss the heat flux \mathbf{q}_h appearing in Eq. (2.4). We write \mathbf{q}_h in the following form

$$\mathbf{q}_h = q_0 \mathbf{e}_z + \mathbf{q}_\perp \quad (2.31)$$

Note that the fluid turbulence takes place predominantly in the (x,y) plane and thus the quantity q_0 is given by

$$q_0(z, t) = -\kappa_{h0} \frac{\partial T_{h0}}{\partial z} \quad (2.32)$$

where κ_{h0} is the physical thermal conductivity of the helium. In the perpendicular direction we assume the following form for \mathbf{q}_\perp ;

$$\mathbf{q}_\perp = -\kappa_T \nabla_\perp T_h = -\kappa_T \nabla_\perp T_{h2} \quad (2.33)$$

where κ_T is the eddy-thermal conductivity. This relation is analogous to Eq. (2.24). Again, using other forms for κ_T does not effect the final 1-D helium energy equation obtained below.

The helium energy equation to leading order is now given by

$$\begin{aligned} \frac{\partial}{\partial t} \left[\rho_{h0} \left(U_{h0} + \frac{1}{2} v_{h0}^2 \right) \right] + \frac{\partial}{\partial z} \left[\rho_{h0} v_{h0} \left(U_{h0} + \frac{1}{2} v_{h0}^2 \right) \right] \\ + \nabla_\perp \cdot \left[\rho_{h0} \mathbf{v}_\perp \left(U_{h0} + \frac{1}{2} v_{h0}^2 \right) \right] = \frac{\partial}{\partial z} \kappa_{h0} \frac{\partial T_{h0}}{\partial z} + \nabla_\perp \cdot \kappa_T \nabla_\perp T_{c2} \\ - \frac{\partial}{\partial z} (p_{h0} v_{h0}) - \nabla_\perp \cdot (p_{h0} \mathbf{v}_{\perp 1}) - \nabla_\perp \cdot [\boldsymbol{\tau}_h \cdot \mathbf{v}_h] \end{aligned} \quad (2.34)$$

We integrate this equation over the helium cross-sectional area to obtain

$$\begin{aligned} \rho_{h0} \left(\frac{\partial}{\partial t} + \overline{v_{h0}} \frac{\partial}{\partial z} \right) \left(U_{h0} + \frac{1}{2} \overline{v_{h0}^2} \right) = \frac{\partial}{\partial z} \kappa_{h0} \frac{\partial T_{h0}}{\partial z} \\ + \frac{1}{A_h} \oint_{S_c + S_w} [\mathbf{n} \cdot \kappa_T \nabla_\perp T_{h2}] dS - \frac{\partial}{\partial z} (p_{h0} \overline{v_{h0}}) \end{aligned} \quad (2.35)$$

where we have used Eqs. (2.8) and (2.10) to equate certain boundary terms to zero. Note that in obtaining this equation we have also assumed

$$\overline{v_{h0}^3} \approx \overline{v_{h0}}^3 \quad (2.36)$$

based on a similar argument that leads to Eq. (2.29). Furthermore, the left-hand side of Eq. (2.35) has been rearranged by using the mass relation.

It is more convenient to consider a different form of the energy conservation relation involving the helium temperature T_h , instead of U_h . To proceed, we multiply Eq. (2.30) by $\overline{v_{h0}}$ and subtract the resulting equation from Eq. (2.35). The result is given by

$$\begin{aligned} \rho_{h0} \left(\frac{\partial}{\partial t} + \overline{v_{h0}} \frac{\partial}{\partial z} \right) U_{h0} &= \frac{\partial}{\partial z} \kappa_{h0} \frac{\partial T_{h0}}{\partial z} + \frac{1}{A_h} \oint_{S_c + S_w} [\mathbf{n} \cdot \kappa_T \nabla_{\perp} T_{c2}] dS \\ &\quad - p_{h0} \frac{\partial \overline{v_{h0}}}{\partial z} + \frac{f \rho_{h0} |\overline{v_{h0}}| \overline{v_{h0}}^2}{2d_h} \end{aligned} \quad (2.37)$$

Next, we use the thermodynamic relation $U_{h0} = U_{h0}(\rho_{h0}, T_{h0})$, in order to manipulate the left hand side of Eq. (2.35) as follows;

$$\frac{\partial U_{h0}}{\partial t} = \left(\frac{\partial U_{h0}}{\partial \rho_{h0}} \right)_{T_{h0}} \frac{\partial \rho_{h0}}{\partial t} + \left(\frac{\partial U_{h0}}{\partial T_{h0}} \right)_{\rho_{h0}} \frac{\partial T_{h0}}{\partial t} \quad (2.38)$$

$$\frac{\partial U_{h0}}{\partial z} = \left(\frac{\partial U_{h0}}{\partial \rho_{h0}} \right)_{T_{h0}} \frac{\partial \rho_{h0}}{\partial z} + \left(\frac{\partial U_{h0}}{\partial T_{h0}} \right)_{\rho_{h0}} \frac{\partial T_{h0}}{\partial z} \quad (2.39)$$

Multiplying Eq. (2.39) by $\overline{v_{h0}}$ and adding the result to Eq. (2.38), we find

$$\frac{\partial U_{h0}}{\partial t} + \overline{v_{h0}} \frac{\partial U_{h0}}{\partial z} = - \left(\frac{\partial U_{h0}}{\partial \rho_{h0}} \right)_{T_{h0}} \rho_{h0} \frac{\partial \overline{v_{h0}}}{\partial z} + C_{h0} \left(\frac{\partial T_{h0}}{\partial t} + \overline{v_{h0}} \frac{\partial T_{h0}}{\partial z} \right) \quad (2.40)$$

In deriving this equation we have used Eq. (2.22), together with the definition of the specific heat at constant volume, given by

$$C_{h0} = \left(\frac{\partial U_{h0}}{\partial T_{h0}} \right)_{\rho_{h0}} \quad (2.41)$$

Next we use the thermodynamic identity given by [1,7]

$$\left(\frac{\partial U_{h0}}{\partial \rho_{h0}} \right)_{T_{h0}} = - \frac{1}{\rho_{h0}^2} [-p_{h0} + T_{h0} \rho_{h0} C_{\beta 0}] \quad (2.42)$$

where

$$C_{\beta 0} \equiv \frac{1}{\rho_{h0}} \frac{\partial}{\partial T_{h0}} p_{h0}(\rho_{h0}, T_{h0}) \quad (2.43)$$

Using Eqs. (2.40) and (2.42) we obtain the following form of the energy conservation equation;

$$\begin{aligned} \rho_{h0} C_{h0} \left(\frac{\partial T_{h0}}{\partial t} + \overline{v_{h0}} \frac{\partial T_{h0}}{\partial z} \right) + \rho_{h0} T_{h0} C_{\beta 0} \frac{\partial \overline{v_{h0}}}{\partial z} = \frac{\partial}{\partial z} \kappa_{h0} \frac{\partial T_{h0}}{\partial z} \\ + \oint_{S_c + S_w} [\mathbf{n} \cdot \kappa_T \nabla_{\perp} T_{c2}] dS \\ + \frac{f \rho_{h0} |\overline{v_{h0}}| \overline{v_{h0}}^2}{2d_h} \end{aligned} \quad (2.44)$$

The final step is to consider a similar simplification as was used in Eq. (2.17). Such a simplification, together with the boundary conditions given by Eqs. (2.9) and (2.11) results in

$$\begin{aligned} \rho_{h0} C_{h0} \left(\frac{\partial T_{h0}}{\partial t} + \overline{v_{h0}} \frac{\partial T_{h0}}{\partial z} \right) + \rho_{h0} C_{\beta 0} T_{h0} \frac{\partial \overline{v_{h0}}}{\partial z} = \\ + \frac{1}{A_h} \left[\sum_{j=1}^N [P_c h_{c0} (T_{c0} - T_{h0})]_j + P_w h_{w0} (T_{w0} - T_{h0}) \right] \\ + \frac{\partial}{\partial z} \kappa_{h0} \frac{\partial T_{h0}}{\partial z} + \frac{f \rho_{h0} |\overline{v_{h0}}| \overline{v_{h0}}^2}{2d_h} \end{aligned} \quad (2.45)$$

This is the desired 1-D energy conservation equation for the helium. Note that this equation is coupled to the N conductor strand equations plus the energy equation of the conduit wall. Below, after discussing the conduit wall, we present a compact (usable) form of this equation by performing the sum that appears on the right hand side. Also note that for a typical flow of helium in the conduit, the thermal conduction is much less than the heat convection. Specifically, comparing the

conduction term to the convective term, we have $(\kappa_{h0}T'_{h0})' / \rho_{h0}C_{h0}\overline{v_{h0}}T'_{h0} \sim \kappa_{h0} / \rho_{h0}C_{h0}\overline{v_{h0}}L$, where L is the characteristic length scale in the z -direction. For a typical flow in a CICC we have, $\kappa_{h0} \sim 0.1$ W/m-K, $\rho_{h0} \sim 100$ kg/m³, $C_{h0} \sim 1000$ W/kg-K, $\overline{v_{h0}} \sim 1$ m/sec, and $L \sim 10$ m, which results in $\kappa_{h0} / \rho_{h0}C_{h0}\overline{v_{h0}}L \sim 10^{-7}$! Thus, it is well justified to neglect the conduction term in Eq. (2.45).

The Conduit Wall

The conduit wall is treated in exactly the same manner as the conductor. Using a similar expansion for T_w as given by Eq. (2.12), retaining the leading order terms in Eq. (2.6), and integrating over the conduit wall area, we have

$$\rho_w C_{w0} \frac{\partial T_{w0}}{\partial t} = \frac{\partial}{\partial z} \kappa_{w0} \frac{\partial T_{w0}}{\partial z} + \frac{1}{A_w} \oint_{S_w + S_i} [\mathbf{n} \cdot \kappa_{w0} \nabla_{\perp} T_{w2}] dS \quad (2.46)$$

By using Eqs. (2.9) and (2.46), we find

$$\rho_w C_{w0} \frac{\partial T_{w0}}{\partial t} = \frac{\partial}{\partial z} \kappa_{w0} \frac{\partial T_{w0}}{\partial z} + \frac{h_{w0} P_w}{A_w} (T_{h0} - T_{w0}) \quad (2.47)$$

This is the desired 1-D heat equation for the conduit wall.

Before proceeding to the quench model, we summarize a more convenient form of Eqs. (2.18,22,30,45,47), where we perform the summation that appears on the right hand side of Eq. (2.45).

Summary of the Conductor Equation

The zeroth-order equations for all the conductor strands are mathematically identical. This is evident from Eq. (2.18) after replacing $\langle T_h \rangle$ by T_{h0} . Thus we may add all the strand equations to arrive at a single equation for the whole conductor. This equation is given by

$$\rho_c C_c(T_c) \frac{\partial T_c}{\partial t} = \frac{\partial}{\partial z} \kappa_c(T_c) \frac{\partial T_c}{\partial z} + Q_c(T_c, x, t) + \frac{h_c P_c}{A_c} (T_h - T_c) \quad (2.48)$$

where P_c and A_c are the total perimeter and the total cross-sectional area, respectively, of the conductor. For convenience we have dropped the 0 subscript.

Equation (2.48) is a heat diffusion equation for the total assembly of conductor strands, each strand assumed indistinguishable from all others. The quantity Q_c is the heat source existing in the conductor strands. This source is due to the joule heating that occurs in conductor regions where the temperature is above the critical temperature T_{cr} ; that is, in regions where the conductor is normal. The source is given by

$$Q_c(T_c, x, t) = \eta_c J^2 H(T_c) \quad (2.49)$$

where $J(t) = I(t)/A_{cu}$ is the current density in the copper, $I(t)$ is the prescribed current in the conductor, A_{cu} is the fractional area of A_c occupied by copper, $\eta_c(T_c, B)$ is the resistivity of copper (a strong function of the temperature), $B(x, t)$ is the magnetic field in the cable, and H is a Heaviside-like transition function from the normal to superconducting regions. $H(T_c)$ is illustrated in Fig. 2.1. Note that in this figure the critical temperature is a function of the B-field; $T_{cr} = T_{cr}(B)$. Similarly, $T_{cs} = T_{cs}(I, B)$. (More information about these quantities may be found in reference [1] of Chapter 1.)

Summary of the Helium Equations

The 1-D mass, momentum and energy conservation equations for the helium are given by

$$\frac{\partial \rho_h}{\partial t} + \frac{\partial}{\partial z}(\rho_h v_h) = 0 \quad (2.50)$$

$$\rho_h \frac{\partial v_h}{\partial t} + \rho_h \frac{\partial v_h}{\partial z} = -\frac{\partial p_h}{\partial z} - \frac{f \rho_h |v_h| v_h}{2d_h} \quad (2.51)$$

$$\begin{aligned} \rho_h C_h \left(\frac{\partial T_h}{\partial t} + v_h \frac{\partial T_h}{\partial z} \right) + \rho_h C_\beta T_h \frac{\partial v_h}{\partial z} &= \frac{h_c P_c}{A_h} (T_c - T_h) \\ &+ \frac{h_w P_w}{A_h} (T_w - T_h) + \frac{f \rho_h |v_h| v_h^2}{2d_h} \end{aligned} \quad (2.52)$$

where for convenience, we have drop the 0 subscript and the over-bars. Again, the friction factor $f(\rho_h, T_h, v_h)$ models the turbulent friction between the solid components and the helium, and its functional dependence is assumed known from experimental measurements. The quantity d_h is the hydraulic diameter given by $4A_h/(P_w + P_c)$.

In Eq. (2.52) the terms on the left-hand side represent convection and compressibility, respectively. The quantity $C_h(\rho_h, T_h)$ is the specific heat of helium at constant volume, and $C_\beta(\rho_h, T_h)$ is defined as $C_\beta \equiv (1/\rho_h) \partial p_h(\rho_h, T_h) / \partial T_h = -\rho_h \partial \hat{S}(\rho_h, T_h) / \partial \rho_h$ where \hat{S} is the entropy. The first two terms on the right-hand side involve the heat transfer coefficients $h_c(\rho_h, T_h, v_h)$ and $h_w(\rho_h, T_h, v_h)$, and account for the heat exchange between the helium and the solid components. These coefficients model the turbulent heat transfer taking place in the helium, and their values are assumed known from experimental correlations. The last term on the right-hand side of Eq. (2.52) represents the viscous (frictional) heating of the helium. The thermal conduction in the helium has been neglected because its value is small compared to the convective terms.

Summary of the Conduit Wall Equation

The one dimensional energy conservation equation for the conduit wall is given by

$$\rho_w C_w(T_w) \frac{\partial T_w}{\partial t} = \frac{\partial}{\partial z} \kappa_w(T_w) \frac{\partial T_w}{\partial z} + \frac{h_w P_w}{A_w} (T_h - T_w) \quad (2.53)$$

where for convenience we have dropped the 0 subscript. Note that the thermal properties C_w and κ_w are functions of T_w .

Equations (2.48–53) describe the basic core of superconducting magnet thermofluid models. Even though they are “only” one dimensional plus time, they are difficult to solve numerically for quench events, almost always requiring at least several hours of CRAY CPU time for such simulations. There are fundamental reasons for these difficulties as discussed below.

Consider the typical parameters characterizing a quench event in a large superconducting magnet. The time scale of interest is ~ 1 sec to a few minutes, during which the quench region expands in length, starting from a few centimeters and reaching tens of meters in conductors of total length ~ 100 -1000 m. During this time the temperature of the system behind the quench front rises from cryogenic values of ~ 5 K to near room temperature. Over this large temperature range several of the thermal properties of the system (C_c, C_w, η_c) increase by two to three orders of magnitude. This is the first of the computational difficulties.

Next, note that the dominant mechanism for propagating the quench front in a CICC is convection of helium. The joule heated normal conductor heats the adjacent helium which is then convected away from the quench zone. The leading edge of the hot gas then heats conductor material still in its superconducting state ahead of the quench zone. This heat causes the conductor to go normal thus increasing the size of the quench zone. Essentially, the high temperature helium

gas expands like a bubble against the cold helium ahead of the quench front, thereby propagating the quench as it comes in contact with the cold conductor. Typically, the quench front may be several centimeters wide out of total conductor length of 100-1000 m. This narrow moving boundary layer is the second of the computational difficulties.

The third computational problem is a consequence of the fact that typical quench velocities are of the order 1-10 m/sec, which are much slower than the speed of sound c in the helium: $v_h/c \sim 0.01$. Thus, explicit time advance algorithms require a very large number of integration time steps ($\sim 10^4$), because of the Courant condition, significantly increasing the CPU time required.

The final difficulty is a result of the high heat transfer between the conductor and the helium arising from the large wetted-perimeter of the combined conductor strands. The net effect is that the thermal coupling terms $\sim h_c(T_c - T_h)/d_h$ in Eqs. (2.48) and (2.52) are characterized by $h_c/d_h \rightarrow \infty, T_c - T_h \rightarrow 0$, the classic situation of a mathematically stiff set of equations.

To summarize, the one dimensional core model presented here will be shown to accurately describe a variety of phenomena in superconducting magnets including the important problem of quench propagation. However, numerical simulations using the full model are costly in terms of CPU time because of four problems,

1. Large variations in the physical properties.
2. A very narrow moving boundary layer.
3. Highly subsonic flow velocities.
4. High heat transfer between the various CICC components.

2.3 The Quench Model

The numerical difficulties just described can be greatly alleviated by focussing attention solely on the phenomena of quench. As a result, additional analytic approximations can be made which exploit the subsonic flow velocity and high heat transfer characteristic of quench in long CICC. Furthermore, a sophisticated numerical solver discussed in chapter 3 substantially reduces the difficulties associated with the moving boundary layer. This solver also has no great difficulty treating the large variation in the material properties.

In this section we describe the analytic approximations used to simplify the general model and show that the errors involved are indeed small for engineering purposes. The numerical issues are discussed in the following chapter.

High Heat Transfer Approximation

During the quench process in a CICC the heat transfer between the conductor and the helium is very high. This is due to the large wetted-perimeter of the conductor ($P_c \approx 1$ m) in contact with the helium, as well as the high value of the heat transfer coefficient $h_c \approx 1000$ W/m²-K. For example, consider an assembly of conductor strands with $A_c \approx 10^{-4}$ m², $\rho_c C_c \approx 10^6$ W/m³-K, and a characteristic quench time scale $\tau \approx 5$ sec. Next, balance the time derivative term on the left-hand side of Eq. (2.48) with the heat transfer term on the right-hand side. We find $(T_h - T_c)/T_c \approx A_c \rho_c C_c / h_c P_c \tau \approx 0.02$. The high heat transfer forces the temperature difference between the conductor and the helium to be small. We exploit this fact by annihilating the heat transfer terms in Eqs. (2.48) and (2.52) (by adding appropriate linear combinations of the two equations) and then setting $T_c \approx T_h \equiv T$. This results in a single energy equation for T , the temperature of the conductor and the helium. We have thus eliminated mathematically stiff terms from the system.

A related problem associated with mathematical stiffness concerns the conduit wall. Its thermal conductivity is generally small. Typically, $\kappa_w/\kappa_c \approx 10^{-3} \ll 1$, which justifies neglecting the conduction term in this equation. Doing so eliminates another mathematically stiff term from the system.

Note that in general the heat transfer between the helium and the conduit is not as good as for the helium and the conductor since $P_w \ll P_c$. The implication is that the conduit temperature can lag behind the helium temperature by a finite amount. Hence, it is *not* a good approximation to set $T_w \approx T_h$ as was done for the conductor. It is for this reason that the quench model maintains two temperatures T and T_w .

The Subsonic Flow Approximation

The helium flow characteristics in the CICC are dominated by the friction between the cable strands and the helium. The friction force is quite high due to the small hydraulic diameter of the channel (typically $d_h \approx 10^{-3}$ m), and in the momentum equation it is balanced primarily by the pressure gradient force. In other words, the helium inertia $\rho dv/dt$ is small compared to either of the terms on the right-hand side of Eq. (2.51). As an example consider a helium density of 100 kg/m^3 , $v \approx 5 \text{ m/sec}$, $\tau \approx 5 \text{ sec}$, $L \approx 100 \text{ m}$ and a pressure drop of $\Delta p \approx 10 \text{ atm}$. Comparing terms we have $\rho v L / \Delta p \tau \sim 10^{-2}$. On this basis, the helium inertia is neglected in the momentum equation. In terms of wave propagation, the large friction and corresponding subsonic flow velocities cause sound waves to be highly damped in these channels.

In order to place these arguments on a more firm ground we consider a mathematical justification of neglecting the helium inertia. For simplicity we consider the adiabatic flow of helium in the conduit (the non-adiabatic case leads to the same conclusions). The mass and momentum conservation relations are given by Eqs. (2.50) and (2.51), repeated here for convenience;

$$\frac{\partial \rho_h}{\partial t} + \frac{\partial}{\partial z}(\rho_h v_h) = 0 \quad (2.54)$$

$$\rho_h \frac{\partial v_h}{\partial t} + \rho_h v_h \frac{\partial v_h}{\partial z} = -\frac{\partial p_h}{\partial z} - \frac{f \rho_h |v_h| v_h}{2d_h} \quad (2.55)$$

For an adiabatic flow, this system is mathematically closed by noting that the entropy $\hat{S}_h = \hat{S}_0 = \text{const.}$ We consider normalizing Eqs. (2.54–55) by using the following definitions $\hat{\rho} \equiv \rho_h/\rho_0$, $\hat{v} \equiv v_h/v_0$, $\hat{p} \equiv p_h/p_0$, $\hat{z} \equiv z/L$, and $\hat{t} \equiv tv_0/L$. Here, ρ_0 , p_0 and v_0 are taken to be the characteristic density, pressure and flow velocity of the helium in the conduit. The typical scale length in the axial direction is represented by L . Note that for a given quantity f , the normalization is such that $\hat{f} \sim 1$. By using these definitions, Eqs. (2.54) and (2.55) can be rewritten as

$$\frac{p_0/\rho_0}{c^2} \left(\frac{\partial \hat{p}}{\partial \hat{t}} + \hat{v} \frac{\partial \hat{p}}{\partial \hat{z}} \right) + \hat{\rho} \frac{\partial \hat{v}}{\partial \hat{z}} = 0 \quad (2.56)$$

$$\hat{\rho} \left(\frac{\partial \hat{v}}{\partial \hat{t}} + \hat{v} \frac{\partial \hat{v}}{\partial \hat{z}} \right) = \frac{p_0/\rho_0}{v_0^2} \left(-\frac{\partial \hat{p}}{\partial \hat{z}} \right) - \left(\frac{fL}{2d_h} \right) \hat{\rho} \hat{v}^2 \quad (2.57)$$

where we have eliminated the helium density in terms of the pressure through the thermodynamic relation $p_h = p_h(\hat{S}_0, \rho_h)$. The quantity c is the speed of sound in the helium defined as

$$c \equiv \left(\frac{\partial p_h}{\partial \rho_h} \Big|_{\hat{S}} \right)^{1/2} \quad (2.58)$$

From Eqs. (2.56) and (2.57), we now easily obtain the condition that allows the neglect of the helium inertia. This condition is given by

$$\frac{fL}{d_h} \sim \frac{p_0/\rho_0}{v_0^2} \gg 1 \quad (2.59)$$

During a quench in a typical CICC, $p_0 \sim 5 \times 10^5 \text{ N/m}^2$, $\rho_0 \sim 100 \text{ kg/m}^3$, and $v_0 \sim 5 \text{ m/sec}$, which results in $p_0/\rho_0 v_0^2 \sim 200$. It is important to note that the flow of

helium in the conduit is highly compressible since the quantity p_0/ρ_0c^2 , appearing in Eq. (2.56) is of order unity. For a flow to be considered incompressible we must have $p_0/\rho_0c^2 \ll 1$. Thus neglecting helium inertia does not imply an infinite sound velocity in the helium. Even so, sound propagation in the form of waves is no longer admitted when we neglect the inertia term. For a compressible gas, Eq. (2.59) corresponds to having a low Mach number flow in the conduit.

A somewhat subtle question arises in regard to observing the flow variables such as v_h at some distance $x = L$ away from the zone of “action” $x = 0$. The speed of sound time delay (L/c) is not present in the solution when inertia is neglected (typically $c \approx 200$ m/sec). Thus, for a certain period (until the sound wave reaches $x = L$) the solution for, say v_h , is unphysical for this case. This issue is discussed in detail in Appendix B, where we show that for low Mach numbers, and for $t > L/c$ the solution obtained by neglecting the inertia is an excellent approximation to v_h .

Neglect of the helium inertia allows us to eliminate the shortest time scale from the problem (i.e., sound wave propagation time scale). Thus, the quench event can be followed on the helium velocity time scale, which is approximately two orders of magnitude slower.

The Quench Model

In view of the above simplifications, the final quench model reduces to

$$\frac{\partial \rho}{\partial t} + \frac{\partial}{\partial z}(\rho v) = 0 \quad (2.60)$$

$$\frac{\partial p}{\partial z} = -\frac{f \rho v |v|}{2d_h} \quad (2.61)$$

$$\begin{aligned} \rho \hat{C}_t \frac{\partial T}{\partial t} + \rho \hat{C}_h v \frac{\partial T}{\partial z} + \rho \hat{C}_\beta T \frac{\partial v}{\partial z} &= \frac{\partial}{\partial z} \left(\kappa \frac{\partial T}{\partial z} \right) + Q(T, z, t) \\ &+ \frac{h P_w}{A_c} (T_w - T) + \left(\frac{A_h}{A_c} \right) \frac{f \rho |v| v^2}{2d_h} \end{aligned} \quad (2.62)$$

$$p = p(\rho, T) \quad (2.63)$$

$$\rho_w C_w \frac{\partial T_w}{\partial t} = \frac{h P_w}{A_w} (T - T_w) \quad (2.64)$$

where $\hat{C}_h = (A_h/A_c)C_h$, $\hat{C}_\beta = (A_h/A_c)C_\beta$, $\hat{C}_t = \hat{C}_h + (\rho_c/\rho)C_c$, $\kappa = \kappa_c$ and $Q(T, z, t)$ is given by Eq. (2.49). For convenience, the subscript h has been suppressed from ρ_h , T_h , and v_h . We also use h in place of h_w since this is the only heat transfer coefficient that appears in the model. Equations (2.60–64) represent the desired, simplified, quench model, hereafter referred to as “Quencher.”

Boundary and Initial Conditions

As stated, the primary goal of Quencher is to simulate quench events in superconducting magnets. To accomplish this an appropriate set of initial and boundary-conditions must be provided. The conditions chosen generate a quench by a three-step procedure. First, the system is initialized with profiles representing “standard steady state operation;” the entire magnet is superconducting and no external sources are present. Second, a high power pulse, localized in space and time, is applied to raise the corresponding local temperature above the critical temperature. Third, after the source is removed, the local quench just initiated is allowed to propagate along the coil. It is the detailed behavior of this propagation that is our primary interest.

The actual specification of the initial and boundary-conditions is somewhat complicated, since Quencher describes the behavior of a composite material (i.e. conductor plus helium). Thus standard conditions for a single material may be inappropriate. Even so, it is clear from the basic mathematical structure of the model that three initial-conditions and four boundary conditions are required; the helium/conductor equations have a double set of parabolic characteristics while the wall equation is a simple initial value problem.

Consider first the initial conditions which correspond to “steady state operation.” The simplest case corresponds to the situation where the helium is purely static. For such operation the initial conditions are given by

$$\rho(z, 0) = \rho_0 = \text{const.} \tag{2.65a}$$

$$T(z, 0) = T_w(z, 0) = T_0 = \text{const.}$$

where ρ_0 and T_0 are input parameters. As expected, the Quencher model then implies that $p = p(\rho_0, T_0) = \text{const}$ and $v = 0$ for steady state operation. A more

general case allows forced flow of the helium in the conduit. In this case the helium pressure at both ends of the conduit are specified, and for most situations of interest, the coils are sufficiently long so that the pressure, density, and temperature gradients are weak. The steady state equations can then be solved numerically by simply setting the time derivative terms to zero (in Chapter 3 we present the numerical scheme used to solve these equations). This steady state solution is then used as an initial-condition for the quench problem. In chapter 3 (see section 3.1) we discuss the forced flow initial conditions in detail.

Assume now that appropriate initial conditions have been specified. The next step is to add an external high power, short duration, spatially localized heat source $Q = Q_{ext}$ to the energy equation in order to raise the conductor temperature above T_{cr} . In Quencher, Q_{ext} has the form

$$Q_{ext}(z, t) = Q_0 \exp[-3(z - z_0)^2/L_q^2] \quad 0 < t < t_1. \quad (2.66)$$

Equation (2.66) describes a Gaussian pulse, centered at $z = z_0$ of width $L_q\sqrt{3}$. The total power input is approximately equivalent to that of a rectangular pulse of amplitude Q_0 and width L_q . For large coils, typically $Q_0 \sim 10^8$ w/m³. The source length $L_q \sim 0.1 - 20$ m out of a total length of $200 \sim 1000$ m indicating a strong spatial localization. The pulse duration $t_1 \sim 10^{-3}$ sec, which is much shorter than the characteristic quench time $\sim 1 - 10$ sec. For $t > t_1$ the external source is eliminated, and the local quench just initiated is allowed to evolve over the long quench time scale. This is the regime of primary interest.

In order to evolve the system from its initial state over both the initiation phase $0 < t < t_1$, and the quench phase $t_1 < t \lesssim 10$ sec, appropriate boundary conditions must be supplied. The boundary conditions are slightly subtle for two reasons. First, conditions must be provided that allow for both inlet and outlet flows, including a smooth transition from one to the other (e.g. when a quench induced pressure pulse forces helium out of the inlet channel). Second, the presence of the thermal conductivity requires an additional boundary condition

since the order of the system has been raised by one. This condition, however, on physical grounds seems an extra one, with no natural way for its specification. These difficulties are resolved as follows.

To begin, we specify the pressure at both ends of the channel. These are standard conditions, valid for both inlet and outlet flows. For an inlet situations (e.g. forced flow) we also specify the inlet temperature. Consider now the effect of thermal conductivity. During a quench two narrow oppositely moving fronts propagate away in each direction from the heating source. Each front is actually a boundary layer whose width is determined by the thermal conductivity. If thermal conductivity is not included, discontinuities appear in the solution, making it more difficult to solve numerically.

Even so, either behind or ahead of the front, the thermal conductivity has a negligible effect. To see this, note that the ratio of thermal conduction to convection is given by $(\kappa T')' / (\rho_h \hat{C}_h v T') \sim \kappa / \rho_h \hat{C}_h v L$. Behind the quench front $\kappa \sim 1000$ W/m-K, $\rho_h \sim 10$ kg/m³, $\hat{C}_h \sim 3000$ J/kg-K, $v \sim 1$ m/sec and $L \sim 10$ m indicating that $\kappa / \rho_h \hat{C}_h v L \sim 3 \times 10^{-3}$. Similarly, ahead of the quench front $\kappa \sim 1000$ W/m-K, $\rho_h \sim 100$ kg/m³, $\hat{C}_h \sim 3000$ J/kg-K, $v \sim 5$ m/sec and $L \sim 100$ m giving $\kappa / \rho_h \hat{C}_h v L \sim 7 \times 10^{-6}$.

We see that what is required at an outlet is a boundary condition that allows the thermal conductivity to play its role in the quench front, but does not introduce an undue artificial influence at either end. This goal is achieved by the nonstandard condition of setting $(\kappa T')' = 0$ at an outlet of the channel, which is clearly consistent with the idea that thermal conduction is unimportant ahead of the front. Other boundary conditions involving T or $\kappa T'$ directly, introduce spurious boundary layers at the outlet. The condition $(\kappa T')' = 0$ allows both T and $\kappa T'$ to float freely, thereby assuming their natural (physical) values. In Appendix C we consider a simple "model-problem" to illustrate how this boundary condition differs from, and is more accurate than some of the other boundary conditions (i.e. $T' = 0$). Note also that the smallness of κ makes the equations

mathematically stiff. However, the global nature of the collocation procedure discussed in the next chapter has no difficulty whatsoever with this problem.

In summary, the boundary conditions used to initiate and evolve the quench, with either static or forced flow, are given by

$$p(x = 0) = p_i \quad (2.67a)$$

$$p(x = L) = p_o \quad (2.67b)$$

$$T(x = 0) = T_i \text{ (inlet)} \quad ; \quad \left. \frac{\partial}{\partial z} \left(\kappa \frac{\partial T}{\partial z} \right) \right|_0 \text{ (outlet)} \quad (2.67c)$$

$$T(x = L) = T_o \text{ (inlet)} \quad ; \quad \left. \frac{\partial}{\partial z} \left(\kappa \frac{\partial T}{\partial z} \right) \right|_L \text{ (outlet)} \quad (2.67d)$$

where depending on whether $x = 0$ and $x = L$ are an inlet or and outlet, the appropriate “inlet” or “outlet” conditions are used in Eqs. (2.67c) and (2.67d), respectively. The initial and boundary-conditions used in the Quencher model are further discussed in Chapter 3, where the numerical implementation of these conditions are also presented. This completes the mathematical specification of the boundary conditions.

Material Properties

In order to obtain a numerical solution to the Quencher model, it is necessary to evaluate the material properties that appear as coefficients in the equations. This is more or less straightforward with the exception of the heat transfer coefficient as shown below.

To begin, note that the properties of helium including p , $\partial p / \partial \rho$, $\partial p / \partial T$, κ_h , μ_h , C_h and C_p , which are all functions of ρ and T , are available as library routines.

Similarly, the basic properties of the cable and conduit wall $\kappa_c, \eta_c, C_c, C_w$, which are functions of T , are also readily available in library form. The properties of the cable actually model the composite copper-superconductor strands; that is

$$\begin{aligned}\rho_c C_c &= \frac{1}{A_c} [A_{cu} \rho_{cu} C_{cu} + A_{sc} \rho_{sc} C_{sc}] \\ \kappa_c &\approx \frac{A_{cu}}{A_c} \kappa_{cu} \\ \eta_c &\approx \frac{A_{cu}}{A_c} \eta_{cu}\end{aligned}\tag{2.68}$$

and $A_c = A_{cu} + A_{sc}$. In addition, the critical temperature of the superconductor $T_{cr} = T_{cr}(B, I)$ is known experimentally. The properties thus far discussed are accurate to within $\pm 10\%$.

The next quantity of interest is the Darcy friction factor f . Experimental observations [11,12] indicate that in the regime of interest f can be approximated by

$$f \approx k_f \frac{0.184}{R^{0.2}}\tag{2.69}$$

where $R = \rho v d_h / \mu_h$ is the Reynolds number and $\mu_h(\rho, T)$ is the helium viscosity. The quantity k_f is a constant whose value depends upon the roughness of the solid surface in contact with the helium. For typical CICC channels $k_f \approx 3$. It is believed to be accurate to within $\pm 20\%$. In Fig. 2.2 we show how the measured values of f for a CICC compare with the friction factor in a circular pipe (i.e. the usual Moody chart). This figure is taken directly from reference [12].

Before proceeding, some important issues must be discussed in regard to Eq. (2.69). In the literature, there are a large number of different correlations for f [8]. Anyone of these correlations can easily be substituted in place of Eq. (2.69) and the numerical procedure discussed in chapter 3 will have no difficulty with this replacement. We have chosen Eq. (2.69) because of its simplicity, considering

that many other, only slightly more accurate correlations require the solution of transcendental equations. More importantly, all the parameters of interest during a quench event are insensitive to the particular representation of f . This fact will be clearly demonstrated in chapter 5, where it is evident from the analytic results that quench propagation is indeed a very weak function of f . It is important to note that Eq. (2.69) is most appropriate for turbulent flow of helium in the conduit. This is the case in the region outside of the quench zone where typical Reynolds numbers are of the order of 5×10^4 . In the center of the quench region the helium flow is much closer to the laminar regime. However, in this region the helium density is rapidly depleted and therefore the friction force is nearly zero. Thus, use of Eq. (2.69) in the quench region does not introduce any substantial error since the friction force itself is negligible.

The final quantity of interest is the heat transfer coefficient h defined in terms of the Nusselt number N as follows

$$h \equiv \frac{\kappa_h N}{d_h}. \quad (2.70)$$

Here, $\kappa_h(\rho, T)$ is the thermal conductivity of helium. For typical flow velocities $v \sim 1 - 10$ m/sec, the Reynolds number is sufficiently high (i.e. $R > 10^4$) along most of the coil that the turbulent Nusselt number N_t would appear to be the appropriate choice for Eq. (2.70). The value of N_t most often used in CICC design is a modified form of the Dittus-Boelter coefficient given by [8,12,13]

$$N_t = 0.026 R^{0.8} P^{0.4} \left(\frac{T}{T_w} \right)^{0.716} \quad (2.71)$$

where $P = \mu_h C_p / \kappa_h$ is the Prandtl number. Equation (2.71) is valid if $R \gtrsim 10^4$.

Just as in the case of the friction factor, there are a large number of correlations for the Nusselt number [8]. In regard to Eq. (2.71) it is important to note the following: (1) this representation of N_t is used to describe the heat transfer between the helium and the conduit wall. For this purpose, the equation is rea-

sonably accurate.¹ (2) Equation (2.71) is particularly valid in the region outside of the quench zone where the helium flow is highly turbulent. In this region, however, there are no external heat sources (of substantial magnitude) present in the system. Thus, for a wide range of values of the heat transfer coefficient, the helium and the conduit wall temperatures are approximately the same since they were set equal initially. That is, the particular representation of the Nusselt number in this region does not greatly effect the accuracy of quench propagation properties.

Somewhat surprisingly, Eq. (2.71) is often *not* valid behind the quench front where the rapid depletion of helium can lower the density by as much as two orders of magnitude. At these low densities the Reynolds number is typically $R \sim 500 - 3000$; that is, in the important region where joule heating takes place, the flow is essentially laminar, characterized by a Nusselt number [1,8]

$$N_\ell = 4. \tag{2.72}$$

This equation represents the heat transfer between the wall and the helium for laminar flow in a conduit, or in concentric cylinders [8]. Unlike N_t , the quantity N_ℓ greatly influences some of the important parameters during a quench event. Specifically, the maximum temperatures during a quench are substantially effected by N_ℓ . The value of this parameter, chosen in Eq. (2.72) is believed to be reasonably accurate in the quench region [8]. Other major quench codes [14,15] choose the value of $N_\ell = 8$. This difference is not yet fully agreed upon in the quench community.

¹ The heat transfer between the conductor and the helium is not very accurately modeled with this equation, since the geometry for the helium flow among the strands is quite different than the flow near the wall. The Quencher model has eliminated this difficulty as discussed earlier in this chapter: that is when $P_c h_c / A_c$ is sufficiently large, the temperatures are nearly equal and independent of the specific value of h_c . In the general models, where the conductor temperature is different than that of the helium, other correlations should be used for h_c . To the authors knowledge this has not been done in the two major computer codes [14,15] that have been developed to study general CICC behavior.

In the so-called transition region between $2 \times 10^3 \lesssim R \lesssim 10^4$ there is a sparsity of data and the detailed behavior of the Nusselt number is not well known. The Quencher code uses a hybrid model for N to substitute into Eq. (2.70). It has the form

$$N = (N_\ell N_t)^{1/2} \left[\frac{N_\ell^{1/2} + N_t^{1/2} (R^2/R_\ell R_t)^{\nu/2}}{N_t^{1/2} + N_\ell^{1/2} (R^2/R_\ell R_t)^{\nu/2}} \right] \quad (2.73)$$

where $R_\ell = 2 \times 10^3$ and $R_t = 10^4$ are the transition Reynolds numbers. The quantity ν is an arbitrary parameter that sets the steepness of the transition from laminar to turbulent flow. A plot of N vs. R for various values of ν is shown in Fig. 2.3. Note that as $R \rightarrow 0$, then $N \rightarrow N_\ell$. Similarly as $R \rightarrow \infty$, then $N \rightarrow N_t$. These are the appropriate limits. In practice most of the quantities of interest are insensitive to the value of ν . In Quencher the value of ν is chosen to be $\nu = 4$.

This completes the discussion of the material properties.

Chapter 2 References

- [1] Bird, R. B., Stewart, W. E., Lightfoot, E. N., Transport Phenomena, John Wiley & Sons, New York, 1960.
- [2] White, F. M., Fluid Mechanics, McGraw-Hill Book Company, 1986.
- [3] Chapman, S. and Cowling, T. G., The Mathematical Theory of Non-Uniform Gases, Cambridge University Press, 1970.
- [4] Resibois, P. and De Leener, M., Classical Kinetic Theory of Fluids, John Wiley & Sons, 1977.
- [5] Hirschfelder, J. O., Curtiss, C. F., Bird, R. B., Molecular Theory of Gases and Liquids, John Wiley & Sons, 1964.
- [6] Speziale, C. G., Annual Review of Fluid Mechanics, Annual Reviews Inc., Vol. 23, 1991, pp. 107-157.
- [7] Hinze, J. O., Turbulence, Second Ed., McGraw-Hill Inc., 1975, pp. 3-30.
- [8] Kakac, S., Shah, R. K., Aung, W. (editors), Handbook of Single-Phase Convective Heat Transfer, John Wiley & Sons, 1987.
- [9] Whittaker, E. T., Watson, G. N., A Course of Modern Analysis, Cambridge University Press, 1927, pp. 150-154.
- [10] Reif, F., Fundamentals of Statistical and Thermal Physics, McGraw-Hill Publishing Company, 1965, pp. 171-172.
- [11] Lue, J. W., Miller, J. R., Lottin, J. C., *Pressure Drop Measurements on Forced Flow Cable Conductors*, IEEE Trans. Magnet. Mag-15, 53 (1979).
- [12] Van Sciver, S. W., Helium Cryogenics, Plenum Press, New York, 1986, pp. 243-244.
- [13] Giarratano, P. J., Arp, V. D., Smith, R. V., *Forced Convection Heat Transfer to Supercritical Helium*, Cryogenics, Vol. 11, 1971.
- [14] Bottura, L., Zienkiewicz, O. C., *Quench Analysis of Large Superconducting*

Magnets Parts I and II. Cryogenics, Vol. 32, No. 7, 1992.

- [15] Wong, R. L., *Program CICC Flow and Heat Transfer in Cable-In-Conduit Conductors - Equations & Verification*, Lawrence Livermore National Laboratory Internal Report, UCID 21733, May 1989.

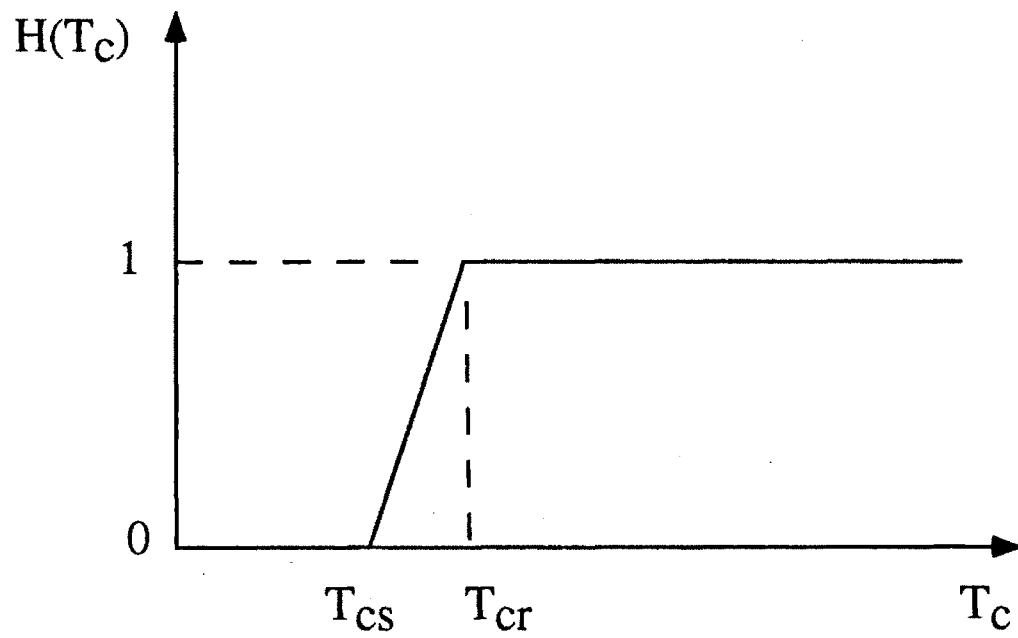


Figure 2.1: Functional dependence of $H(T_c)$ appearing in Eq. (2.49).

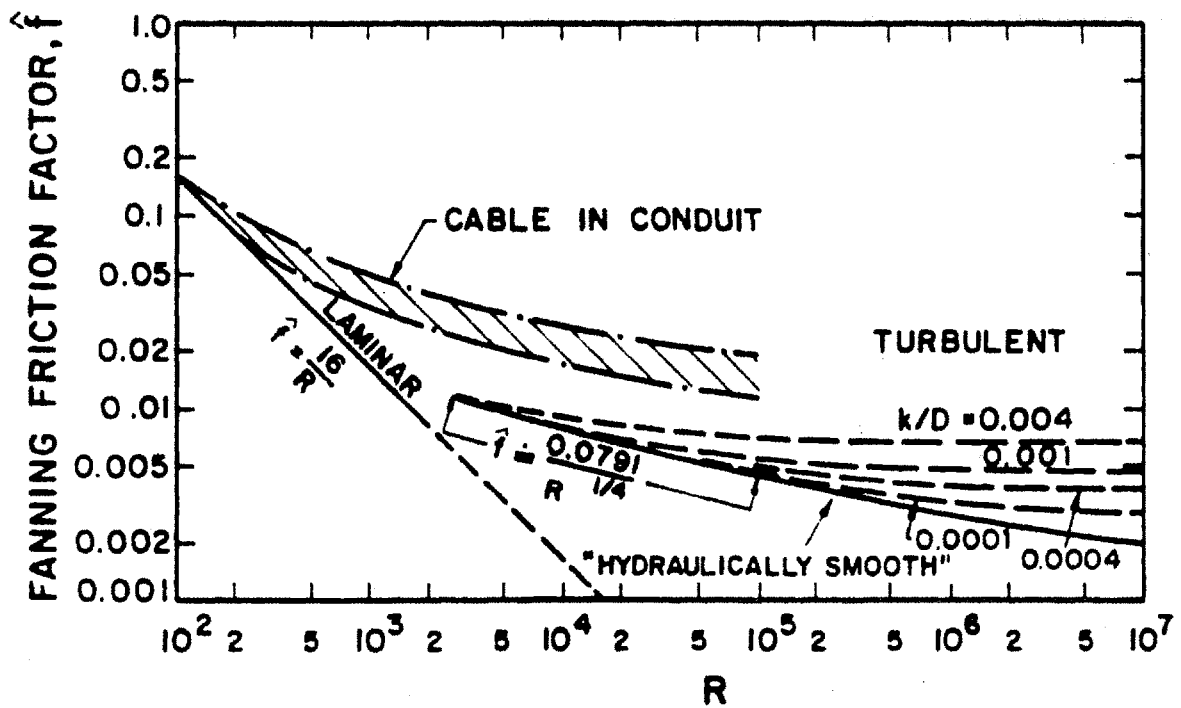


Figure 2.2: Dependence of the friction factor f on the Reynolds's number R . Note that the Fanning friction factor, by definition is given by $\hat{f} \equiv f/4$. (This figure is taken directly from reference [12].)

Nusselt Number Vs. Reynolds Number

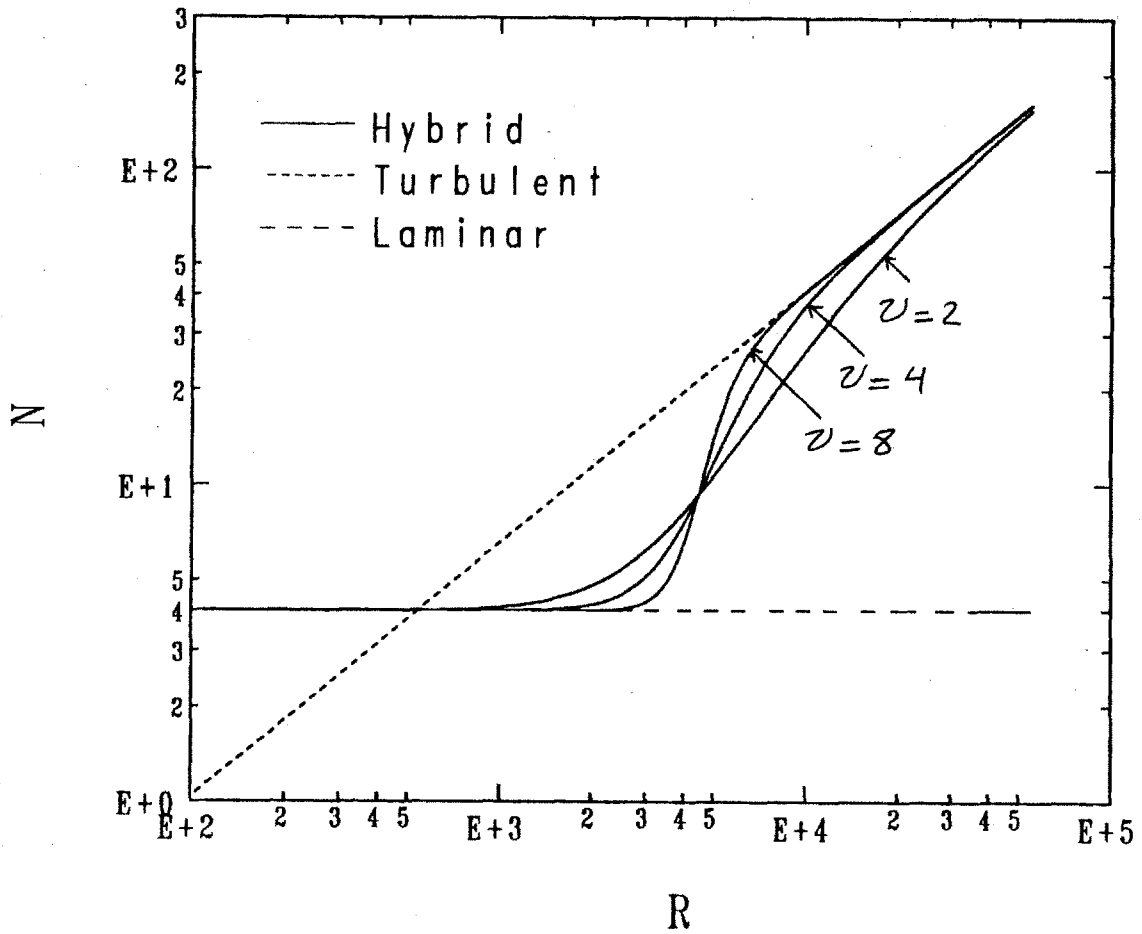


Figure 2.3: Dependence of the Nusselt number on the Reynolds number, from Eqs. (2.71-73).

Chapter 3

Numerical Solution

Chapter 3. Numerical Solution

In this chapter we first describe the numerical procedure to solve the Quencher model (section 3.1). Next, in section 3.2 we make extensive comparisons between the numerical solution of the Quencher model and other existing general computer codes, and finally in section 3.3 we compare the Quencher results with experimental data. For reference we summarize the Quencher equations [Eqs. (2.60–64)] below;

$$\frac{\partial \rho}{\partial t} + \frac{\partial}{\partial x}(\rho v) = 0 \quad (3.1)$$

$$\frac{\partial p}{\partial x} = -\frac{f\rho v|v|}{2d_h} \quad (3.2)$$

$$\begin{aligned} \rho \hat{C}_t \frac{\partial T}{\partial t} + \rho \hat{C}_h v \frac{\partial T}{\partial x} + \rho \hat{C}_\beta T \frac{\partial v}{\partial x} = \frac{\partial}{\partial x} \left(\kappa \frac{\partial T}{\partial x} \right) + S(T, x, t) \\ + \frac{hP_w}{A_c} (T_w - T) + \frac{A_h}{A_c} \frac{f\rho|v|v^2}{2d_h} \end{aligned} \quad (3.3)$$

$$p = p(\rho, T) \quad (3.4)$$

$$\rho_w C_w \frac{\partial T_w}{\partial t} = \frac{hP_w}{A_w} (T - T_w) \quad (3.5)$$

where all the variables have been defined in Chapter 2 and are also summarized in Table 3.1. For convenience, we have replaced the variable z by x and also S is used in place of Q to represent the heating source. The source term S in general consists of the external heat source given by Eq. (2.66) as well as the Joule heating term given by Eq. (2.49).

t	time
x	axial length along the channel
ρ	helium density
v	helium velocity
p	helium pressure
T	helium/conductor temperature
C_h	specific heat of helium at constant volume
C_β	$(1/\rho)(\partial p/\partial T)$
C_α	$(1/T)(\partial p/\partial \rho)$
A_h	helium cross-sectional area
d_h	hydraulic diameter for helium flow
ρ_{cu}	density of copper
C_{cu}	specific heat of copper
κ_{cu}	thermal conductivity of copper
η_{cu}	electrical resistivity of copper
A_{cu}	copper cross-sectional area
ρ_{sc}	density of superconductor
C_{sc}	specific heat of superconductor
A_{sc}	superconductor cross-sectional area
ρ_w	density of conduit wall
T_w	conduit wall temperature
C_w	specific heat of conduit wall
A_w	conduit wall cross-sectional area
P_w	wall perimeter in contact with helium
A_c	$A_{cu} + A_{sc}$
κ	$(A_{cu}/A_c)\kappa_{cu}$
η_c	$(A_{cu}/A_c)\eta_{cu}$
\hat{C}_h	$(A_h/A_c)C_h$
\hat{C}_β	$(A_h/A_c)C_\beta$
$\rho_c C_c$	$(A_{cu}\rho_{cu}C_{cu} + A_{sc}\rho_{sc}C_{sc})/A_c$
\hat{C}_t	$\hat{C}_h + \rho_c C_c/\rho$
f	friction factor [see Eq. (2.69)]
h	heat transfer coefficient [see Eqs. (2.70-73)]
S	$\eta_c J^2 H + S_{ext}$ [see Eqs. (2.49) and (2.66)]

Table 3.1: Parameters used in Eqs. (3.1-5).

3.1 Numerical Procedure

In choosing the appropriate numerical procedure to solve the Quencher model it is important to first consider the mathematical nature of the equations. Below, we show that the Quencher model consists of a set of parabolic differential equations.

Nature of the Equations

Quencher is a set of nonlinear, coupled one dimensional plus time partial differential equations. Before proceeding with the analysis, we mention that it is not difficult to observe the parabolic nature of the Quencher model by simply expanding Eq. (3.4) in terms of the density and temperature, through the equation of state. Next, solving the resulting equation for v in terms of T and ρ , and then substituting $v(\rho, T)$ in the mass and energy equations we find two equations (neglecting the conduit wall) for the two unknowns ρ and T . These equations both involve the time derivatives ($\partial/\partial t$) of ρ and T as well as the second order spatial derivative $\partial^2/\partial x^2$ of these variables. This is a classic characteristic of a parabolic system.

We now take a different, more systematic approach in order to investigate the nature of the Quencher model. This is done by using a linearization process. That is, we consider the following expansion for the various variables;

$$T = T_0 + T_1(x, t) + \dots \quad (3.6a)$$

$$\rho = \rho_0 + \rho_1(x, t) + \dots \quad (3.6b)$$

$$p = p_0 + p_1(x, t) + \dots \quad (3.6c)$$

$$v = v_0 + v_1(x, t) + \dots \quad (3.6d)$$

For simplicity, and without loss of generality we assume that no conduit wall is present in the system. Note that in general the zeroth order quantities are functions of x and t .

Using the above expansion in the Quencher model, and considering the case

$$\frac{\partial Q_1}{\partial t} \gg \frac{\partial Q_0}{\partial t} \quad (3.7a)$$

$$\frac{\partial Q_1}{\partial x} \gg \frac{\partial Q_0}{\partial x} \quad (3.7b)$$

for any quantity Q , we find

$$\frac{\partial p_1}{\partial t} + \rho_0 \frac{\partial v_1}{\partial x} + v_0 \frac{\partial p_1}{\partial x} = 0 \quad (3.8)$$

$$\frac{\partial p_1}{\partial x} = -\frac{f}{2d_h} (\rho_1 v_0^2 + 2\rho_0 v_0 v_1) \quad (3.9)$$

$$\rho_0 \hat{C}_{t0} \frac{\partial T_1}{\partial t} + \rho_0 \hat{C}_{h0} v_0 \frac{\partial T_1}{\partial x} + \rho_0 \hat{C}_{\beta 0} T_0 \frac{\partial v_1}{\partial x} = \kappa_0 \frac{\partial^2 T_1}{\partial x^2} \quad (3.10)$$

$$p_1 = \frac{\partial p_0}{\partial \rho_0} \rho_1 + \frac{\partial p_0}{\partial T_0} T_1 \quad (3.11)$$

Note that $f = f_0 \equiv f(R_0)$.

Considering an infinite domain in x , we write the general solution for any quantity Q_1 as follows;

$$Q_1(x, t) = \hat{Q}_1 \exp(ikx - i\omega t) \quad (3.12)$$

where \hat{Q}_1 is a constant. Using this form for the solution of Eqs. (3.8–11) we find, as a solvability condition, the following dispersion relation;

$$(ak^2 - i\omega) \left(\frac{ib\omega}{k^2} - 1 \right) = -ic\omega \quad (3.13)$$

where a , b , and c are defined as follows

$$a \equiv \frac{\kappa_0}{\rho_0 \hat{C}_{t0}} \quad (3.14a)$$

$$b \equiv \frac{f\nu_0}{d_h(\partial p_0/\partial \rho_0)} \quad (3.14b)$$

$$c \equiv \frac{\hat{C}_{\beta 0}}{\hat{C}_{t0}} \frac{(\partial p_0/\partial T_0)T_0}{(\partial p_0/\partial \rho_0)\rho_0} \quad (3.14c)$$

We now assume that the wave length k is a given real quantity. Thus, we proceed to solve Eq. (3.13) for the frequency ω . We find that both roots of the quadratic Eq. (3.13) are complex numbers;

$$\frac{\omega}{k^2} = -i \frac{1 + ab + c}{2b} \left[1 \mp \left(1 - \frac{4ab}{(1 + ab + c)^2} \right)^{1/2} \right] \quad (3.15)$$

These equations conclude that the Quencher model consists of a double set of parabolic characteristics. Having determined the nature of the Quencher equations we now proceed to outline the numerical procedure that is used to obtain the solution of these equations.

Numerical Procedure

After testing several possible numerical methods, we selected the procedure described below because of its speed and robustness. In essence, the method utilizes a fully implicit time advance algorithm which transforms the model into a set of ordinary differential equations at each time step. These ODE's are then solved by a global collocation procedure [1,2,3].

The time advance is accomplished by a standard, second order accurate algorithm as follows. Assume all quantities are known at times t and $t - \Delta t$. To

evaluate the time derivative of any quantity Q at the new time $t + \Delta t$, we approximate

$$\left(\frac{\partial Q}{\partial t}\right)_{t+\Delta t} \approx L_2 Q \equiv \frac{1}{2\Delta t} [3Q(t + \Delta t, x) - 4Q(t, x) + Q(t - \Delta t, x)] \quad (3.16a)$$

This equation may also be generalized to the case in which the time step Δt is not a constant. In this case for given values of Q at times $t - \Delta t_1$ and t , we find the time derivative of Q at time $t + \Delta t_2$ as follows;

$$\left(\frac{\partial Q}{\partial t}\right)_{t+\Delta t_2} \approx L_2 Q \equiv \frac{1}{c} [aQ(t + \Delta t_2, x) - bQ(t, x) + Q(t - \Delta t_1, x)] \quad (3.16b)$$

where a , b and c are given by

$$a = \frac{(\Delta t_1 + \Delta t_2)^2}{(\Delta t_2)^2} - 1 \quad (3.16c)$$

$$b = \frac{(\Delta t_1 + \Delta t_2)^2}{(\Delta t_2)^2} \quad (3.16d)$$

$$c = \frac{\Delta t_1}{\Delta t_2} (\Delta t_1 + \Delta t_2) \quad (3.16e)$$

Equation (3.16b) may easily be derived by simple application of Taylor's theorem. Note that for $\Delta t_1 = \Delta t_2$, Eq. (3.16b) reduces to Eq. (3.16a).

This is substituted into the quench model. All the variables and coefficients in the non-time derivative terms are evaluated at $t + \Delta t$; that is, the time advance is purely implicit. After defining a new variable $q \equiv -\kappa(T)\partial T/\partial x$, we can rewrite the quench model as a set of first order ordinary differential equations of the form

$$\frac{d\mathbf{u}}{dx} = \mathbf{F}(x, \mathbf{u}) \quad (3.17)$$

where the vector \mathbf{u} is given by

$$\mathbf{u} = \begin{bmatrix} \rho \\ v \\ T \\ q \end{bmatrix} \quad (3.18)$$

and \mathbf{F} is given as

$$F_1 = -\frac{1}{C_\alpha T} \left(\frac{f\rho|v|v}{2d_h} - \frac{\rho C_{\beta} q}{\kappa} \right) \quad (3.19)$$

$$F_2 = -\frac{1}{\rho} (L_2 \rho + v F_1) \quad (3.20)$$

$$F_3 = -\frac{q}{\kappa} \quad (3.21)$$

$$F_4 = S(T) - S_w - \rho \hat{C}_t L_2 T + \frac{\hat{C}_h \rho v q}{\kappa} - \hat{C}_\beta \rho T F_2 + \frac{A_h}{A_c} \frac{f\rho|v|v^2}{2d_h} \quad (3.22)$$

All terms have been previously defined except C_α and S_w . The quantity C_α is defined as $C_\alpha \equiv (1/T)\partial p(\rho, T)/\partial \rho$. The term S_w represents the coupling of the conductor/helium with the conduit wall. It is found by explicitly solving Eq. (3.5) using the time advance algorithm described above, evaluating the material properties at the previous time step. Thus,

$$T_w(t + \Delta t) = \frac{T(t + \Delta t) + \epsilon[4T_w(t) - T_w(t - \Delta t)]}{1 + 3\epsilon} \quad (3.23)$$

where $\epsilon = (A_w/hP_w)(\rho_w C_w/2\Delta t)$ is evaluated at t (this is an implicit/explicit method for the wall). The coupling term then becomes

$$\begin{aligned} S_w(t + \Delta t) &\equiv \frac{hP_w}{A_c} (T - T_w) \\ &= \frac{hP_w}{A_c} \epsilon(t) \left[\frac{3T(t + \Delta t) - 4T_w(t) + T_w(t - \Delta t)}{1 + 3\epsilon(t)} \right] \end{aligned} \quad (3.24)$$

Note, as $hP_w/A_w \rightarrow \infty$, then $\epsilon \rightarrow 0$ and $T_w \rightarrow T$ implying that

$$S_w \rightarrow (A_w/A_c)\rho_w C_w L_2 T.$$

As expected, in this limit S_w just adds a wall contribution to the combined heat capacity \hat{C}_t .

Equation (3.17) represents the basic set of equations to be solved at each time step. Before discussing the procedure used in Quencher observe that this equation constitutes a fourth order boundary-value problem. Thus, four boundary conditions are required to obtain the solution. Furthermore, Eq. (3.17) is also a mathematically stiff system of ODE's. This stiffness is due to the thermal conductivity term as well as the $1/\Delta t$ terms appearing in Eqs. (3.19–22). Thus, explicit shooting methods are inappropriate as a solution procedure. Implicit shooting schemes do appear to be appropriate, but we have not found standard packages for this purpose. Most existing ODE solvers that utilize shooting methods use an explicit scheme.

In view of the above discussion we choose “global schemes” instead of shooting methods [2,4]. A finite difference global solver is available in both the NAG and IMSL libraries. Both of these solvers are based on the numerical procedure outlined in reference [4]. We have found this procedure to be inefficient, however, because of its inability to remesh the problem at every time step. This solver does introduce additional mesh points into the problem in order to obtain the specified accuracy of the solution. However, the solver does not remove the additional mesh points from regions where a large number of mesh points are no longer needed. This poses a very serious difficulty, since as time increases the number of added points become prohibitively large. Furthermore, this solver has not proven to be numerically robust, often having convergence problems from one time step to the next.

The numerical solver in Quencher makes use of a sophisticated collocation procedure developed by U. Ascher et al. [1–3]. This procedure also falls in the

category of “global schemes”. We do not attempt to describe the details of the numeric of this package since this is done in reference [1–3]. It is important to note that this package has the distinct advantage of rapidly and automatically remeshing the problem at every time step in accordance with the motion of the quench front. As an example, a typical mesh might contain 150-200 points with the narrowest spacing corresponding to 1 cm out of a total simulation length of 1000 m. The mesh redistribution is vital to achieve both a high computational efficiency and an accurate solution to the problem. To demonstrate the value of remeshing consider the temperature and density profiles at time $t = 10$ seconds during a quench in a typical CICC. In Fig. 3.1a–b we show the temperature and the helium density profiles, respectively, as obtained by Quencher. In these figures we have plotted the actual mesh points used in the calculation at this particular time step. Note the distribution of mesh points along the length of the conductor. The boundary layer at the location of the quench front can be observed in these figures. In addition to the remeshing capability the collocation procedure has proven remarkably robust, converging over a wide class of applications using a wide range of time steps.

Boundary and Initial Conditions

In this section we discuss the numerical implementation of the initial and boundary conditions used in Quencher. As discussed in Chapter 2, the most general, and important case to be considered is one in which before the initiation of quench the inlet and the outlet pressure as well as the inlet temperature of the helium are specified. Thus at $t = 0$ there exists a flow field in the conduit with a corresponding temperature, pressure, velocity and density distributions. In order to obtain these distributions we use the following boundary conditions

$$p(x = 0) = p_i \quad (3.25a)$$

$$p(x = L) = p_o \quad (3.25b)$$

$$T(x = 0) = T_i \quad (3.25c)$$

$$\left. \frac{\partial}{\partial z} \left(\kappa \frac{\partial T}{\partial z} \right) \right|_L = 0 \quad (3.25d)$$

where p_i , p_o and T_i are specified constants. Let us further describe the boundary condition given by Eq. (3.25d). In order to implement this condition we set

$$F_4(u_1, u_2, u_3, u_4) \Big|_{x=L} = 0 \quad (3.26)$$

where F_4 is given by Eq. (3.22).

At this stage we run the code for a few time steps (~ 10) until steady state is achieved. That is, no changes (in time) occur in any of the parameters. The time scale to reach such a steady state is of the order of L/v_i , where v_i is the inlet helium velocity and L is the length of the channel. For a typical background flow in a CICC a good priori estimate for v_i is given by $v_i^2 \approx (2d_h/f\rho_i)(p_i - p_o)/L$, where $\rho_i = \rho(p_i, T_i)$ is a known quantity and f may be approximated by a constant ($f \approx 0.08$). This is the procedure used to initialize Quencher.

Once steady state is reached we may proceed to simulate the quench event. The steady state solution just obtained now serves as the initial condition ($t = 0$) to the Quencher model. From this point the boundary conditions are given by

$$p(x = 0) = p_i \quad (3.27a)$$

$$p(x = L) = p_o \quad (3.27b)$$

$$T = T_i \quad (v_i > 0) \quad ; \quad \left. \frac{\partial}{\partial z} \left(\kappa \frac{\partial T}{\partial z} \right) \right|_0 \quad (v_i < 0) \quad (3.27c)$$

$$\left. \frac{\partial}{\partial z} \left(\kappa \frac{\partial T}{\partial z} \right) \right|_L = 0 \quad (3.27d)$$

where again Eq. (3.27c) (for $v_i < 0$) and Eq. (3.27d) are enforced by setting $F_4 = 0$ at $x = 0$ and L , respectively. In Eq. (3.27c) the inflow condition $v_i > 0$ is used as long as the inlet velocity v_i is positive and the outflow condition $v_i < 0$ is used otherwise (here we take the usual case in which $p_i > p_o$). Note that the value of v_i at any given time step depends on the helium velocity profile at that time step. Thus v_i is a function of time which the code solves for. The value of v_i is monitored during the time evolution of the system in order to determine the time at which flow reversal occurs.

In order to demonstrate these points consider a non-quench scenario in which a low amplitude heat source S_{ext} is substituted in place of S in Eq. (3.3). The conductor considered here is a 260 m sample of a conductor similar to the one discussed in section 3.4. We use the following form of S_{ext} ;

$$S_{ext} = S_0 \exp[-6(1 - 2x/L)^2] \quad (3.28)$$

where we choose $S_0 = 2./A_{cu} \text{ W/m}^3$.

In Fig. 3.2a we plot the temperature profile at various time steps during a 12 sec evolution of the system. Note the temperature profile at time $t = 0$. The outlet temperature at $t = 0$ is greater than T_i due to the frictional heating of the helium in the conduit. Also observe that the outlet temperature is increasing as time increases since the high temperature helium from the heated region in the conduit starts to leave the system at $x = L$. The inlet temperature, however, remains at $T = T_i$ until flow reversal occurs at the inlet of the channel. After this point the temperature at $x = 0$ also starts to increase by the same reasoning as for the temperature at $x = L$. In Fig. 3.2b we plot the density profile at various times steps. Again, note the profile at $t = 0$. In Fig. 3.2c we show the velocity profile at various time steps. In this figure the phenomena of flow reversal is clearly demonstrated. In such an event the pressure at a location inside the

conduit exceeds the inlet pressure which reverses the flow of helium toward the inlet-section of the channel. Figure 3.2d shows the helium pressure profile for this case. In Fig. 3.2e we plot the quantity q given by $q = -(\kappa T)'$. Note how at both ends of the conduit ($x = 0, L$) this quantity varies as a function of time. From Figs. 3.2a and 3.2e, in accord with the discussions presented in section 2.3, observe that both the heat flux and the temperature (for an outflow) are allowed to float.

The mass flux $\dot{m} = A_h \rho v$ is shown in Fig. 3.2f where we observe that at $t = 0$ (the initial profile) this quantity is a constant. Finally in Fig. 3.3 we plot the inlet velocity as a function of time in order to further demonstrate the phenomena of flow reversal. Observe that at $t \approx 1.8$ seconds the value of v_i goes to zero (i.e. the flow at the inlet reverses). Thus for $t < 1.8$ seconds we use the boundary condition $T = T_i$ at $x = 0$, and for times greater than 1.8 seconds we use the $(\kappa T)' = 0$ condition at $x = 0$.

Numerical Convergence

In order to show the dependence of some of the parameters on the integration time step Δt we consider a 4 second quench in a conductor very similar to the TF coil of the ITER machine. (The exact parameters describing this conductor are given in section 3.2, table 2.) In Fig. 3.4a we show how the maximum temperature evolves for various values of Δt . Here, the time steps used are given by; $\Delta t = 0.1, 0.04, 0.02, 0.01, 0.005, 0.002, 0.001$ seconds. In Fig. 3.4b–4d we show how the time evolution of the maximum helium pressure, the length of the normal region, and the voltage, respectively, depend on Δt . Finally in Fig. 3.5 we plot the value of the maximum helium pressure and the length of the normal region (both at $t = 4$ sec) versus Δt . These figures clearly demonstrate the dependence of these parameters on the time step Δt . Typically $\Delta t \lesssim 0.1$ sec for good convergence in cases where the conductor current is held fixed. Larger time steps may be used

during typical current-dump cases in which the conductor current is exponentially decreasing ($\Delta t \sim 0.5$ sec after the current dump).

The collocation scheme used in Quencher obtains the solution of Eq. (3.17) such that the relative error for each component of \mathbf{u} [see Eq. (3.18)] remains less than a specified tolerance tol_i . This is done by remeshing at every time step. We have found that the various parameters of interest during the quench are only weakly dependent ($\lesssim 1\%$) on tol_i in the range $tol_i \sim 10^{-6} - 10^{-4}$ (using a single precision algorithm).

3.2 Comparison With Computational Data

In this section we compare the results of the Quencher model with those of other general purpose CICC computer codes. In particular, we compare Quencher results with those of the more general code Saruman [5] for three different conductor configurations. We also show that Quencher is sufficiently fast in terms of CPU time to simulate realistically long quench events. During the completion of this thesis, we learned that L. Bottura was finishing development of an implicit version [6] of his general explicit magnet design code. This new code should significantly reduce the CPU time and in the near future we plan to compare it in detail with the code developed here.

ITER Conductor

To begin, consider a conductor very similar to the proposed design for the Toroidal Field Coil of the International Thermonuclear Experimental Reactor (ITER). This conductor is of length 530 m, with $d_h = 1.6 \times 10^{-3}$ m, $A_h = 4.5 \times 10^{-4}$ m², $A_{cu} = 3.9 \times 10^{-4}$ m², $A_{sc} = 2.6 \times 10^{-4}$ m², $A_w = 2.6 \times 10^{-4}$ m², $P_w = 0.13$ m, and $I = 4.3 \times 10^4$ A. In this example, the current is kept constant for a period of 2 sec, after which it decays exponentially with a time constant of

20 sec. The conductor is in a uniform magnetic field of 13 T, and for simplicity of comparison with Saruman the heat transfer coefficient is taken to be a constant; $h = 500 \text{ W/m}^2\text{-K}$. Before the initiation of quench, the helium in the channel is stagnant at a temperature of 5 K and a pressure of 5 atm. In Table 3.2 we summarize the parameters that characterize this conductor.

Conductor Length (m)	530
Copper Area (mm^2)	390
Nb ₃ Sn Area (mm^2)	260
Helium Area (mm^2)	450
Wall Area (mm^2)	260
Hydraulic Diameter (mm)	1.6
Wall Inner Perimeter (mm)	130
Initial Current (kA)	43
Detection Time (sec)	2
Dump Time (sec)	20
Inlet Pressure (atm)	5
Outlet Pressure (atm)	5
Inlet Temp. (K)	5
Copper RRR	100

Table 3.2: Characteristic Parameters of the ITER Coil.

Quench is initiated by depositing $1 \times 10^5 \text{ W/m}$, at the center of the channel, over a 2 m length for a period of 0.01 sec. Thus, in Eq. (2.49) after replacing Q and z by S and x respectively, we have $S_0 = 10^5/A_{cu} \text{ W/m}^3$, $x_0 = 530/2 \text{ m}$, and $L_q = 2 \text{ m}$. Also t_1 in this equation is given by $t_1 = 0.01 \text{ sec}$. The temperature and density profiles as functions of x , at $t = 10 \text{ sec}$ from Quencher were presented in Figs. 3.1a and 3.1b, respectively. The temperature in the quench zone is increasing due to the joule heating. This tends to increase the pressure, giving rise to a flow of helium, thereby depleting the density in this region. In these figures we have plotted the actual mesh points used in the calculation at this particular time step.

The computer code Saruman which is of the class of general codes discussed in chapter 2, is used to compare with Quencher. Saruman is a finite element code that solves the fluid equations described in chapter 2 (see section 2.1) using

an explicit time advance algorithm [5]. We carry out the same 2 second quench simulation of the ITER coil as computed by Quencher. In Saruman we use a total of 800 elements with 600 placed within a 30 m length at the center of the channel for maximum resolution. The length of each element within the quench region is thus 5 cm; note that within the boundary layer the spacing between grid points used in Quencher is between 3 to 5 cm. Figures 3.6a–c show the comparison of the maximum conductor temperature, maximum wall temperature, and the maximum helium pressure, respectively, as functions of time. Since the problem is symmetric these maxima occur at the center of the channel. The length of the normal zone, $X_q(t)$ and the quench-voltage as functions of time are shown in Figs. 3.6d and 3.6e, respectively. The quench voltage is an important quantity of interest which is given by

$$V(t) \equiv \frac{I(t)}{A_{cu}} \int_{x=0}^L \eta_{cu}(T) dx \quad (3.29)$$

where $\eta_{cu}(T)$ is the electrical resistivity of copper, and $T(x, t)$ is the temperature distribution in the conductor.

The differences observed in Figs. 3.6a–e are indeed small and are believed to be due to the slightly different initial conditions used in the two models. In Saruman the external heat pulse used to initiate the quench is directly deposited in the conductor. In Quencher, this external heat is deposited in both the conductor and helium. Thus the amplitude of the external heat required to initiate the quench is slightly different in the two models. This difference gives rise to the constant offsets observed in Figs. 3.6a–e.

The velocity of helium at either end of the channel is presented in Fig. 3.6f. In Quencher the speed of sound time delay is not present; thus, helium expulsion from the channel occurs earlier than is physically possible (see Appendix B). This early expulsion of helium, however, does not reduce the accuracy of the solution of the problem within the quench region as evidenced by Fig. 3.6a–e, and in accordance with the discussions presented in Appendix B. In order to

obtain the physical value of the helium velocity at the end of the channel, the results of Quencher are valid only after a time $t = L/2c_0$, where L is the length of the channel and c_0 is the speed of sound in the helium (c_0 is evaluated at the background ($t = 0$) pressure and temperature). For $t < L/2c_0$ the expulsion velocity is zero. For the particular case under consideration $L = 530$ m and $c_0 \approx 200$ m/sec, giving $L/2c_0 \approx 1.3$ sec (see Fig. 3.6f).

The CPU time used by Saruman during the 2 second quench simulation presented in Fig. 3.6a-f, is approximately 10 hours on a CRAY-2 Supercomputer. Quencher requires approximately 50 minutes of CPU time on a VAX Station 4000/90. This saving in computing cost is essential in order to perform studies of quench for realistically long periods of time. In Fig. 3.7 we show the normal length as a function of time during a 50 second quench in the ITER conductor as computed by Quencher. The results represent the extension, from 2 to 50 seconds, of the quench event discussed above. After the current starts to decay, which is at $t = 2$ sec in this case, larger time steps can be used without losing accuracy in the solution. The CPU time used in the 50 second simulation is approximately 6 hours on the VAX 4000/90.

TPX Conductor

For the second comparison between Quencher and Saruman we consider the TF coil of the TPX machine. The parameters that characterize this conductor are summarized in Table 3.3. Note that the conductor current (and the B-field) is not a constant. The current is kept constant at $I = I_0$ until the detection time $\tau_{det} = 1$ sec, after which I decays exponentially in time; $I = I_0 \exp[-(t - \tau_{det})/\tau_{dump}]$. For the TPX coil $\tau_{dump} = 4$ sec. The conductor current as a function of time is shown in Fig. 3.8a, and in Fig. 3.8b we show the B-field profile, at various time steps during the current dump (note that $B(x, t) = B_0(x)$ for $t < \tau_{det}$ and $B(x, t) = B_0(x) \exp[-(t - \tau_{det})/\tau_{dump}]$ for $t > \tau_{det}$). We consider a 10 sec quench

in this conductor with two different initial quench zones, each of length 1 m, that are approximately 10 m apart. For this analysis we use (in both Quencher and Saruman) the heat transfer coefficient and the friction factor given by Eqs. (2.69) and (2.73), respectively. The value of ν in Eq. (2.73) is $\nu = 4$, and similarly we choose $k_f = 3$ in Eq. (2.69). (Note the complexity of this quench simulation.)

Conductor Length (m)	168.08
Copper Area (mm ²)	157.8
Nb ₃ Sn Area (mm ²)	76.97
Helium Area (mm ²)	127.0
Wall Area (mm ²)	192.0
Hydraulic Diameter (mm)	0.529
Wall Inner Perimeter (mm)	75.92
Initial Current (kA)	33.48
Detection Time (sec)	1
Dump Time (sec)	4
Inlet Pressure (atm)	9
Outlet Pressure (atm)	5
Inlet Temp. (K)	6.3
Copper RRR	75

Table 3.3: Characteristic Parameters of the TPX Coil.

In Fig. 3.9a and 3.9b we compare the conductor temperature profiles as obtained by Quencher and Saruman, respectively. Observe the close agreement in these profiles. In Fig. 3.10a and 3.10b we present the pressure profile, and the maximum pressure evolution in time, as obtained by Quencher. Note that the maximum pressure starts to decrease after an initial rise to 22 atm. This pressure rise is sufficient to cause a flow reversal at $x = 0$. In Fig. 3.11 we plot the inlet velocity which demonstrate the flow reversal event. This decreases is due to the conductor current-dump. Finally, in Table 3.4 we compare the important parameters of interest at the end of the quench evolution ($t = 10$ sec) as obtained by the two codes. Considering the complexity of the quench simulation, noting that the material property packages used in Saruman and Quencher are not identical, and finally noting that the quench initiation procedure is not the

same in the two codes (as was discussed above), the agreement is quite good.

	Quencher	Saruman
Maximum Conductor Temp.	149.5 K	145.1 K
Maximum Wall Temp.	115.4 K	107.5 K
Maximum Helium Press.	22.1 atm	20.5 atm
Length of Normal Zone	32.4 m	27.0 m
Resistive Voltage	5.4 Volts	4.4 Volts

Table 3.4: Comparison of Quencher and Saruman for the TPX Coil.

Other Comparisons

In several other cases where we have made detailed comparisons between Quencher and Saruman, the agreement has been equally good. We have found Quencher to be 30-50 times faster than Saruman in terms of the CPU time required to study quench events. One somewhat more difficult comparison occurs when the area of the conduit wall A_w becomes very small. In this regime a much larger number of elements in Saruman is required to achieve convergence. This causes Saruman to require prohibitively large CPU time. Even so, the results of Saruman appear to be converging to those of Quencher in the limit of small A_w . As an example consider a conductor nearly identical to the ITER coil summarized in Table 3.2. Here, we consider the case where $A_w = 1 \times 10^{-6} \text{ m}^2$. For this case we have plotted the normal length and the maximum pressure evolution, respectively, in Figs. 3.12a and 3.12b during a 2 sec quench. In these figures we show how the results obtained by Saruman depend on the number of elements (or the length of the elements) within a specified region at the center of the conductor. In Fig. 3.12c compare the maximum conductor temperature as obtained by Quencher and Saruman. These figures illustrate how as the number of elements is increased in Saruman, the results of this code come closer to those predicted

by Quencher. In Fig. 3.13a-b we further demonstrate this issue by plotting the length of the normal zone and the maximum pressure (both at $t = 1$ sec) versus the inverse of the length of the smallest element used in Saruman.

3.3 Comparison With Experimental Data

In order to compare the results of Quencher with experimental data we consider the clean and unambiguous measurements carried out by T. Ando et al. [8]. The CICC used in this experiment has a length 26 m, $A_{cu} = 1.02 \times 10^{-5} \text{ m}^2$, $A_{sc} = 3.4 \times 10^{-6} \text{ m}^2$, $A_w = 2.5 \times 10^{-5} \text{ m}^2$, $A_h = 1.4 \times 10^{-5} \text{ m}^2$, $d_h = 6.9 \times 10^{-4} \text{ m}$, and $P_w = 0.019 \text{ m}$. The conductor is in a uniform magnetic field of 7 T. Before initiation of quench, the helium is stagnant at a temperature of 4.5 K and a pressure of 10 atm. The ends of the channel are connected to pressure relief valves which maintain the helium pressure at 10 atm. In Table 3.5 we summarize all the parameters that characterize this conductor, and in Fig. 3.14 we show a picture of the cross-section of the conductor.

The results of this experiment are presented in the form of a plot of the normal length as a function of time, for various values of the conductor current. Such a measurement was done by placing 50 voltage taps along the length of the conductor. Both in the experiment and Quencher the quench is initiated by depositing the external heat at the center of the conductor, over a 40 mm length for a period of 0.1 msec. In Quencher the amount of heat deposited to initiate the quench is $2.7 \times 10^6 \text{ W/m}$ (this corresponds to a total energy deposition of 2.7 J/cm.) This value is not explicitly given in the paper by Ando et al. [8]. It has been chosen to match the first data point for the case $I = 2 \text{ kA}$ and is then held fixed for all other values of I .

Conductor Length (m)	26
Copper Area (mm ²)	10.2
NbTi Area (mm ²)	3.4
Helium Area (mm ²)	14
Wall Area (mm ²)	25
Hydraulic Diameter (mm)	0.69
Wall Inner Perimeter (mm)	18.8
Initial Current (kA)	1.5–2.0
Detection Time (sec)	∞
Inlet Pressure (atm)	10
Outlet Pressure (atm)	10
Inlet Temp. (K)	4.5
Copper RRR	100

Table 3.5: Characteristic Parameters of the Coil Used by Ando et al. [8].

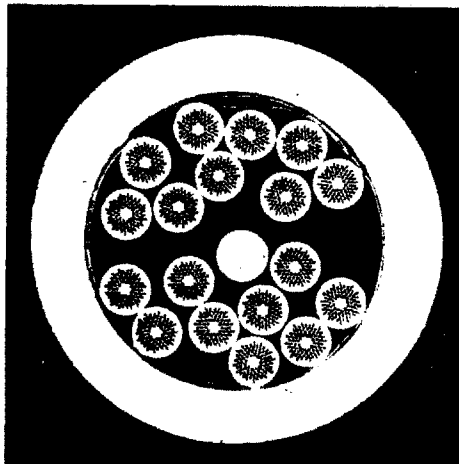


Figure 3.14: Cross-sectional view of the conductor used in the experiment of Ando et al. [8]. (This figure is taken directly from Reference [8].)

Before proceeding with a direct comparison between the Quencher and the experimental results, consider some of the various profiles during the quench for the case where $I = 1.5$ kA. In Fig. 3.15a we show the temperature profile for various time steps and during a 7 second quench simulation. Observe the large temperature rise and the expansion of the quench region at the end of the 7 seconds. This figure clearly demonstrates that this experiment covers a very large range in both the temperature rise and also in the evolution of the quench region. In Fig. 3.15b we show the conduit wall temperature profile at the various time steps during the quench evolution. Note that the wall and the conductor temperatures are approximately different by 70 K at the end of the simulation. In Fig. 3.15c we plot the pressure profile and finally in Figs. 3.15d and 3.15e we show the helium density and the Reynold's number, respectively. From Fig. 3.15c we observe that the pressure rise during the quench event is reasonably small which is due to the rapid depletion of the helium density shown in Fig. 3.15d. We have plotted the Reynold's number in Fig. 3.15e in order to emphasize the large range of Reynold's numbers encountered in this quench event. In the quench region the Reynold's numbers are below 2000 while in the outer region, numbers as high as 40000 are observed. Thus, both the laminar and the turbulent regimes of the heat transfer coefficient discussed in chapter 2 (see also Fig. 2.3) are encountered in this experiment. Typical helium expulsion velocities are approximately 1-2 m/sec.

Finally, the comparison of Quencher results with the experimental data is presented in Fig. 3.16. The minimum and maximum values of the current used in the experiment are 1.5 and 2 kA, respectively. Note the large variation of the normal length with current at any given time; the dependence of normal length on current is in fact nearly exponential. Here, the heat transfer coefficient and the friction factor used in Quencher are given by the models presented in section 2.3. We have found the Quencher results presented in Fig. 3.16 to be nearly independent (≤ 1 %) of the value of ν used in Eq. (2.73), for $2 \leq \nu \leq 8$. Also, the dependence is very weak (≤ 15 %) on the value of k_f used in Eq. (2.69), for

$1 \leq k_f \leq 5$. The agreement of the computational data and the experiment is very good and well within the uncertainties of the material properties of the various components.

Chapter 3 References

- [1] Ascher, U. M., Christiansen, J., Russell, R. D., *Collocation Software for Boundary-Value ODE's*, ACM Transactions on Mathematical Software, Vol. 7, No. 2, 1981.
- [2] Ascher, U. M., Mattheij, R. M. M., Russell, R. D., Numerical Solution of Boundary Value Problems for Ordinary Differential Equations, Prentice Hall Inc., New Jersey, 1988.
- [3] Ascher, U. M., Christiansen, J., Russell, R. D., Codes for Boundary-Value Problems in Ordinary Differential Equations, Proceedings of a Working Conference, Edited by B. Childs et al., Springer-Verlag, New York, 1979, pp.164–185.
- [4] Pereyra, V., Codes for Boundary-Value Problems in Ordinary Differential Equations, Proceedings of a Working Conference, Edited by B. Childs et al., Springer-Verlag, New York, 1979, pp.67–88.
- [5] Bottura, L., Zienkiewicz, O. C., *Quench Analysis of Large Superconducting Magnets Parts I and II*. Cryogenics, Vol. 32, No. 7, 1992.
- [6] Bottura, L., private communication, 1993.
- [7] Wong, R. L., Program CICC Flow and Heat Transfer in Cable-In-Conduit Conductors – Equations & Verification, Lawrence Livermore National Laboratory Internal Report, UCID 21733, May 1989.
- [8] Ando, T., Nishi, M., Kato, T., Yoshida, J., Itoh, N., Shimamoto, S., *Propagation Velocity of the Normal Zone in a Cable-In-Conduit Conductor*, Advances in Cryogenic Engineering, Vol. 35, Plenum Press, New York, 1990.

Conductor Temperature vs. x

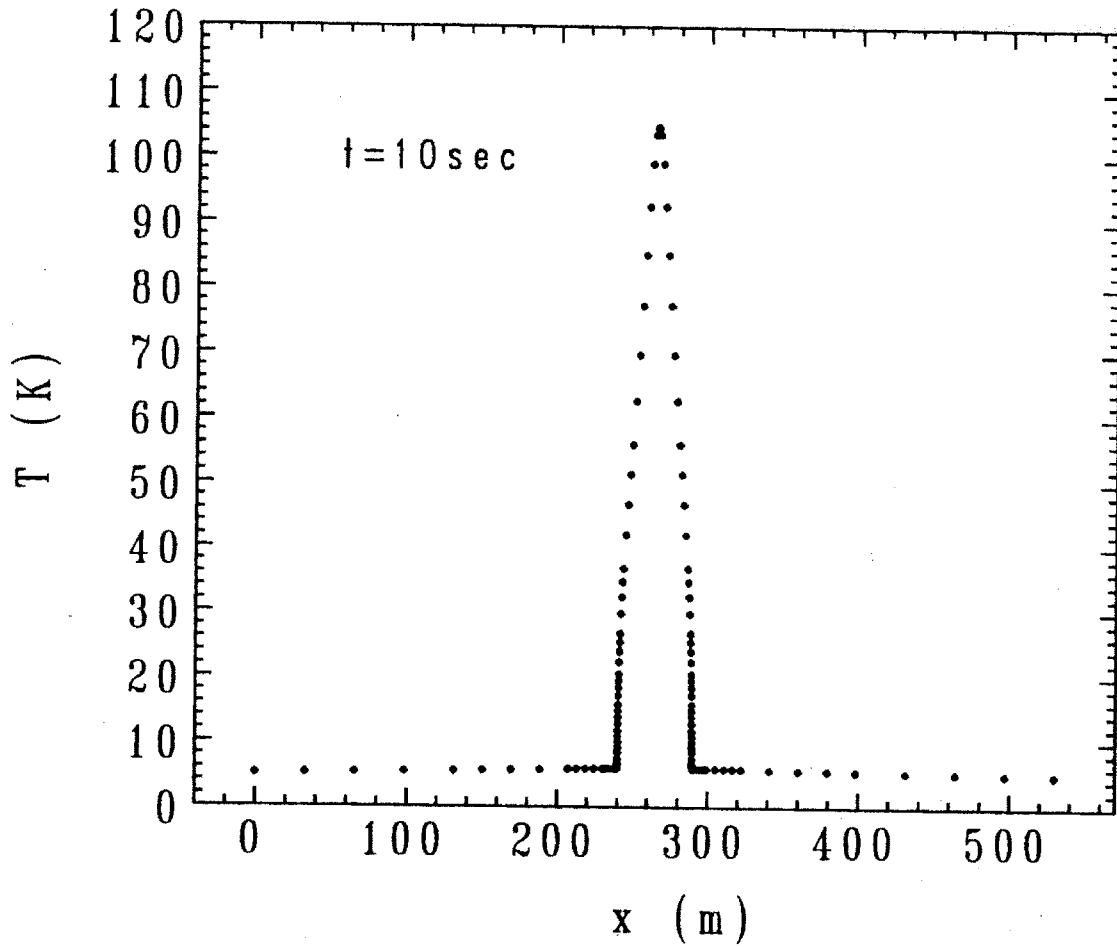


Figure 3.1a: The temperature profile during quench.

Helium Density vs. x

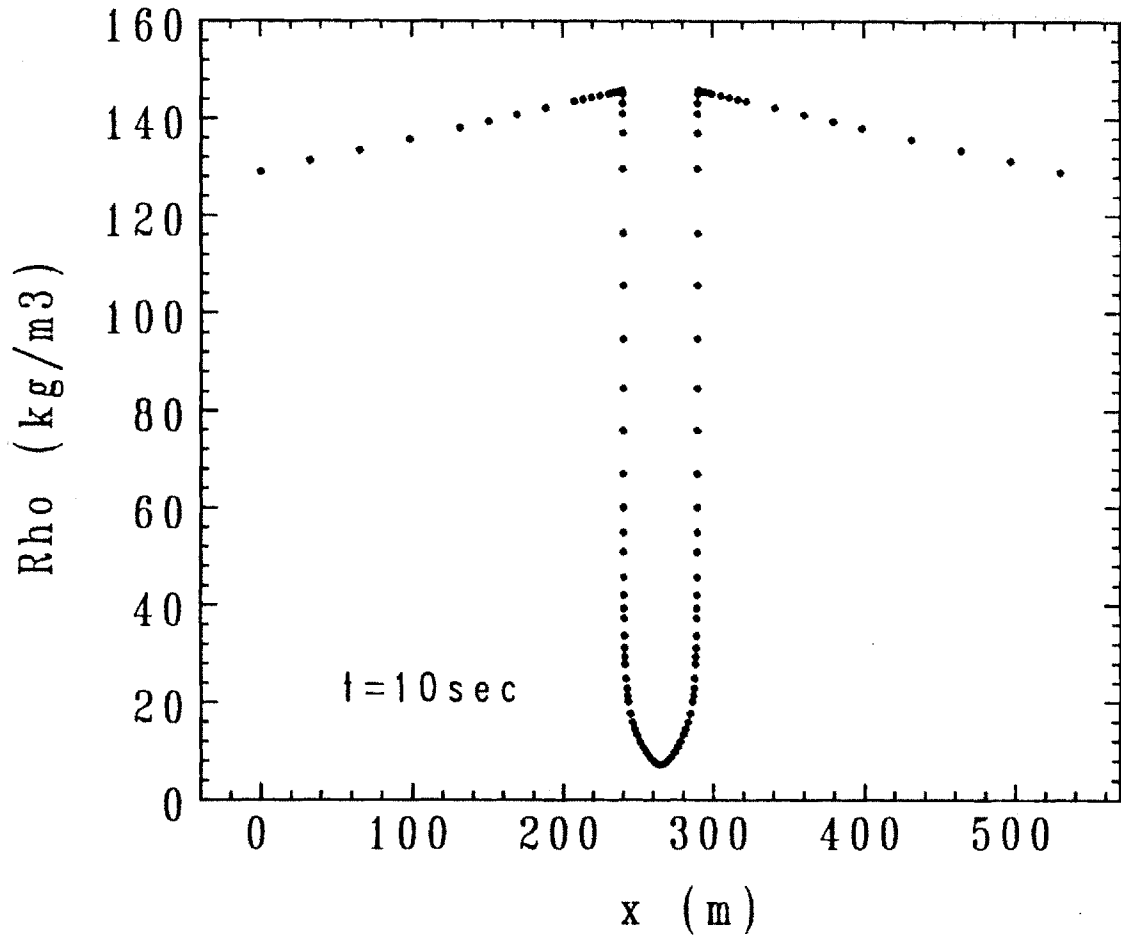


Figure 3.1b: The helium density profile during quench.

Temperature vs. x

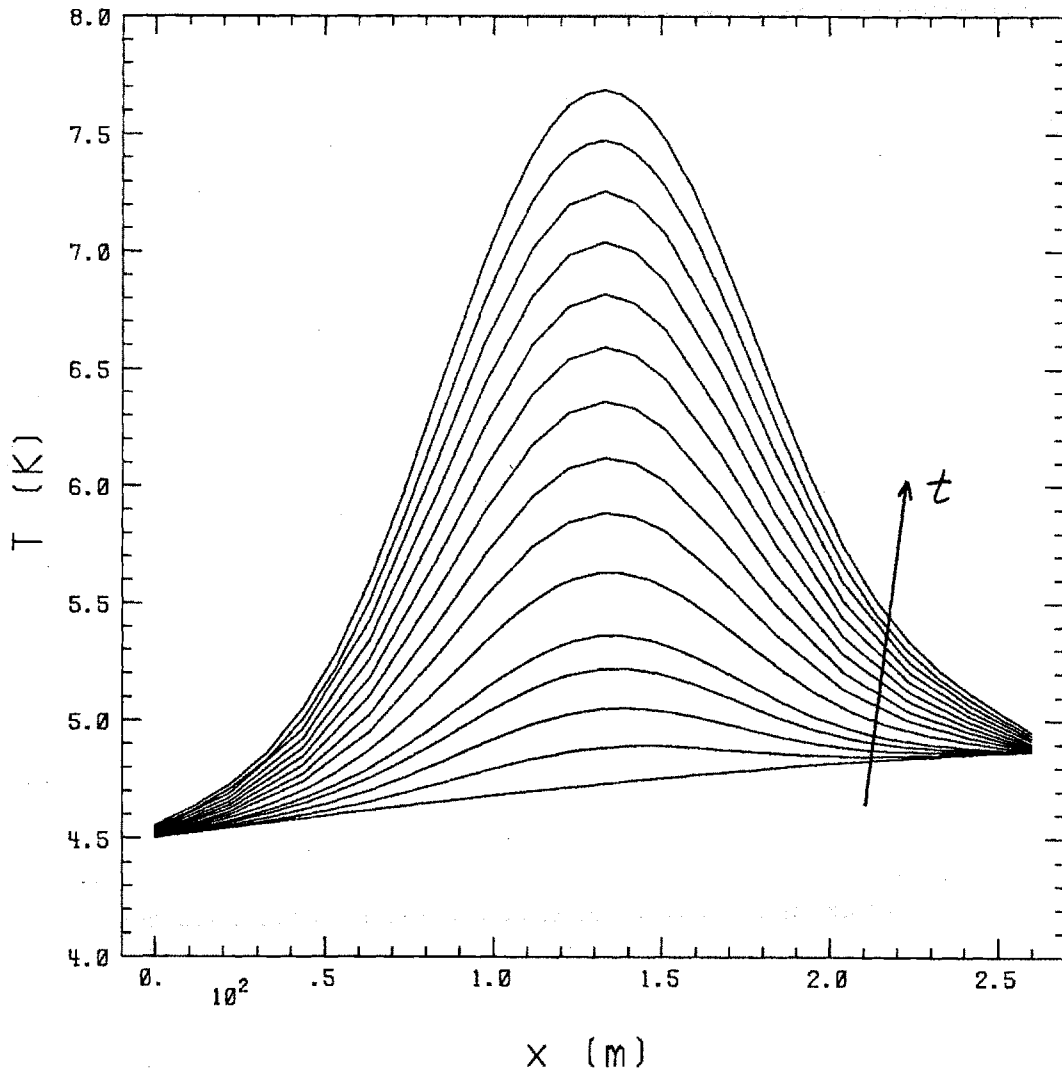


Figure 3.2a: Conductor temperature profile, at various time steps, in a CICC with an external heat source given by Eq. (3.28).

Helium Density vs. x

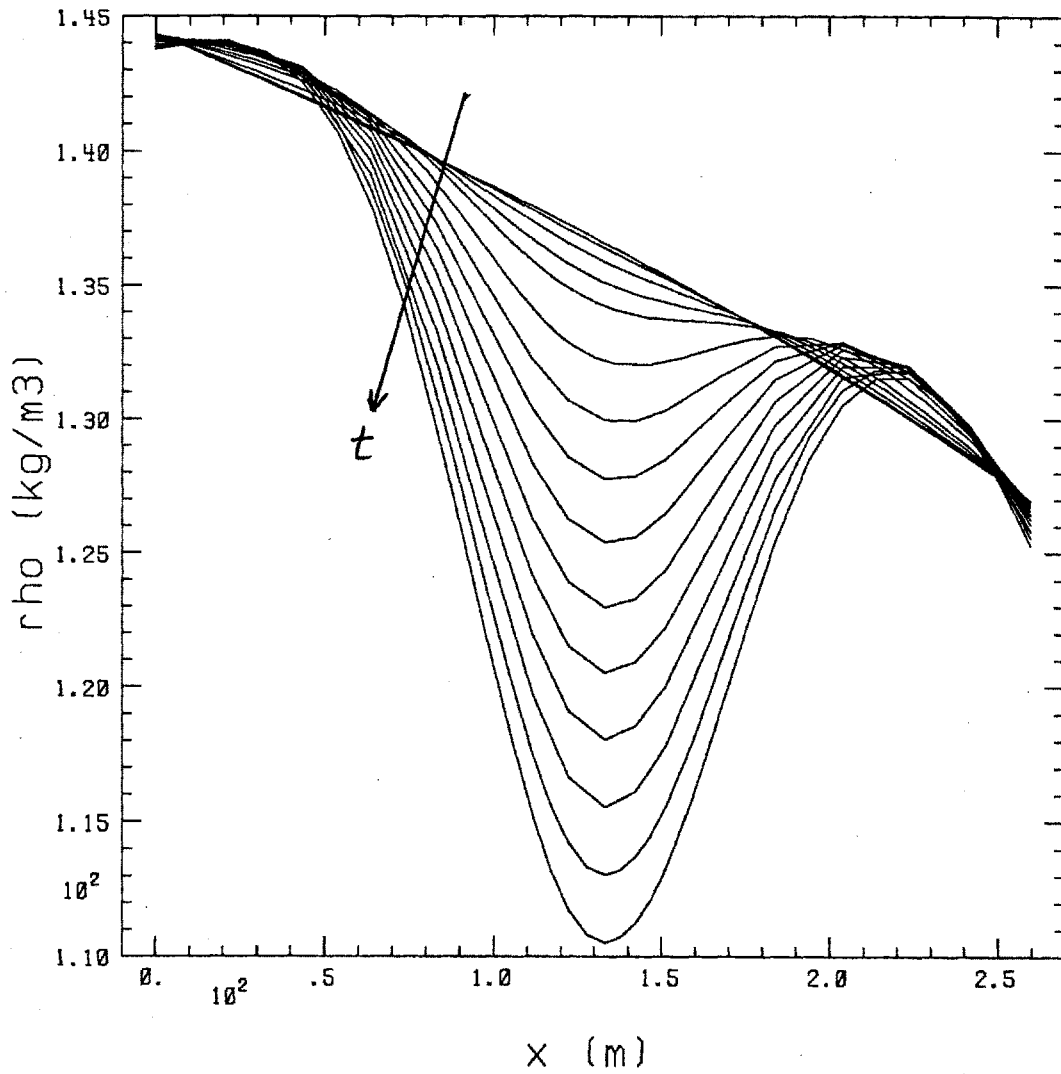


Figure 3.2b: Helium density profile, at various time steps, in a CICC with an external heat source given by Eq. (3.28).

Helium Velocity vs. x

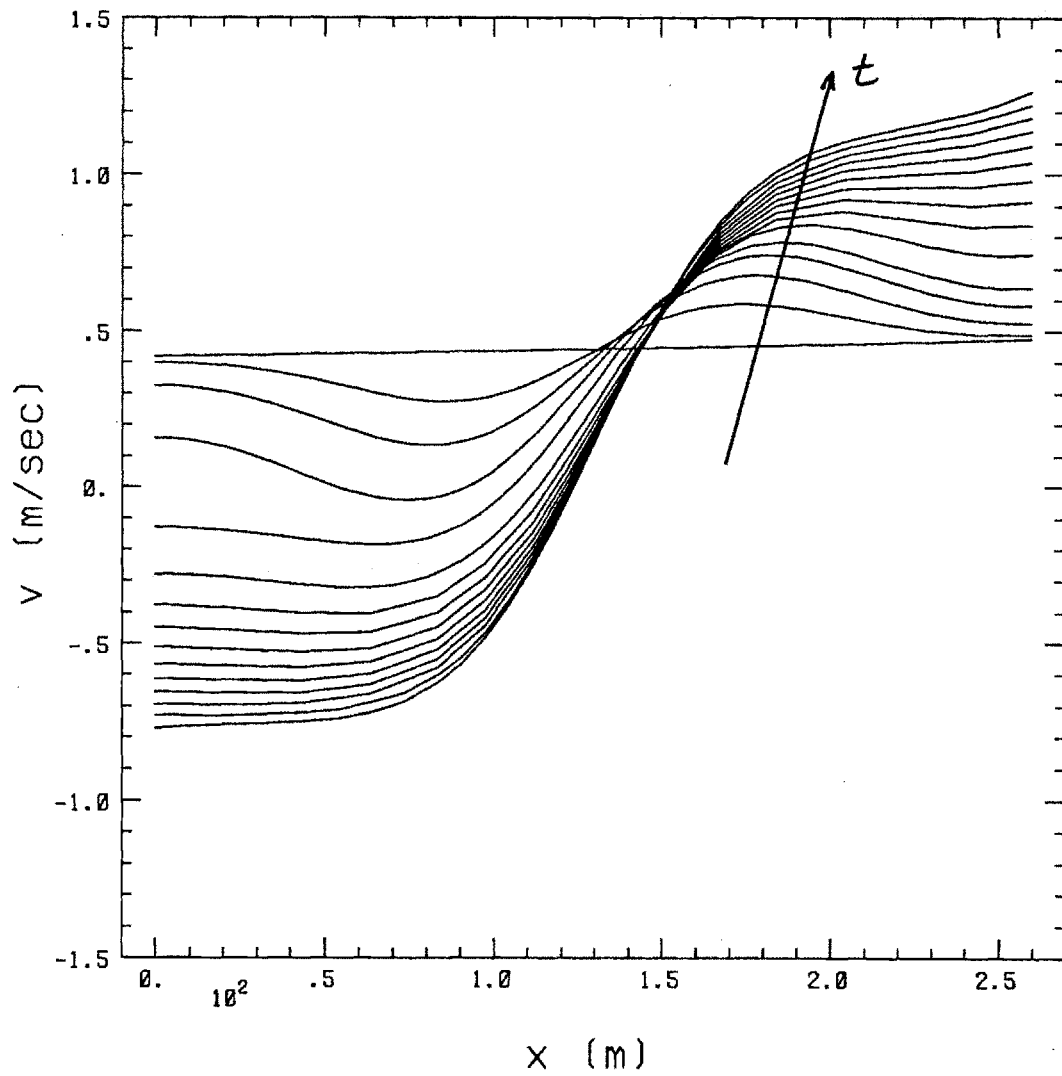


Figure 3.2c: Helium velocity profile, at various time steps, in a CICC with an external heat source given by Eq. (3.28).

Helium Pressure vs. x

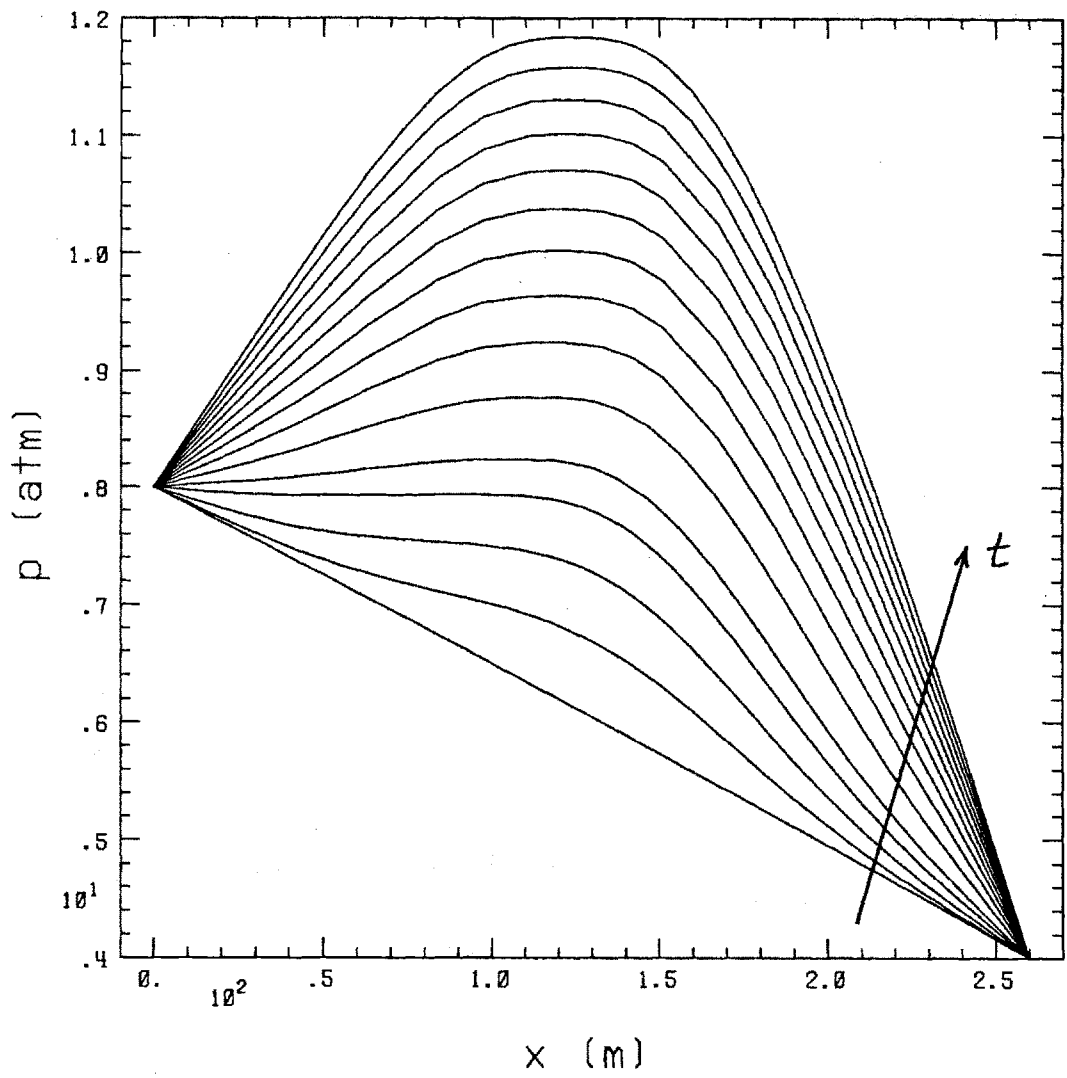


Figure 3.2d: Helium Pressure profile, at various time steps, in a CICC with an external heat source given by Eq. (3.28).

Heat Flux vs. x

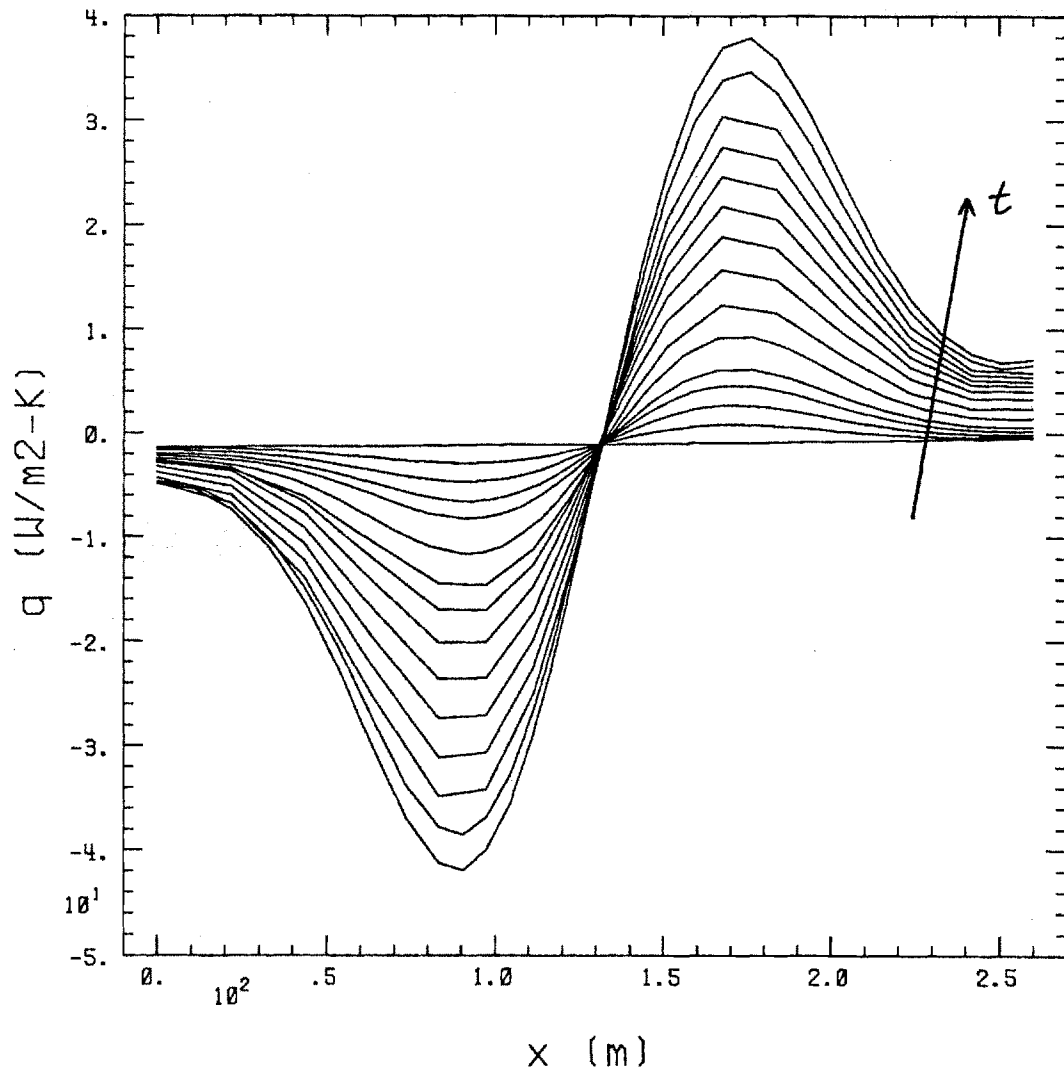


Figure 3.2e: Heat flux profile, at various time steps, in a CICC with an external heat source given by Eq. (3.28).

Mass Flux vs. x

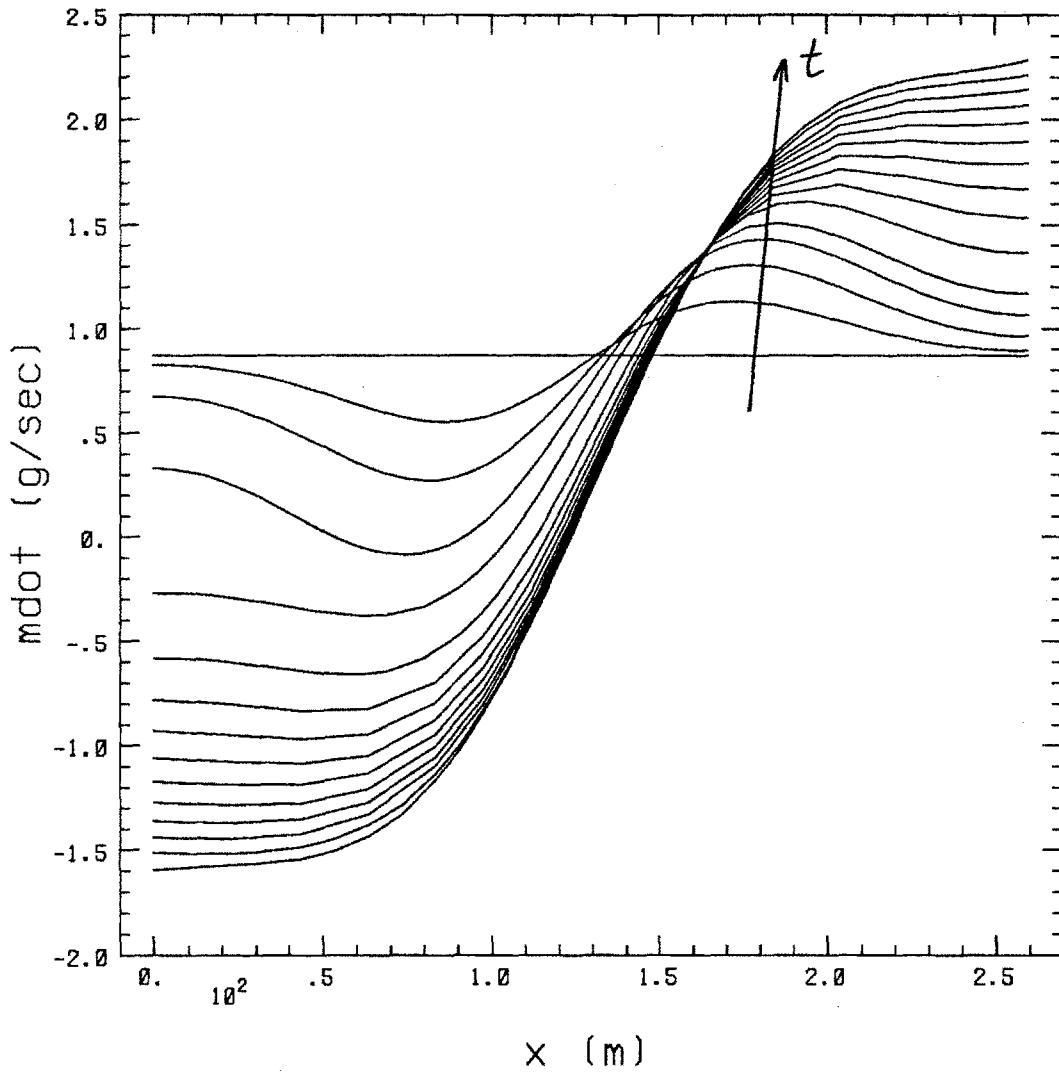


Figure 3.2f: Helium mass flux profile, at various time steps, in a CICC with an external heat source given by Eq. (3.28).

Inlet Velocity vs. time

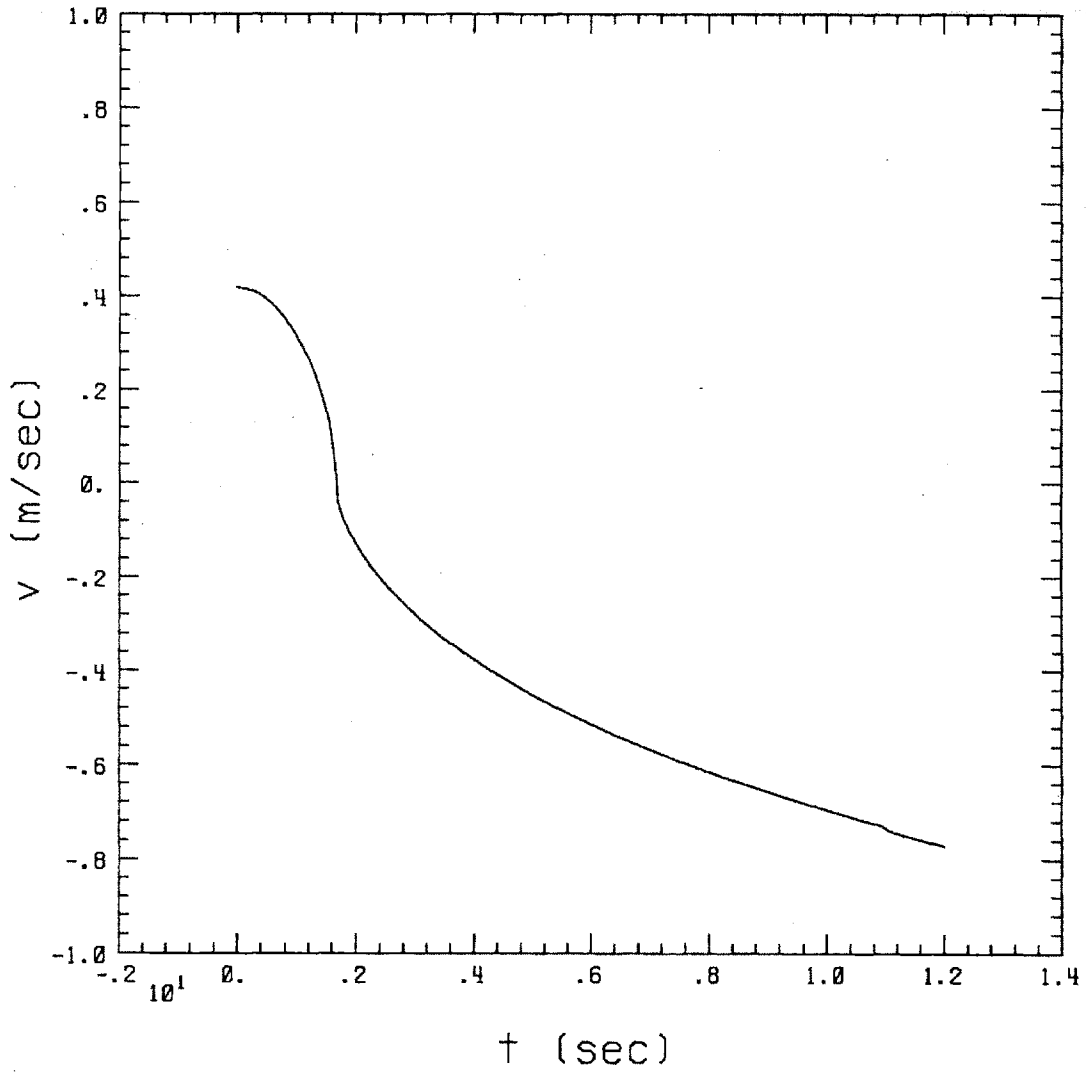


Figure 3.3: Helium inlet velocity in a CICC with an external heat source given by Eq. (3.28).

Conductor Temperature vs. Time

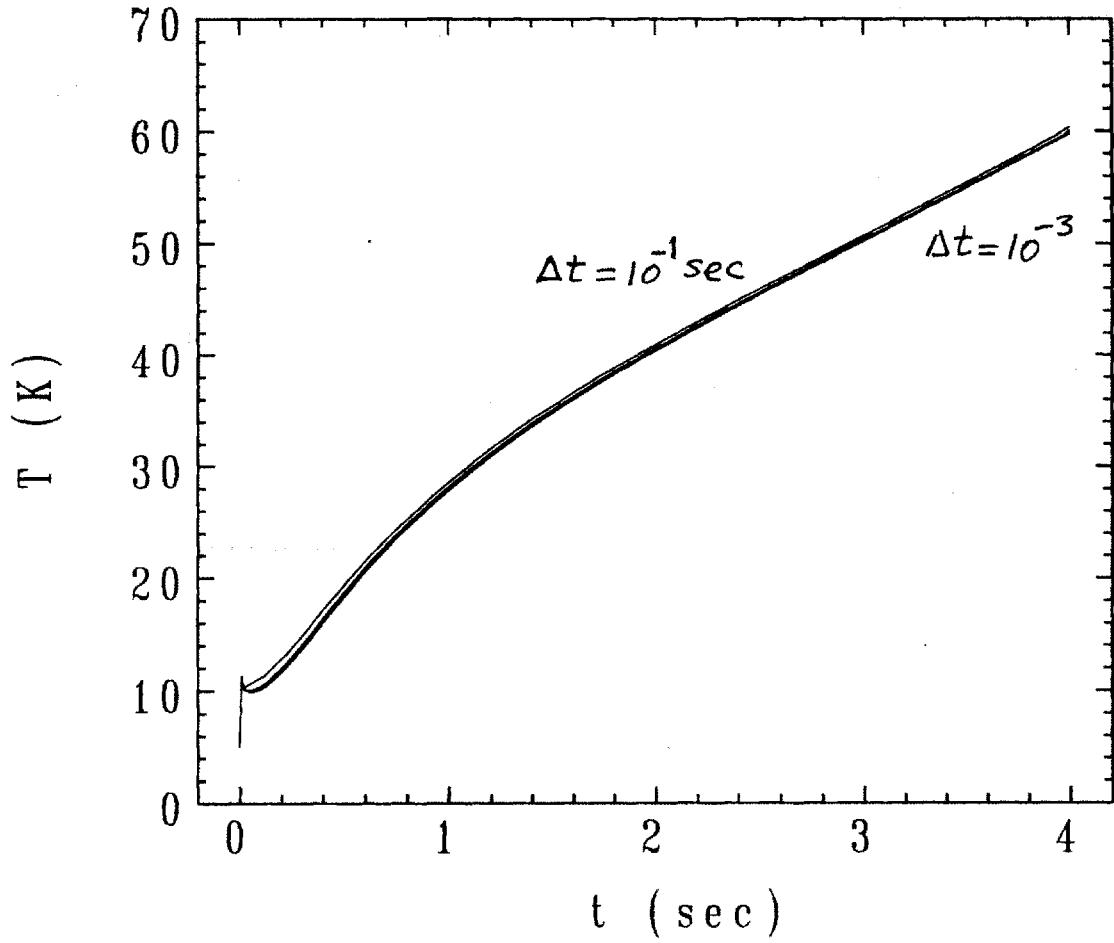


Figure 3.4a: The maximum conductor temperature versus time for various values of Δt .

Maximum Helium Pressure vs. Time

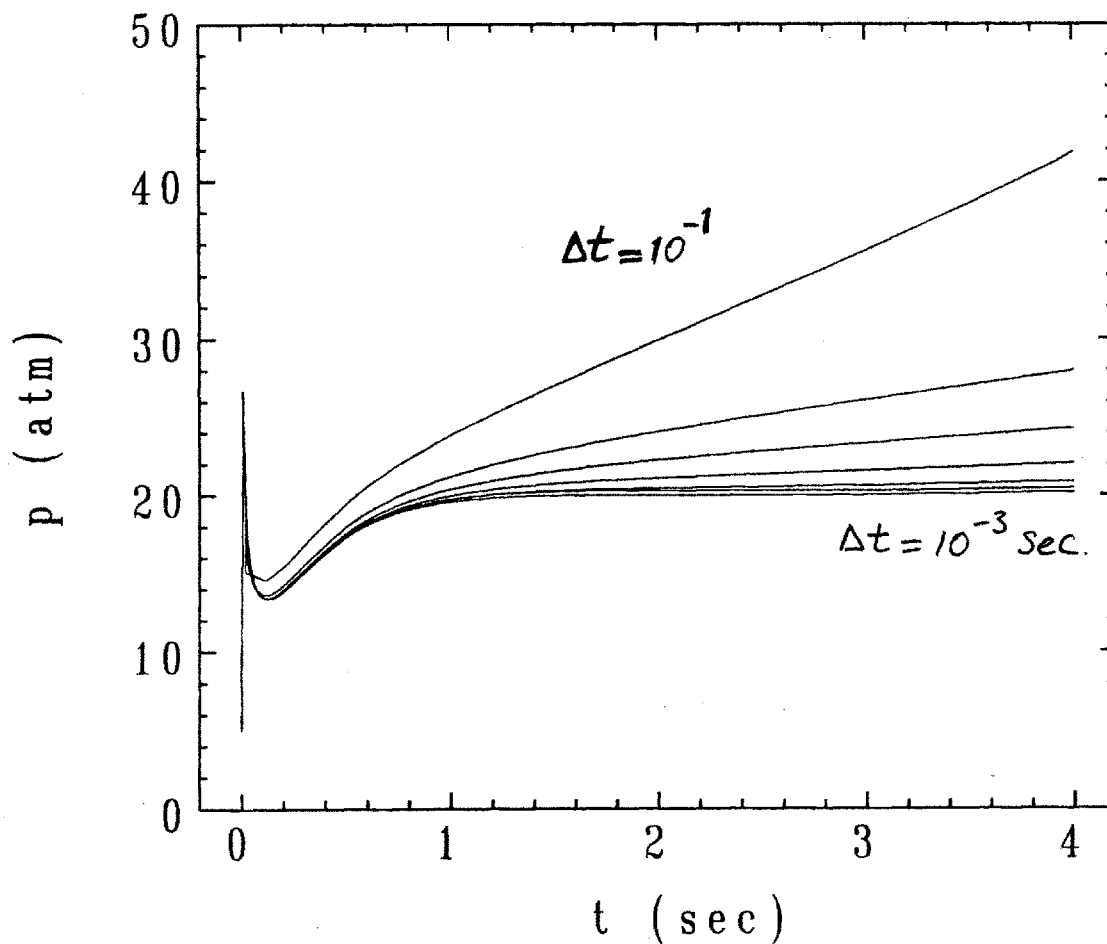


Figure 3.4b: The maximum helium pressure versus time for various values of Δt .

Normal Length vs. Time

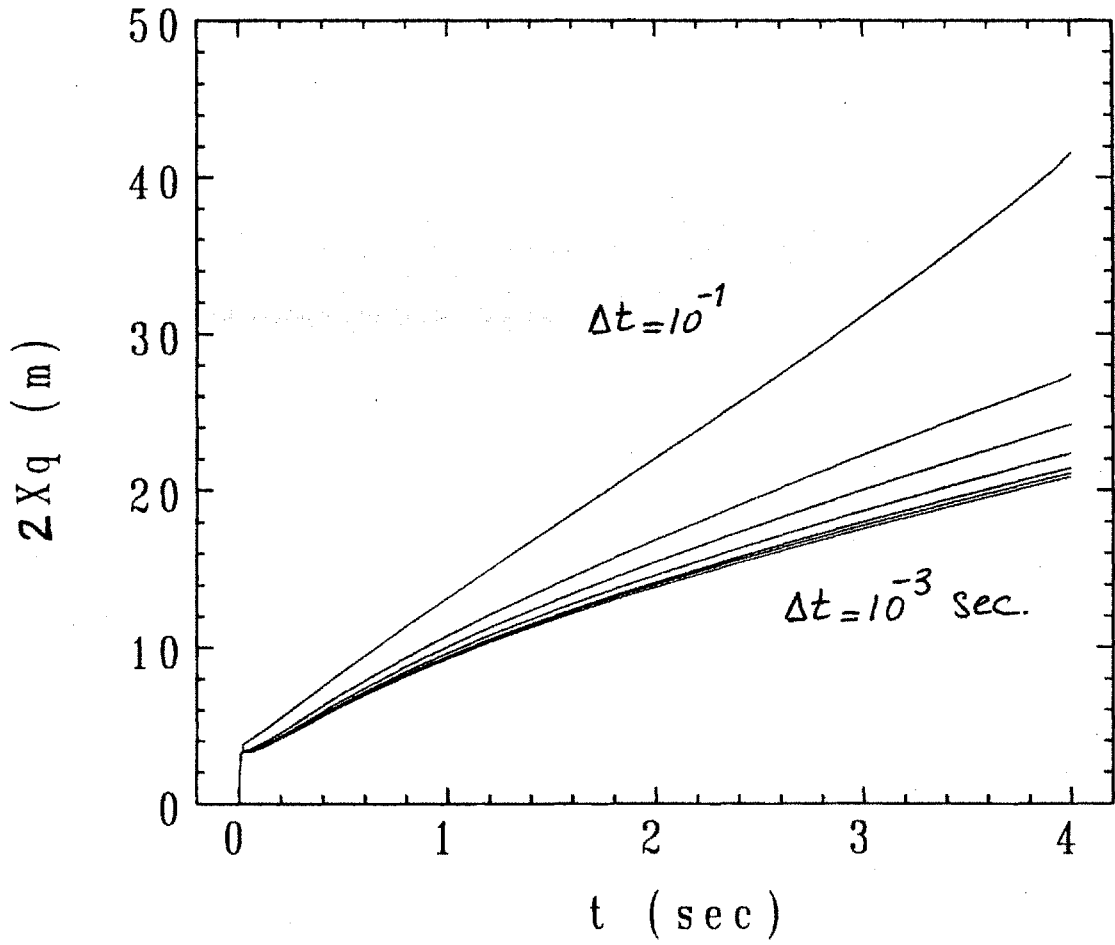


Figure 3.4c: The length of the normal region versus time for various values of Δt .

Quench Voltage vs. Time

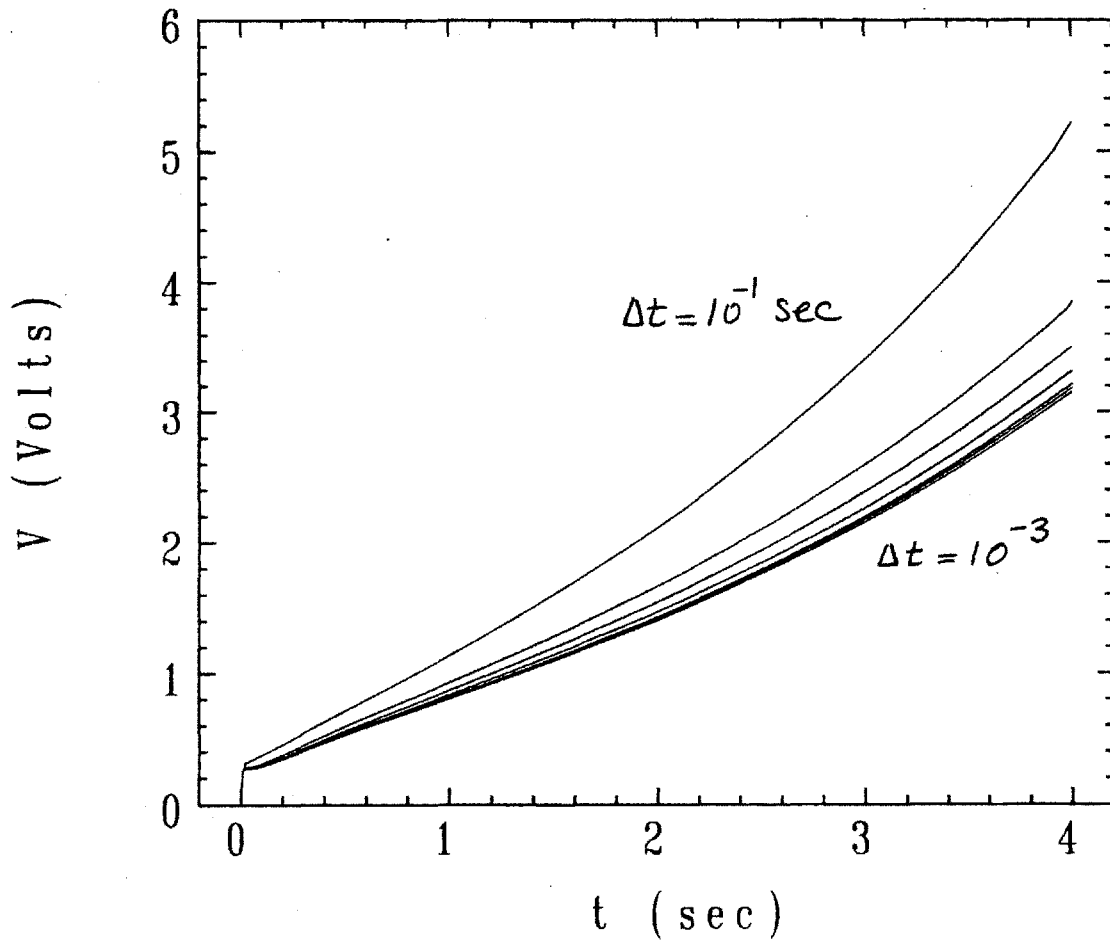


Figure 3.4d: The quench voltage versus time for various values of Δt .

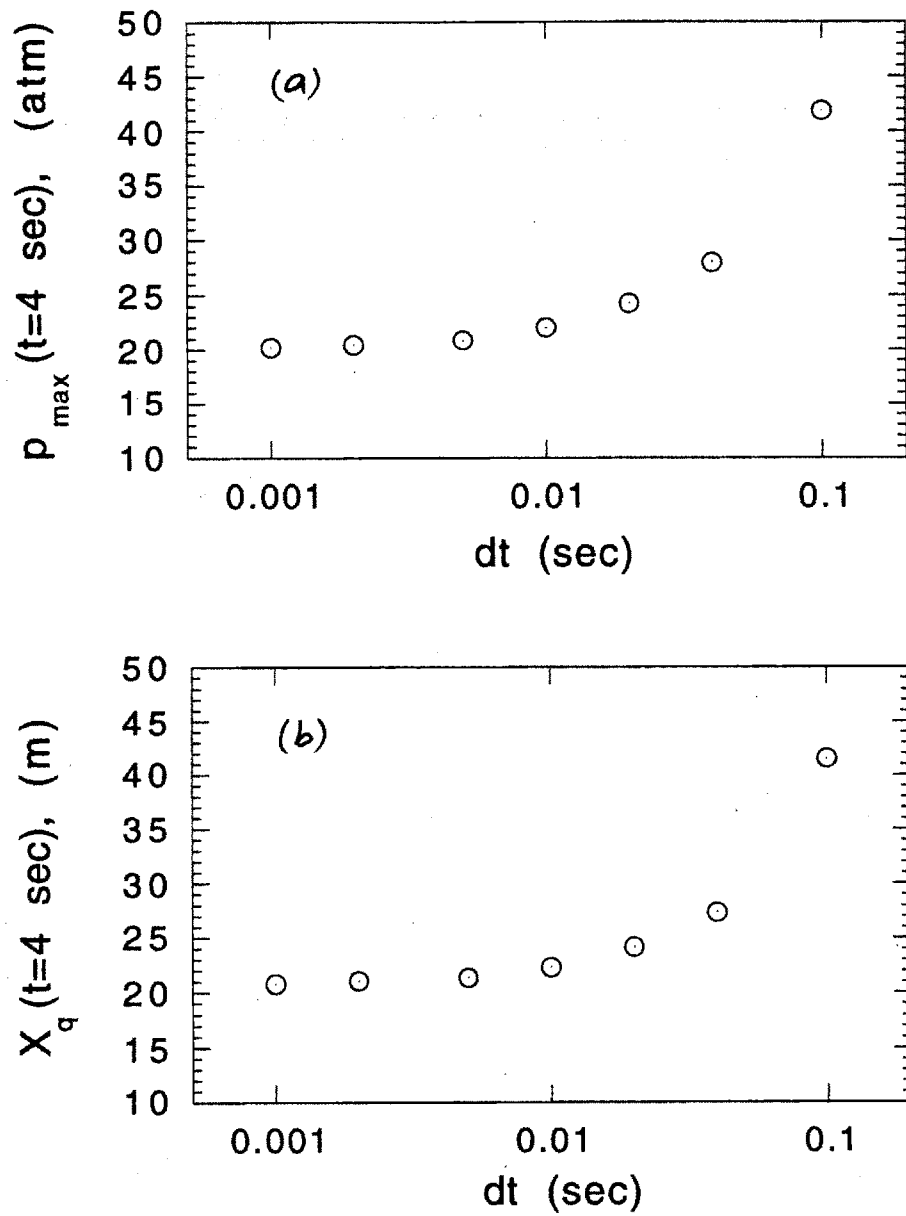


Figure 3.5: (a) The maximum helium pressure at $t = 4$ sec versus Δt , and (b) the length of the normal region at $t = 4$ sec versus Δt .

Conductor Temperature Vs. Time

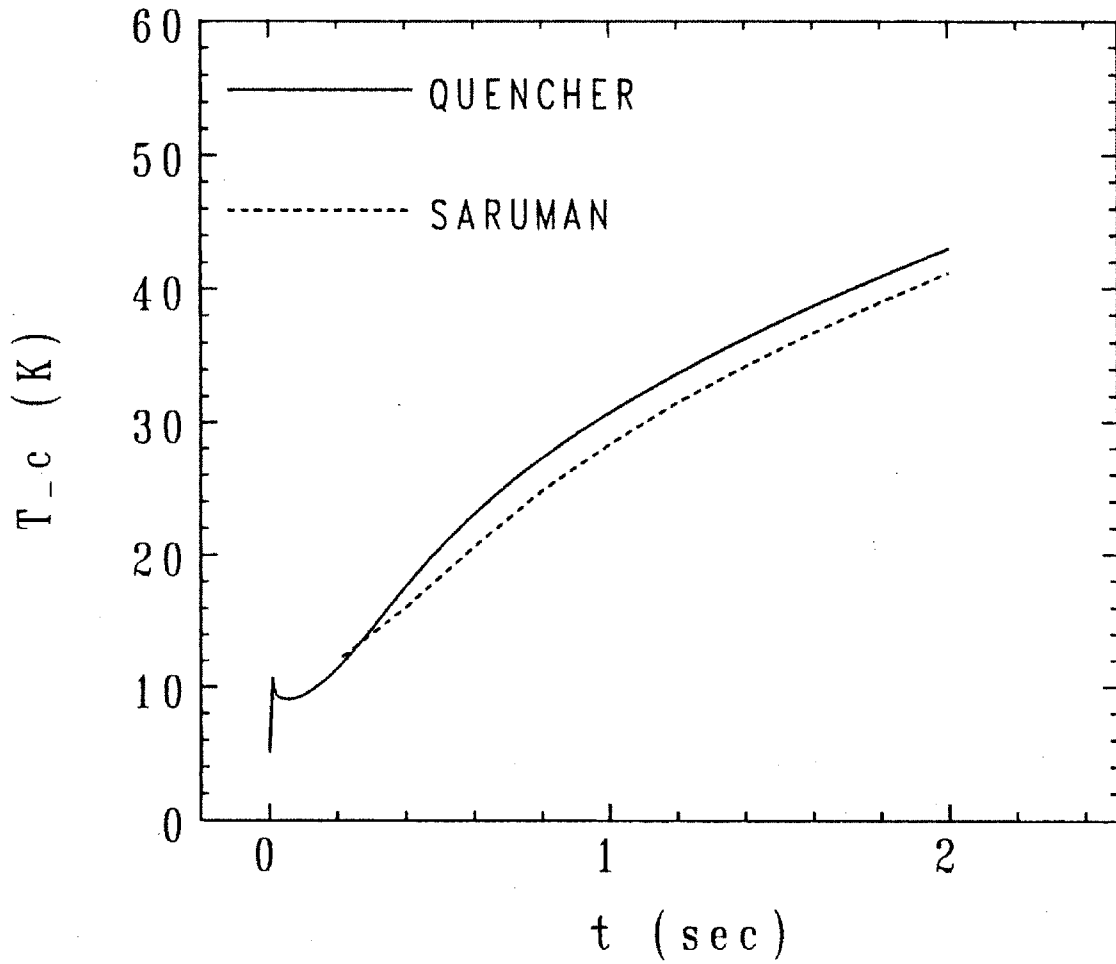


Figure 3.6a: Comparison of the maximum conductor temperature as calculated by Quencher and Saruman.

Wall Temperature Vs. Time

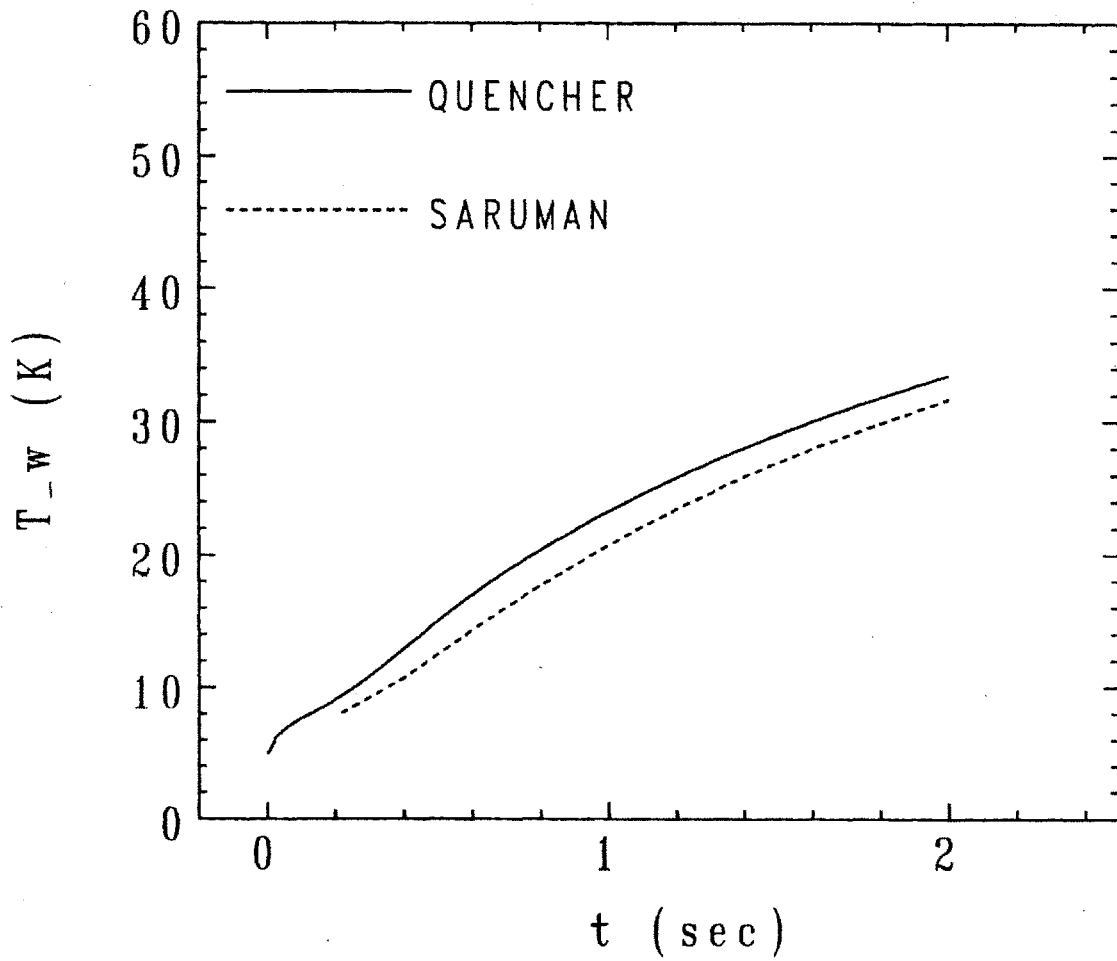


Figure 3.6b: Comparison of the maximum wall temperature as calculated by Quencher and Saruman.

Maximum Pressure Vs. Time

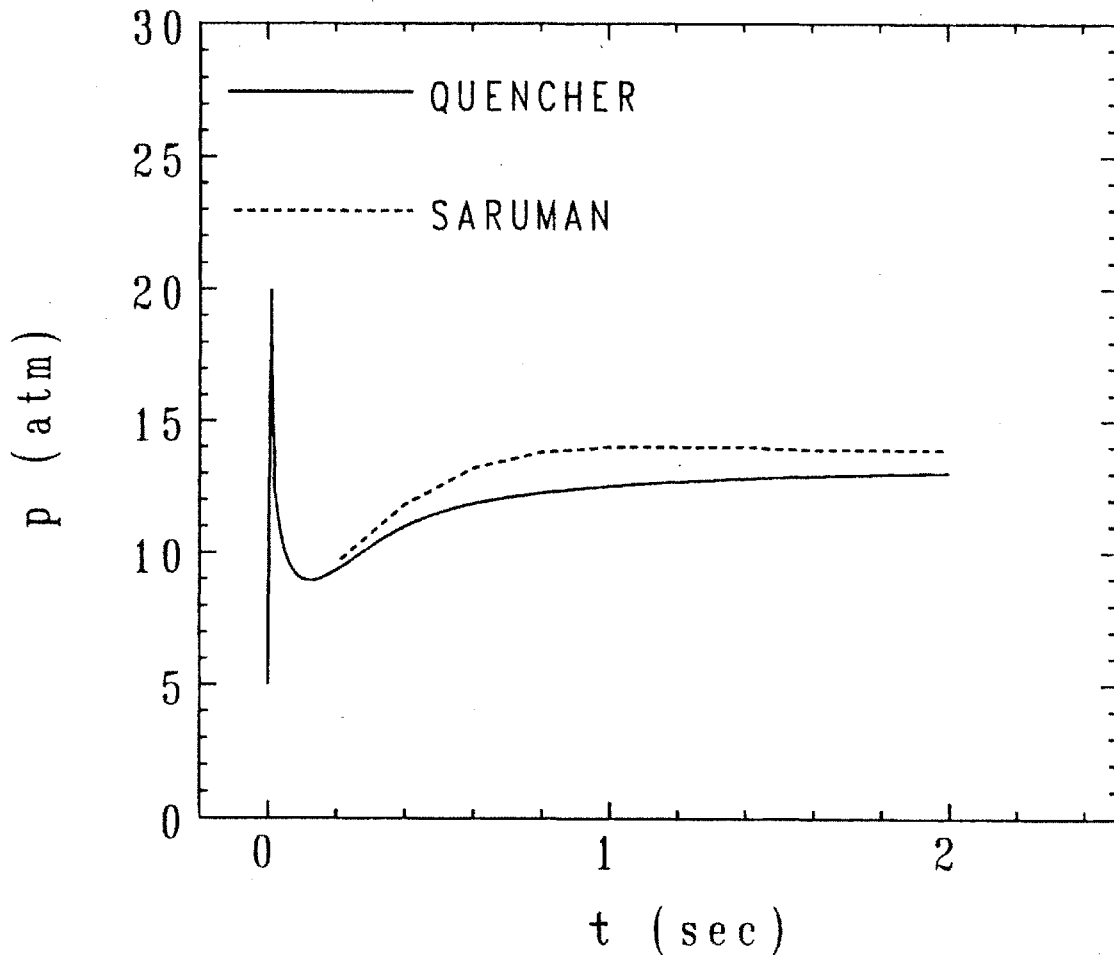


Figure 3.6c: Comparison of the maximum helium pressure, as calculated by Quencher and Saruman.

Length of Normal Region Vs. Time

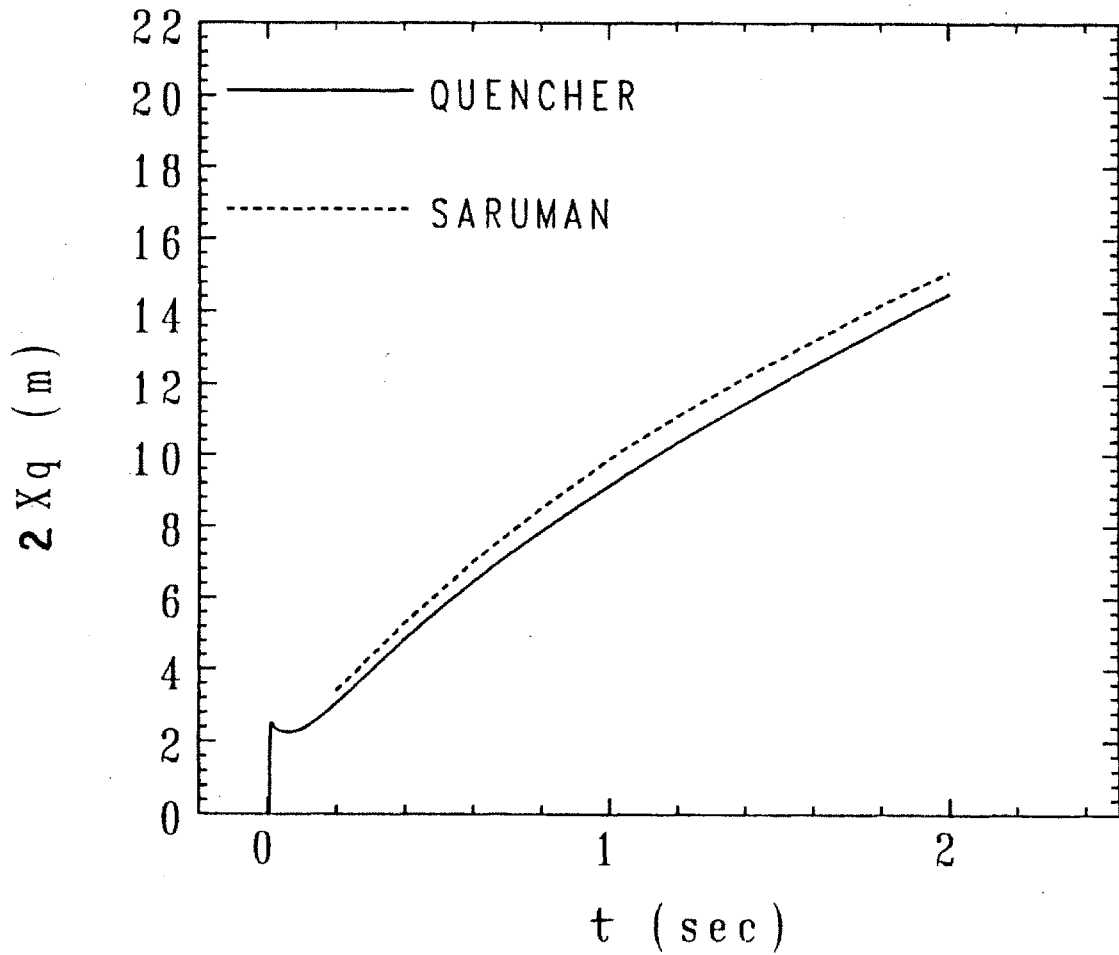


Figure 3.6d: Comparison of the normal length as calculated by Quencher and Saruman.

Voltage Vs. Time

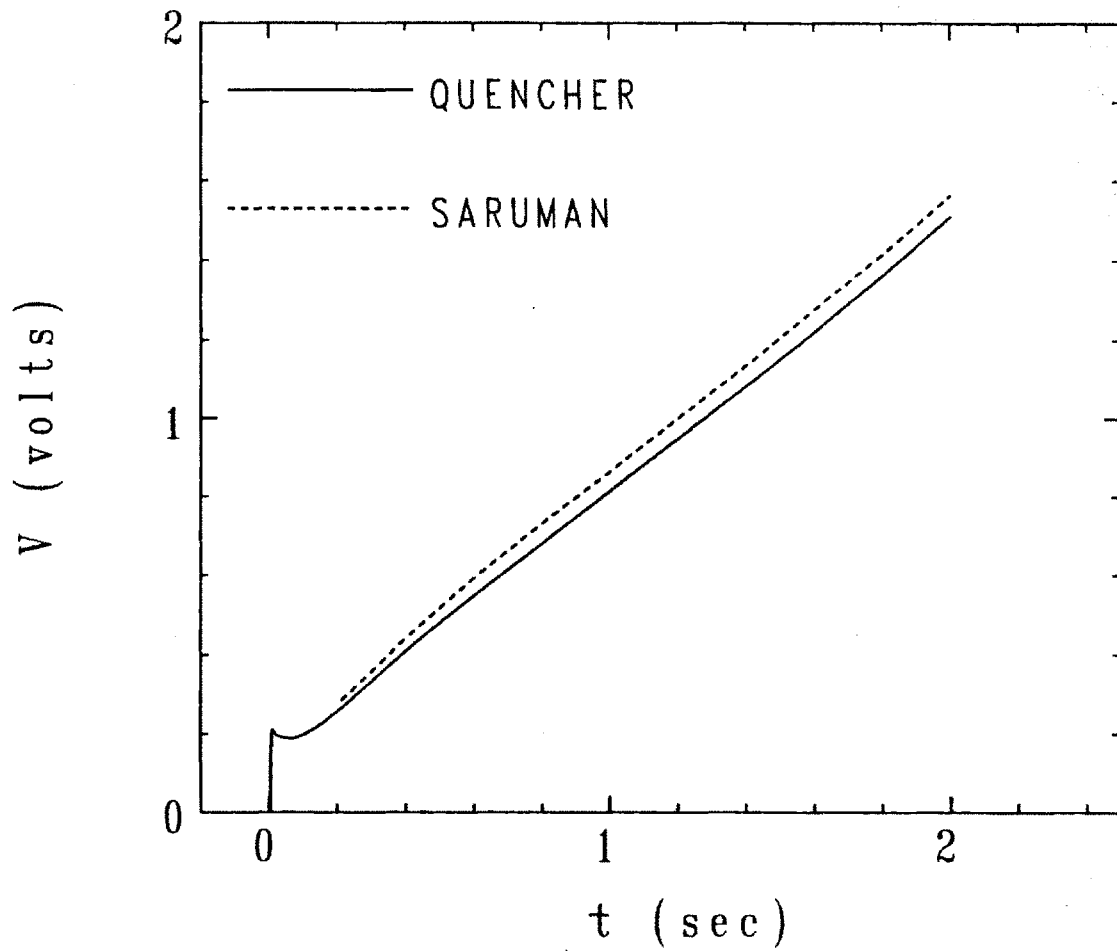


Figure 3.6e: Comparison of the quench-voltage as calculated by Quencher and Saruman.

Expulsion Velocity Vs. Time

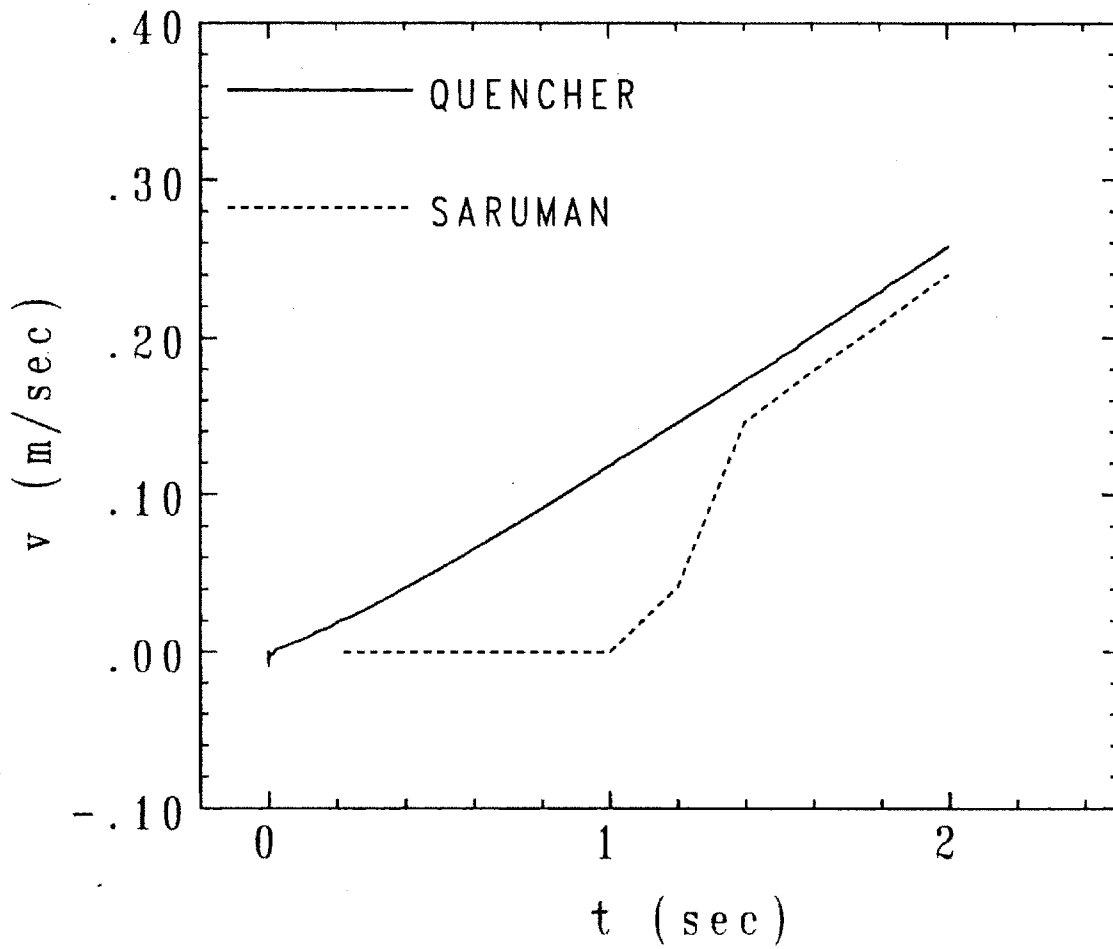


Figure 3.6f: Comparison of the helium expulsion velocity as calculated by Quencher and Saruman.

Length of Normal Region Vs. Time

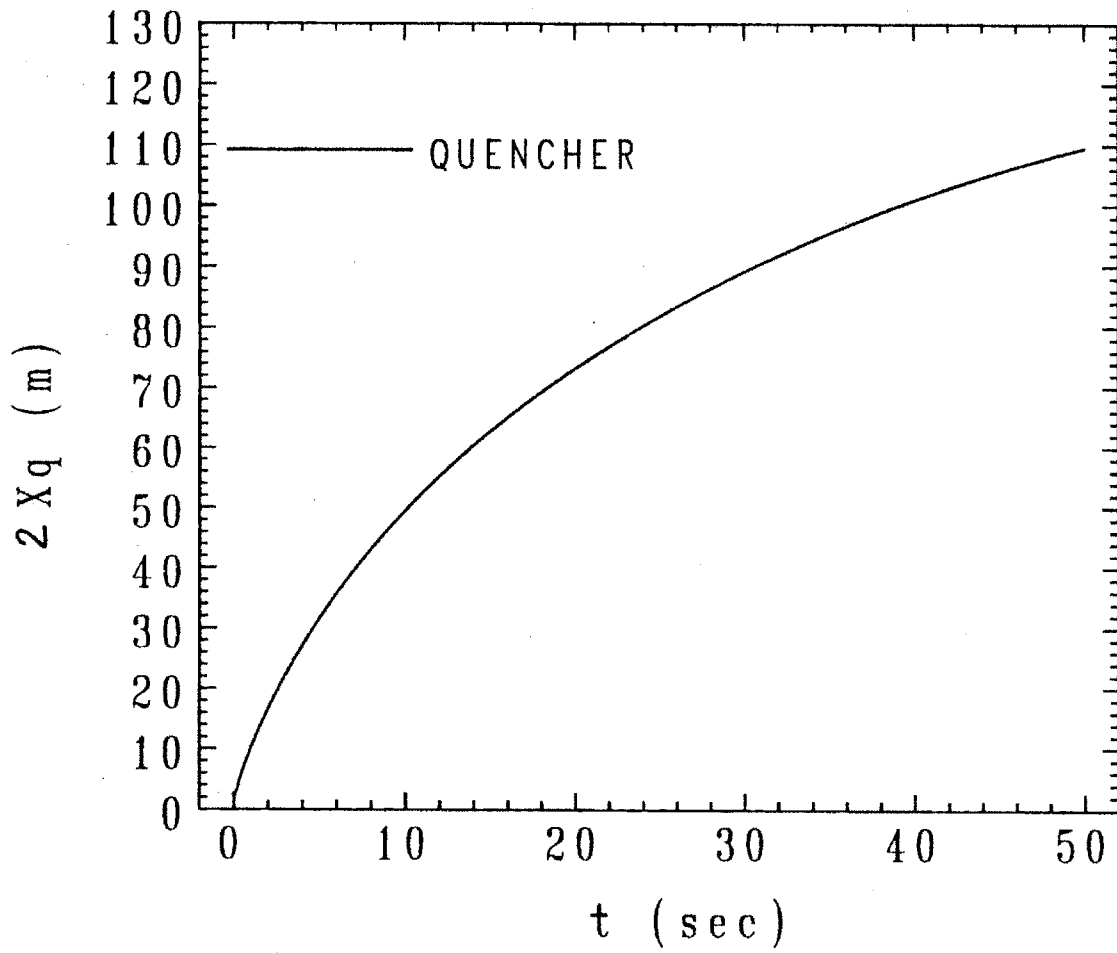


Figure 3.7: Normal length propagation during a 50 sec quench in the ITER conductor.

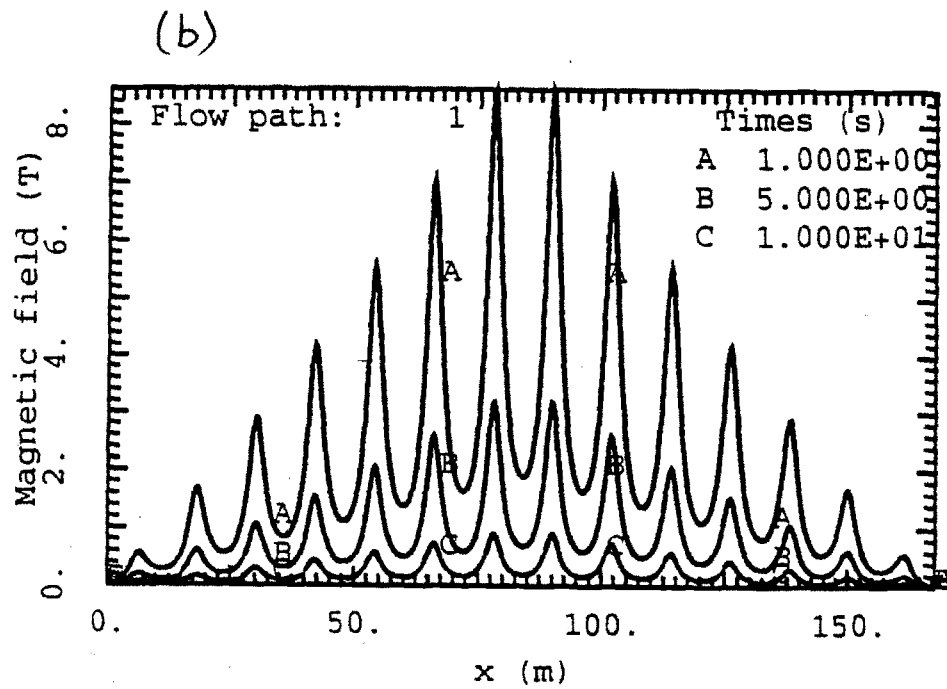
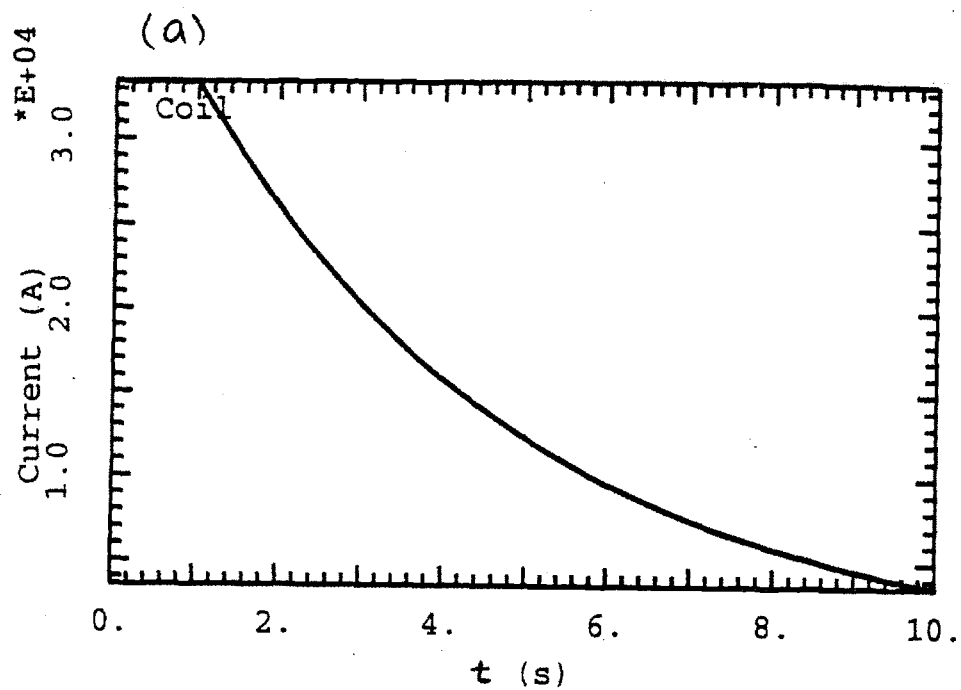


Figure 3.8: (a) Conductor current in the TPX coil versus time, and (b) the B-field profile in the TPX coil at various time steps. Both figures (a) and (b) are courtesy of Saruman.

TPX 2.4cm Conductor
Tcond vs. Position

Tc(max) = 149.5 at t = 6.9, x = 78.0
Tc(min) = 5.6 at t = 0.0, x = 168.1

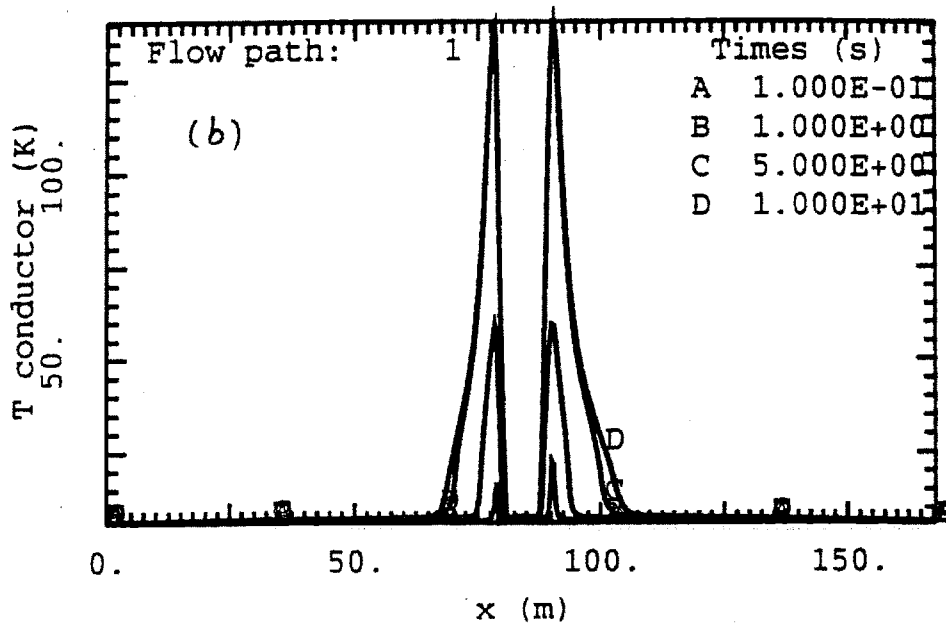
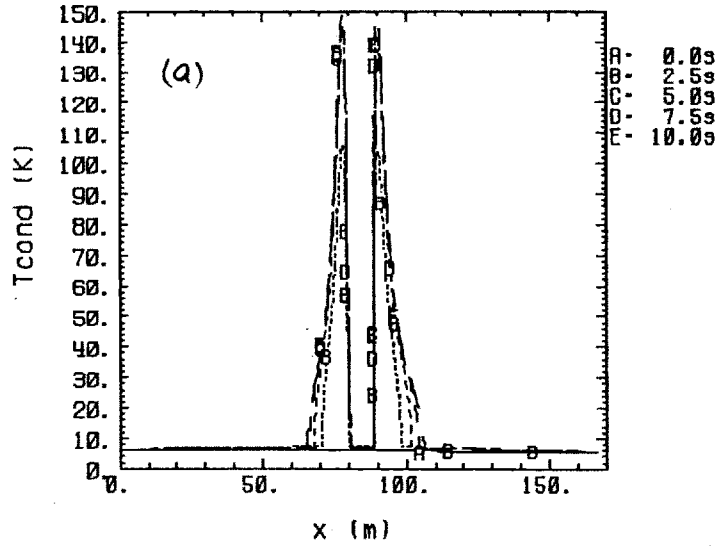
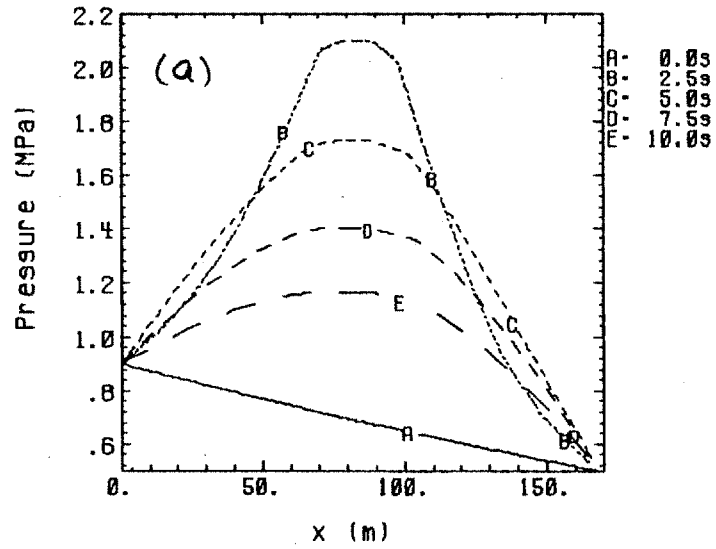


Figure 3.9: (a) Conductor temperature profile during a quench in the TPX coil as obtained by Quencher, and (b) the conductor temperature profile obtained by Saruman.

TPX 2.4cm Conductor
Pressure vs. Position

$P(\text{max}) = 2.2$ at $t = 1.3$, $x = 79.9$



Pressure vs. Time

$P(\text{max}) = 2.2$ at $t = 1.3$, $x = 79.9$

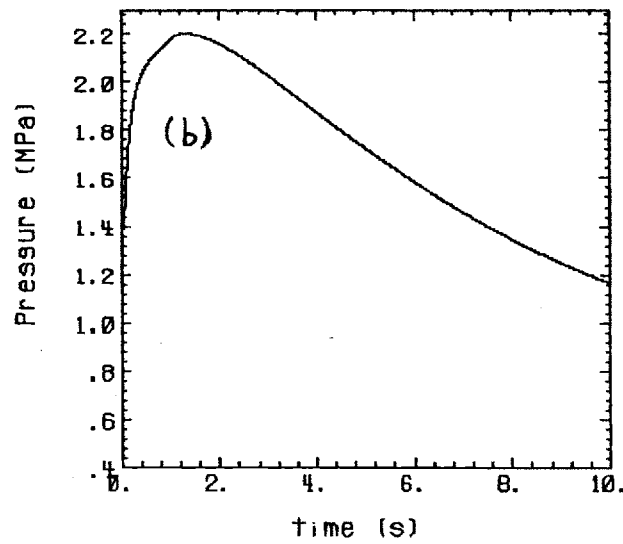


Figure 3.10: (a) The helium pressure profile during a quench in the TPX coil, and (b) the maximum helium pressure versus time during the quench. Both (a) and (b) are obtained by Quencher.

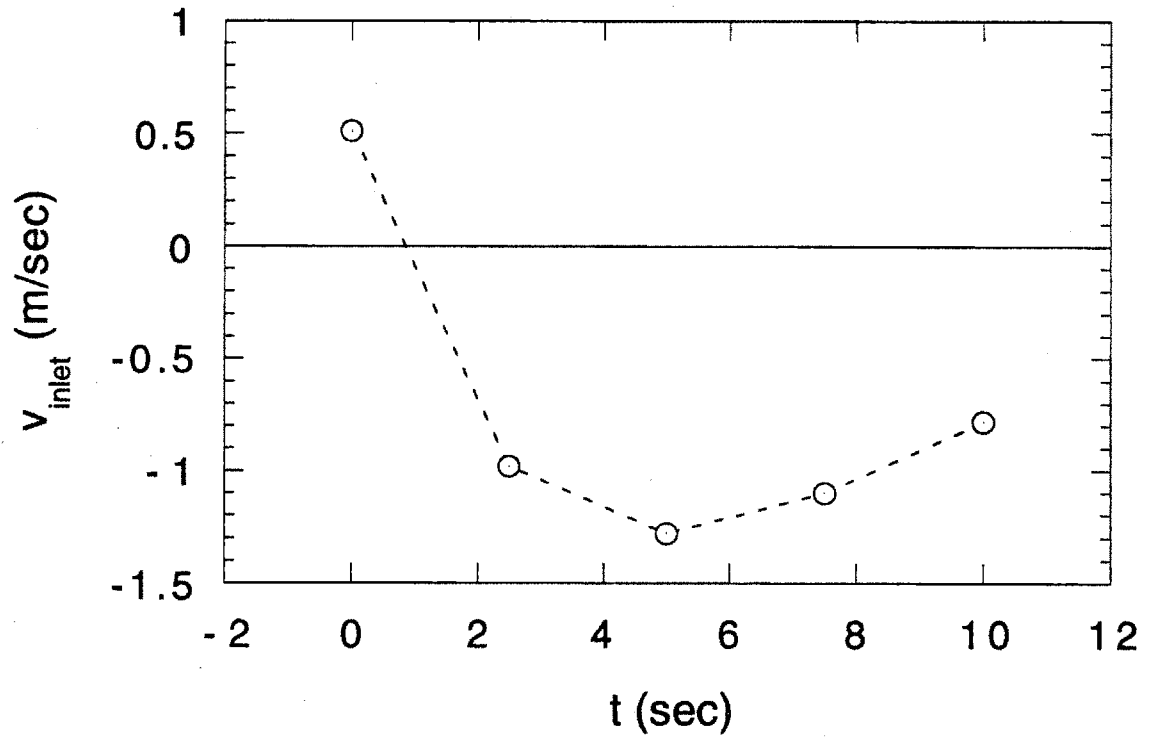


Figure 3.11: The inlet helium velocity versus time, as obtained by Quencher.

Helium Pressure Vs. time

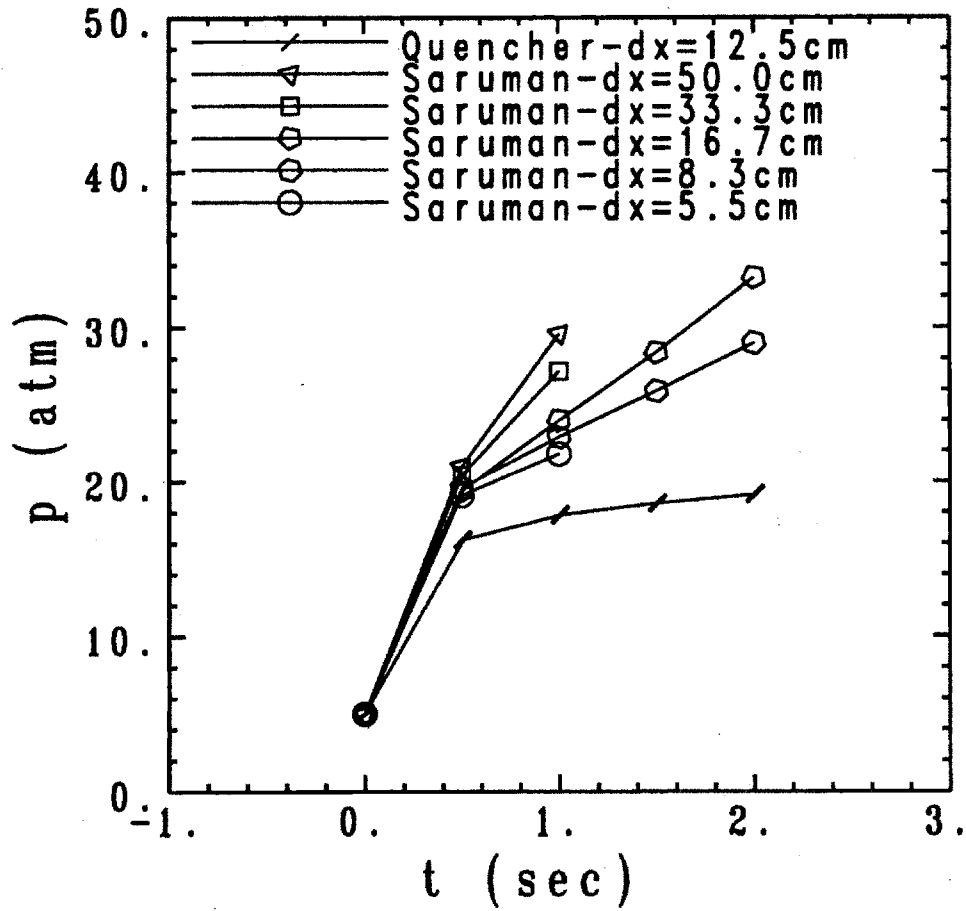


Figure 3.12a: Comparison of the maximum helium pressure as, obtained by Quencher and Saruman for a case where A_w becomes small. The various curves from Saruman correspond to different sized elements.

2Xq Vs. time

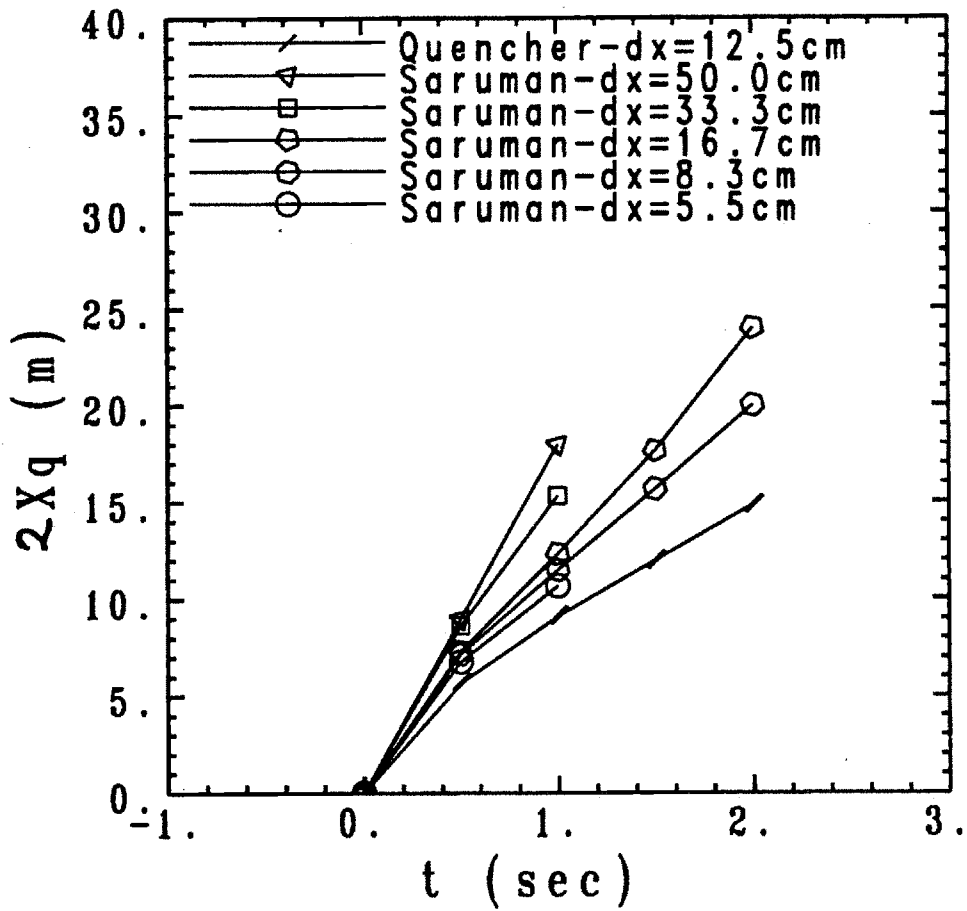


Figure 3.12b: Comparison of the normal length as obtained by Quencher and Saruman for a case where A_w becomes small. The various curves from Saruman correspond to different sized elements.

Maximum Temperature Vs. time

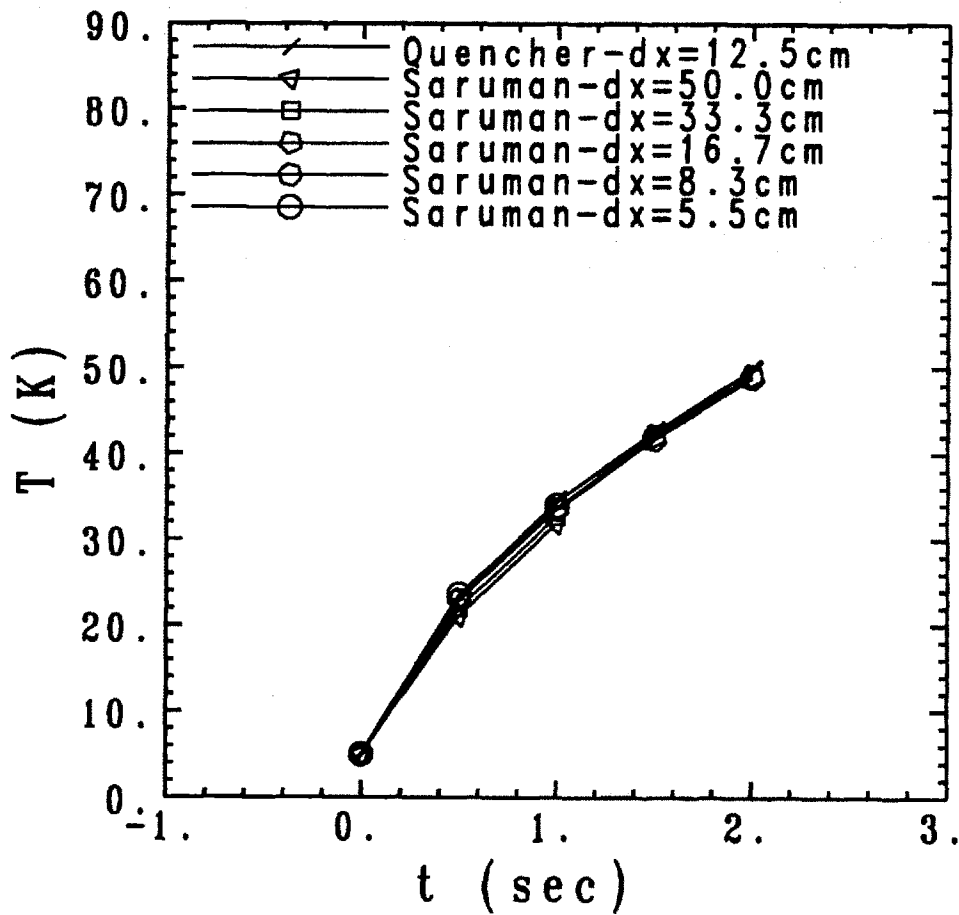


Figure 3.12c: Comparison of the maximum conductor temperature as obtained by Quencher and Saruman for a case where A_w becomes small. The various curves from Saruman correspond to different sized elements.

2Xq Vs. 1/dx @ t=1sec

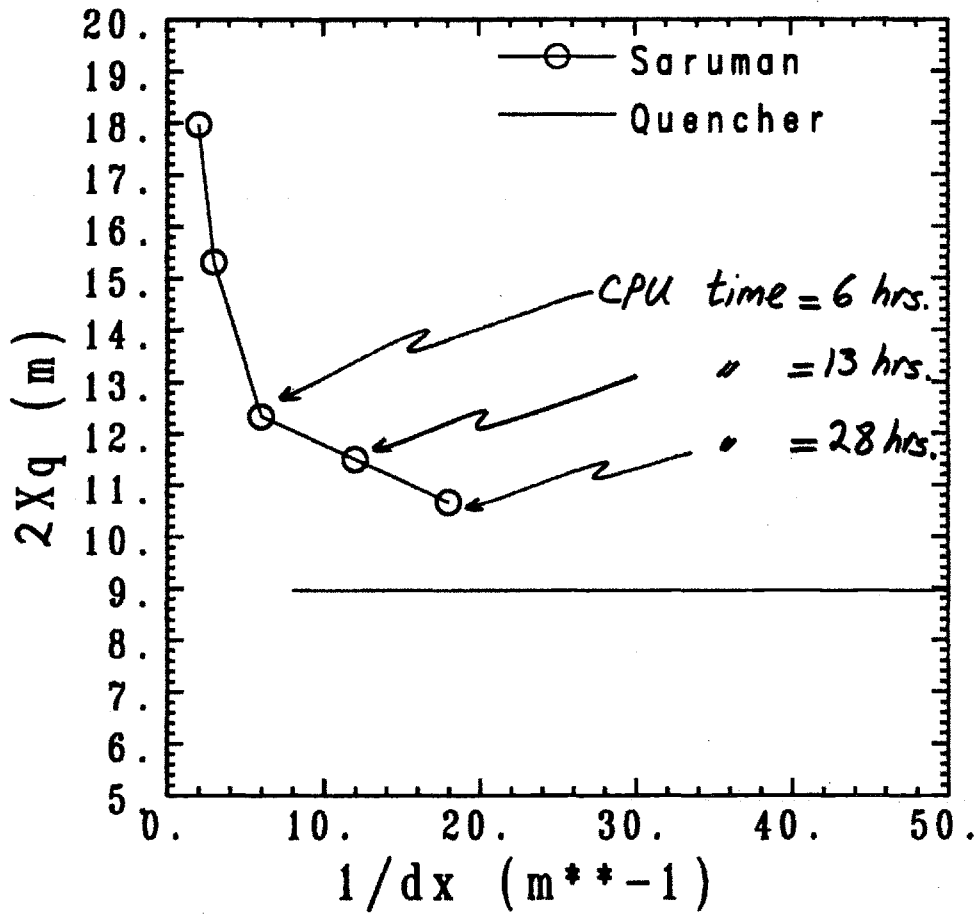


Figure 3.13a: The length of the normal region after 1 sec, as obtained by Saruman, versus 1/dx where dx is the length of the smallest element used in the computation.

Helium Pressure Vs. $1/dx$ @ $t=1\text{sec}$

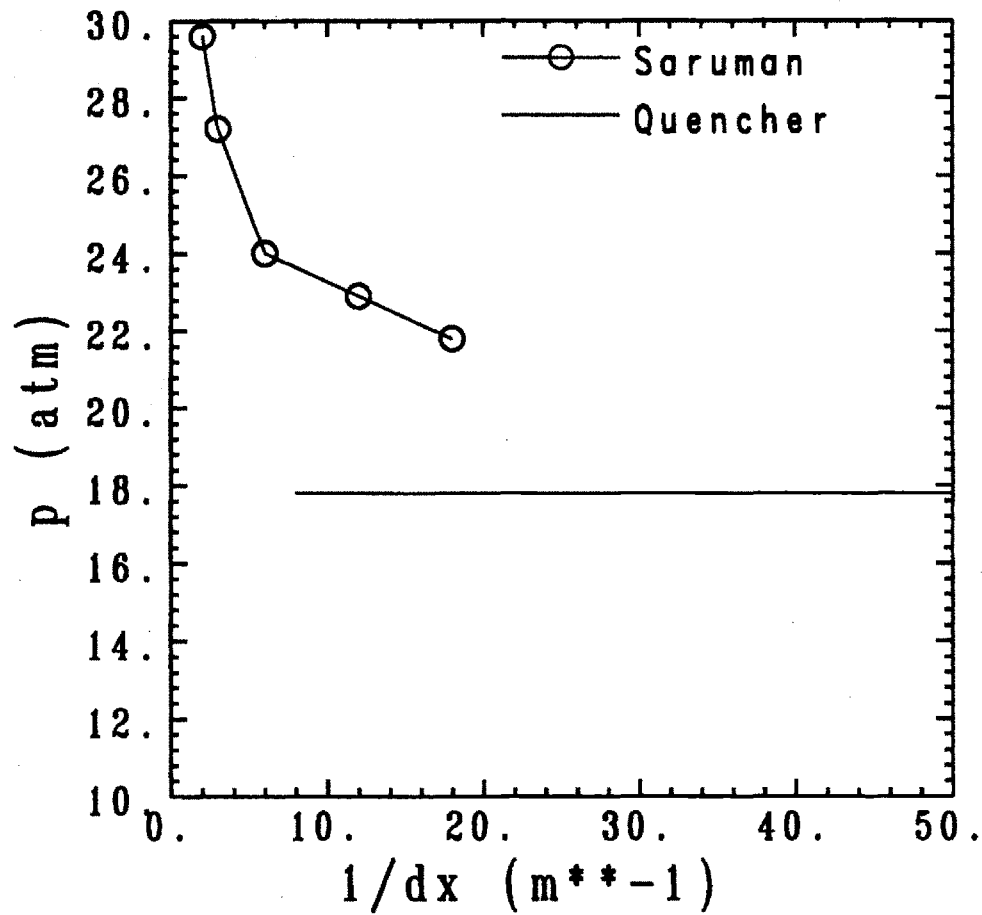


Figure 3.13b: The maximum helium pressure after 1 sec, as obtained by Saruman, versus $1/dx$ where dx is the length of the smallest element used in the computation.

Conductor Temperature vs. x

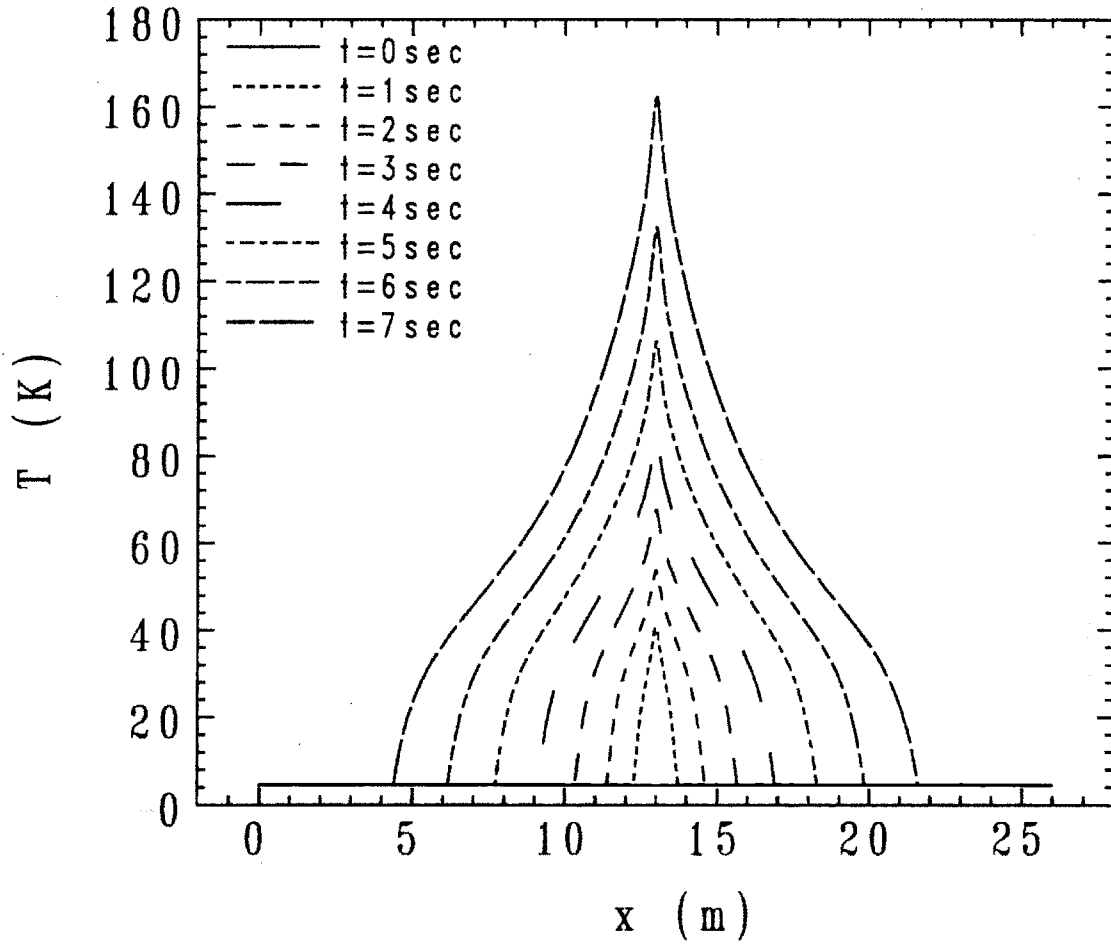


Figure 3.15a: Conductor temperature profile obtained by Quencher during a 7 sec quench in the conductor used by Ando et al. [8]. Here $I = 1.5$ kA.

Wall Temperature vs. x

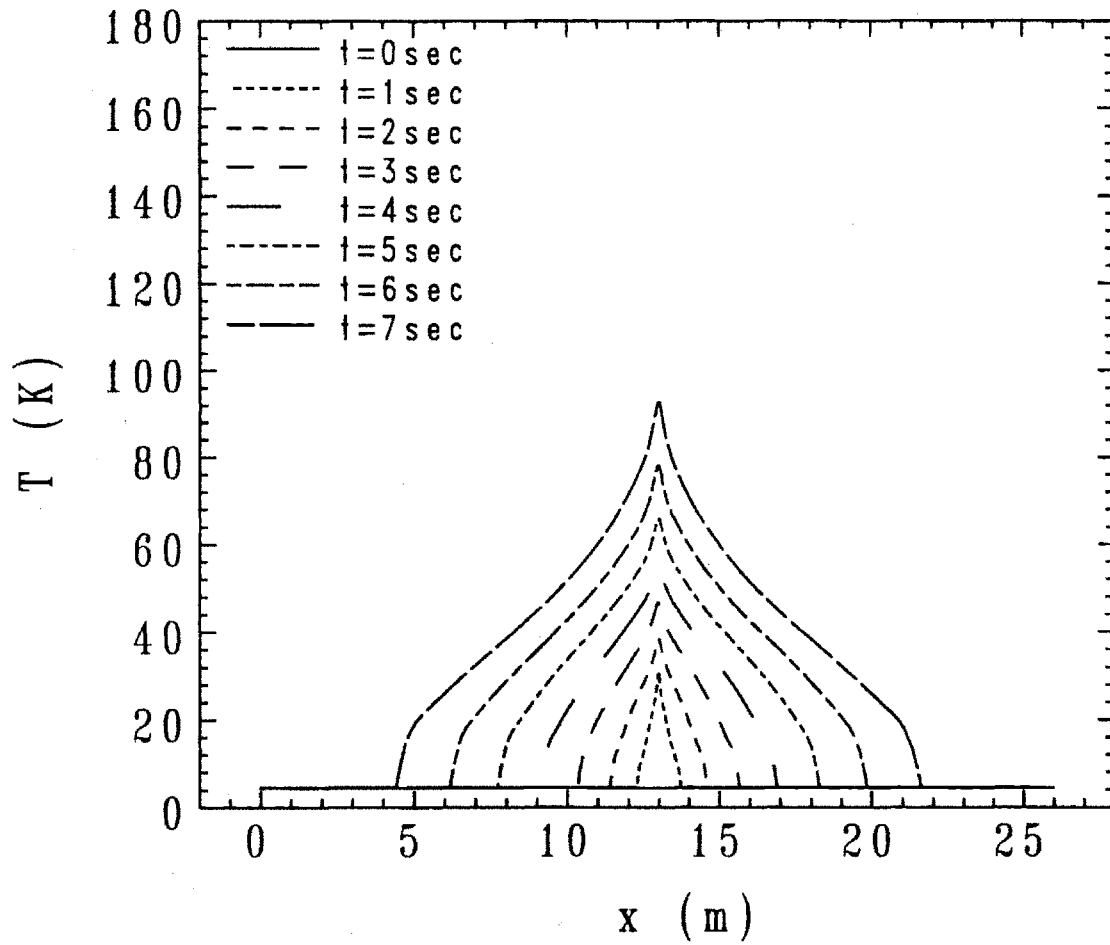


Figure 3.15b: Conduit wall temperature profile obtained by Quencher during a 7 sec quench in the conductor used by Ando et al. [8]. Here $I = 1.5$ kA.

Helium Pressure vs. x

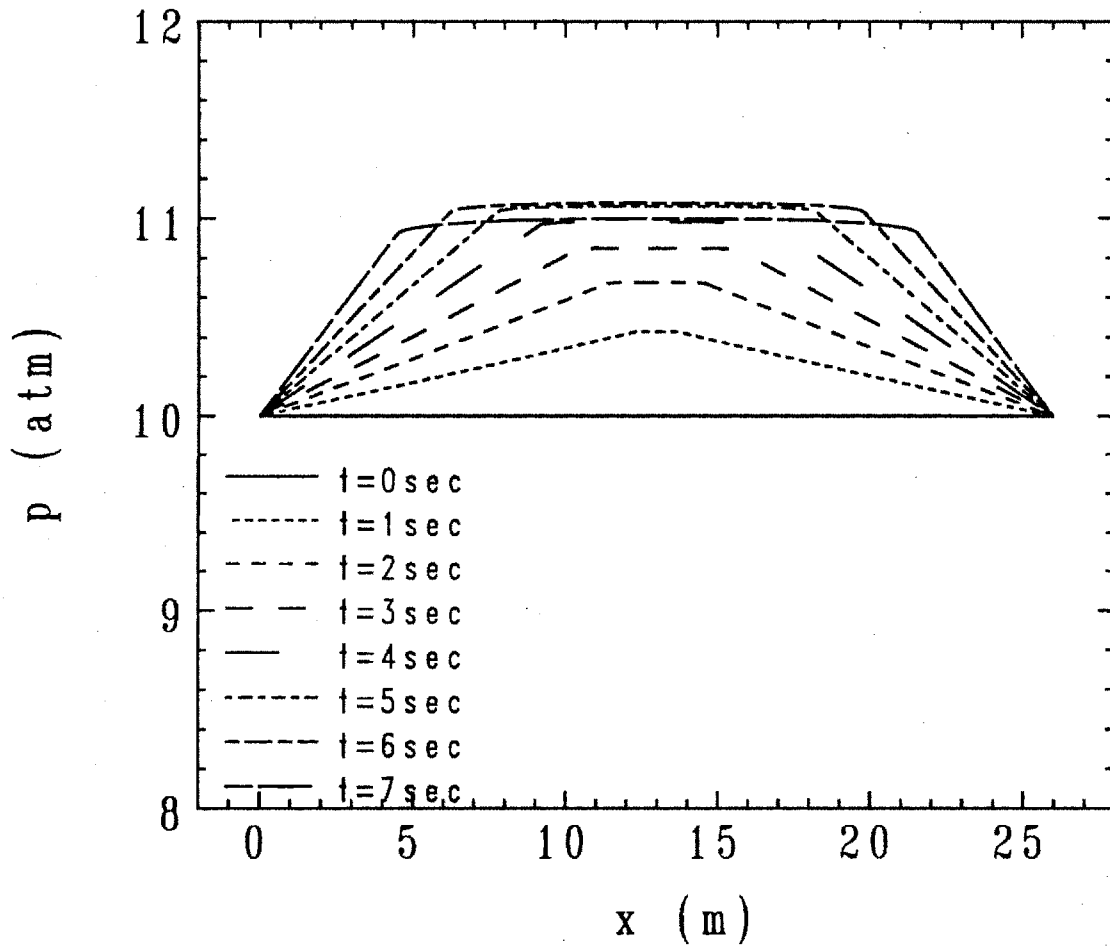


Figure 3.15c: Helium pressure profile obtained by Quencher during a 7 sec quench in the conductor used by Ando et al. [8]. Here $I = 1.5$ kA.

Helium Density vs. x

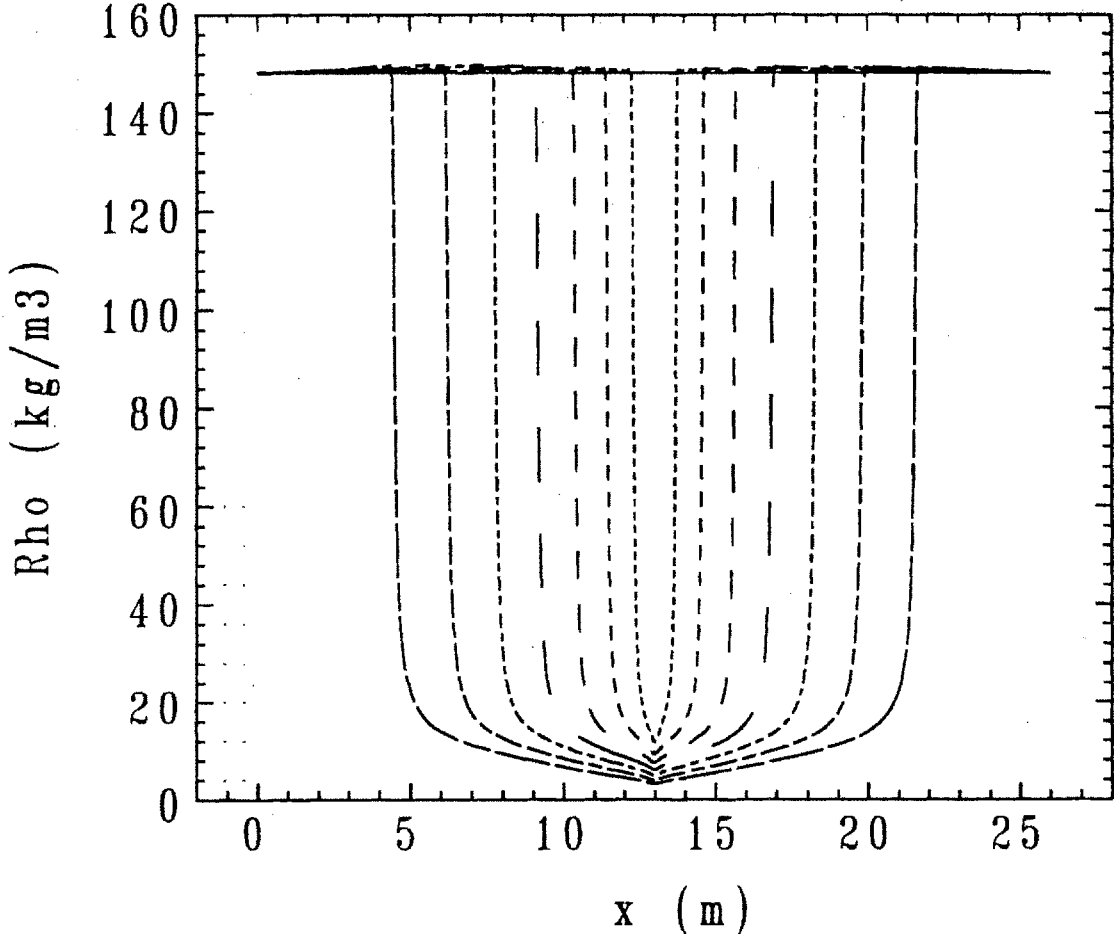


Figure 3.15d: Helium density profile obtained by Quencher during a 7 sec quench in the conductor used by Ando et al. [8]. Here $I = 1.5$ kA.

Reynolds Number vs. x

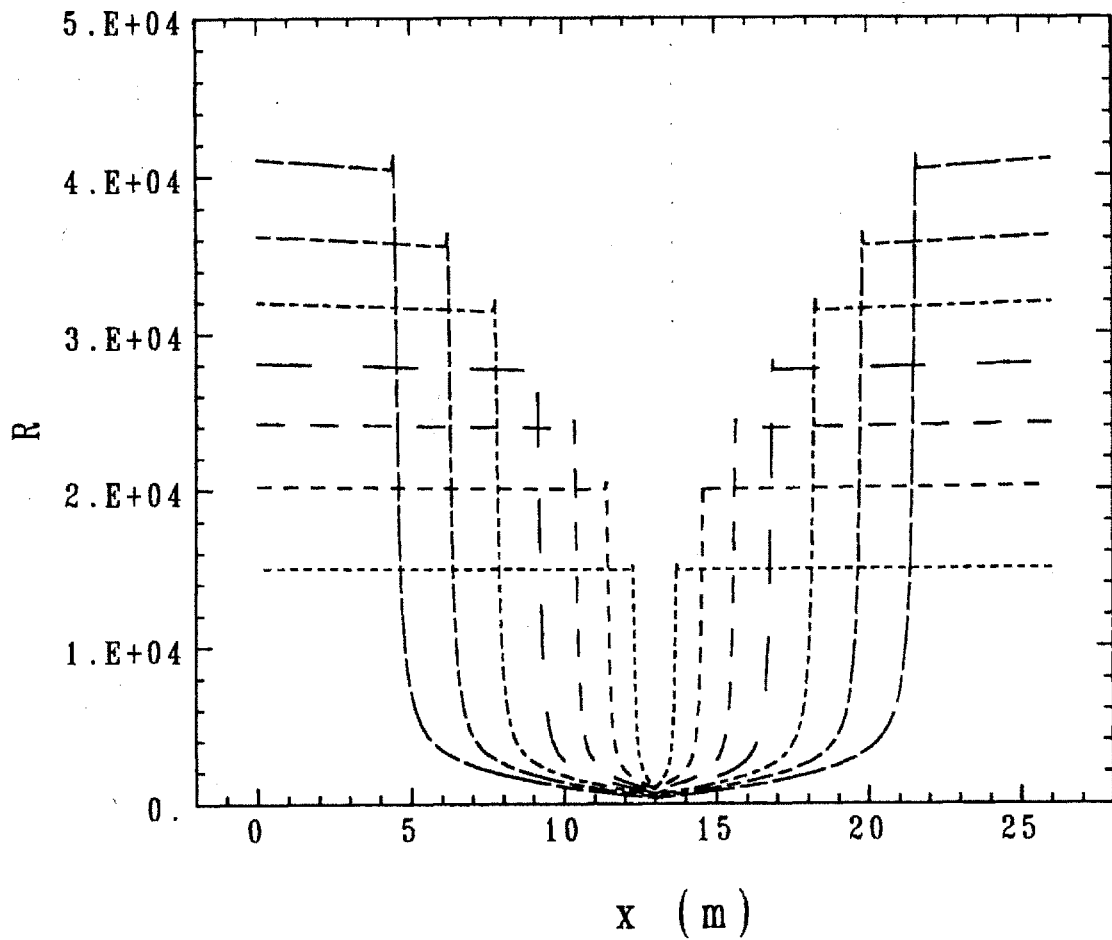


Figure 3.15e: The Reynold's number profile obtained by Quencher during a 7 sec quench in the conductor used by Ando et al. [8]. Here $I = 1.5$ kA.

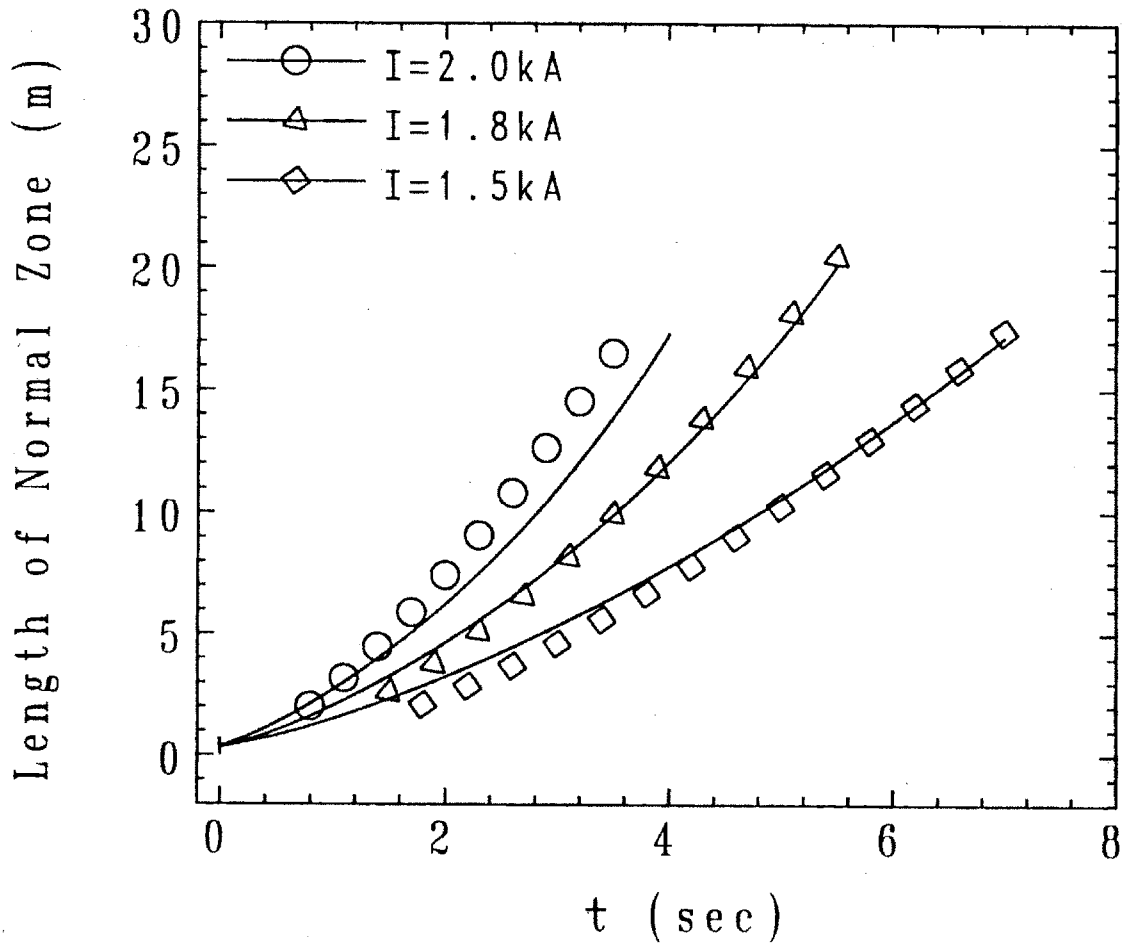


Figure 3.16: Comparison of Quencher results with experimental data [8].

Chapter 4

Analytic Solution

Chapter 4. Analytic Solution

In this chapter we present a set of analytic solutions for the problem of quench propagation in Cable In Conduit Conductors (CICC). The starting point is the Quencher model discussed in chapters 2 and 3. By introducing a series of justified approximations we first arrive at a simplified quench model (MacQuench) that is suited for "system studies" because of its high computational speed. Next, after further simplifications, an analytically tractable model describing three different practical regimes of operation is presented. These regimes are denoted by: 1) the "short coil," in which the end-boundaries of the conduit affect the propagation of the quench, 2) the "long coil," in which these end-effects are negligible, and 3) the "small pressure rise regime," in which the helium pressure rise in the quench region remains small. Analytic solutions are derived which distinguish each of these regimes as well as elucidating the basic underlying physics. Furthermore, we verify the validity of the analytic results, in each regime by extensive comparisons with numerical (Quencher and MacQuench) and experimental data.

The MacQuench model simultaneously describes all three regimes and requires only minutes of CPU time per simulation on a Macintosh PC compared to minutes on a CRAY supercomputer for Quencher. The model has much of the flexibility of Quencher (e.g. time dependent current density, time dependent B-field, etc.) and as is shown in the paper, is nearly as accurate, usually to within 5 %. Still, it does require computation and as such is not as convenient or insightful as the analytic theory. Typically, the quantitative accuracy of the analytic theory is $\sim 15\%$ or better. The scaling accuracy of the analytic theory with respect to the physical parameters is excellent in all cases thus far investigated.

The analytic solutions for each of the three regimes are quite distinct. In the short coil, for instance, we find that the quench propagation velocity depends on the length of the conductor L . This dependence is very important when attempting to extrapolate experimental results from short test coil samples to long coils where the quench propagation properties are independent of L . Substantial

differences are also observed in the dependence of the quench velocity (V_q) on the current density J . For example, in both the long and the short coil, $V_q \sim J$, while in the low pressure rise regime $V_q \sim J^2$. One common feature of all three regimes is the inherent dependence of V_q on the initial length of the quench region L_q .

In the past, a significant amount of the analytic work on the problem of quench propagation in CICC has been carried out by Dresner [1]. In fact, the quench propagation mechanism due to convection of helium, first considered by Dresner, is one of the central assumptions of this paper. Other assumptions made here, however, differ greatly. Dresner's analysis makes use of an elegant similarity solution and is thus applicable to long coils. The specific assumptions introduced in his calculations result in a theory that is valid for relatively short times and low conductor temperatures ($T \lesssim 25$ K). As essentially the only existing analytic results treating the problem of quench in CICC magnets, Dresner's theory is used widely in the superconducting magnet community, although often in regimes where it is inapplicable (i.e. the theoretical assumptions are not satisfied).

In the present work we make use of some of the ideas of Dresner, but introduce an alternate set of approximations that make our solution valid over much longer periods of time (up to and including a full current dump) and higher temperatures ($T \lesssim 300$ K). Our analytic solutions are least accurate for very short times. The present theory is thus complementary to Dresner's theory.

The main differences in modelling between the two theories of quench propagation are as follows:

- a. The contribution of the conductor heat capacity in the quench region is maintained in the formulation presented here. We show this to be the dominant effect in the quench region for long times and high temperatures. For short times the helium heat capacity is dominant and it is this assumption that is made in Dresner's analysis.
- b. The dependence of the thermal properties of the conductor are taken into account in the derivation presented here. We believe this is an important

ingredient in obtaining quantitative agreements with numerical and experimental results for long times. For short times this is not as critical and thus the material properties are assumed to be constant in Dresner's formulation.

- c. As mentioned above, we present analytic solutions in three different regimes of operation. This is important because for long times qualitatively different types of quench behavior are possible. Dresner's work focuses on the long coil regime since for short times all coils are long coils; that is, there is insufficient time for the end-effects to play a role. The distinction of the various regimes is of central importance in properly interpreting, and extrapolating any experimental results on quench propagation in test coils to large CICC magnets. A detailed comparison of the present results with those of Dresner is made in the discussion of the long coil.

It is worth emphasizing at this point that the MacQuench model and the analytic results apply only to the problem of "classical" quench propagation in CICC, the problem of primary importance to the future large magnets being designed in the magnetic fusion program. The interesting regime of Thermal Hydraulic Quenchback, wherein the temperature ahead of the quench front rises above its critical value, causing a greatly enhanced propagation speed, is not treated here, but is under current investigation. In Appendix D we discuss the process of THQB and we show how the analytic theory developed in this chapter can be used to predict the onset of this process.

The remainder of the chapter is organized in three sections. In section 4.1 we consider the approximations that lead to a simpler quench model (MacQuench) that is well suited for performing numerical studies on a personal computer. The analytic solution is derived in section 4.2, and finally in section 4.3 we present comparisons of the analytic results with numerical and experimental data.

4.1 The MacQuench Model

The basic insight that allows reduction of the Quencher model is that for the practical cases of interest, quench is propagated by a narrow moving front whose behavior is similar to that of a contact discontinuity. Thus, it is possible to solve the equations separately behind and ahead of the quench front, and then close the model by appropriate matching conditions across the discontinuity. Before proceeding with this analysis, it is helpful to begin with a short discussion of the somewhat subtle initial conditions used in MacQuench.

Initial Conditions

To understand the MacQuench initial conditions, consider first a deliberate, externally excited quench initiation as might be used to test an actual CICC. A magnet of length L operating in its desired superconducting state, is cooled by stagnant supercritical helium to a temperature T_0 , pressure p_0 , and density ρ_0 . A large external heat source ($S_{ext} \gg \eta_{cu} J^2$) is applied over a short length of conductor $L_q (L_q \ll L)$ for a short period of time $t_q (t_q \sim 0.001 \text{ sec})$. The heat pulse rapidly heats the local temperature above the critical temperature T_{cr} . When S_{ext} is removed, the magnet hot spot is cooled by convection, but heated by $\eta_{cu} J^2$ since this section of magnet is in its normal state. Since $\eta_{cu} J^2 \ll S_{ext}$, the hot spot temperature first decreases due to convection. However, if the initial source S_{ext} was sufficiently large, the joule heating can begin to reheat the hot spot before T falls below T_{cr} . When this occurs, a quench is initiated. The state of the magnet at this point serves as the initial conditions for the MacQuench simulation.

The difficulty in specifying initial conditions lies in the fact that the state of magnet at quench initiation depends upon the details of the initial heating pulse S_{ext} ; its magnitude, time duration, spatial length, and spatial profile. A general

approach that avoids these difficulties is as follows. First, assume that S_{ext} is experimentally adjusted to the minimum value required to initiate the quench. Under this assumption the initial value for T in MacQuench is given by

$$T(x, 0) = (T_q - T_0) H(L_q/2 - |x|) + T_0 \quad (4.1)$$

where $T_q \approx T_{cr}$ and H is the Heaviside step function.

Note that the initial hot spot temperature distribution is chosen to be symmetric and uniform in space. This choice is primarily for simplicity. Tests with other profiles show only a weak sensitivity as long as the total energy input and average profile width are held constant. The quantity L_q in Eq. (4.1) can usually be set to the length over which the external source is applied. In some experiments, this region can expand slightly because of convection during the short time before quench initiation. If experimental data is available, the measured value of L_q should be used in Eq. (4.1).

A second initial condition is required for the density. In MacQuench it is assumed that

$$\rho(x, 0) = \rho_0. \quad (4.2)$$

Equation (4.2) is justified when the external source is applied over such a short period of time, that a negligible amount of density is depleted in the quench region by convection. This corresponds to an external source duration that is much shorter than the characteristic time scale L_q/v . With a typical flow of $v \sim 10$ m/sec and $L_q \sim 1$ m, we find $L_q/v \sim 0.1$ sec. Typically the quench is initiated by sources applied over a period of $\sim 0.001 - 0.01$ sec; thus the aforementioned condition is generally well satisfied in most quench initiation events. From the equation of state we next find the initial helium pressure in the quench region is given by

$$p_q = p(\rho_0, T_q). \quad (4.3)$$

Observe that in general $p_q > p_0$.

Equations (4.1) and (4.2) specify the initial conditions for the helium/conductor in MacQuench. For experimental applications one sets $T_q = T_{cr}$, and assumes that L_q is obtained by direct measurement. For design applications, one sets $T_q = T_{cr}$ and $L_q = L_{qmin}$ where L_{qmin} represents the minimum length in which a quench event can initiate in a CICC. (For typical thermal disturbances that occur during the operation of a magnet the minimum value of the initial quench region may be as small as a fraction of a twist-pitch; that is, $L_{qmin} \sim 1$ cm.) As shown later, these choices correspond to the "worst" case where "worst" is defined as producing the smallest quench detection signal for a given allowable temperature rise in the conductor.

A final initial condition is required for T_w . In MacQuench it is assumed that

$$T_w(x, 0) = T(x, 0). \quad (4.4)$$

The heat transfer during the initiation of quench is quite high and this fact coupled with the low specific heat of the conduit wall at low temperatures, causes the equilibration of the two temperatures (helium/conductor and conduit wall) at quench initiation.

Note that the MacQuench initial conditions display discontinuities in the values of T and p , at the locations $x = \pm L_q/2$. These discontinuities, however, are quickly resolved and pose no numerical problems since the system of Eqs. (3.1–3.5) is purely diffusive for the density, temperature, and pressure variables.

Quench Region

Having established the initial conditions, we now consider the behavior of the quench region (i.e. the region behind the quench front). A plot of the temperature, pressure, velocity, and density profiles is shown in Fig. 4.1a–d, respectively. These curves, obtained from a Quencher simulation, correspond to typical profiles in a CICC after the quench has been well established. The location of the quench front is denoted by $X_q(t)$. Within the quench region, $|x| \leq X_q$, the joule heating causes the temperature of the system to increase (Fig. 4.1a). This in turn increases the helium pressure, (Fig. 4.1b) inducing a flow of helium in the channel (Fig. 4.1c). The high temperature helium in the quench region expands against the cold helium ahead of the front, thereby propagating the quench. As shown in Fig. 4.1d, the expansion causes a depletion of helium density in the quench region, resulting in a compression ahead of the front. The quench front separating the two regions behaves like a moving “contact discontinuity” across which the temperature and density are discontinuous, while the pressure and velocity remain continuous. (The exact nature of the boundary layer, at $x = X_q$ is considered in the discussion of the matching conditions.)

In order to obtain a simple relation for the temperature of the helium/conductor we assume that the CICC is in a uniform magnetic field B . Therefore the joule heating source S in Eq. (3.3) is independent of x , and is given by $S(T, t) = \eta_c J^2$, where $\eta_c \approx (A_{cu}/A_c)\eta_{cu}(T)$, $J(t) = I(t)/A_{cu}$, and $I(t)$ is the prescribed current in the conductor. Next, note that once the quench is established, the density in the quench region quickly decreases from its initial value ρ_0 , while simultaneously the heat capacity of the copper increases in parallel with T . This combination of events, in association with typical values of the quench variables, implies that in the quench region convection, compression, and heat conduction are negligible compared to the time derivative term; that is, the behavior is dominated by the large heat capacity of the conductor. Equation (3.3) then assumes a form similar to Eq. (3.5). The equations for T and T_w thus satisfy

$$\rho \hat{C}_t \frac{\partial T}{\partial t} \approx S(T, t) + \frac{hP_w}{A_c} (T_w - T) \quad (4.5)$$

$$\rho_w C_w \frac{\partial T_w}{\partial t} = \frac{hP_w}{A_w} (T - T_w). \quad (4.6)$$

Note that in the quench region the reduced density, and corresponding reduced Reynold's number, cause the heat transfer coefficient h to assume its laminar value; that is $h \approx h(T) = 4d_h/\kappa_h$ where $\kappa_h(T)$ is the thermal conduction of helium. Under this approximation, Eqs. (4.5) and (4.6) become ordinary differential equations, implying that with our spatially uniform initial conditions $T(x, t) \rightarrow T(t)$ and $T_w(x, t) \rightarrow T_w(t)$. The appropriate initial conditions are thus $T(0) = T_w(0) = T_q$.

Consider next the density and velocity in the quench region. The low values of density reduce the friction force (proportional to $f\rho v|v|/2d_n$) resulting in a weak pressure gradient. The approximately flat pressure, combined with the spatially homogeneous temperature just discussed, imply that the density profile is also spatially homogeneous; $\rho(x, t) \approx \rho(t)$. This approximation, when substituted into the mass equation [Eq. (3.1)], leads to a solution for $v(x, t)$ of the form $v(x, t) = -(\dot{\rho}/\rho)x$. Furthermore, since the velocity of the quench front \dot{X}_q is carried by the flow of helium it follows by definition that $\dot{X}_q = v(X_q, t)$. These simple relations can be easily manipulated, leading to expressions for ρ and v in terms of $X_q(t)$:

$$v(x, t) = \frac{x}{X_q} \frac{dX_q}{dt} \quad (4.7)$$

$$\rho(t) = \frac{\rho_0}{2} \frac{L_q}{X_q} \quad (4.8)$$

where we have used the initial conditions $X_q(0) = L_q/2$ and $\rho(0) = \rho_0$.

The final quantity of interest in the quench region is the pressure. Once the quench is established, the high temperatures ($T \gtrsim 30\text{K}$) and low densities ($\rho \lesssim 50$

kg/m³) imply that the helium equation of state is closely approximated by the ideal gas law. Thus, the pressure is given by

$$p(t) = R\rho T = \frac{\rho_0 R L_q}{2} \frac{T(t)}{X_q(t)}. \quad (4.9)$$

Equations (4.5–4.9) describe the behavior of $T(t)$, $T_w(t)$, $\rho(t)$, and $p(t)$ in terms of $X_q(t)$, a quantity whose dependence is ultimately determined by solving a simplified model ahead of the quench and then matching across the front.

Outer Region

The region ahead of the quench front ($|x| > X_q$) is denoted as the outer region and is characterized by zero joule heating ($S = 0$). Thus the only heat source in this region is due to viscous dissipation ($f\rho v^3/2d_h$). This heating mechanism plays an important role in the initiation of “Thermal Hydraulic Quench-Back” (THQB). Here, viscous heating, together with the heating due to the compression of the helium may raise the temperature in the outer region above $T = T_{cr}$. When this occurs, Joule heating develops almost instantaneously over large segments of the conductor in the outer region. Hence, a rapid increase of the normal zone is observed. The THQB process has been observed in recent experiments, and is a subject of current research. As mentioned in the introduction, the main underlying assumptions of the present paper deliberately exclude the process of THQB (see appendix D). Furthermore, in our studies the viscous dissipation in the outer region only slightly effects the quench propagation in the “classical” (non-THQB) regime, the most common quench regime in a CICC. Thus in the following analysis we neglect the viscous dissipation term in the outer region.

In view of the above discussion, consider first the temperature. In the outer region the value of the heat transfer coefficient h is very large ($h \sim 5000$ W/m-K) due to substantial helium flow velocities (~ 5 m/sec) and the high density of

helium ($\rho \sim 150 \text{ kg/m}^3$). The large heat transfer between the helium and the conduit wall results in temperature equilibration ($T_w \approx T$). By appropriately adding Eqs. (3.3) and (3.5), such that the heat transfer term, $h(T - T_w)$ is cancelled, and setting $T_w = T$, we obtain a single energy equation in the outer region. The result is identical to Eq. (3.3), except the total specific heat, \hat{C}_t now includes the contribution of the conduit wall: $\rho \hat{C}_t \rightarrow \rho_c C_c + (A_h/A_c)\rho C_h + (A_w/A_c)\rho_w C_w$. Even so, the high density and low temperature of the helium causes the helium contribution to dominate the specific heat so that $\rho \hat{C}_t \approx (A_h/A_c)\rho C_h$. Also, as seen in Fig. 4.1a-d, the spatial gradients are weak, implying that the heat conduction term is negligible. Combining these results leads to the following equation for the temperature in the outer region

$$\frac{\partial T}{\partial t} + v \frac{\partial T}{\partial x} + (C_\beta/C_h)T \frac{\partial v}{\partial x} = 0. \quad (4.10)$$

An alternate form of Eq. (4.10), obtained from the conservation of mass and the definitions of C_β and C_h , is given by $d\hat{S}/dt = 0$ where \hat{S} is the entropy. Thus, $\hat{S}(\rho, T) = \hat{S}(\rho_0, T_0) = \text{const.}$ in the outer region.

The density can be related to the temperature by eliminating $\partial v/\partial x$ from Eq. (4.10) by means of the conservation of mass. The result is

$$\frac{dT}{d\rho} = \frac{T C_\beta(T, \rho)}{\rho C_h(T, \rho)}. \quad (4.11)$$

Equation (4.11) can easily be solved numerically by assuming $T = T_0$ when $\rho = \rho_0$ and we shall hereafter assume that $T = T(\rho)$ is a known function.

The next step is to obtain a relationship between v and ρ . Consider $p = p(\rho, \hat{S})$ with $\hat{S} = \hat{S}_0 = \text{const.}$ The momentum equation then yields the following expression for v

$$v = \left(\frac{2d_h}{f} \right)^{1/2} \left(-\frac{c^2}{\rho} \frac{\partial \rho}{\partial x} \right)^{1/2} \quad (4.12)$$

where $c^2(\rho, \hat{S}_0) = (\partial p / \partial \rho)_{\hat{S}_0}$ is the square of the sound speed. Note that in this equation we assume the friction factor f is a constant. This assumption is well justified because of the weak dependence of f on the Reynold's number ($f \propto 1/R^{0.2}$). The final results are not strongly dependent on f , and using a constant value of $f \approx 0.06 - 0.08$ is a good approximation for the friction factor in the outer region.

At this point the velocity and temperature are expressed in terms of the helium density ρ in the outer region. The final relation that determines ρ is obtained by substituting v , given by Eq. (4.12), into the mass equation. The resulting equation is given by

$$\frac{\partial \rho}{\partial t} + \left(\frac{2d_h}{f}\right)^{1/2} \frac{\partial}{\partial x} \left(-c^2 \rho \frac{\partial \rho}{\partial x}\right)^{1/2} = 0 \quad (4.13)$$

which is a nonlinear diffusion equation requiring one initial and two boundary conditions. The initial condition is $\rho(x, 0) = \rho_0$, where ρ_0 is the initial density of the stagnant helium. The boundary condition at $x = L/2$ is given by $\rho(L/2, t) = \rho_0$ and is consistent with the constant pressure boundary condition discussed in Chapter 3. The second boundary condition is specified at the quench front $X_q(t)$, and follows from the matching conditions discussed shortly. Note that the treatment of the outer region is reduced to solving a single parabolic partial differential equation.

Matching Conditions

In order to mathematically close the MacQuench model two additional conditions are required; one for the remaining boundary condition on Eq. (4.13) and one to determine the location of the quench front $X_q(t)$. These are obtained by

noting that the quench front behaves like a contact discontinuity satisfying certain jump conditions. We start by moving to the quench front reference frame and then integrating the mass equation across the front. The result is

$$\frac{dX_q}{dt} = \frac{[[\rho v]]}{[[\rho]]} \quad (4.14)$$

where $[[Q]]$ denotes $Q(X_q^+, t) - Q(X_q^-, t)$. In order to avoid the formation of a shock in the conduit we require $[[v]] = 0$. Equation (4.14) then automatically becomes consistent with Eq. (4.7). Since the velocity is continuous across $x = X_q$, equating Eqs. (4.12) and (4.14), leads to the first matching condition;

$$\frac{dX_q}{dt} = \left(\frac{2d_h}{f} \right)^{1/2} \left(-\frac{c^2}{\rho} \frac{\partial \rho}{\partial x} \right)^{1/2} \Big|_{x=X_q^+} \quad (4.15)$$

This equation relates the location of the quench front to the density profile in the outer region (specifically X_q is determined by the value of ρ and $\partial \rho / \partial x$ at $x = X_q^+$). Note also that Eq. (4.14) allows an arbitrary jump in ρ across the front.

The second matching condition is obtained by integrating the momentum equation across the moving quench front yielding

$$[[p]] = 0. \quad (4.16)$$

This relation states that helium pressure is continuous across $x = X_q$. A more convenient form of Eq. (4.16) can be written as

$$\frac{\rho_0 R L_q}{2} \frac{T}{X_q} \Big|_{X_q^-} = p(\rho, \hat{S}_0) \Big|_{X_q^+} \quad (4.17)$$

Equations (4.15) and (4.17) determine the location of the quench front and the remaining boundary condition on ρ , respectively

Observe that the MacQuench model is now closed. However, we have yet to use the jump condition information from the energy equation. An analysis of

the energy equation shows that integrating across the front does not impose any constraints on the temperature jump, but instead determines the width of the layer. Specifically, below it is shown that in the layer

$$T(x, t) \approx T(X_q^+, t) + [T(X_q^-, t) - T(X_q^+, t)]e^{-(x-X_q^-)/\Delta} \quad (4.18)$$

where $\Delta(t) \approx \kappa(T_0)/\dot{X}_q \rho_c C_c(T_0)$. For typical experimental values $\Delta \lesssim 0.20$ m, a value similar to those observed in Quencher simulations. Note that in the entire MacQuench model, the conductor thermal conductivity only plays a role in the quench front layer, determining its width. As in many fluid dynamic boundary layer problems, this implies that most of physically observable quantities of interest are independent of κ . This too is born out in Quencher simulations.

Boundary Layer at $x = X_q$

By considering the mass and momentum equations in the region $x \approx X_q$ we have determined the two conditions required to mathematically close the system of equations describing the quench and the outer regions. We now show that analyzing the energy equation in this region will not result in an over determined system and the information gained from analyzing the energy equation is only in regard to the structure of the boundary layer at the location of the quench front. Equation (3.3) does not allow the existence of an exact contact discontinuity at $x = X_q$, because the quantity \hat{C}_t includes the contribution of both the helium and the conductor. In the case where $\hat{C}_t = \hat{C}_h$, and neglecting $(\kappa T')'$, integration of Eq. (3.3) across $x = X_q$ would result in a relation of the form

$$[\dot{X}_q - v(x = X_q, t)][T] = 0$$

which is satisfied for $\dot{X}_q = v(x = X_q)$ and the quantity $[T]$ is thus arbitrary and undetermined from this relation. To analyze Eq. (3.3) in the region $x \approx X_q(t)$

we define a new coordinate given by; $z = x - X_q(t)$. In this coordinate system the quench zone is in the region $z < 0$ and the outer zone is in the region $z > 0$. Furthermore, we denote the temperature in the boundary layer by T_B . In the vicinity $z \approx 0$ the dominant terms in the energy equation are the conduction and the convection terms, since these terms involve the spatial derivative of the temperature. Keeping the leading order terms in Eq. (3.3), near $z \approx 0$, we have

$$\Delta \frac{\partial^2 T_B}{\partial z^2} + \frac{\partial T_B}{\partial z} \approx 0 \quad (4.19)$$

where $\Delta \equiv (\kappa/\dot{X}_q \rho_c C_c)$ is a function of the temperature. (For determining the qualitative behavior of the solution in this region the temperature dependence of Δ is first neglected.)

The appropriate boundary conditions for Eq. (4.19) are such that the temperature remains continuous in extending from the quench region to the outer region. Thus at $z = 0$ we choose $T_B(z = 0, t) = T(t)$, where $T(t)$ is the temperature in the quench region. For $z \gg \Delta$ the value of T_B must match the temperature in the outer region which is well approximated by that of the background T_0 . Thus the boundary layer solution for T_B is given by

$$T_B(x, t) \approx T_0 + [T(t) - T_0] e^{-z/\Delta} \quad (4.20)$$

with the width of the boundary layer determined by the value of Δ .

The quantity Δ is given by $\Delta = (\kappa/\dot{X}_q \rho_c C_c)$, where in deriving Eq. (4.20) κ and C_c were assumed to be constants. Assuming κ to be a constant is a good approximation since the value of the thermal conductivity is not strongly dependent on the temperature. The quantity C_c is however a strong function of the temperature and to understand the structure of the boundary layer with this temperature dependence we assume the following form for the specific heat of the conductor; $C_c = C_{c0}(T_B/T_0)^n$. Here T_0 and C_{c0} are the temperature and the value of the specific heat, respectively, at the background temperature. It

is possible to obtain the analytic solution of Eq. (4.19) using this form for the specific heat, with $n = 1, 2$ or 3 . The width of the boundary layer for any of these cases is given by $\Delta = (\kappa/\dot{X}_q \rho_c C_{c0})$. This indicates that the width of the boundary layer is determined by the value of C_c evaluated at the background temperature T_0 . Using a value of $\rho_c C_c(T = T_0) \sim 10^3$ J/m³-K, $\kappa \sim 1000$ W/m-K, and $dX_q/dt \sim 5$ m/s results in $\Delta \sim 20$ cm. This is very similar to what is observed in the numerical solution of Eqs. (3.1–3.5).

The MacQuench Model

To summarize, the final simplified MacQuench model reduces to a set of equations determining $T(t), T_w(t)$ in the quench region, $\rho(x, t)$ in the outer region, and the front location $X_q(t)$. These have the form

$$\rho \hat{C}_t \frac{dT}{dt} = \eta_c J^2(t) + \frac{hP_w}{A_c} (T_w - T) \quad (4.21)$$

$$\rho_w C_w \frac{dT_w}{dt} = \frac{hP_w}{A_w} (T - T_w) \quad (4.22)$$

$$\frac{\partial \rho}{\partial t} = - \left(\frac{2dh}{f} \right)^{1/2} \frac{\partial}{\partial x} \left(-c^2 \rho \frac{\partial \rho}{\partial x} \right)^{1/2} \quad (4.23)$$

$$\frac{dX_q}{dt} = \left(\frac{2dh}{f} \right)^{1/2} \left(-\frac{c^2}{\rho} \frac{\partial \rho}{\partial x} \right)_{X_q^+}^{1/2} \quad (4.24)$$

The corresponding initial and boundary conditions are given by

$$T(0) = T_w(0) = T_q \quad (4.25)$$

$$\rho(x, 0) = \rho(L/2, t) = \rho_0 \quad (4.26)$$

$$p[\rho(X_q, t), \hat{S}_0] = \frac{\rho_0 R L_q}{2} \frac{T(t)}{X_q(t)} \quad (4.27)$$

$$X_q(0) = L_q/2 \quad (4.28)$$

In the quench region it is assumed that $C_c(T)$, $\eta_c(T)$, $h(T)$, and $C_w(T_w)$ are known property functions. Similarly, in the outer region $\hat{S}_0 = \hat{S}(\rho_0, T_0)$, $c^2(\rho, \hat{S}_0)$, and $p(\rho, \hat{S}_0)$ are assumed to be known properties of supercritical helium.

Numerical Solution

The numerical solution of the MacQuench model consists of solving the ODE's given by Eqs. (4.21), (4.22), (4.24), and the diffusion equation (4.23). The ODE's are standard. The diffusion equation is solved by approximating the partial time derivative $\partial/\partial t$, in Eq. (4.23) by a second order accurate finite difference scheme, and solving the resulting boundary value problem by standard techniques. The treatment of Eq. (4.23) is similar to the Quencher model, discussed in chapter 3. This numerical procedure requires only few minutes of CPU time on a Macintosh PC. In section 4.3 we present detailed comparisons of the MacQuench model with the solution of Eqs. (3.1–3.5).

We now proceed to present the steps that lead to the numerical solution of the MacQuench model. In the discussions that follow we use the finite difference approximation of $\partial/\partial t$ discussed in chapter 3. For reference we rewrite this scheme below;

$$\left(\frac{\partial Q}{\partial t}\right)_{t+\Delta t_2} \approx L_2 Q \equiv \frac{1}{c} [aQ(t + \Delta t_2, x) - bQ(t, x) + Q(t - \Delta t_1, x)] \quad (4.29)$$

where a , b and c are given by

$$a = \frac{(\Delta t_1 + \Delta t_2)^2}{(\Delta t_2)^2} - 1 \quad (4.30a)$$

$$b = \frac{(\Delta t_1 + \Delta t_2)^2}{(\Delta t_2)^2} \quad (4.30b)$$

$$c = \frac{\Delta t_1}{\Delta t_2} (\Delta t_1 + \Delta t_2) \quad (4.30c)$$

Note that the quantities a and b are dimensionless while c has units of time. Again, we assume that all quantities are known at times t and $t - \Delta t_1$ and we proceed to obtain the solution at time $t + \Delta t_2$. For convenience we use a slightly different notation than what is used in Eq. (4.29). We represent any quantity Q at time step $t - \Delta t_1$ by Q^{n-1} , and similarly for $Q(t)$ and $Q(t + \Delta t_2)$ we use Q^n and Q^{n+1} , respectively. With this notation Eq. (4.29) may be rewritten as

$$(L_2 Q)^{n+1} = \frac{1}{c} [aQ^{n+1} - bQ^n + Q^{n-1}] \quad (4.31)$$

Consider first Eqs. (4.21) and (4.22). By using the finite difference approximation to the time derivative terms we have

$$\rho^n \hat{C}_t^n (L_2 T)^{n+1} = [\eta_c J^2]^n + \frac{h^n P_w}{A_c} (T_w^{n+1} - T^{n+1}) \quad (4.32)$$

$$\rho_w C_w^n (L_2 T_w)^{n+1} = \frac{h^n P_w}{A_c} (T^{n+1} - T_w^{n+1}) \quad (4.33)$$

Note that we have evaluated most of the terms explicitly (at time step n) with the exception of the temperature variables in the $h(T - T_w)$ terms. This is done to avoid numerical difficulties in the case when these terms become mathematically stiff. In evaluating these terms implicitly we may take large time steps without any numerical instabilities. In evaluating some terms at time step n and others at $n + 1$ we are thus using an explicit/implicit scheme to solve Eqs. (4.21) and (4.22).

Equations (4.34) and (4.35) represent two linear equations for the two unknowns T^{n+1} and T_w^{n+1} . The solution of this system may be written as

$$T^{n+1} = \left(\frac{1 + a\epsilon_w^n/c}{1 + (1 + a\epsilon_w^n/c)(1 + a\epsilon_c^n/c)} \right) \left[\frac{(\eta_c J^2)^n A_c}{P_w h^n} + \frac{\epsilon_c^n}{c} (bT^n - T^{n-1}) + \frac{\epsilon_w^n/c}{1 + a\epsilon_w^n/c} (bT_w^n - T_w^{n-1}) \right] \quad (4.34)$$

$$T_w^{n+1} = \frac{1}{1 + a\epsilon_w^n/c} \left[T_w^{n+1} + \frac{\epsilon_w^n}{c} (bT_w^n - T_w^{n-1}) \right] \quad (4.35)$$

where ϵ_c and ϵ_w both have units of time and are defined as

$$\epsilon_c \equiv \frac{A_c \rho \hat{C}_t}{P_w h} \quad (4.36)$$

$$\epsilon_w \equiv \frac{A_w \rho_w C_w}{P_w h} \quad (4.37)$$

Equations (4.34) and (4.35) represent the explicit solution for T and T_w at time $t + \Delta t_2$.

Next we consider the diffusion equation for the density. Here, it is more convenient to make a coordinate transformation from (t, x) to (t, ξ) , where ξ is defined as

$$\xi \equiv \frac{x - X_q(t)}{L/2 - X_q(t)} \quad (4.38)$$

The time and spatial derivatives now become

$$\frac{\partial}{\partial x} = \frac{1}{L/2 - X_q} \frac{\partial}{\partial \xi} \quad (4.39a)$$

$$\frac{\partial}{\partial t} = \frac{\dot{X}_q}{L/2 - X_q} (\xi - 1) \frac{\partial}{\partial \xi} + \frac{\partial}{\partial t} \quad (4.39b)$$

Equation (4.23) may now be written as

$$\frac{\partial \rho}{\partial t} + A(t) (\xi - 1) \frac{\partial \rho}{\partial \xi} = - \left(\frac{2d_h}{f} \right)^{1/2} B(t) \frac{\partial}{\partial \xi} \left(-c^2 \rho \frac{\partial \rho}{\partial \xi} \right)^{1/2} \quad (4.40)$$

where A and B are defined as

$$A(t) \equiv \frac{\dot{X}_q}{L/2 - X_q} \quad (4.41)$$

$$B(t) \equiv \frac{1}{(L/2 - X_q)^{3/2}} \quad (4.42)$$

The corresponding initial and boundary conditions [Eqs.(4.26) and (4.27)] are given by

$$\rho(\xi, t = 0) = \rho_0 \quad (4.43)$$

$$\rho(\xi = 1, t) = \rho_0 \quad (4.44)$$

$$p[\rho(\xi = 0, t), \hat{S}_0] = \frac{\rho_0 R L_q}{2} \frac{T(t)}{X_q(t)} \quad (4.45)$$

In the (t, ξ) coordinate system, Eq. (4.24) becomes

$$\frac{dX_q}{dt} = \left(\frac{2d_h}{f} \right)^{1/2} B(t)^{1/3} \left(-\frac{c^2}{\rho} \frac{\partial \rho}{\partial \xi} \right)^{1/2} \Big|_{\xi=0} \quad (4.46)$$

Before proceeding to present the numerical approximation to Eq. (4.40) we define a new variable u given by

$$u \equiv \left(-\rho c^2 \frac{\partial \rho}{\partial \xi} \right)^{1/2} \quad (4.47)$$

Using the finite difference approximation in place of the time derivative in Eq. (4.40) we have

$$\begin{aligned} (L_2 \rho)^{n+1} + A^n (\xi - 1) \frac{\partial}{\partial \xi} \rho^{n+1} = \\ - \left(\frac{2d_h}{f} \right)^{1/2} B^n \frac{\partial}{\partial \xi} \left[-(c^2 \rho)^{n+1} \frac{\partial}{\partial \xi} \rho^{n+1} \right]^{1/2} \end{aligned} \quad (4.48)$$

Again, note that we have used an explicit/implicit scheme in evaluating the various non-time derivative terms. By evaluating A and B at the previous time step we avoid a great deal of difficulty in coupling Eqs. (4.23) and (4.24), while avoiding any numerical complications. By using Eq. (4.47) we now write Eq. (4.48) as a system of two ordinary differential equations for the variables ρ^{n+1} and u^{n+1} ;

$$\frac{d}{d\xi}\rho^{n+1} = - \left[\frac{u^2}{\rho c^2} \right]^{n+1} \quad (4.49)$$

$$\frac{d}{d\xi}u^{n+1} = - \left(\frac{f}{2d_h} \right)^{1/2} \frac{1}{B^n} \left[(L_2\rho)^{n+1} - A^n(\xi - 1) \left(\frac{u^2}{\rho c^2} \right)^{n+1} \right] \quad (4.50)$$

where the boundary conditions are given by

$$\rho^{n+1} = \rho_0 \quad ; \quad \xi = 0 \quad (4.51)$$

$$p[\rho^{n+1}, \hat{S}_0] = \frac{\rho_0 R L_q T^{n+1}}{2 X_q^{n+1}} \quad ; \quad \xi = 1 \quad (4.52)$$

The ODE's given by Eqs. (4.49) and (4.50) represents a boundary-value problem that may be solved by various different standard techniques. We use the same collocation solver as was used for the Quencher model. Note that all of the quantities in Eqs. (4.49) and (4.50) are either known through T^{n+1} which is given by Eq. (4.34) or they can be written in terms of ρ^{n+1} and u^{n+1} . The only exception is X_q^{n+1} needed in Eq. (4.52). In order to obtain this quantity we write the finite difference approximation to Eq. (4.46) in the following form;

$$(L_2 X_q)^{n+1} = \left(\frac{2d_h}{f} \right)^{1/2} (B^n)^{1/3} \frac{u^n}{\rho^n} \Bigg|_{\xi=0} \quad (4.53)$$

where all the terms on the right hand side are evaluated at time step n . This purely explicit scheme is simple and does not introduce any numerical stability criteria in the system while greatly simplifying the coupling of Eqs. (4.40) and (4.46). We now solve Eq. (4.53) for X_q^{n+1} to obtain

$$X_q^{n+1} = \frac{1}{a} \left[b X_q^n - X_q^{n-1} + c \left(\frac{2d_h}{f} \right)^{1/2} (B^n)^{1/3} \frac{u^n}{\rho^n} \Bigg|_{\xi=0} \right] \quad (4.54)$$

This is the explicit solution for X_q at time $t + \Delta t_2$. In Eqs. (4.50) and (4.54) the quantities A^n and B^n are easily evaluated as follows;

$$B^n = \frac{1}{(L/2 - X_q^n)^{3/2}} \quad (4.55)$$

$$A^n = \frac{1}{L/2 - X_q^n} \left(\frac{2d_h}{f} \right)^{1/2} (B^n)^{1/3} \frac{u^n}{\rho^n} \Big|_{\xi=0} \quad (4.56)$$

This concludes the description of the numerical scheme used to solve MacQuench. The MacQuench computer code thus involves the evaluation of the algebraic relations given by Eqs. (4.34), (4.35) and (4.54) together with the solution of the system of two ODE's [Eqs. (4.49) and (4.50)] at every time step. Therefore, it is not surprising that this code is considerably more efficient in terms of CPU time than the Quencher code.

4.2 Analytic Solution

This section presents a derivation of an approximate analytic solution to the MacQuench model. By making several additional plausible assumptions, it is possible to obtain solutions in both the quench and outer regions in terms of $X_q(t)$. Matching across the quench front then leads to a single ODE for the quantity $X_q(t)$. In its initial form this equation is still too complicated to solve analytically. However, by considering several special limits we obtain explicit analytical solutions as well as the boundaries in parameter space that define each regime.

The specific goals of the analysis are to calculate $T(t)$ in the quench region and $X_q(t)$. All other quantities of interest can be easily obtained by simple subsidiary relations. Throughout the following analysis, unlike the MacQuench model, we assume that the current density J is constant in time.

Quench Region

Equations (4.21) and (4.22) for $T(t)$ and $T_w(t)$ determine the temperature in the quench region. Recall that helium depletion has led to the approximation $\rho\hat{C}_t \equiv \rho_c C_c + \rho\hat{C}_h \approx \rho_c C_c$ in Eq. (4.21). Thus, these two equations are a set of closed, coupled ODE's for the unknowns T and T_w . In most situations of interest, the heat transfer coefficient is reasonably high so that the temperature difference is not very large: $(T - T_w)/T < 1$. Exploiting this fact we introduce new variables

$$\bar{T} = \frac{1}{2}(T + T_w) \quad (4.57)$$

$$\Delta T = \frac{1}{2}(T - T_w) \quad (4.58)$$

and for mathematical simplicity assume $\Delta T \ll \bar{T}$. Equations (4.21) and (4.22) are added to cancel the heat transfer terms;

$$(A_c \rho_c C_c + A_w \rho_w C_w) \frac{d\bar{T}}{dt} = A_c \eta_c J^2 - (A_c \rho_c C_c - A_w \rho_w C_w) \frac{d}{dt}(\Delta T) \quad (4.59)$$

Neglecting the ΔT terms leads to a single equation for the average temperature

$$\frac{d\bar{T}}{dt} = \alpha(\bar{T}) J^2 \quad \bar{T}(0) = T_q \quad (4.60)$$

where

$$\alpha(\bar{T}) = \frac{A_{cu} \eta_{cu}(\bar{T})}{A_c \rho_c C_c(\bar{T}) + A_w \rho_w C_w(\bar{T})}. \quad (4.61)$$

For CICC magnets, the temperature dependence of $\alpha(\bar{T})$ can be approximated by

$$\alpha(\bar{T}) \approx \alpha_0 (1 + \bar{T}^2 / T_\eta^2)^{1/2}. \quad (4.62)$$

The quantity α is constant out to T_η after which it increases linearly with \bar{T} . The parameters α_0 and T_η are functions of the conduit material (e.g. stainless steel, aluminum) and the area ratio A_w/A_c . Typically $\alpha_0 \sim 5 \times 10^{-16} \text{ m}^4\text{-K/A}^2\text{-sec}$, $T_\eta \sim 100\text{K}$. A simple, practical, and reasonably accurate method to determine α_0 is to set $\alpha_0 = \alpha_{min}$, where α_{min} is the minimum value of $\alpha(\bar{T})$. Figure 4.2 demonstrates the accuracy of this approximation for the proposed ITER toroidal magnet characterized by $A_w/A_c = 0.39$, $A_{cu}/A_c = 0.61$, and assuming a stainless steel wall (here $\alpha_0 = 7 \times 10^{-16} \text{ m}^4\text{-K/A}^2\text{-sec}$ and $T_\eta = 100 \text{ K}$). Note that this approximation breaks down at lower temperatures ($\lesssim 20 \text{ K}$) where the specific heat of the solid components is small. However, the approximation given by Eq. (4.62) does not result in large errors in predicting the temperature for two reasons; first, the actual value of α in the low temperature regime includes the contribution of the helium specific heat in the denominator of Eq. (4.61). This contribution tends to lower the value of α in this regime. In Fig. 4.2 we also plot α including the specific heat of helium as obtained from Quencher during a typical quench simulation. Note that as the temperature increases the helium contribution to α diminishes. Secondly, in this regime, the temperature increases very rapidly since α is large. Thus in a very short period of time Eq. (4.62) becomes a good approximation to α .

For reference, we plot the quantity α_0 as a function of A_w/A_c in Fig. 4.3. Note that in this figure we have used $A_{cu}/A_c = 2/3$ and $A_{sc}/A_c = 1/3$. These are the typical values encountered in CICC magnets. Also observe that the quantity α_0 is a function of the magnetic field B . This dependence results from the variation of η_{cu} with B . For a given value of α_0 , the only quantity that is still required to compute the temperature is T_η . For most applications T_η may be approximated by $T_\eta \approx 100$.

Using Eq. (4.62) in Eq. (4.60) and assuming J to be constant (no current dump) yields an ODE that can be easily integrated. The result is

$$\bar{T} = T_\eta \sinh \left[\frac{\alpha_0 J^2}{T_\eta} (t + t_\eta) \right] \approx T_q + \alpha_0 J^2 t \quad (4.63)$$

where t_η satisfies $\sinh(\alpha_0 J^2 t_\eta / T_\eta) = T_q / T_\eta$. For large CICC magnets, typically $t_\eta \sim 0.5$ sec. The approximate form is valid for $\bar{T} \lesssim T_\eta$, which is the usual situation of interest.

From Eq. (4.22) one can easily obtain the following relation for $\Delta T(t)$;

$$\frac{d\bar{T}}{dt} - \frac{d}{dt}(\Delta T) = \frac{2hP_w}{A_w \rho_w C_w} \Delta T \quad (4.64)$$

By using Eq. (4.59) we obtain an ordinary differential equation for ΔT ;

$$\frac{d}{dt}(\Delta T) = -\frac{\Delta T}{\tau_w} + \frac{A_w \rho_w C_w}{2hP_w \tau_w} \alpha J^2 \quad (4.65)$$

where

$$\frac{1}{\tau_w} = hP_w \left(\frac{1}{A_c \rho_c C_c} + \frac{1}{A_w \rho_w C_w} \right) \quad (4.66)$$

and all coefficients are evaluated at $T = \bar{T}(t)$. The general solution of Eq. (4.65) is given by

$$\Delta T = e^{-g(t)} \int_0^t \left[\frac{A_w \rho_w C_w}{2hP_w \tau_w} \alpha J^2 \right] e^{g(t_1)} dt_1 \quad (4.67)$$

where

$$g(t) \equiv \int_0^t \frac{1}{\tau_w(t_1)} dt_1 \quad (4.68)$$

Equation (4.67) is slightly complicated and in general requires numerical integration. A simplification of this equation may be obtained by noting that the dependence of the quantity τ_w on \bar{T} , and thus on time, is not very strong. We may therefore approximate $g(t)$ as follows

$$g(t) \approx t/\tau_w \quad (4.69)$$

Furthermore, neglecting the time dependence of the quantity in square brackets in Eq. (4.67), we obtain the following simplified relation for ΔT ;

$$\Delta T(t) \approx \frac{A_w \rho_w C_w}{2hP_w} \alpha(\bar{T}) J^2 \left(1 - e^{-t/\tau_w}\right) \quad (4.70)$$

Again, all coefficients are evaluated at $T = \bar{T}(t)$.

The final quantity of interest is the helium pressure. In the quench region the temperature rises and the helium density is quickly depleted. As a consequence, the helium equation of state can be accurately approximated by that of an ideal gas. Thus, shortly after the quench has been initiated $p \approx R\rho(\bar{T} + \Delta T)$. With ρ given by Eq. (4.8), the pressure can be expressed as

$$p(t) = \frac{R\rho_0 L_q}{2} \left(\frac{\bar{T} + \Delta T}{X_q}\right). \quad (4.71)$$

Equations (4.63), (4.70) and (4.71) provide analytic expressions for the quench variables in terms of the unknown function $X_q(t)$.

Outer Region

The expansion of the high temperature helium behind the quench causes a compression of the helium in the outer region. Because of the large volume of the outer region, and the supercritical state of the helium in this region the compression causes only a slight increase in the density and temperature above their background values. Consequently, ρ and T can be accurately approximated by

$$\rho(x, t) \approx \rho_0 + \rho_1(x, t) \quad (4.72)$$

$$T(x, t) \approx T_0 + T_1(x, t) \quad (4.73)$$

where $\rho_1 \ll \rho_0$ and $T_1 \ll T_0$. Substituting this expansion in Eq. (4.11) leads to a simple relationship for T_1 in terms of ρ_1 given by

$$T_1(x, t) = \left[\frac{T_0 C_\beta(\rho_0, T_0)}{\rho_0 C_h(\rho_0, T_0)} \right] \rho_1(x, t). \quad (4.74)$$

Similarly, the pressure in the outer region can be expressed in terms of ρ_1 by expanding the equation of state

$$p(x, t) \approx p_0 + c_0^2 \rho_1(x, t). \quad (4.75)$$

where $c_0^2 = c^2(\rho_0, \hat{S}_0)$.

The next step is to solve for ρ_1 from the simplified form of Eq. (4.23), which can be written as

$$\frac{\partial \rho_1}{\partial t} = -\nu_0 \frac{\partial}{\partial x} \left(-\frac{\partial \rho_1}{\partial x} \right)^{1/2}. \quad (4.76)$$

Here,

$$\nu_0 = (2d_h \rho_0 c_0^2 / f)^{1/2}. \quad (4.77)$$

With little loss of accuracy, f can be assumed constant at $f \approx 0.07$. Note that even though $\rho_1/\rho_0 \ll 1$, the equation for ρ_1 remains nonlinear.

Equation (4.76) does not have a simple analytical solution. However, an approximate solution can be obtained by transforming to similarity coordinates as follows: $\tau = t, \xi = (x - L_q/2)/t^{2/3}$. The time and spatial derivatives become

$$\frac{\partial}{\partial t} = \frac{\partial}{\partial \tau} - \frac{2}{3} \left(\frac{\xi}{\tau} \right) \frac{\partial}{\partial \xi} \quad (4.78a)$$

$$\frac{\partial}{\partial x} = \frac{1}{\tau^{2/3}} \frac{\partial}{\partial \xi} \quad (4.78b)$$

Equation (4.76) is now written as

$$\tau \frac{\partial \rho_1}{\partial \tau} - \frac{2}{3} \left(\xi \frac{\partial \rho_1}{\partial \xi} \right) = -\nu_0 \frac{\partial}{\partial \xi} \left(-\frac{\partial \rho_1}{\partial \xi} \right)^{1/2}. \quad (4.79)$$

For the moment assume $\partial \rho_1 / \partial \tau = 0$. Then Eq. (4.79) has a pure similarity solution given by

$$\frac{\partial \rho_1}{\partial \xi} = -\frac{9\nu_0^2}{(K + \xi^2)^2} \quad (4.80)$$

where K is an integration constant.

If the boundary conditions could be satisfied with $K = \text{const}$, then Eq. (4.80) would be the exact solution to the problem. This is not the case. However, in the analysis that follows it is shown that Eq. (4.80) is an approximate solution to the problem in the sense that the K required to satisfy the boundary conditions is a slowly varying function of time: $K = K(\tau)$. Under this assumption, the outer region solution is given by Eqs. (4.74), (4.75) and (4.80) with $K(\tau)$ as yet undetermined function.

Matching Conditions

The system of equations is closed by applying the matching conditions. Consider first the pressure balance jump condition given by Eq. (4.27). The quench region pressure at $x = X_q^-$ has been calculated in Eq. (4.71). The outer region pressure at any x follows from integrating Eq. (4.75), assuming $\rho_1(L/2, t) = 0$, and then substituting into Eq. (4.75). Setting $x = X_q^+$ and balancing the pressures leads to

$$\frac{\rho_0 R L_q}{2} \left(\frac{\bar{T} + \Delta T}{X_q} \right) = p_0 + 9\nu_0^2 c_0^2 t^2 \int_{X_q}^{L/2} \frac{dx}{[(x - L_q/2)^2 + X_D^2]^2} \quad (4.81)$$

where $X_D(t) = t^{2/3} K^{1/2}$ represents the location of the leading edge of the diffusion front. In general $X_D \gg X_q$. This is the first of the expressions relating the two unknowns $X_q(t)$ and $X_D(t)$.

The second relation follows from the velocity jump condition described by Eq. (4.24). A simple calculation, again making use of Eq. (4.80) yields

$$\frac{dX_q}{dt} = \frac{3\nu_0^2}{\rho_0} \frac{t}{(X_q - L_q/2)^2 + X_D^2}. \quad (4.82)$$

Equations (4.81) and (4.82) represent a closed model for the unknowns $X_q(t)$ and $X_D(t)$. In its present form the model is still too difficult to solve analytically. However, there are several special limits in which explicit analytic solutions can be obtained. These are the “short coil”, the “long coil”, and the “low pressure rise regime”, which are discussed next.

Short Coil

To decide whether a given coil is “short” or “long” one must compare two different time scales. First there is the nonlinear diffusion time t_D , determined from the solution of Eq. (4.76). For $t < t_D$ (or equivalently $X_D < L/2$) end effects are unimportant. Conversely for $t > t_D$. The second time scale is defined as the characteristic time required for the temperature in the conductor to rise to some maximum allowable value T_m . This time is easily estimated from Eq. (4.63) and is defined by $t_m \equiv T_m/\alpha_0 J^2$. When the time scale of interest exceeds the diffusion time ($t_m > t_D$) the magnet behaves like a short coil. In the discussion that follows, analytic solutions are presented for the short coil regime as well as an explicit criterion for the critical coil length defining the region of validity.

The analysis begins by recognizing that the short coil limit corresponds to the assumption $(L/2)^2 \ll X_D^2(t_m)$ in Eq. (4.81), thus allowing us to neglect the $(x - L_q/2)^2$ term in the integrand. We further assume that $X_q \ll L/2$ (i.e. the

quench front at $t = t_m$ is still some distance away from the end of the coil) and use the approximate form for $\bar{T} \approx T_q + \alpha_0 J^2 t$, valid for $T_m \lesssim T_\eta$. Also, in both the short and long coil limits we find X_q is weakly dependent on the helium temperature T , and thus ΔT . This, together with the relation $\Delta T < \bar{T}$, justifies neglecting ΔT in Eq. (4.81) (this assumption is not used in the low pressure rise regime, since there X_q is linearly dependent on ΔT). Similarly, once the quench is initiated, the pressure behind the quench front usually greatly exceeds the initial pressure ahead of the front, thereby allowing us to neglect the p_0 term in Eq. (4.81) (when this is not the case we have the low pressure rise regime which is discussed separately). These approximations yield the following expression for $X_D(t)$ as a function of $X_q(t)$

$$\frac{t^2}{X_D^4} \approx \frac{\rho_0 R L_q}{9\nu_0^2 c_0^2 L} \left(\frac{\alpha_0 J^2 t}{X_q} \right). \quad (4.83)$$

The expression given by Eq. (4.83) is to be substituted into Eq. (4.82). The resulting equation can be simplified by assuming $X_q^2 \ll X_D^2$ in the denominator, an assumption that is well satisfied for the short coil (except for t very close to zero) since $X_q^2 \ll (L/2)^2 \ll X_D^2(t_m)$. The end result is a single equation for $X_q(t)$ given by

$$\frac{dX_q}{dt} \approx \left(\frac{2d_h R L_q}{fL} \right)^{1/2} \left(\frac{\alpha_0 J^2 t}{X_q} \right)^{1/2}. \quad (4.84)$$

The solution, valid once the quench is well initiated, ($X_q \gg L_q/2$) has the form

$$X_q = \left[(L_q/2)^{3/2} + (V_q t)^{3/2} \right]^{2/3} \quad (4.85)$$

$$V_q = \left(\frac{2d_h R}{fL} L_q \alpha_0 J^2 \right)^{1/3}. \quad (4.86)$$

The coefficient V_q is the asymptotic quench velocity and is an important quantity of experimental interest.

Equation (4.86) shows that in a short coil, the quench front propagates with a constant velocity. Observe that V_q is a function of the product $L_q J^2$. Small L_q and/or J lead to a slow quench velocity V_q . Since T in the quench region is independent of L_q , a very localized quench initiation (i.e. small L_q) leads to a small V_q for a given temperature rise, thereby increasing the difficulty of detection. Note that V_q is a weak function of L : $V_q \propto L^{-1/3}$. Since end effects are important in a short coil it is not surprising that $V_q = V_q(L)$.

Knowing X_q , we can substitute back into the expression for K . The result is $K(t) \approx (3\nu_0^2/\rho_0 V_q)t^{-1/3} \propto t^{-1/3}$ which is relatively slowly varying. The value of $K(t_m)$ can next be inserted into the inequality criterion defining the regime of validity for the short coil $[(L/2)^2 \ll X_D^2(t_m)]$. We conclude that a CICC is a short coil if

$$L^2 \ll \frac{24d_h c_0^2 t_m}{fV_q}. \quad (4.87)$$

The density in the outer region is obtained from Eq. (4.80), which for the short coil may be written as

$$\frac{\partial \rho_1}{\partial \xi} \approx -\frac{9\nu_0^2}{K^2} \quad (4.88)$$

This equation may easily be integrated to obtain $\rho_1 \approx -(9\nu_0^2/K)\xi + C$ where C is a constant that is evaluated by using the boundary condition $\rho_1(x = L/2, t) = 0$. Once ρ_1 is known, the velocity v is obtained from a linear form of Eq. (4.12);

$$v(x, t) = \left[\frac{2d_h c_0^2}{f\rho_0} \right]^{1/2} \left(-\frac{\partial \rho_1}{\partial x} \right)^{1/2} \quad (4.89)$$

We find that ρ_1 and v are given by

$$\rho_1(x, t) = \left(\frac{\rho_0 f V_q^2}{2d_h c_0^2} \right) \left(\frac{L}{2} - x \right) \quad (4.90)$$

$$v(x, t) = V_q \quad (4.91)$$

Thus, the short coil limit corresponds to the steady state solution of Eq. (4.76). Observe that the density decreases linearly with x while the velocity is a constant. This is the expected behavior in situations where the time scale of interest is sufficiently long to allow the profiles to come into a quasi-static equilibrium with respect to the diffusive processes. Interestingly, once the quench is well established the propagation properties are independent of T_{cr} . This situation persists until the onset of THQB (see Appendix D).

Long Coil

Most of the large CICC magnets currently being designed can be characterized as “long coils.” In terms of the basic analytical model given by Eqs. (4.81) and (4.82) a long coil is defined by the two criteria $(L/2)^2 \gg X_D^2(t_m)$ and $X_q^2 \ll X_D^2(t_m)$. Physically this corresponds to $X_q \ll X_D \ll L/2$: the location of the diffusion edge (X_D) at the time of interest (t_m) is well short of reaching the end of the coil ($L/2$) but is far ahead of the quench front (X_q). Under this definition the limits of integration in Eq. (4.81) transform from $(X_q, L/2)$ to $(0, \infty)$. Note that replacing X_q by 0 is consistent with the long coil assumption except for t very close to zero.

If we again assume $\bar{T} \lesssim T_\eta$, Eq. (4.81) can be easily integrated yielding an expression for X_D in terms of X_q

$$\frac{t^2}{X_D^3} \approx \frac{2}{9\pi} \frac{\rho_0 R L_q}{\nu_0^2 c_0^2} \left(\frac{\alpha_0 J^2 t}{X_q} \right). \quad (4.92)$$

Equation (4.92) is substituted into Eq. (4.82), where, as for the short coil, we assume $X_q^2 \ll X_D^2$. The resulting equation for X_q has the form

$$\frac{dX_q}{dt} \approx 3 \left(\frac{2}{9\pi} \right)^{2/3} \left(\frac{2d_h R^2 L_q^2}{f c_0^2} \right)^{1/3} \left(\frac{\alpha_0 J^2 t}{X_q} \right)^{2/3} \left(\frac{1}{t} \right)^{1/3}. \quad (4.93)$$

This equation can be easily solved yielding

$$X_q = \left[(L_q/2)^{5/3} + (V_q t)^{5/3} \right]^{3/5} \quad (4.94)$$

where the asymptotic quench velocity \dot{X}_q is related to V_q by $V_q = (5/4)\dot{X}_q$ and

$$V_q(t) = 0.766 \left(\frac{2d_h}{f} \right)^{1/5} \left(\frac{RL_q\alpha_0 J^2}{c_0} \right)^{2/5} \frac{1}{t^{1/5}}. \quad (4.95)$$

Observe that V_q has a similar qualitative behavior with $L_q J^2$ as for the short coil. However, V_q decreases slowly with time: $V_q \propto t^{-1/5}$. In comparing short and long coils we see that some of the scaling is quite different. In particular, there is, as expected, no dependence on L in the long coil.

Consider next the evaluation of $K(t)$. Substituting back into Eq. (4.82) yields $K(t) \approx (3\nu_0^2/\rho_0\dot{X}_q)t^{-1/3}$, $K \propto t^{-2/15}$. The slow K approximation is very plausible. The criteria defining the regime of the long coil $(L/2)^2 \gg X_D^2(t_m)$ and $X_q^2 \ll X_D^2(t_m)$ can now be expressed as

$$L^2 \gg \frac{24d_h c_0^2 t_m}{fV_q} \gg 4V_q^2 t_m^2. \quad (4.96)$$

Equation (4.96) is well satisfied for many large CICC magnets.

The final quantities of interest are the profiles for ρ_1 and v in the outer region. These are easily extracted from the analysis and using Eq. (4.80) together with the boundary condition $\rho_1(x = L, t) = 0$. The integration of Eq. (4.80) results in

$$\rho_1 = \frac{9\nu_0^2}{K^2} \int_{\xi}^{\infty} \frac{d\xi}{(1 + \xi^2/K)^2} \quad (4.97)$$

This integral may easily be evaluated to obtain

$$\rho_1(x, t) = \frac{9\nu_0^2}{2K^{3/2}} \left(\cot^{-1} \frac{\xi}{K^{1/2}} - \frac{K^{1/2}\xi}{K + \xi^2} \right) \quad (4.98)$$

This equation is slightly complicated. We may write ρ_1 in a simpler form by first noting that the quantity in parenthesis may be written as

$$f(y) \equiv \cot^{-1}(y) - \frac{y}{1+y^2} \quad (4.99)$$

where $y \equiv \xi/\sqrt{K}$. In the two limiting cases $y \rightarrow 0$ and $y \rightarrow \infty$, f is given by

$$f(y) \approx \frac{\pi}{2} \quad ; \quad y \rightarrow 0 \quad (4.100a)$$

$$f(y) \approx \frac{2}{3y^3} \quad ; \quad y \rightarrow \infty \quad (4.100b)$$

These two limiting cases may be combined to obtain the following uniform approximation to $f(y)$;

$$f(y) \approx \frac{1}{\left(\sqrt{2/\pi} + \sqrt{3y^3/2}\right)^2} = \frac{\pi/2}{\left(1 + \sqrt{3\pi y^3/4}\right)^2} \quad (4.101)$$

In Fig. 4.4 we show the accuracy of this approximation by comparing Eqs. (4.99) and (4.101). We may now write ρ_1 in the following simplified form

$$\rho_1 \approx 3\nu_0^2 \frac{\lambda_2^3 t^2}{\left[t^{3/4} + \lambda_2^{3/2}(x - L_q/2)^{3/2}\right]^2} \quad (4.102)$$

where $\lambda_1^2(t) = \rho_0(4V_q/5)/3\nu_0^2$ and $\lambda_2(t) = (3\pi/4)^{1/3}\lambda_1$. The velocity in the outer region is obtained by using Eq. (4.89) together with $K(t)$ obtained for the long coil;

$$v(x, t) = \frac{(4/5)V_q t}{t + \lambda_1^2(x - L_q/2)^2} \quad (4.103)$$

Note that we do not differentiate Eq. (4.101) in obtaining the velocity, instead we use the more accurate form of $\partial\rho_1/\partial x$ given by Eq. (4.80). As expected, in a long coil both the velocity and density profiles decay for large x and spread in

width as time progresses. An important quantity of interest during a quench in long coils is the helium expulsion velocity from the conduit. In accord with the long coil limit we find, from Eq. (4.103), that the expulsion velocity is given by

$$v(x = L/2, t) \approx \frac{24d_h c_0^2}{fL^2} t. \quad (4.104)$$

Just as in the short coil, once the quench is well established the propagation properties are independent of T_{cr} . This situation persists until the onset of THQB (see Appendix D).

Comparison with Dresner's Results

At this point we can make a direct comparison between the long coil solution presented above, and the analytic solution given by Dresner. To begin, we summarize Dresner's results for $T(t)$, $p(t)$ and $V_q(t)$ [1];

$$T_D(t) = \frac{0.10}{R\rho_0 L_q} \left(\frac{4d_h}{f\rho_0^2 c_0^2} \right)^{1/3} (\eta_0 J^2)^{5/3} t^{7/3} \quad (4.105)$$

$$p_D(t) = 0.21 \eta_0 J^2 t \quad (4.106)$$

$$V_{qD} \equiv \frac{5}{4} \dot{X}_q = 0.42 \left(\frac{4d_h}{f\rho_0^2 c_0^2} \right)^{1/3} (\eta_0 J^2)^{2/3} t^{1/3} \quad (4.107)$$

where we use the subscript D to denote Dresner's results. All variables have been defined previously except η_0 . This quantity represents the resistivity of the copper which is assumed to be constant. It makes little sense to attempt a quantitative comparison between these equations and the long coil solution presented in this paper, since the two sets of results are inherently based on very different assumptions. This fact is evident in the large qualitative differences in the scaling of T , p , and V_q with t between the two sets of solutions.

Specifically, consider the following. In Eq. (4.105) the contribution of the conduit wall has not been included. Thus, this equation should be compared with Eq. (4.63), with $\Delta T = 0$ which results in $\bar{T} = T$. Next, Eq. (4.106) describes the maximum helium pressure in the quench region. For the assumptions used in Dresner's derivation, this equation is to be compared with Eq. (4.71) in the following form

$$p(t) = 0.653 \left(\frac{f c_0^2 \rho_0^5}{2d_h} \right)^{1/5} (RL_q \alpha_0 J^2)^{3/5} t^{1/5} \quad (4.108).$$

Finally, Eq. (4.107) should be compared with Eq. (4.95). Again, the qualitative differences are apparent. The only parameter that is the same in both theories is the helium expulsion velocity. The expulsion velocity obtained by Dresner is the same as Eq. (4.104). This is a consequence of assuming an infinite conductor length and thus discarding all information from the quench region, when considering $x = L/2$. In Table 4.1 we have summarized the important scaling differences between the long-coil solution and Dresner's results.

Dresner's Solution	Long Coil Solution
$T_{max} \propto t^{7/3}$ $p_{max} \propto t$ $V_q \propto t^{1/3}$	$T_{max} \propto t$ $p_{max} \propto t^{1/5}$ $V_q \propto t^{-1/5}$
$T_{max} \propto J^{10/3}$ $p_{max} \propto J^2$ $V_q \propto J^{4/3}$	$T_{max} \propto J^2$ $p_{max} \propto J^{6/5}$ $V_q \propto J^{4/5}$
$T_{max} \propto L_q^{-1}$ $p_{max} \propto L_q^0$ $V_q \propto L_q^0$	$T_{max} \propto L_q^0$ $p_{max} \propto L_q^{3/5}$ $V_q \propto L_q^{2/5}$

Table 4.1: Comparison of various scaling between the long coil and Dresner's solution.

“Small Δp ” Regime

The last regime of interest corresponds to the case in which the pressure rise Δp in the quench region remains small. This regime corresponds to the limit of a “weak” quench. When the current density is low, the frictional force small, or the quench initiation length short, the helium coolant easily removes the quench generated heat, leaving the pressure in the quench region only slightly higher than the background value. The experiment of Ando et al. [2] discussed in Chapter 3 lies in the small Δp regime.

When Δp is small the quench pressure can be expressed as $p = p_0 + p_1(t)$, with $p_1/p_0 \ll 1$. Using this relation on the right-hand side of Eq. (4.81) allows us (to leading order in p_1/p_0) to neglect the integral contribution. Thus, $X_q \approx R\rho_0 L_q(\bar{T} + \Delta T)/2p_0$. In order to match the initial condition we add a small first order constant, yielding

$$X_q \approx R\rho_0 L_q(\bar{T} + \Delta T - T_q)/2p_0 + L_q/2. \quad (4.109)$$

For the case where $\Delta T \ll \bar{T}$, and $\bar{T} \lesssim T_\eta$, we find $V_q \equiv \dot{X}_q \approx R\rho_0 L_q \alpha_0 J^2 / 2p_0$. Note the strong dependence of the quench velocity on J . This dependence is much stronger than in the short and long coils. For $T > T_\eta$, X_q increases exponentially with J^2 . Also, Eq. (4.109) is valid for the entire temperature range (20-300 K), while in deriving Eqs. (4.85) and (4.94) we assumed $\bar{T} \lesssim T_\eta$. Interestingly, the propagation of quench in the “small Δp ” regime is independent of the thermal hydraulics of the helium in the conduit.

Next, we proceed to obtain the first order pressure rise $p_1(t)$. From the first order part of Eq. (4.81) we find

$$p_1(t) = 9\nu_0^2 c_0^2 t^2 \int_{X_q}^{L/2} \frac{dx}{[(x - L_q/2)^2 + X_D^2]^2} \quad (4.110)$$

where for both the long and the short coils, from Eq. (4.82) we have

$$X_D^2 = \frac{3\nu_0^2}{\rho_0} \frac{t}{V_q}. \quad (4.111)$$

In order to evaluate the integral in Eq. (4.110) we consider the two limits given by Eqs. (4.87) and (4.96), respectively. For the short coil we find

$$p_1(t) = \left(\frac{f\rho_0 L}{4d_h} \right) V_q^2. \quad (4.112)$$

Similarly for the long coil we obtain

$$p_1(t) = 1.36 \left(\frac{f}{2d_h} \right)^{1/2} \rho_0 c_0 t^{1/2} V_q^{3/2} \quad (4.113)$$

where $V_q(t) = \dot{X}_q$ is obtained from Eq. (4.109). Just as in the long and short coil limits, we may obtain the solution for $\rho_1(x, t)$ and $v(x, t)$ in the outer region from Eqs. (4.80) and (4.89).

Having determined p_1 in the quench region we may now state the explicit relation that distinguishes the small Δp regime. This relation is given by

$$p_1/p_0 < 1 \quad (4.114)$$

during the time scale of interest.

As was the case in both short and long coils, once the quench is well established the propagation properties are independent of T_{cr} . This situation persists until the onset of THQB (see Appendix D).

Summary of Analytic Results

To summarize, we have characterized three different regimes of operation during a quench in a CICC. In Fig. 4.5 we present the criteria that distinguish each of these regimes. All the relevant parameters are summarized in the figure caption. We suggest that to properly interpret any experimental results on quench propagation, it is vital to clearly distinguish the regime of operation of the magnet (e.g. distinction between long and short coils is specially important in trying to extrapolate experimental test coil results to long coils).

In Fig. 4.6 we summarize a simple form of the analytic results for each regime. These analytic solutions represent the first such results that remain valid for the long time scales of interest during a quench process. In the next section, important analytic scaling are verified by direct comparisons with numerical as well as experimental data.

4.3 Discussion

In the discussions that follow, we provide detailed comparisons of the Quencher, MacQuench and Analytic models, as well as comparisons with experimental data.

Long Coil

Conductor Length (m)	530
Copper Area (mm ²)	390
Nb ₃ Sn Area (mm ²)	250
Helium Area (mm ²)	450
Wall Area (mm ²)	250
Hydraulic Diameter (mm)	0.5
Wall Inner Perimeter (mm)	130
Initial Current (kA)	43
Detection Time (sec)	∞
Dump Time (sec)	no dump
Inlet Pressure (atm)	5
Outlet Pressure (atm)	5
Inlet Temp. (K)	5
Copper RRR	100

Table 4.2: Characteristic parameters of the “ITER like” conductor.

We consider a conductor of length 530 m, similar to the TF coil of ITER. The parameters describing this conductor are $A_h = 4.5 \times 10^{-4} \text{ m}^2$, $A_{cu} = 3.9 \times 10^{-4} \text{ m}^2$, $A_{sc} = 2.5 \times 10^{-4} \text{ m}^2$, $A_w = 2.5 \times 10^{-4} \text{ m}^2$, $P_w = 0.13 \text{ m}$, and $d_h = 5 \times 10^{-4} \text{ m}$. The transport current is $I = 43 \text{ kA}$ and the conductor is assumed to be in a constant magnetic field of 13 T. Before the initiation of quench, the stagnant helium in the channel is at a temperature of 5 K, and a pressure of 5 atm. In Table 4.2 we summarize the characteristic parameters of this conductor. Two quench scenarios are investigated. In scenario (1) $L_q = 3 \text{ m}$ while in scenario (2) $L_q = 8 \text{ m}$. The studies have three goals: first, to compare the accuracy of the different models in the long coil regime, second to determine quantitatively the effect of quench initiation length L_q on quench propagation, and third to ascertain the accuracy of the analytic scaling relations with I .

In Fig. 4.7a–d we compare the cable temperature $T = \bar{T} + \Delta T$, the normal length $2X_q$, the quench helium pressure p , and the helium expulsion velocity $v(x = L/2, t)$, respectively, as obtained by the various models during a 6 second

quench. The analytic results are given by Eqs. (4.63), (4.70), (4.71), (4.94–95), and (4.104) with $\alpha_0 = 7 \times 10^{-16} \text{ m}^4\text{-K/A}^2\text{-sec}$ (for an approximate value of α_0 see Fig. 4.3 with $A_w/A_c \approx 0.4$ and $B = 13 \text{ T}$), $J = 1.1 \times 10^8 \text{ A/m}^2$, $T_\eta = 100 \text{ K}$, $T_q = 10 \text{ K}$, $R = 2080 \text{ J/kg-K}$, $\rho_0 = 130 \text{ kg/m}^3$, $c_0 = 215 \text{ m/sec}$, and $f = 0.07$. In Fig. 4.7a, only case (1) is presented, since less than $\sim 6 \%$ difference in T between the two scenarios was found. The dependence of the normal length and the helium pressure on L_q is evident in Figs. 4.7b and 4.7c, where we observe good agreement between the various models. Finally, in Fig. 4.7d we compare the helium expulsion velocity as obtained by Quencher, MacQuench and Eq. (4.104). Only the case $L_q = 3 \text{ m}$ is presented since less than $\sim 1 \%$ difference was observed between the two scenarios. Note that the six second quench simulation observed in these figures took approximately 4 hours of CPU time on a Vax 4000/90 with Quencher, while less than 2 minutes of CPU time was used by MacQuench on the same machine (this is equivalent to less than 10 minutes of CPU time on a Macintosh Centris 650).

Consider now the dependence of the average temperature \bar{T} , and the normal length on the transport current I . In Fig. 4.8 we plot $(\bar{T} - T_q)$ and $2X_q$ each evaluated at $t = 4 \text{ sec}$ versus the square of the transport current I^2 . We have normalized these quantities such that $A \equiv (\bar{T} - T_q)/(\bar{T} - T_q)_r$ and $B \equiv (X_q)/(X_q)_r$, where the subscript r denotes the value of the relevant quantities at the reference $I = I_r = 30 \text{ kA}$. In this figure we compare A and B as obtained by Quencher, MacQuench and the analytic results. From Eqs. (4.63), (4.94) and (4.95), in the regime $\bar{T} \lesssim T_\eta$ (which is the case for all the points in Fig. 4.8) we have $A \propto I^2$ and $B \propto I^{4/5}$, which is clearly observed in Fig. 4.8.

Short Coil

One of the most distinct differences between the long and the short coil is the dependence of the quench velocity on the coil length L . In the short coil regime $X_q \propto L^{-1/3}$, while the long coil solution of X_q is independent of L [see Eqs. (4.94) and (4.95)]. This dependence is important in designing and interpreting results from experiments carried out on shorter, less expensive test coil samples. Care must be exercised to guarantee that the test coil does not inadvertently operate in the short coil regime, while the actual coil of interest lies in the long coil regime. Such a difference could lead to erroneous extrapolations, particularly with respect to X_q . One of the main goals of the short coil studies is to quantify this issue.

We consider a 4 sec quench scenario in a 50 m long sample of the ITER conductor just described. The initial quench length is assumed to be $L_q = 3$ m. First, note that using the relevant parameters discussed above in Eq. (4.86) we find $V_q = 2.47$ m/sec. Using this value, together with $t_m = 4$ sec in Eq. (4.87) we find the criteria for the short coil to be $L^2/1.3 \times 10^4 \ll 1$. For $L = 50$ m, we find $L^2/1.3 \times 10^4 = 0.19$ which satisfies the short coil criteria. It is important to note that for the long coil case where $L = 530$ m, we find $L^2/1.3 \times 10^4 = 22$ which clearly satisfies the long coil criteria.

In Fig. 4.9a–b we compare the normal length and the maximum helium pressure, respectively, as obtained by the various models. The temperature dependence is not presented, since again less than 5% difference is observed between this case and Fig. 4.7a. The various models are in good agreement. In order to verify the dependence of X_q on L , in Fig. 4.10 we show the dependence of the normal length (at $t = 4$ sec) as L is varied. The y-axis is $X_q/(X_q)_r$, where $(X_q)_r$ is the normal length at $t = 4$ sec, in the case where $L = L_r = 50$ m. From Eqs. (4.85) and (4.86), we expect $X_q \propto 1/L^{1/3}$ in the short coil regime. This is clearly observed in Fig. 4.10, and as L is increased we start to enter the long coil regime, where from Eqs. (4.94) and (4.95) X_q becomes independent of L . The transition between the long and the short coil regimes is clearly observed in

Fig. 4.10, and is well predicted by the analytic theory.

Small Δp Regime

This regime is very different from both the long and the short coil regimes just described which each assumed $p(t_m)/p_0 > 1$. In the long and short coil solutions X_q displayed the same qualitative behavior, with the exception of the dependence on L . For small Δp , however, X_q is a much stronger function of L_q and J , while not dependent for example on the friction term f/d_h nor the coil length L .

In order to test the validity of the analytic solution in this region, we consider the experimental results of Ando et al. [2] together with the numerical results obtained by Quencher (see Figs. 3.15 and 3.16). These experiments fall in the "small Δp " regime as will be shown below when the pressure in the quench region is calculated. The conductor temperature for various transport currents is shown in Fig. 4.11a, where we compare the analytic results of Eqs. (4.63) and (4.70) with those of Quencher. For this conductor $\alpha_0 = 3.9 \times 10^{-16} \text{ m}^4\text{-K/A}^2\text{-sec}$ (for an approximate value of α_0 see Fig. 4.3 with $A_w/A_c \approx 1.8$ and $B = 7 \text{ T}$), and $T_\eta = 60 \text{ K}$. The quench is initiated such that at $t = 0^+$, the value of $L_q = 0.35 \text{ m}$ and $T_q = 35 \text{ K}$. (Note that there is a growth of the normal region beyond the initial length ($L_q(t = 0^-) = 0.04 \text{ m}$) where the external heat is deposited since the value of the heat source is relatively large.) Observe that the theoretical models are in good agreement. We have plotted only the analytic and the Quencher results in order to more clearly point out the accuracy of the analytic solution. Similarly good agreement is obtained with the MacQuench model. There are no published direct experimental measurements of T to add to the comparison. In Fig. 4.11b, however, we compare the published experimental measurements [2] of $2X_q$ with the analytic predictions given by Eq. (4.109) with $\rho_0 = 148 \text{ kg/m}^3$ and $p_0 = 10 \text{ atm}$. Good agreement between the analytic and the experimental

results is observed, quite comparable to the comparisons with Quencher discussed in Chapter 3.

We next calculate the helium pressure in the quench region for the case $I = 2$ kA ($J = 1.96 \times 10^8$ A/m²). From Eq. (4.109), we find $V_q \approx R\rho_0 L_q \dot{\bar{T}}/2p_0 = R\rho_0 L_q \alpha(\bar{T}) J^2/2p_0$. At $t = t_m = 4$ sec, we find \bar{T} is approximately 130 K. Using this value in Eq. (4.62) we find $\alpha(t_m) = 9.3 \times 10^{-16}$ m⁴-K/A²-sec. Thus, $V_q(t_m) = 1.9$ m/sec. Using this value together with $f = 0.07$, $L = 26$ m and $d_h = 6.9 \times 10^{-4}$ m in Eq. (4.112), we find $p_1(t_m) \approx 3.7$ atm. This value agrees very well with the pressure rise of 3.3 atm observed from the Quencher results for this case. Also note that since $p_1(t_m)/p_0 \lesssim 1$ this coil is in the small Δp regime.

Chapter 4 References

- [1] Dresner, L., *Protection Considerations for Forced-Cooled Superconductors*, 11th Symposium on Fusion Engineering, Proceedings Vol. 2, IEEE, New York, 1986.
- [2] Ando, T., Nishi, M., Kato, T., Yoshida, J., Itoh, N., Shimamoto, S., *Propagation Velocity of the Normal Zone in a Cable-In-Conduit Conductor*, Advances in Cryogenic Engineering, Vol. 35, Plenum Press, New York, 1990.

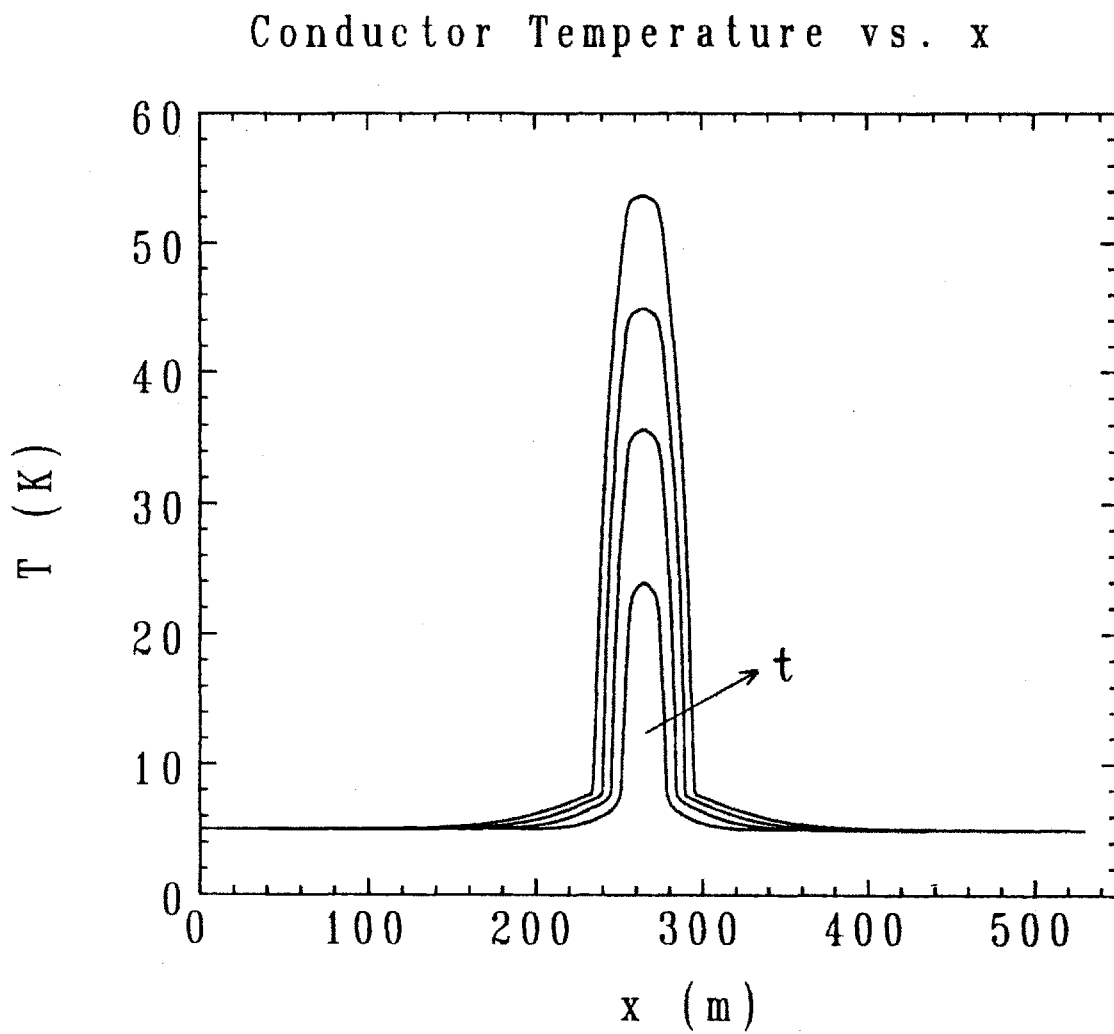


Figure 4.1a: Calculated conductor temperature profile during a quench in CICC.

Helium Pressure vs. x

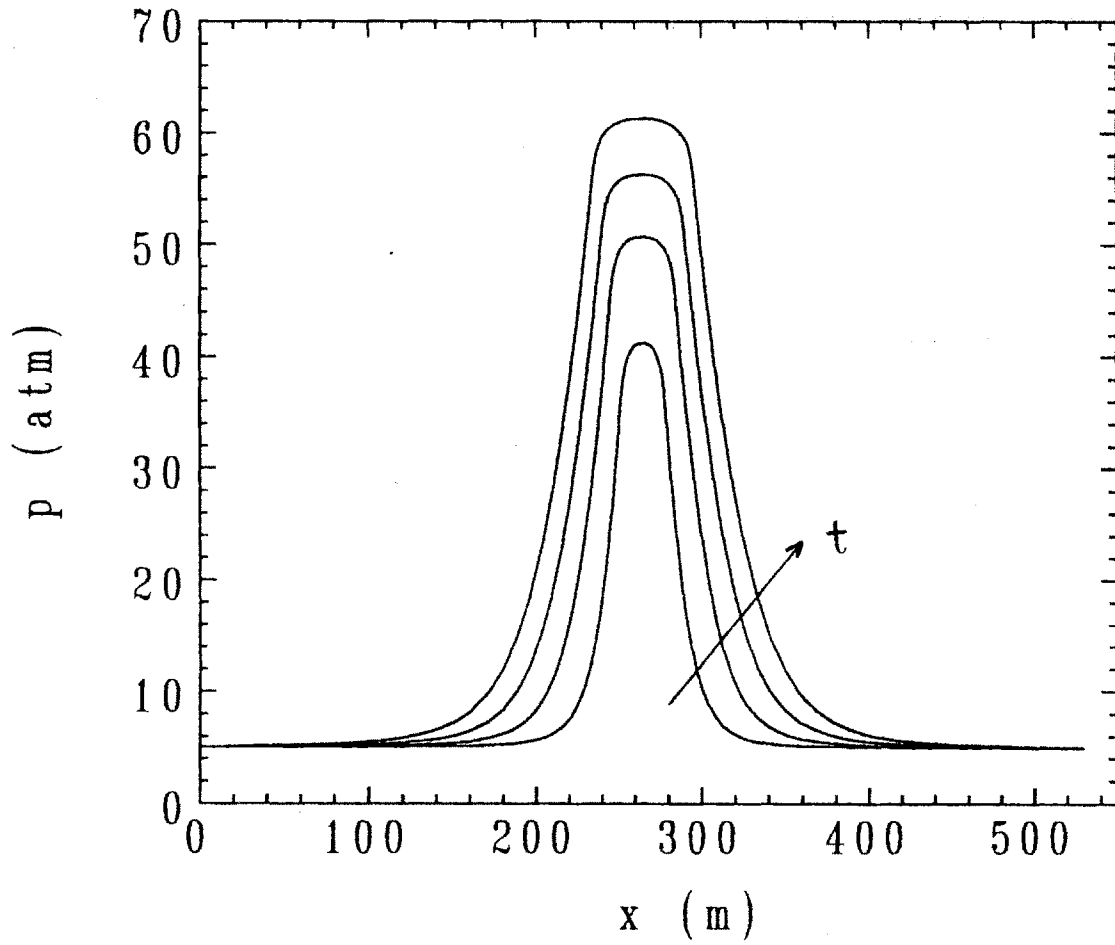


Figure 4.1b: Calculated helium pressure profile during a quench in CICC.

Helium Velocity vs. x

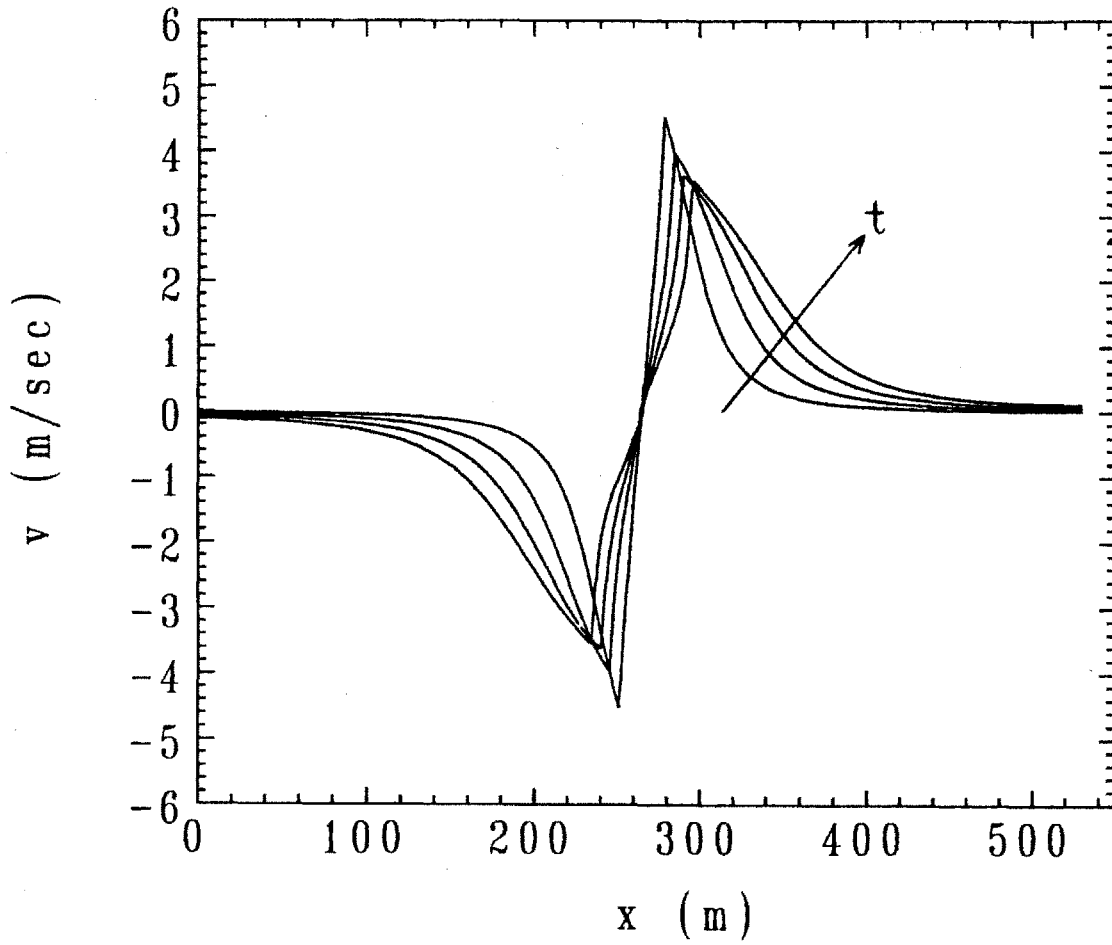


Figure 4.1c: Calculated helium velocity profile during a quench in CICC.

Helium Density vs. x

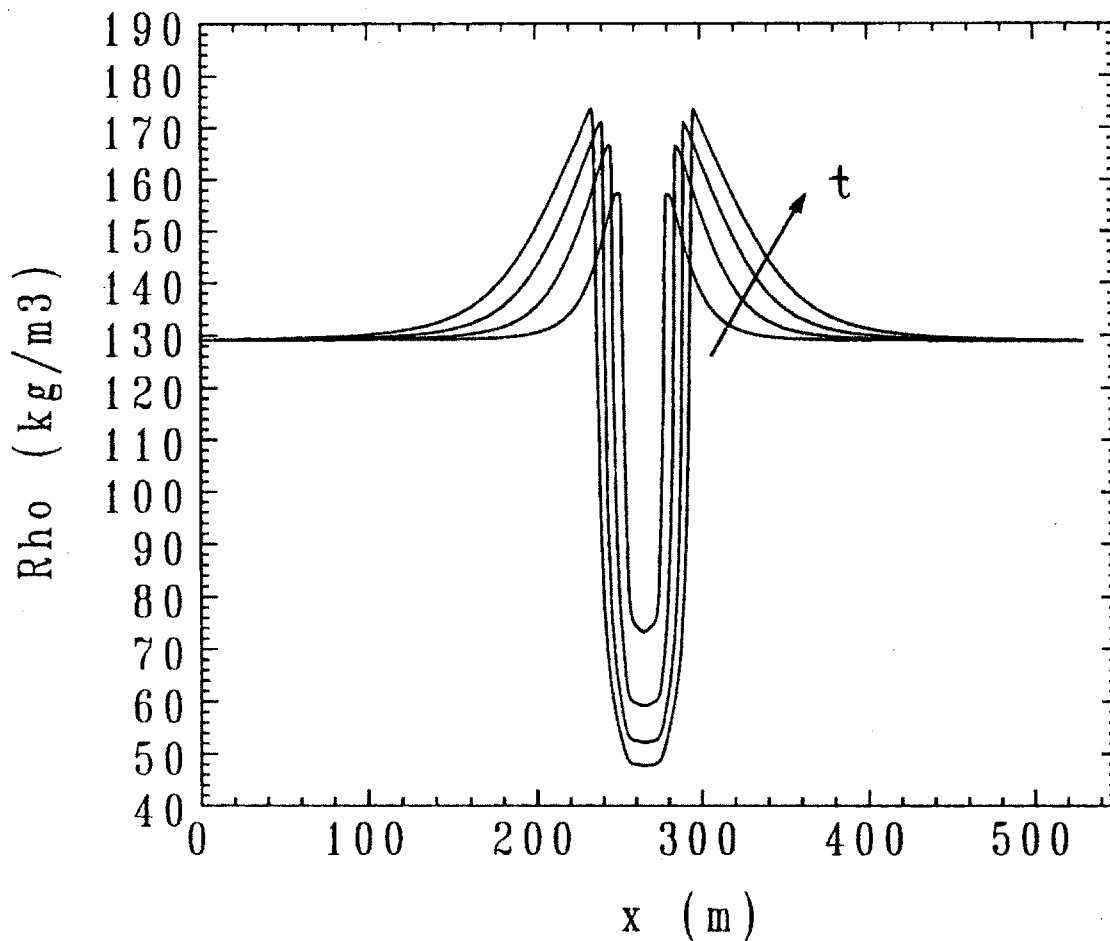


Figure 4.1d: Calculated helium density profile during a quench in CICC.

Alpha vs. Temperature

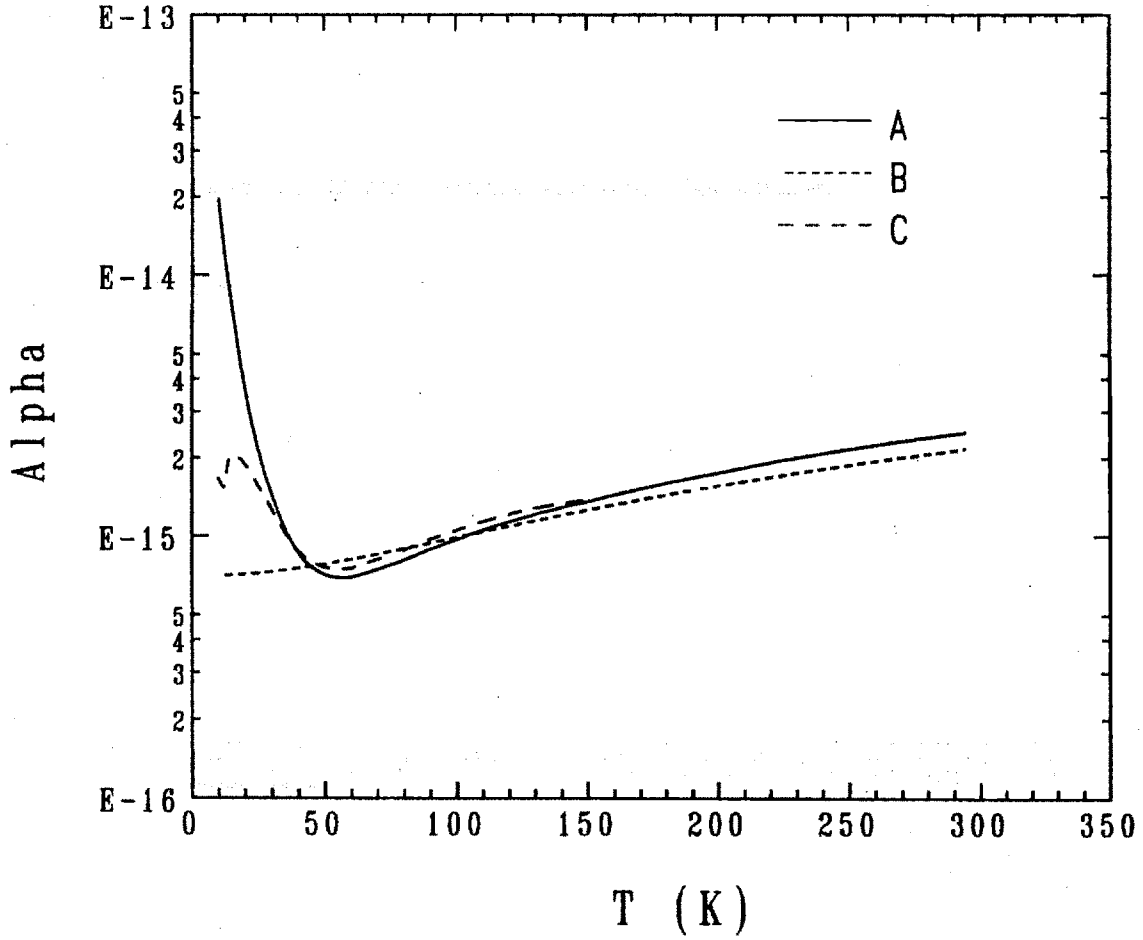


Figure 4.2: The parameter α as given by the following: (A) Eq. (4.61), (B) Eq. (4.62) and (C) including the helium specific heat contribution in Eq. (4.61).

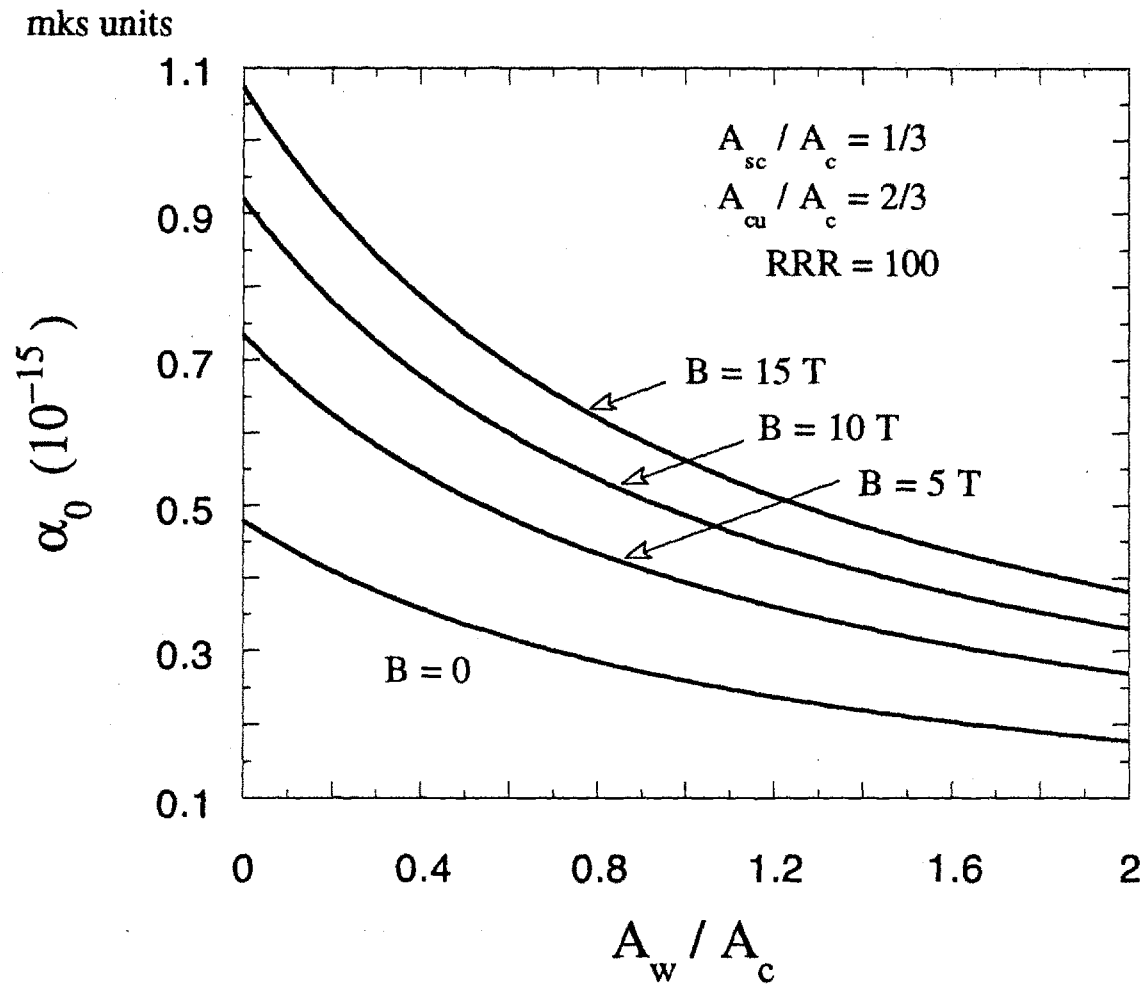


Figure 4.3: The dependence of α_0 on A_w/A_c .

Comparison of Eqs. (4.99) and (4.101)

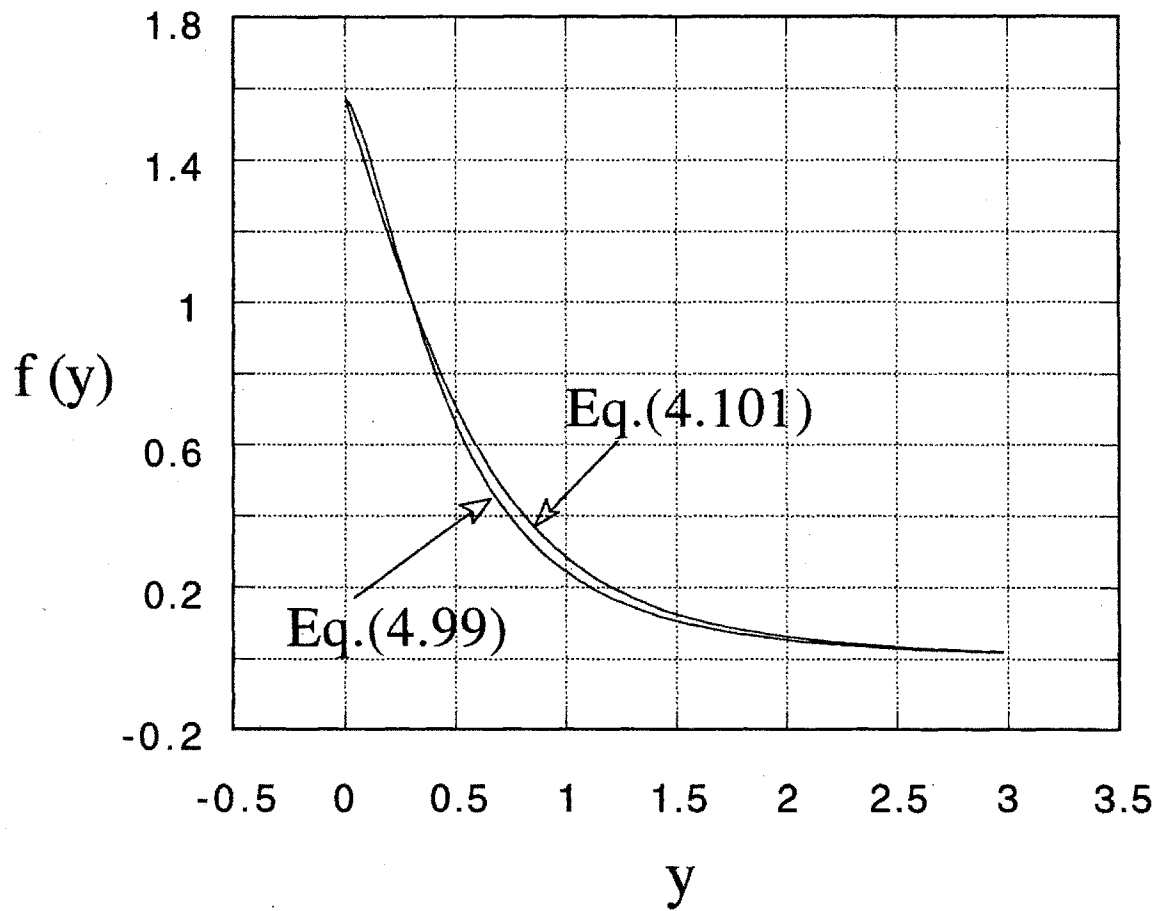


Figure 4.4: Comparison of Eqs.(4.99) and (4.101).

Short Coil	Long Coil
$L^2 < \frac{24d_h c_0^2 t_m}{fV_q}$	$L^2 > \frac{24d_h c_0^2 t_m}{fV_q(t_m)}$
$\frac{R\rho_0 L_q \alpha_0 J^2}{2p_0 V_q} > 1$	$\frac{R\rho_0 L_q \alpha_0 J^2}{2p_0 V_q(t_m)} > 1$
$V_q = \left(\frac{2d_h R}{fL} L_q \alpha_0 J^2 \right)^{1/3}$	$V_q(t) = 0.766 \left(\frac{2d_h}{f} \right)^{1/5} \left(\frac{RL_q \alpha_0 J^2}{c_0} \right)^{2/5} \frac{1}{t^{1/5}}$

Small dp Regime

$$p_1(t_m)/p_0 < 1$$

$$V_q \approx R\rho_0 L_q \alpha_0 J^2 / 2p_0$$

$$L^2 < \frac{24d_h c_0^2 t_m}{fV_q}$$

$$p_1(t) = \left(\frac{f\rho_0 L}{4d_h} \right) V_q^2$$

$$L^2 > \frac{24d_h c_0^2 t_m}{fV_q}$$

$$p_1(t) = 1.36 \left(\frac{f}{2d_h} \right)^{1/2} \rho_0 c_0 t^{1/2} V_q^{3/2}$$

Figure 4.5: Description of various regimes during a quench in CICC. Here, L is the length of the conductor, d_h is the hydraulic diameter, c_0 is the speed of sound in the background (ρ_0, p_0) state, f is the friction factor assumed constant ($f \approx 0.07$), $R = 2080$ J/kg-K, L_q is the length of the initial normal zone, $J = \text{const.}$ is the current density in the copper, α_0 is given in Fig. 4.3, and t_m is the time scale of interest during quench; $t_m \sim \tau_{det}$ where τ_{det} is the quench detection time.

Short Coil	Long Coil
$\bar{T}_{max}(t) \approx \alpha_0 J^2 t + T_q$	$\bar{T}_{max}(t) \approx \alpha_0 J^2 t + T_q$
$V_q(t) \approx \left[\frac{2d_h}{fL} \right]^{1/3} (RL_q \alpha_0 J^2)^{1/3}$	$V_q(t) \approx 0.766 \left[\frac{2d_h}{f c_0^2} \right]^{1/5} (RL_q \alpha_0 J^2)^{2/5} \frac{1}{t^{1/5}}$
$X_q(t) \approx V_q t + L_q/2$	$X_q(t) \approx V_q t + L_q/2$
$p_{max}(t) \approx \frac{R\rho_0 L_q}{2} \frac{\bar{T}}{X_q}$	$p_{max}(t) \approx \frac{R\rho_0 L_q}{2} \frac{\bar{T}}{X_q}$
$v_{ex}(t) = V_q \quad ; \quad t \geq L/2c_0$	$v_{ex}(t) = \frac{24d_h c_0^2}{fL^2} t \quad ; \quad t \geq L/2c_0$

Small dp Regime

$$\bar{T}_{max}(t) \approx \alpha_0 J^2 t + T_q$$

$$p_{max}(t) \approx p_0$$

$$V_q(t) \approx \frac{R\rho_0}{2p_0} L_q \alpha_0 J^2$$

$$X_q(t) \approx V_q t + L_q/2$$

$$L^2 < \frac{24d_h c_0^2 t_m}{fV_q}$$

$$v_{ex} = V_q \quad ; \quad t \geq L/2c_0$$

$$L^2 > \frac{24d_h c_0^2 t_m}{fV_q}$$

$$v_{ex}(t) = \frac{24d_h c_0^2}{fL^2} t \quad ; \quad t \geq L/2c_0$$

Figure 4.6: Analytic solution for quench in CICC in various regimes. For definition of the various parameters see the caption of Figure 5. Here, \bar{T} is the average temperature; $\bar{T} = (T + T_w)/2$, T_q is the initial temperature in the quench region (for most cases $T_q \approx T_{cr}$ where T_{cr} is the critical temperature of the superconductor), \bar{T}_{max} and p_{max} are the maximum average temperature and helium pressure, respectively. The quantity v_{ex} is the expulsion velocity of helium. Note that $v_{ex} = 0$ for $t < L/2c_0$ in all regimes.

Conductor Temperature vs. Time

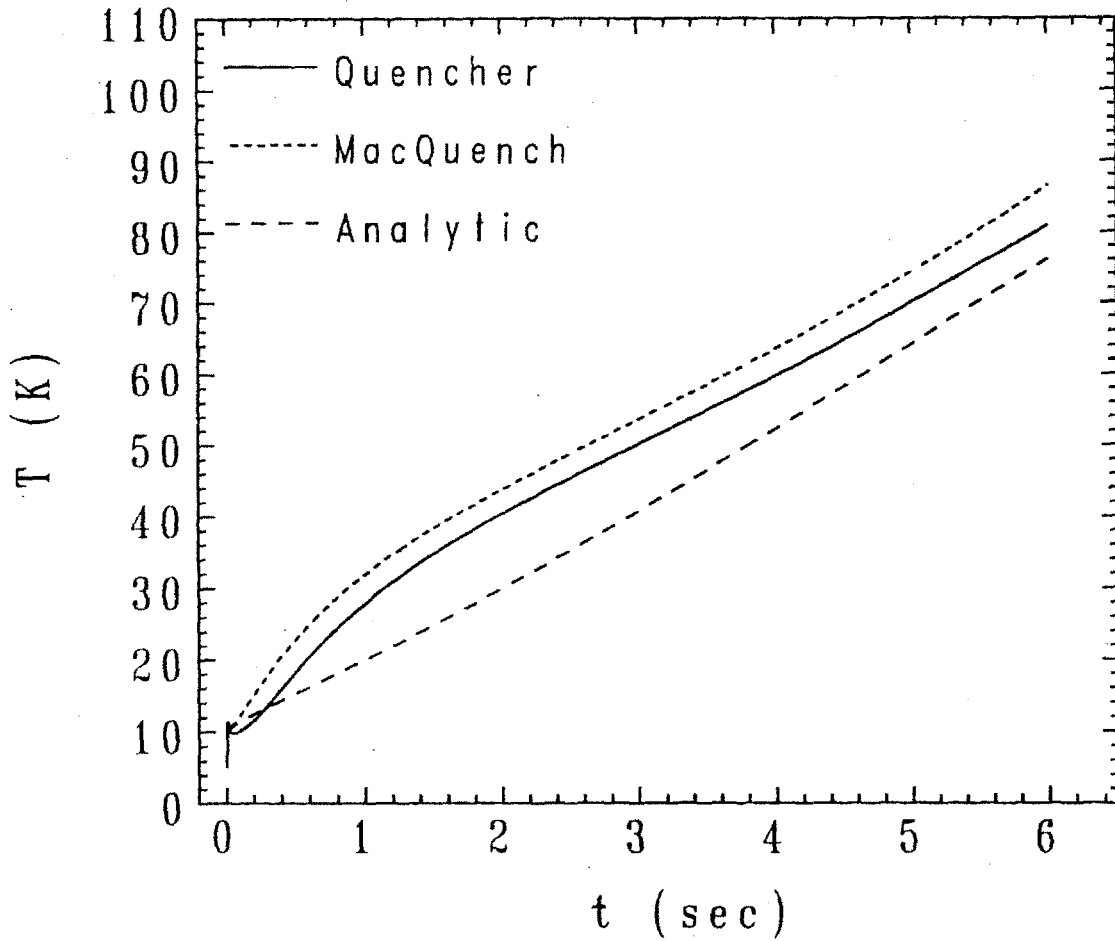


Figure 4.7a: Comparison of the maximum conductor temperature in a long coil as obtained by the various models.

Length of Normal Region vs. Time

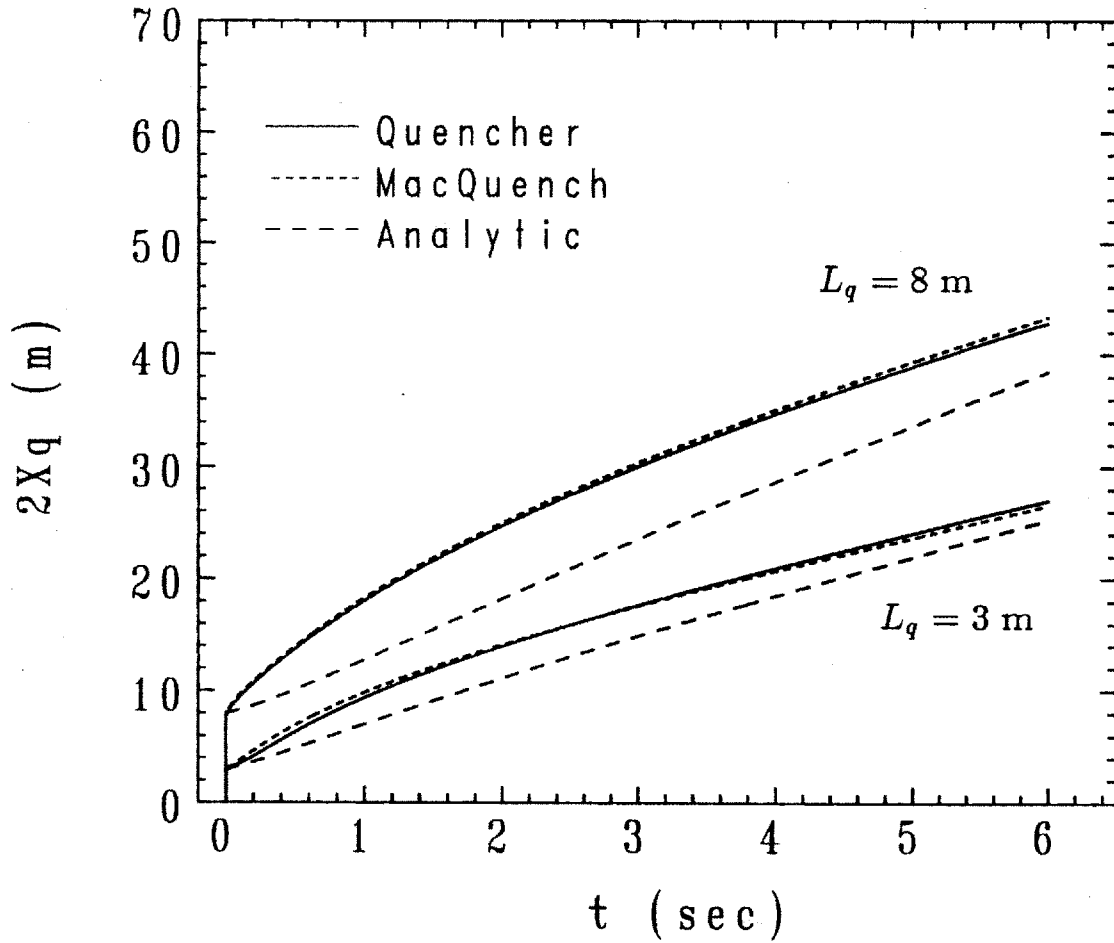


Figure 4.7b: Comparison of the length of the quench region in a long coil as obtained by the various models.

Maximum Helium Pressure vs. Time

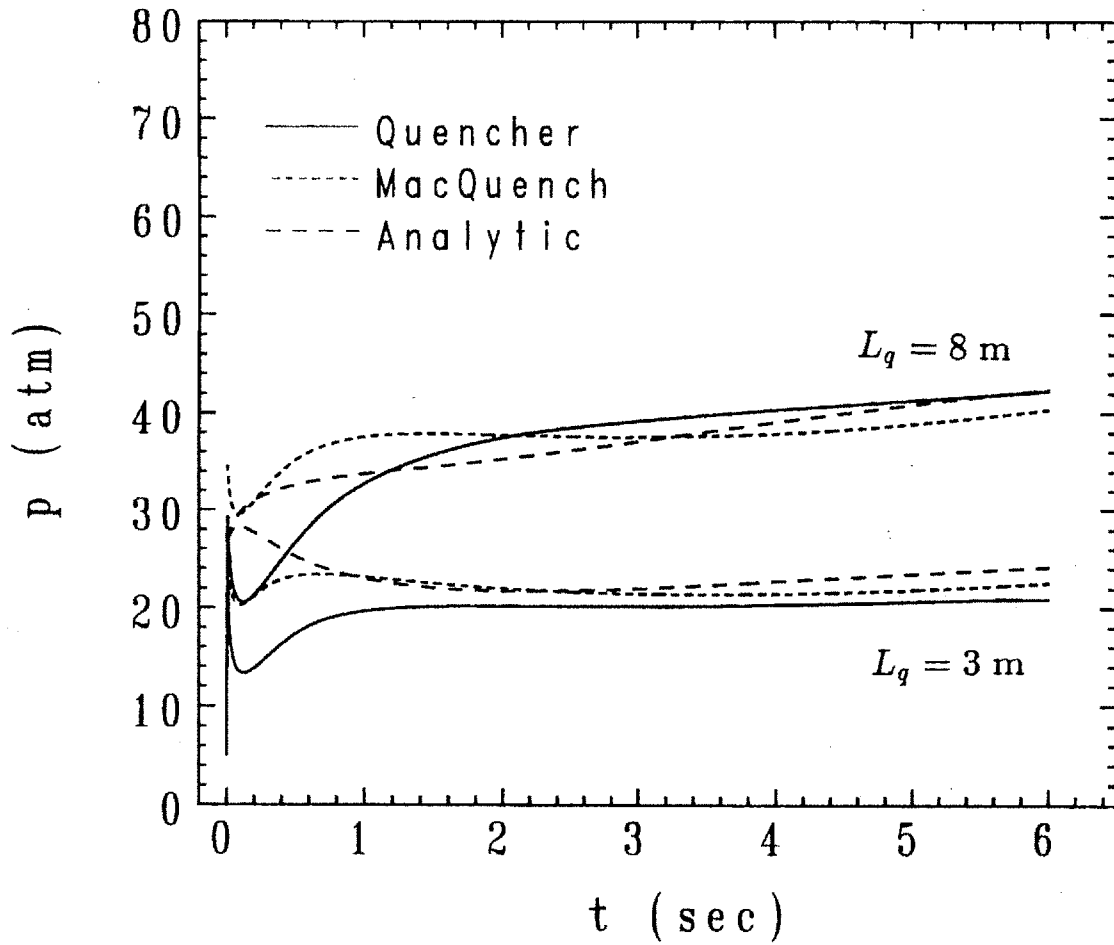


Figure 4.7c: Comparison of the maximum helium pressure in a long coil as obtained by the various models.

Helium Expulsion Velocity vs. Time

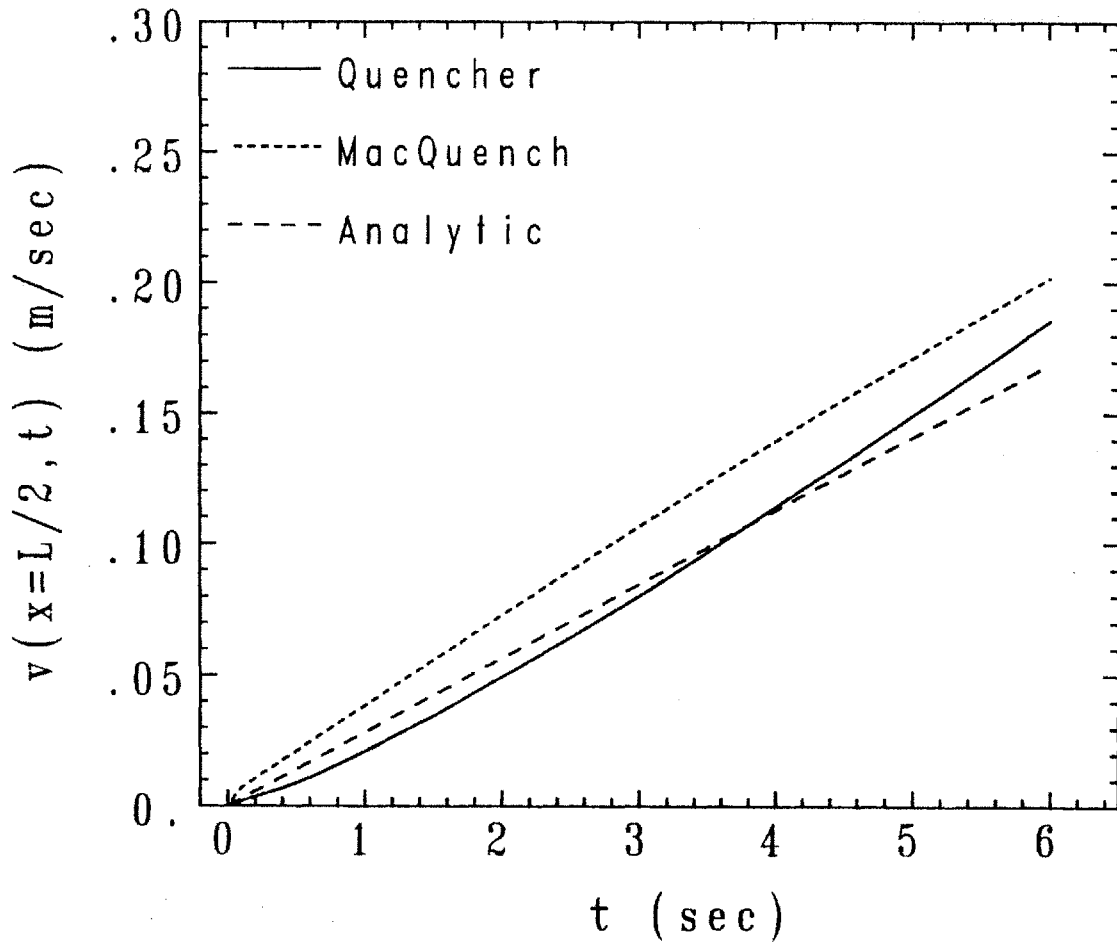


Figure 4.7d: Comparison of the helium expulsion velocity in a long coil as obtained by the various models.

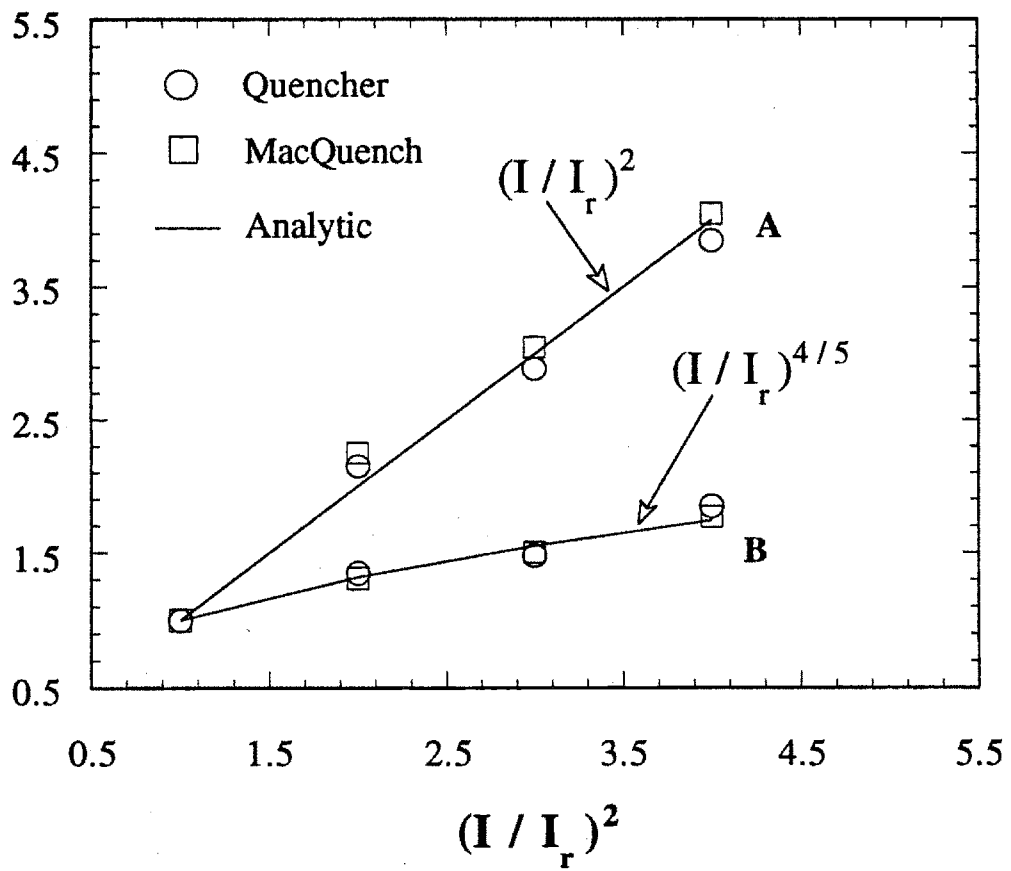


Figure 4.8: Comparison of $(\bar{T} - T_q)$ and $2X_q$ versus I^2 as obtained by the various models.

Length of Normal Region vs. Time

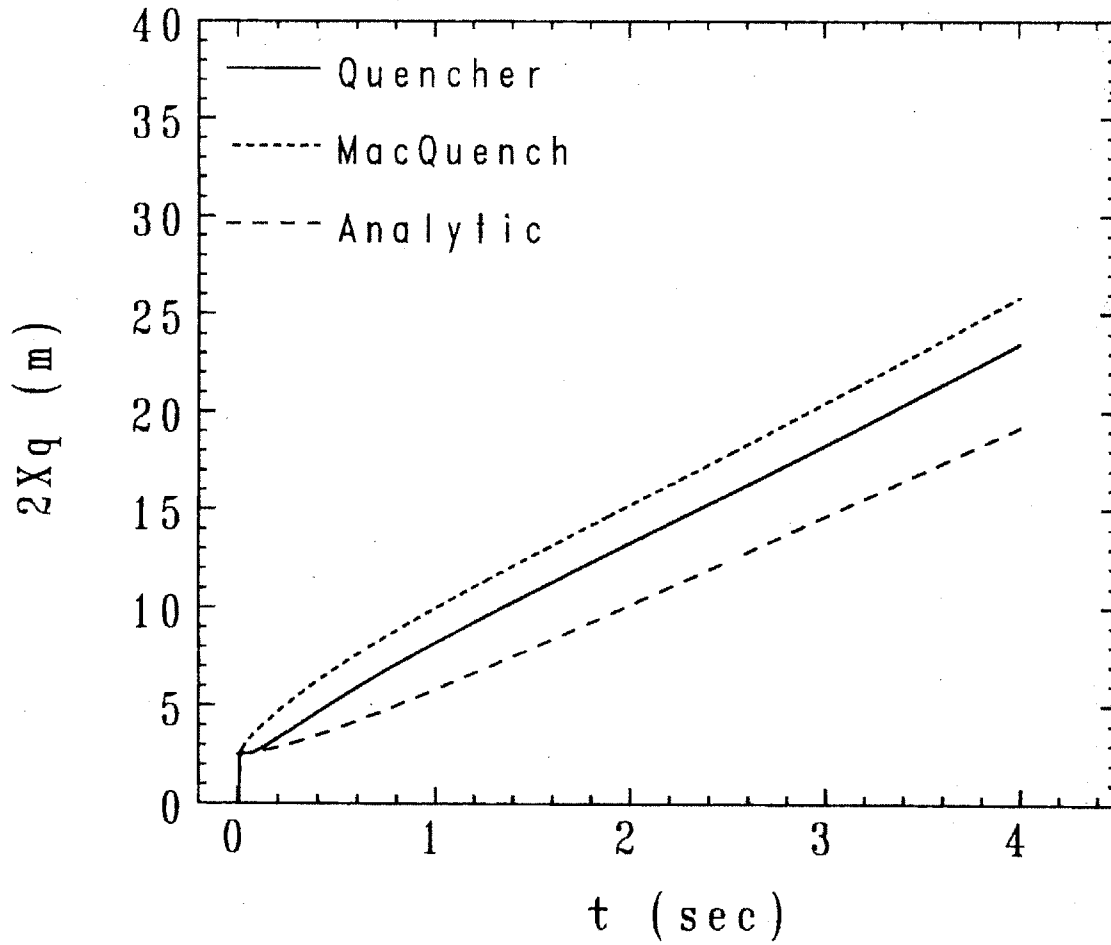


Figure 4.9a: Comparison of the length of the normal region in a short coil as obtained by the various models.

Maximum Pressure vs. Time

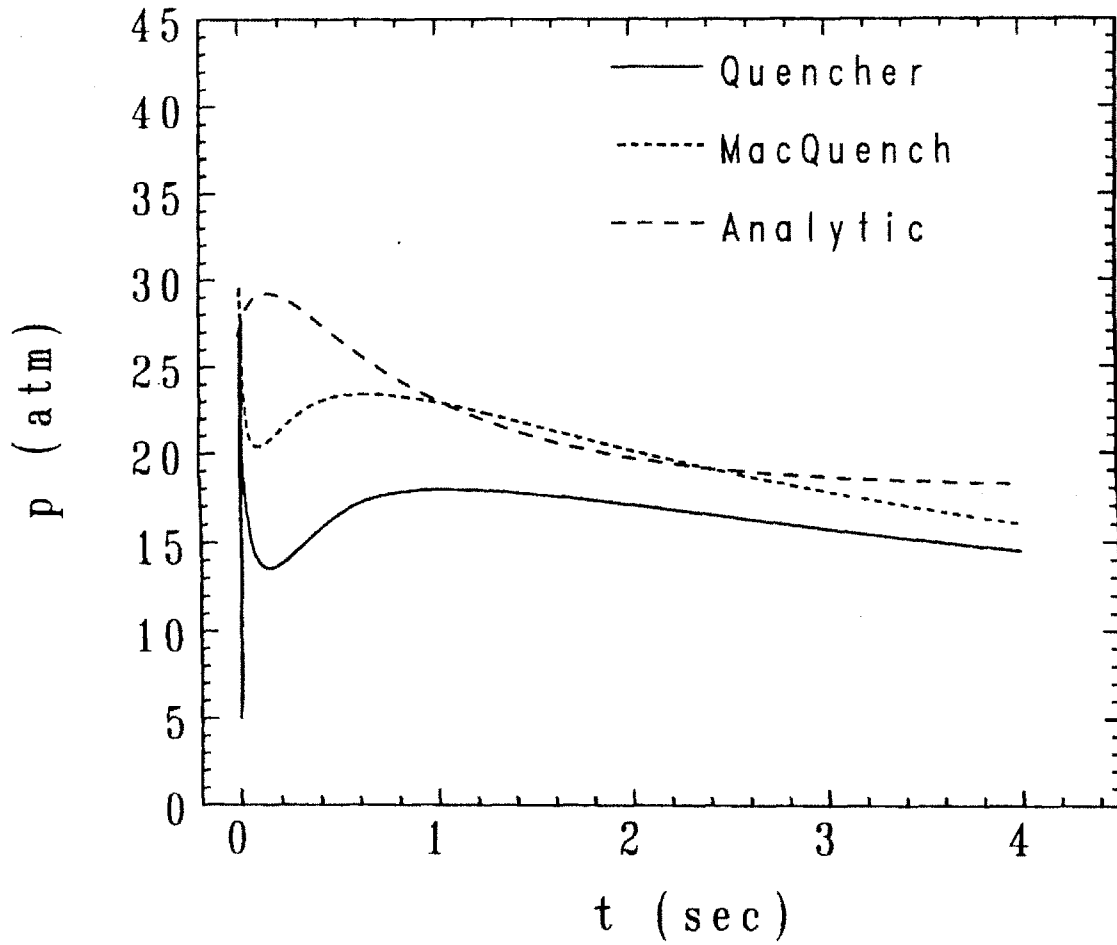


Figure 4.9b: Comparison of the maximum helium pressure in a short coil as obtained by the various models.

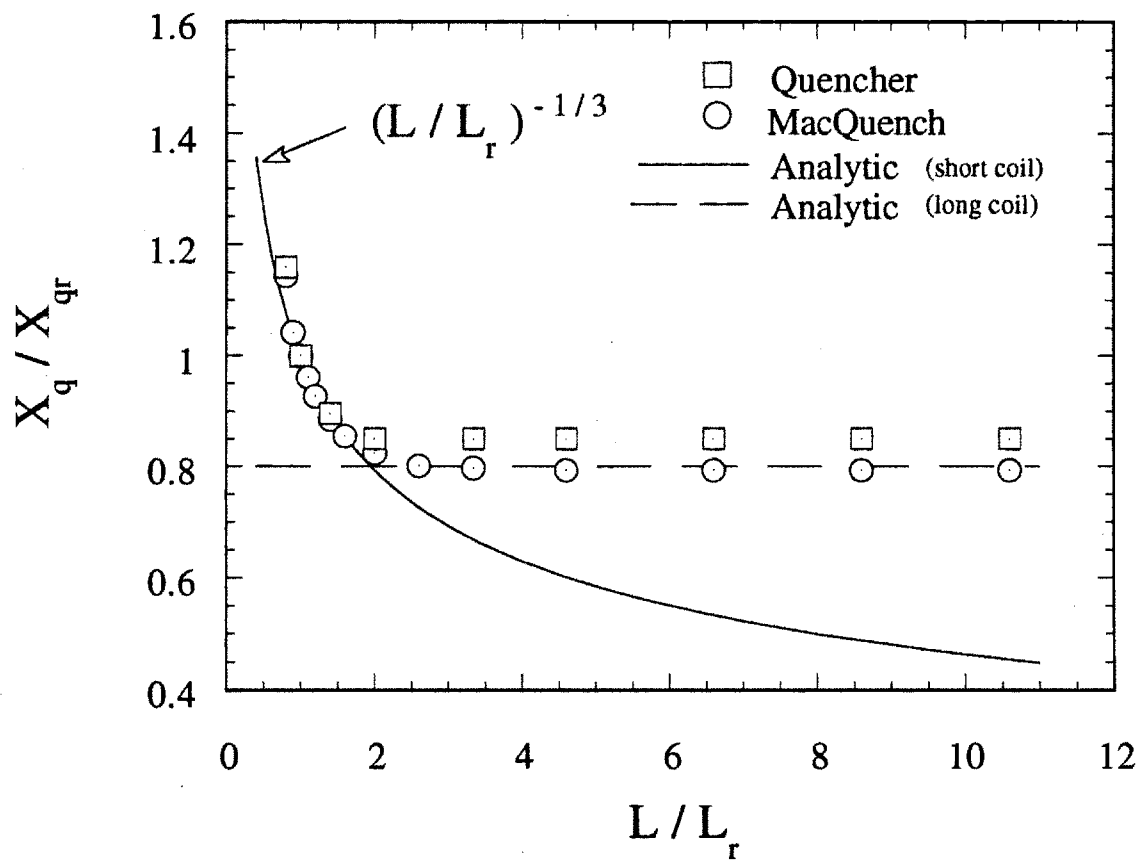


Figure 4.10: Comparison of the length of the normal region versus the length of the conduit, as obtained by the various models.

Conductor Temperature vs. Time

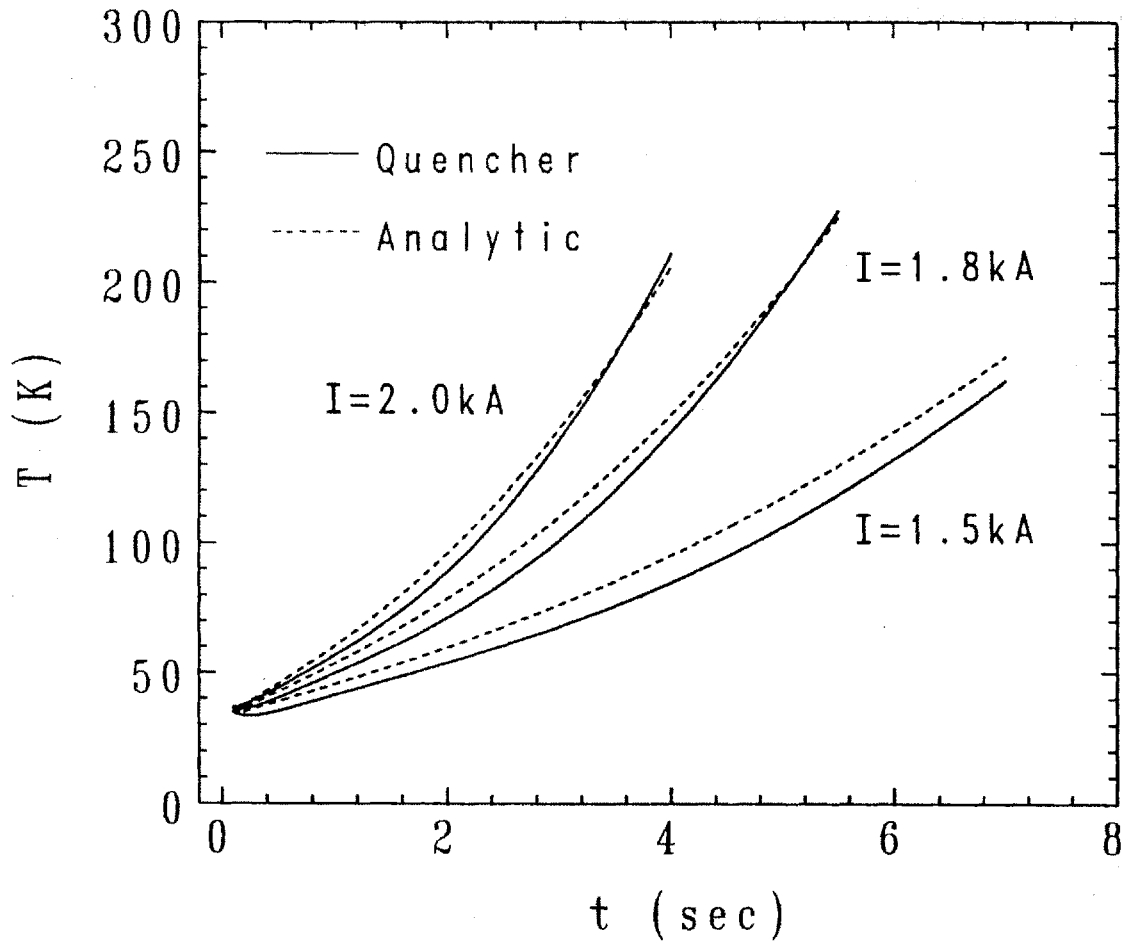


Figure 4.11a: Comparison of the conductor temperature in a small- Δp regime, as obtained by Quencher and the analytic results.

Comparison of Analytic and Experimental Results

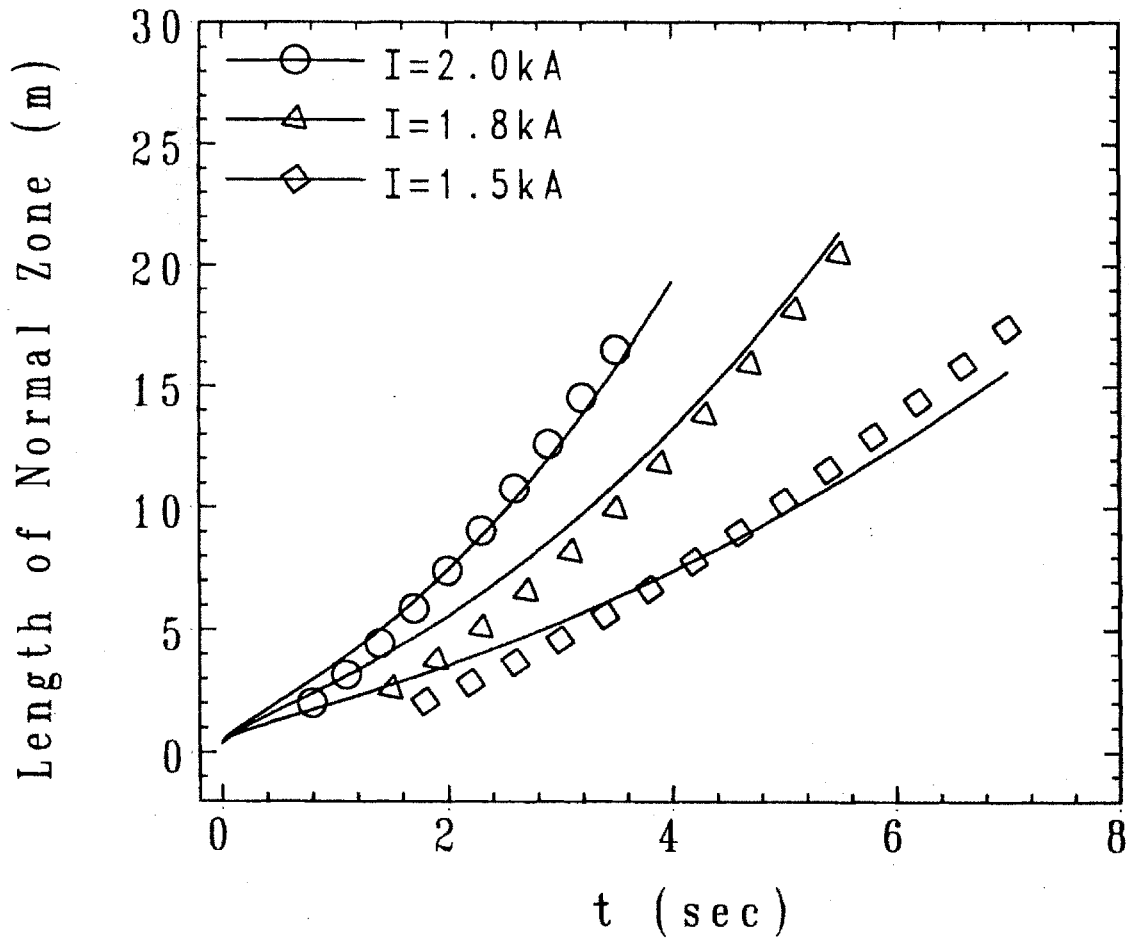


Figure 4.11b: Comparison of the length of the normal region as obtained by experiments of Ando et al. [2] and the analytic results.

Chapter 5
Dual-Channel CICC

Chapter 5. Dual-Channel CICC

This Chapter presents a theoretical model describing quench propagation in Cable-In-Conduit Conductors (CICC) with an additional central flow channel. The central channel is used to enhance the flow capabilities in the conduit during steady state operation as well as during quench events. Such a system is the proposed design for certain conductors in the International Thermonuclear Experimental Reactor (ITER). Here, the additional channel is formed by a metal spring located at the center of the conduit. We describe the separate thermal evolution in both the cable bundle and the central channel; in particular, the mass, momentum and heat transfer due to flow between the cable bundle and the central channel are included in the model. Several simplifications are introduced which greatly reduce the complexity of the model without sacrificing accuracy. The resulting reduced model is solved both numerically and approximately analytically for ITER parameters.

A schematic diagram of the CICC with an additional central channel is shown in Fig. 5.1. In practice the cable and primary coolant (region 1 helium) are separated from the central hole (region 2 helium) by a stiff but loosely wound spring. Because of the larger hydraulic diameter of the central hole, it should be possible to pump supercritical helium along the length of the cable with greater ease during standard operation. Thus, a given cooling requirement should be attainable with a lower pumping power. This would clearly be a desirable feature.

The purpose of the present Chapter is to examine the effect of the central hole on the problem of quench propagation. We present a numerical model and a corresponding analytic theory based on the QUENCHER model presented in Chapters 2 and 3. Similar studies are simultaneously being carried out by Bottura using the SARUMAN code [1,2]. Both the present work and Bottura's work appear to make the same engineering approximations to describe the interaction between the region 1 and 2 helium flows.

A qualitative description of the results presented here is as follows. First,

during quench the maximum temperature of the quenched conductor is essentially unaffected by the central hole. This is a consequence of the fact that the heating rate depends primarily on the resistivity of the copper matrix and the heat capacities of the copper and wall. It only very weakly depends on the thermal hydraulic behavior of the helium (see Chapter 4).

Second, the average propagation velocity of the quench front increases because of the central hole: if $X_q(t)$ is the location of the quench front, then $V_q = \dot{X}_q$ increases. The reason is that the helium directly heated by the quenched conductor easily passes through the spacing between adjacent spring turns. Once in region 2, the hot helium flows ahead much faster because of the large hydraulic diameter, thereby increasing the quench speed.

Third, the maximum pressure is slightly lower for the CICC with the central hole. This is a consequence of having a lower frictional resistance for the flow of helium. The qualitative features described above are quantified numerically and analytically in the main body of this chapter.

5.1 Basic Model

The most general model that may be used to describe the helium flow and heat transfer in a dual-channel CICC, is a set of three dimensional equations for each component. These equations are the same as that described in Chapter 2 with an additional set of equations for the helium in the central channel. The resulting model is unnecessarily complicated and just as in Chapter 2 we may simplify the 3-D equations to a one dimensional model. The procedure is the same as that presented in Chapter 2.

To begin, we denote helium in the cable space as “helium 1” and “helium 2” consists of the helium in the central channel. Since the cable and the conduit wall are only in direct contact with helium 1, their treatment is identical to Eqs. (2.1) and (2.6). Thus, the 1-D equations for the conductor and the wall are given by;

Wall:

$$\rho_w C_w \frac{\partial T_w}{\partial t} = \frac{\partial}{\partial x} \kappa_w \frac{\partial T_w}{\partial x} - \frac{h_w P_w}{A_w} (T_w - T_1) \quad (5.1)$$

Conductor:

$$\rho_c C_c \frac{\partial T_c}{\partial t} = \frac{\partial}{\partial x} \kappa_c \frac{\partial T_c}{\partial x} - \frac{h_c P_c}{A_c} (T_c - T_1) + S_c \quad (5.2)$$

where the quantities h_w and h_c are functions of ρ_1 , T_1 and v_1 .

The helium 1 equations are obtained from Eqs. (2.21), (2.26) and (2.34), by noting that certain boundary terms are no longer zero. Thus, we have

Helium 1:

$$\frac{\partial \rho_1}{\partial t} + \frac{\partial}{\partial x} (\rho_1 v_1) = \alpha \frac{P_s}{A_1} \Gamma_1 \quad (5.3)$$

$$\rho_1 \frac{dv_1}{dt} = -\frac{\partial p_1}{\partial x} - \frac{f_1 \rho_1 |v_1| v_1}{2d_1} \quad (5.4)$$

$$\begin{aligned} \rho_1 \left(\frac{\partial}{\partial t} + v_1 \frac{\partial}{\partial x} \right) \left(U_1 + \frac{1}{2} v_1^2 \right) &= -\frac{\partial}{\partial x} (p_1 v_1) \\ &+ \frac{h_w P_w}{A_1} (T_w - T_1) + \frac{h_c P_c}{A_1} (T_c - T_1) + \frac{P_s}{A_1} (\alpha \Lambda_1 + q_1) \end{aligned} \quad (5.5)$$

$$p_1 = p_1(\rho_1, T_1) \quad (5.6)$$

Similarly, for helium 2 we find

Helium 2:

$$\frac{\partial \rho_2}{\partial t} + \frac{\partial}{\partial x} (\rho_2 v_2) = -\alpha \frac{P_s}{A_2} \Gamma_2 \quad (5.7)$$

$$\rho_2 \frac{dv_2}{dt} = -\frac{\partial p_2}{\partial x} - \frac{f_2 \rho_2 |v_2| v_2}{2d_2} \quad (5.8)$$

$$\rho_2 \left(\frac{\partial}{\partial t} + v_2 \frac{\partial}{\partial x} \right) \left(U_2 + \frac{1}{2} v_2^2 \right) = -\frac{\partial}{\partial x} (p_2 v_2) - \frac{P_s}{A_2} (\alpha \Lambda_2 + q_2) \quad (5.9)$$

$$p_2 = p_2(\rho_2, T_2) \quad (5.10)$$

where the cross-coupling terms are defined as follows;

$$\Gamma_1 = -\frac{\rho_1}{P_s} \oint_{S_s} [\mathbf{n} \cdot \mathbf{v}_{\perp 1}] dS \quad (5.11)$$

$$\Gamma_2 = \frac{\rho_2}{P_s} \oint_{S_s} [\mathbf{n} \cdot \mathbf{v}_{\perp 2}] dS \quad (5.12)$$

$$\Lambda_1 = -\left(U_1 + \frac{1}{2}v_1^2 + \frac{p_1}{\rho_1}\right) \Gamma_1 \quad (5.13)$$

$$\Lambda_2 = \left(U_2 + \frac{1}{2}v_2^2 + \frac{p_2}{\rho_2}\right) \Gamma_2 \quad (5.14)$$

$$q_1 = \frac{1}{P_s} \oint_{S_s} [\mathbf{n} \cdot \kappa_{T1} \nabla_{\perp} T_{h1}] dS \quad (5.15)$$

$$q_2 = -\frac{1}{P_s} \oint_{S_s} [\mathbf{n} \cdot \kappa_{T2} \nabla_{\perp} T_{h2}] dS \quad (5.16)$$

Note that α in these equations is defined as $\alpha \equiv g/(s + g)$ (see Fig. 5.1 for definitions of g and s). This term arises from the fact that only a fraction of the space along the spring is available for helium flow in the transverse direction. Also, note that there are no coupling terms in the momentum equations. This is a consequence of neglecting the cross-friction between helium 1 and helium 2 at the spring interface. This is a valid approximation since this friction is small compared to the friction between helium in each of these regions and the spring itself.

The left hand side of Eqs. (5.5) and (5.9) may be manipulated, as was done in obtaining Eq. (2.44), in order to write these equations in terms of the temperature. In terms of the temperature variable, the general 1-D equations for the various components are given by;

Wall:

$$\rho_w C_w \frac{\partial T_w}{\partial t} = \frac{\partial}{\partial x} \kappa_w \frac{\partial T_w}{\partial x} - \frac{h_w P_w}{A_w} (T_w - T_1) \quad (5.17)$$

Conductor:

$$\rho_c C_c \frac{\partial T_c}{\partial t} = \frac{\partial}{\partial x} \kappa_c \frac{\partial T_c}{\partial x} - \frac{h_c P_c}{A_c} (T_c - T_1) + S_c \quad (5.18)$$

Helium 1:

$$\frac{\partial \rho_1}{\partial t} + \frac{\partial}{\partial x} (\rho_1 v_1) = \alpha \frac{P_s}{A_1} \Gamma_1 \quad (5.19)$$

$$\rho_1 \frac{dv_1}{dt} = -\frac{\partial p_1}{\partial x} - \frac{f_1 \rho_1 |v_1| v_1}{2d_1} \quad (5.20)$$

$$\begin{aligned} \rho_1 C_{h1} \frac{\partial T_1}{\partial t} + \rho_1 C_{h1} v_1 \frac{\partial T_1}{\partial x} + \rho_1 C_{\beta 1} T_1 \frac{\partial v_1}{\partial x} &= \frac{f_1 \rho_1 |v_1| v_1^2}{2d_1} \\ &+ \frac{h_w P_w}{A_1} (T_w - T_1) + \frac{h_c P_c}{A_1} (T_c - T_1) + \frac{P_s}{A_1} (\alpha \Lambda_1 + q_1) \end{aligned} \quad (5.21)$$

$$p_1 = p_1(\rho_1, T_1) \quad (5.22)$$

Helium 2:

$$\frac{\partial \rho_2}{\partial t} + \frac{\partial}{\partial x} (\rho_2 v_2) = -\alpha \frac{P_s}{A_2} \Gamma_2 \quad (5.23)$$

$$\rho_2 \frac{dv_2}{dt} = -\frac{\partial p_2}{\partial x} - \frac{f_2 \rho_2 |v_2| v_2}{2d_2} \quad (5.24)$$

$$\rho_2 C_{h2} \frac{\partial T_2}{\partial t} + \rho_2 C_{h2} v_2 \frac{\partial T_2}{\partial x} + \rho_2 C_{\beta 2} T_2 \frac{\partial v_2}{\partial x} = \frac{f_2 \rho_2 |v_2| v_2^2}{2d_2} - \frac{P_s}{A_2} (\alpha \Lambda_2 + q_2) \quad (5.25)$$

$$p_2 = p_2(\rho_2, T_2) \quad (5.26)$$

The cross-coupling terms Γ , Λ , and q represent the mass flux, the energy flux due to perpendicular convection, and the heat flux due to turbulent convection, respectively. These quantities are not known in general and additional relations must be specified in order to determine them. In the next section we present the cross-coupling approximations that eliminate these terms and hence avoid introducing any additional equations.

5.2 Cross-Coupling Simplifications

A simpler model is obtained by introducing the cross-coupling simplifications described here. The basic assumption is that there is good communication between regions 1 and 2, in terms of mass and energy transfer. Practically, this implies that the gap between alternate turns of the spring is large: $g \gtrsim s$ (see Fig. 5.1). In this situation there is strong mixing of the helium in regions 1 and 2 leading to rapid equilibration of the pressures, densities, and temperatures. The velocities, however, can be quite different, because of the large difference in hydraulic diameters.

The consequences are as follows. From general conservation relations, we require $\Gamma_1 = \Gamma_2 \equiv \Gamma$, and $q_1 = q_2 \equiv q$; that is, there is no build-up of particles or energy in the thin layer separating regions 1 and 2. Because of rapid mixing, $\rho_1 = \rho_2 \equiv \rho$, $T_1 = T_2 \equiv T$, and $p_1 = p_2 \equiv p$ (note that this assumption results in $\Lambda_1 = \Lambda_2 \equiv \Lambda$). These approximations can be exploited by eliminating the cross coupling terms from the mass and energy equations. This is done by appropriately adding Eqs. (5.19) and (5.23) such that the term $\alpha P_s \Gamma$ is cancelled. Similarly adding Eqs. (5.21) and (5.25) such that the term $P_s(\alpha \Lambda + q)$ is cancelled results in the simplified energy relation. The new model is now given by;

Wall:

$$\rho_w C_w \frac{\partial T_w}{\partial t} = \frac{\partial}{\partial x} \kappa_w \frac{\partial T_w}{\partial x} - \frac{h_w P_w}{A_w} (T_w - T_1) \quad (5.27)$$

Conductor:

$$\rho_c C_c \frac{\partial T_c}{\partial t} = \frac{\partial}{\partial x} \kappa_c \frac{\partial T_c}{\partial x} - \frac{h_c P_c}{A_c} (T_c - T_1) + S_c \quad (5.28)$$

Helium 1/Helium 2:

$$A_h \frac{\partial \rho}{\partial t} + \frac{\partial}{\partial x} \rho (A_1 v_1 + A_2 v_2) = 0 \quad (5.29)$$

$$\rho \frac{dv_1}{dt} = -\frac{\partial p}{\partial x} - \frac{f_1 \rho |v_1| v_1}{2d_1} \quad (5.30)$$

$$\rho \frac{dv_2}{dt} = -\frac{\partial p}{\partial x} - \frac{f_2 \rho |v_2| v_2}{2d_2} \quad (5.31)$$

$$A_h \rho C_h \frac{\partial T}{\partial t} + \rho C_h (A_1 v_1 + A_2 v_2) \frac{\partial T}{\partial x} + \rho C_\beta T \frac{\partial}{\partial x} (A_1 v_1 + A_2 v_2) =$$

$$A_1 \frac{f_1 \rho_1 |v_1| v_1^2}{2d_1} + A_2 \frac{f_2 \rho |v_2| v_2^2}{2d_2} + h_w P_w (T_w - T) + h_c P_c (T_c - T) \quad (5.32)$$

$$p = p(\rho, T) \quad (5.33)$$

where $A_h \equiv A_1 + A_2$.

Equations (5.27–33) are very similar to the general model discussed in Chapter 2 (see section 2.2). In fact, these equations reduce to Eqs. (2.48–53) for $A_2 \rightarrow 0$. Only one additional equation to the general model has to be solved. This model is solved by L. Bottura using a modified version of the Saruman computer code [1,2]. In the next section we proceed with the quench simplifications in order to further reduce Eqs. (5.27–33). This procedure is exactly the same as that presented in section 2.3 of Chapter 2, where the general model describing quench in a simple CICC was reduced to the Quencher model.

5.3 Quench Simplifications

By making the same quench simplifications as was done in obtaining the Quencher model we may further reduce Eqs. (5.27–33). To begin, we define the “area-averaged” velocity v as follows;

$$v \equiv \frac{A_1 v_1 + A_2 v_2}{A_1 + A_2} \quad (5.34)$$

Next by neglecting the inertia in both Eqs. (5.30) and (5.31) we find

$$\frac{f_1 \rho v_1^2}{2d_1} = \frac{f_2 \rho v_2^2}{2d_2} \quad (5.35)$$

This is a general relation between v_1 and v_2 which may be used for any given friction factor correlation. For the correlation given by Eq. (2.69) we note that

$$f_1 = k_1 \frac{0.184}{R_1^{0.2}} \quad (5.36)$$

$$f_2 = k_2 \frac{0.184}{R_2^{0.2}} \quad (5.37)$$

where k_1 and k_2 are in general not the same since the roughness in regions 1 and 2 are quite different. The Reynold's numbers are given by $R_1 = d_1 \rho v_1 / \mu_h$ and $R_2 = d_2 \rho v_2 / \mu_h$. We now solve Eqs. (5.34) and (5.35) for the two unknowns v_1 and v_2 in terms of v . We find

$$v_1 = \frac{1 + (A_2/A_1)}{1 + (A_2/A_1)\gamma_N} v \quad (5.38)$$

$$v_2 = \frac{(1 + A_2/A_1)\gamma_N}{1 + (A_2/A_1)\gamma_N} v \quad (5.39)$$

where

$$\gamma_N \equiv \left(\frac{k_1}{k_2}\right)^{1/1.8} \left(\frac{d_2}{d_1}\right)^{1.2/1.8} \quad (5.40)$$

These equations relate the velocity in each of the regions to the average velocity in the conduit. In general $\gamma_N > 1$.

Next, by properly adding Eqs. (5.28) and (5.32) to cancel the heat transfer terms, and using the definition for the average velocity, we find the reduced equations given by;

Wall:

$$\rho_w C_w \frac{\partial T_w}{\partial t} = -\frac{h_w P_w}{A_w} (T_w - T) \quad (5.41)$$

Conductor/Helium:

$$\frac{\partial \rho}{\partial t} + \frac{\partial}{\partial x} \rho v = 0 \quad (5.42)$$

$$\frac{\partial p}{\partial x} = -\frac{f_1 \rho |v_1| v_1}{2d_1} \quad (5.43)$$

$$\rho \hat{C}_t \frac{\partial T}{\partial t} + \rho \hat{C}_h v \frac{\partial T}{\partial x} + \rho \hat{C}_\beta T \frac{\partial v}{\partial x} = \left(\frac{A_h}{A_c} \right) \frac{f_1 \rho |v_1| v_1}{2d_1} v + \frac{h_w P_w}{A_c} (T_w - T) + \frac{\partial}{\partial x} \kappa_c \frac{\partial T}{\partial x} + S_c \quad (5.44)$$

$$p = p(\rho, T) \quad (5.45)$$

$$v_1 = \left[\frac{1 + (A_2/A_1)}{1 + (A_2/A_1)\gamma_N} \right] v \quad (5.46)$$

where γ_N is given by Eq. (5.40). All other terms have been defined in Table 3.1. The quantity h_w is given by a relation similar to Eq. (2.73) where the velocity used to calculate the Reynold's number is v_1 ; that is, $h_w = h_w(\rho, T, v_1)$.

Observe that the system of Eqs. (5.41–46) is nearly identical to the Quencher model with an additional equation for v_1 . Since this additional equation is algebraic, the numerical procedure used in solving this system is the same as that described in Chapter 3. Only a slight modification due to Eq. (5.46) is introduced. Note the degree of simplification that results from neglecting the inertia. Other than the advantages discussed in section 2.3, without this simplification, the differential Eq. (5.31) must be solved instead of the algebraic Eq. (5.46).

Analytic Solution

The system of Eqs. (5.41–46) is very similar to the Quencher model, and in this regard we now proceed to show how the analytic theory developed in Chapter 4 is extended to this model. First, observe that in Chapter 4 the frictional heating was neglected from the energy equation. Doing the same in Eq. (5.44) eliminates v_1 in this equation. The only remaining v_1 is in the momentum equation. Before proceeding to eliminate v_1 from Eq. (5.43) note that quantities f_1 and f_2 are assumed constant in the analytic theory. Recall that $f_1 \approx 0.06 - 0.08$ and f_2 may be approximated by $f_2 \approx 0.03 - 0.04$. Thus, from Eqs. (5.34) and (5.35) we find

$$v_1 = \left[\frac{1 + (A_2/A_1)}{1 + (A_2/A_1)\gamma_A} \right] v \quad (5.47)$$

$$v_2 = \left[\frac{(1 + A_2/A_1)\gamma_A}{1 + (A_2/A_1)\gamma_A} \right] v \quad (5.48)$$

where

$$\gamma_A \equiv \left(\frac{f_1}{f_2} \right)^{1/2} \left(\frac{d_2}{d_1} \right)^{1/2} \quad (5.49)$$

with $f_1/f_2 \approx 2$.

Having determined v_1 we may now eliminate this quantity in term of v in Eq. (5.43). We define the equivalent hydraulic diameter such that

$$\frac{f_1 \rho v_1^2}{2d_1} = \frac{f_1 \rho v^2}{2d_{eq}} \quad (5.50)$$

which is satisfied for

$$d_{eq} \equiv \frac{v^2}{v_1^2} d_1 \quad (5.51)$$

By using Eq. (5.47) we find that d_{eq} is given by

$$d_{eq} = \left[\frac{1 + (A_2/A_1)\gamma_A}{1 + (A_2/A_1)} \right]^2 d_1 \quad (5.52)$$

By using this definition and noting that f_1 in Eq. (5.43) is the same as f in Eq. (3.2), observe that we have recovered the momentum equation used in the Quencher model with d_h replaced by d_{eq} . That is, the governing equations are now given by

Wall:

$$\rho_w C_w \frac{\partial T_w}{\partial t} = -\frac{h_w P_w}{A_w} (T_w - T) \quad (5.53)$$

Conductor/Helium:

$$\frac{\partial \rho}{\partial t} + \frac{\partial}{\partial x} \rho v = 0 \quad (5.54)$$

$$\frac{\partial p}{\partial x} = -\frac{f \rho |v| v}{2d_{eq}} \quad (5.55)$$

$$\rho \hat{C}_t \frac{\partial T}{\partial t} + \rho \hat{C}_h v \frac{\partial T}{\partial x} + \rho \hat{C}_\beta T \frac{\partial v}{\partial x} = \frac{h_w P_w}{A_c} (T_w - T) + \frac{\partial}{\partial x} \kappa_c \frac{\partial T}{\partial x} + S_c \quad (5.56)$$

$$p = p(\rho, T) \quad (5.57)$$

Recall that these equations are the starting point for the derivation of the MacQuench and eventually the analytic model. From this point we may use all of the analytic results developed in Chapter 4 simply by replacing d_h by d_{eq} everywhere except when evaluating h_w . The quantity h_w in the analytic theory is now given by $h_w = 4\kappa_h/d_1$.

5.4 Discussion and Results

In this section we demonstrate how the addition of a central hole effects various parameters during a quench. Consider the ITER conductor discussed in Chapter 4. For reference we summarize the parameters that characterize this conductor in Table 5.1. Note that we consider two different hydraulic diameters: “Dual” is used to denote the case with a central hole, and “Single” denotes the case where no central hole is present. Recall from Table 4.1 that for this conductor $d_1 = 0.5$ mm. Considering the case $A_2/A_1 \approx 0.15$, $d_2 \approx 5$ mm, and $f_1/f_2 \approx 2$, we find $d_{eq} \approx 2d_1 = 1$ mm. Thus, for the following analysis we consider the two cases: (1) Dual-Channel (Dual) with a hydraulic diameter of 1 mm, and (2) the Single-Channel (Single) with a hydraulic diameter of 0.5 mm.

Conductor Length (m)		530
Copper Area (mm ²)		390
Nb ₃ Sn Area (mm ²)		250
Helium Area (mm ²)		450
Wall Area (mm ²)		250
Wall Inner Perimeter (mm)		130
Initial Current (kA)		43
Detection Time (sec)		∞
Inlet Pressure (atm)		5
Outlet Pressure (atm)		5
Inlet Temp. (K)		5
Copper RRR		100
Hydraulic Diameter (mm)	Dual	1
	Single	0.5

Table 5.1: Characteristic Parameters of the ITER Coil.

Recall the long coil solution presented in chapter 4. The maximum temperature was found to be independent of the hydraulic diameter [see Eqs. (4.63) and (4.70)]. The asymptotic formulae for X_q and the maximum pressure are also given by

$$X_q \approx V_q t = 0.766 \left(\frac{2d_h}{f} \right)^{1/5} \left(\frac{RL_q \alpha_0 J^2}{c_0} \right)^{2/5} t^{4/5} \quad (5.58)$$

$$p \approx \left(\frac{R\rho_0 L_q}{2} \right) \frac{\alpha_0 J^2 t}{X_q} = 0.653 \left(\frac{fc_0^2 \rho_0^5}{2d_h} \right)^{1/5} (RL_q \alpha_0 J^2)^{3/5} t^{1/5} \quad (5.59)$$

These equations state that $X_q \propto d_h^{1/5}$ and $p \propto d_h^{-1/5}$. Thus, we expect the length of the normal region to be larger in the Dual case than that of the Single case. Observe the weak dependence of these variables with d_h .

In Figs. 5.2a–c we present numerical results from the MacQuench computer code, comparing the Dual and Single-Channel cases. Here the initial length of the normal region is chosen to be $L_q = 10$ m. It is evident in Fig. 5.2a, in accordance with the analytic theory, that the maximum temperature is very weakly dependent on the hydraulic diameter. The Dual case has a slightly higher maximum

temperature since the helium depletion, as discussed below, occurs more rapidly for this case than that of the Single-Channel. More rapid helium depletion gives rise to a lower total specific heat in the system as time increases. From Fig. 5.2b observe that at the end of 6 sec the length of the quench region $(2X_q)_{dual}$ for the Dual case is larger than that of the single channel $(2X_q)_{sing}$. While the opposite trend is observed for the maximum pressure in Fig. 5.2c. Specifically, at $t = 6$ sec we find

$$\frac{(2X_q)_{dual}}{(2X_q)_{sing}} = \frac{55.0}{48.3} = 1.14 \quad (5.60a)$$

$$\frac{p_{dual}}{p_{sing}} = \frac{42.9}{48.7} = 0.881 \quad (5.60b)$$

Let us now compare these results with the analytic predictions of Eqs. (5.58) and (5.59). From these equations, we find

$$\frac{(2X_q)_{dual}}{(2X_q)_{sing}} = \left[\frac{(d_h)_{dual}}{(d_h)_{sing}} \right]^{1/5} = 1.15 \quad (5.61a)$$

$$\frac{p_{dual}}{p_{sing}} = \left[\frac{(d_h)_{dual}}{(d_h)_{sing}} \right]^{-1/5} = 0.871 \quad (5.61b)$$

The agreement between Eqs. (5.60) and (5.61) is similar to the comparisons presented in Chapter 4.

In conclusion, our results have shown that a central hole in a CICC aids quench detection without increasing the potential for damage due to high temperature. Using the fact that the quench detection voltage V is proportional to X_q , we find that a central hole increases the ease of detection since the hydraulic diameter is increased and $X_q \propto d_h^{1/5}$. Also, the maximum quench pressures are decreased due to the addition of the central channel since $p \propto d_h^{-1/5}$. These results are clearly observed in Figs. 5.2a-c.

Chapter 5 References

- [1] L. Bottura and O. C. Zienkiewicz, "Quench analysis of large superconducting magnets, part I, model description," *Cryogenics*, vol. 32, p. 659, 1992.
- [2] L. Bottura and U. Mszanowski, "Transient thermal analysis of ITER CS and TF coils," NET Team Report N/R/0821/43/A, August 1993.

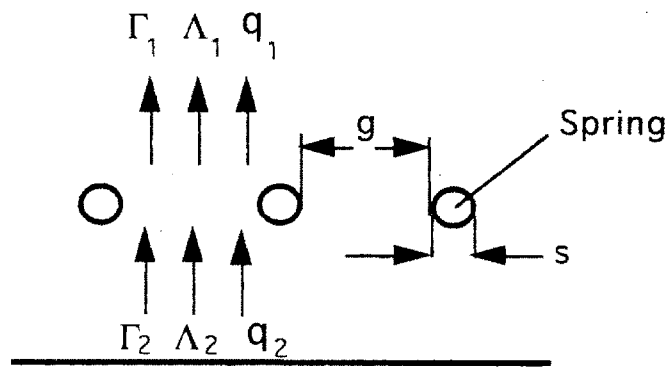
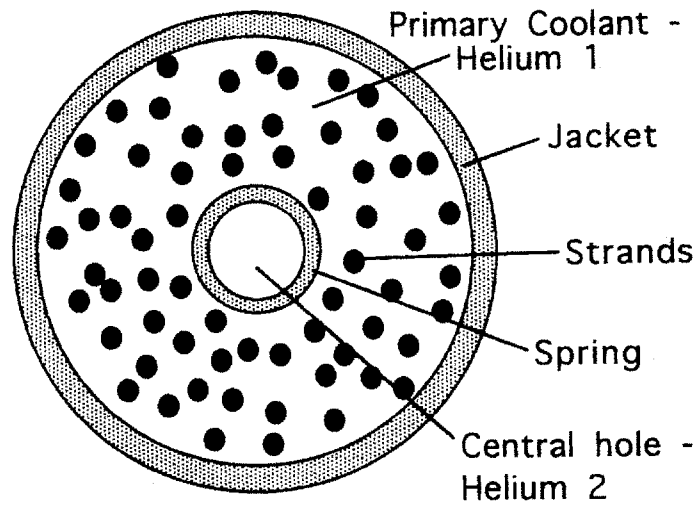


Figure 5.1: Schematic of the cross section of a Dual-Channel CICC.

Maximum Temperature vs. Time

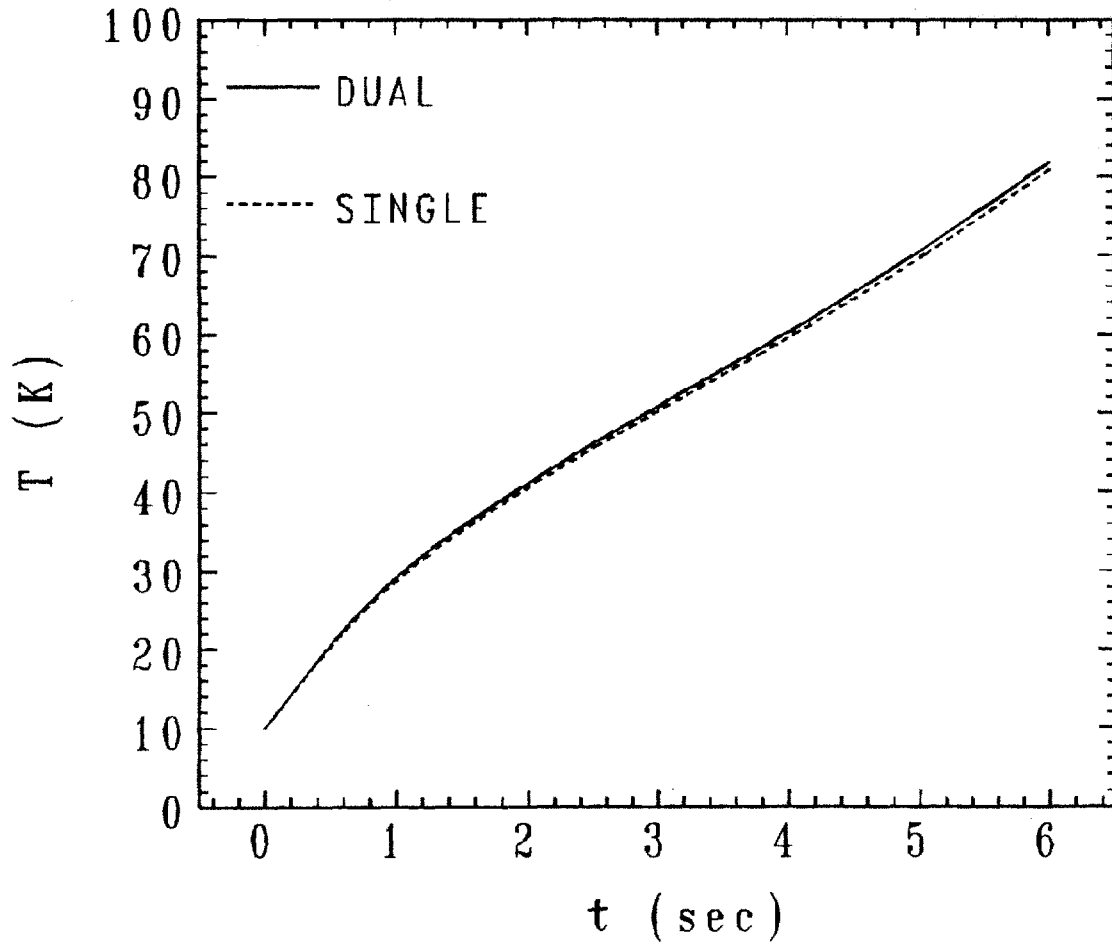


Figure 5.2a: Maximum temperature during quench in the ITER conductor. Here, "Dual" is used to denote the conductor with an additional central hole, and "Single" is the case where no central hole is present.

Length of Normal Region vs. Time

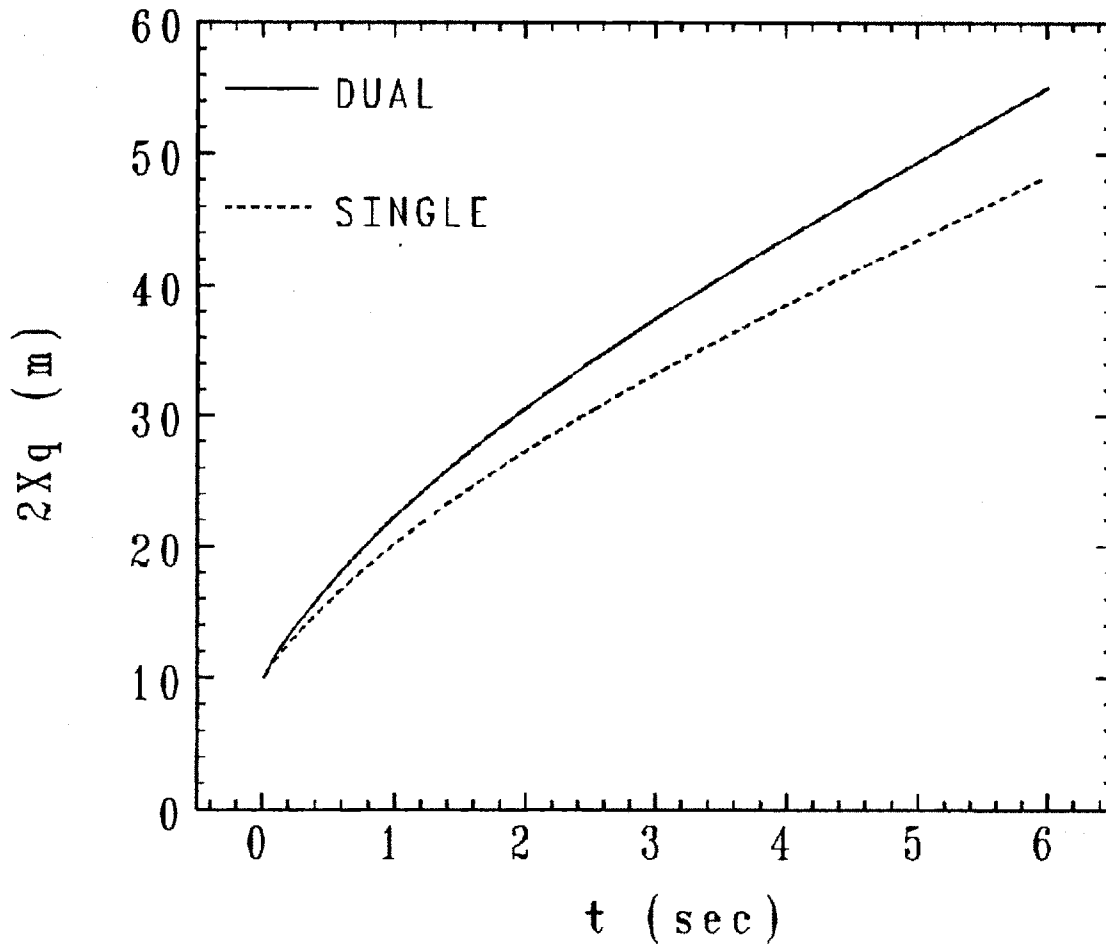


Figure 5.2b: Length of normal region during quench in the ITER conductor. Here, "Dual" is used to denote the conductor with an additional central hole, and "Single" is the case where no central hole is present.

Maximum Pressure vs. Time

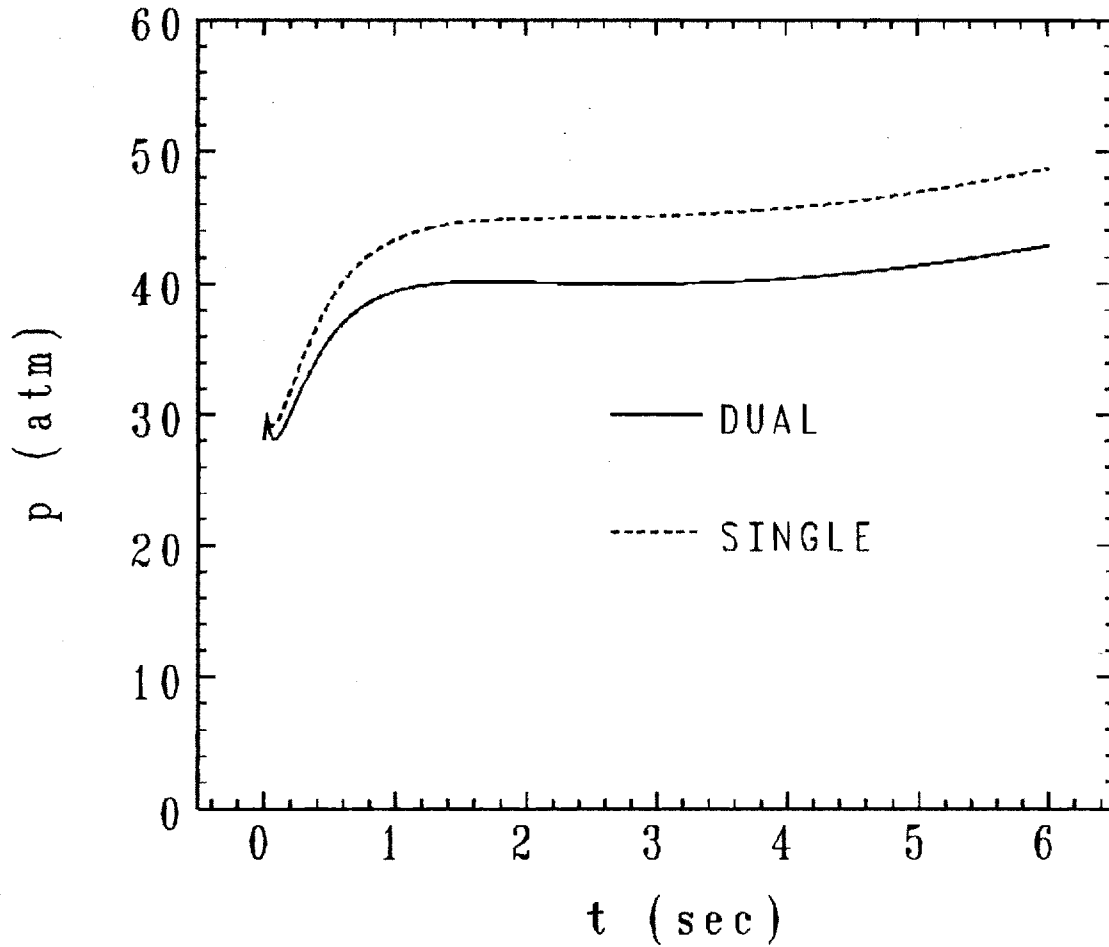


Figure 5.2c: Maximum helium pressure during quench in the ITER conductor. Here, "Dual" is used to denote the conductor with an additional central hole, and "Single" is the case where no central hole is present.

Chapter 6

Applications

Chapter 6. Applications

In this chapter we present some applications of the various tools developed in this thesis in order to study the quench behavior of certain conductors in their design phase.¹ Specifically, in Section 6.1 we present a study of the TF coil of the TPX machine and show how the heat transfer coefficient in the quench region effects the various parameters during a quench. In Section 6.2 we analyze the TF coil of the ITER machine, and show that this coil behaves in the “small pressure rise regime” for low values of the initial normal length L_q . For larger values of L_q this coil behaves as a long coil. In Sections 6.3 and 6.4 we consider two different prototype model coils that are primarily designed to test the behavior of the ITER coil. In these sections we discuss the regime of operation of these coils (short coil, long coil, etc.) and discuss the relevance of experimental measurements during a quench in these conductors, to the ITER coil.

Before proceeding with specific cases we point out a possible difficulty that exists in numerical studies of quench in CICC. This is an artificial Quench-Back behavior that is only a consequence of a lack of numerical convergence. That is, a “Numerical Quench-Back” occurs in certain non-converged solutions. Below, by way of a specific example we show the large discrepancies between a converged and a non-converged quench study.

We consider two quench studies performed by Quencher. Case (1) is a numerically converged study with an integration time step of $\Delta t = 0.005$ sec, and in case (2) we increase the time step by a factor of 20; $\Delta t = 0.1$ sec. The conductor under consideration is the Sultan conductor (see Section 6.3 and Table 6.7). In both studies we consider an initial normal length of $L_q = 2$ m, and a uniform B-field of 13 T. By way of four plots we show the large discrepancy between the two different numerical studies. In Figs. 6.1a and 6.1b we plot the conductor

¹ We wish to acknowledge E. A. Chaniotakis, J. McCarrick, and P. Wang for their help in performing many of the computer simulations presented in this chapter.

temperature profile (in x) for various times during the quench evolution. First, note the difference in the quench propagation velocity between the two cases. In the non-converged case (Fig. 6.1b) the quench propagates approximately 4 times faster than the converged case (Fig. 6.1a). Secondly, note how the boundary layer at the location of the quench front, as clearly observed in Fig. 6.1a, has disappeared in Fig. 6.1b.

In Fig. 6.2a we compare the time evolution of the maximum helium pressure between the two cases. Here, both the amplitude and the profiles are quite different in the two cases. In the non-converged case the helium pressure is approximately 4 times larger than the converged case. The final figure, Fig. 6.2b shows the time evolution of the normal length for the two cases. Again, both the amplitude and the slope of the two curves are quite different. Figures 6.1 and 6.2 clearly demonstrate the difference between a numerically converged quench simulation with a non-converged case.

Next we use the analytic theory of Chapter 4 to further study the quench behavior of the Sultan conductor. Specifically, we show that the analytic solution very closely approximates the converged solution presented in Fig. 6.2. To begin, note that the Sultan conductor falls in the short coil regime. Using the parameters given in Table 6.7 and Eq. (5.52) we first find

$$d_{eq} = \left[\frac{1 + (A_2/A_1)\gamma_A}{1 + (A_2/A_1)} \right]^2 d_1 = 1.74 \times 10^{-3} \text{ m} \quad (6.1)$$

where $\gamma_A \approx \sqrt{2d_2/d_1}$. Similarly, from Eq. (4.86), using $f = 0.07$, $L_q = 2$ m, $R = 2080$ J/kg-K, $L = 100$ m, $J = 1.33 \times 10^8$ A/m², $\alpha_0 \approx 5.5 \times 10^{-16}$ (see Fig. 4.3 with $A_w/A_c \approx 1$ and $B = 13$ T), and noting that $d_h = d_{eq}$, we find

$$V_q = \left(\frac{2d_h R}{fL} L_q \alpha_0 J^2 \right)^{1/3} \approx 2.7 \text{ m/sec.} \quad (6.2)$$

Using this value for V_q together with $c_0 \approx 200$ m/sec and $t_m = 6$ sec, we find

$$\frac{L^2 f V_q}{24 d_{eq} c_0^2 t_m} \approx 0.2 < 1 \quad (6.3a)$$

$$\frac{R \rho_0}{2 p_0} \frac{L_q \alpha_0 J^2}{V_q} \approx 1.9 > 1 \quad (6.3b)$$

and hence, from Fig. 4.5 the short coil criterion are satisfied. From the short coil solution [Eq. (4.85)] we have

$$2X_q \approx 2V_q t. \quad (6.4)$$

The linear time dependence of the normal length is clearly observed in Fig. 6.2b. Note that at $t = 6$ sec, from Eq. (6.4) we find

$$2X_q(t = 6 \text{ sec}) \approx 2 \times 2.7 \times 6 = 32.4 \text{ m}. \quad (6.5)$$

The value of $2X_q$ at $t = 6$ sec, observed in Fig. 6.2b is approximately 33 meters.

Next, we approximate the maximum pressure given by Eq. (4.71) as follows;

$$p \approx \frac{R \rho_0 L_q}{2} \frac{\bar{T}}{X_q} \approx \frac{R \rho_0 L_q}{2} \frac{\alpha_0 J^2}{V_q} \quad (6.6)$$

where $\rho_0 \approx 130 \text{ kg/m}^3$. Using this relation together with the parameters just discussed we find the helium pressure in the quench region is a constant with a value of $p \approx 9.7$ atm. The helium pressure observed in Fig. 6.2a is nearly a constant with a value of approximately 8 to 10 atmospheres. (The pressure decrease observed in Fig. 6.2a is predicted by the more general form of the analytic solution; see Fig. 4.9a)

From this type of comparisons and the curves presented in Figs. 6.1 and 6.2 we observe the importance of performing convergence studies, at least on an occasional basis. We now proceed to present certain converged quench studies of various conductors.

6.1 TPX Conductor

In this section we analyze the TF coil of the TPX machine. Specifically, we show the dependence of the various parameters on the heat transfer coefficient in the quench region. This coil was discussed in Chapter 3 (see section 3.2). There, we used Quencher to study the behavior of a complex quench scenario. Here, we use the MacQuench computer code to study a simpler quench event where the B-field is uniform with a value of 8.6 T (note that this is a simplification of the actual B-field in the TPX coil, as discussed in Chapter 3) and $L_q = 2$ m. For reference, we summarize the characteristic parameters of the TPX coil in Table 6.1

Conductor Length (m)	168.08
Copper Area (mm ²)	157.8
Nb ₃ Sn Area (mm ²)	76.97
Helium Area (mm ²)	127.0
Wall Area (mm ²)	192.0
Hydraulic Diameter (mm)	0.529
Wall Inner Perimeter (mm)	75.92
Initial Current (kA)	33.48
Detection Time (sec)	1
Dump Time (sec)	4
Inlet Pressure (atm)	7
Outlet Pressure (atm)	7
Inlet Temp. (K)	6.3
Copper RRR	75

Table 6.1: Characteristic Parameter of the TPX Coil.

The purpose of this study is to show how the maximum temperature in certain conductors, such as the TPX conductor depend on the value of the heat transfer coefficient. Recall that in Quencher we used a hybrid formula in order to approximate the heat transfer coefficient in both the laminar and turbulent regimes. In Chapter 4, we showed that the heat transfer coefficient in the outer region is generally given by the turbulent correlation. Due to the conditions in

the outer region, however, this quantity does not effect the important quench parameters (see the discussions on the outer region in Chapter 4). Next, we showed how the depletion of the helium density in the quench region results in a laminar flow of helium in this region. The value of the Nusselt number used in this region was $N_\ell = 4$. This value is used in both the laminar regime of the hybrid formula in Quencher, as well as in MacQuench and the analytic theory. Certain investigators [1,2] use a value of 8 for N_ℓ . As mentioned in Chapter 2, we do not understand the justification for this, and in fact from the references discussed in Chapter 2 we have concluded that $N_\ell = 4$ appears to be the most accurate value in the quench region. We now consider two studies. In case (1) we use $N_\ell = 4$ and in case (2) we consider $N_\ell = 8$.

In Fig. 6.3a and 6.3b we compare the maximum conductor and wall temperatures for the two cases, respectively. Observe that the maximum conductor temperature is approximately 20 K larger when $N_\ell = 4$. This is a result of less heat transfer to the conduit wall. The helium pressure in the quench region and the normal length propagation are much less effected by the value of N_ℓ . In Table 6.2 we summarize the important quench parameters for the two cases. Note that less than $\approx 6\%$ difference is observed in the helium pressure and 5% difference is observed in the normal length.

	$N_\ell = 4$	$N_\ell = 8$
T_{max} (K), conductor	158	139
T_{max} (K), wall	122	125
$p(t = 10 \text{ sec})$ (atm)	17	16
$2X_q(t = 10 \text{ sec})$ (m)	42	40

Table 6.2: Quench Characteristics of the TPX coil.

In conclusion, for conductors that have a large conduit wall ($A_w/A_c \sim 1$) the effect of N_ℓ is largest on the maximum temperatures during the quench. Furthermore, until more research is done on a more accurate value for N_ℓ we

believe the relation $N_l = 4$ should be used. This represents the most accurate relation obtained from the literature as of the time of this writing.

6.2 ITER Conductor

In this section we analyze the TF coil of the ITER machine. Specifically, we show (using both numerical and analytic results) that for small values of the initial quench region $L_q \lesssim 0.45$ m this conductor falls in the small pressure rise regime. For larger L_q this conductor behaves as a long coil. It is important to consider this behavior when conducting experiments to study the quench behavior of the ITER conductor. That is, both the small pressure rise and long coil regimes should be accessible during experiments on any ITER test coils.

Two quench protection simulations of the ITER TF coil are presented in this section. A 50 second quench initiated at the center of the conductor with two different values of L_q are considered. In case (1) we use $L_q = 0.2$ m and in case (2) we use $L_q = 20$ m. The complete list of the parameters that characterize this coil are presented in Table 6.3.

Conductor Length (m)	720
Copper Area (mm ²)	407.8
Nb ₃ Sn Area (mm ²)	271.0
Helium Area, Cable (mm ²)	$A_1 = 382.3$
Helium Area, Spring (mm ²)	$A_2 = 78.5$
Wall Area (mm ²)	128.8
Hydraulic Diameter, Cable (mm)	$d_1 = 0.675$
Hydraulic Diameter, Spring (mm)	$d_2 = 10$
Wall Inner Perimeter (mm)	123
Initial Current (kA)	46
Detection Time (sec)	1.0
Dump Time (sec)	20.0
Inlet Pressure (atm)	6
Outlet Pressure (atm)	4
Inlet Temp. (K)	5.5
Copper RRR	100

Table 6.3: Characteristic Parameters of the ITER Coil.

In Fig. 6.4a and 6.4b we compare the conductor temperature profile between the two cases, obtained by Quencher. Note the difference in the propagation speed between the two scenarios. This clearly demonstrates the dependence of the quench evolution on L_q . Also, observe the structure of the temperature profile in Fig. 6.4b as the quench propagates along the conductor. Such a profile is due to the spatial dependence of the B-field that gives rise to a spatially varying Joule Heating in the conductor. In Fig. 6.5a and 6.5b we compare the helium pressure profile between the two cases. In the case $L_q = 0.2$ m, the pressure rise during the quench is approximately given by $\Delta p \approx 2$ atm. Due to the small pressure rise, this quench scenario falls in the low pressure rise regime; $\Delta p/p_0 < 1$. Here, p_0 is taken as the average background pressure; $p_0 \approx 5$ atm. Observe that for $L_q = 20$ m the pressure rise is approximately 50 atm. In this case we start in the long coil regime and eventually fall in the short coil regime as the quench propagates along the conductor.

In Fig. 6.6a and 6.6b we compare the evolution of the maximum conductor and wall temperatures, between the two cases. In the case $L_q = 0.2$ m the helium density depletes more rapidly and thus the specific heat of the helium (ρC_h) has less of a contribution to the total specific heat. For this case, therefore, we observe higher maximum temperatures. The difference in the maximum conductor temperatures between the two scenarios is ≈ 14 %. Recall that in the analytic theory we neglect the contribution of the helium to the total specific heat and therefore can not quantitatively predict this difference. Also observe that in both cases the maximum conductor temperature is above 150 K, the current value of the maximum allowable temperature.

In summary, we present the important parameters during the quench evolution for the two cases in Table 6.4. Note that the maximum pressure often occurs at very early times due to the quench initiation. In such a case the analytic theory predicts $p_{max} \approx p(\rho_0, T_q)$ where T_q is the initial quench temperature at $t = 0^+$. For other cases when the maximum pressure occurs later during the quench evolution, we use the asymptotic analytic solution [Eq. (5.59)] to obtain

the pressure.

	$L_q = 0.2$ m	$L_q = 20$ m
T_{max} (K), conductor	189	166
T_{max} (K), wall	188	165
p_{max} (atm)	7	47
$2X_q$ (m)	35	266

Table 6.4: Quench Characteristics of the ITER coil.

Before proceeding with the analysis of two other conductors that are primarily designed to test the ITER coil we use the analytic theory of Chapter 4 to further analyze this conductor. First, using the parameters in Table 6.3 and Eq. (6.1) we find $d_{eq} = 2.1 \times 10^{-3}$ m. Second, consider a 5 second quench evolution ($t_m = 5$ sec) for a no-dump scenario. Using $f = 0.07$, $R = 2080$ J/kg-K, $J = 1.13 \times 10^8$ A/m², $\alpha_0 = 8.5 \times 10^{-16}$ (see Fig. 4.3 with $A_w/A_c \approx 0.2$ and $B = 13$ T), $c_0 \approx 200$ m/sec, $\rho_0 \approx 130$ kg/m³ and $p_0 = 5$ atm, from Eq. (4.113) we find

$$p_1/p_0 = 1.36 \left(\frac{f}{2d_h} \right)^{1/2} \frac{\rho_0 c_0}{p_0} t^{1/2} V_q^{3/2} \approx 3.2 L_q^{3/2} \quad (6.7)$$

where we have used V_q given by $V_q \approx R\rho_0 L_q \alpha_0 J^2 / 2p_0$. For p_1/p_0 to be less than one, we must therefore have $L_q \lesssim 0.45$ m. That is, for an initial normal length of less than 0.45 m, the ITER conductor behaves in the small pressure rise regime (during the first 5 seconds of a quench in a no-dump situation). For $L_q \gtrsim 0.45$ m, from Fig. 4.5 it is easily shown that this conductor lies in the long coil regime. Consider $L_q = 1$ m; from Eq. (4.95) we find

$$V_q(t = t_m) = 0.766 \left(\frac{2d_h}{f} \right)^{1/5} \left(\frac{RL_q \alpha_0 J^2}{c_0} \right)^{2/5} \frac{1}{t_m^{1/5}} \approx 2.1 \text{ m/sec} \quad (6.8)$$

Using this value, we find $L^2 V_q f / (24 d_{eq} c_0^2 t_m) = 7.6$, and $R\rho_0 L_q \alpha_0 J^2 / (2p_0 V_q) = 1.4$. From Fig. 4.5, we thus satisfy the long coil criterion. Similarly, for any

$L_q > 1$ m, using the same procedure we find that the ITER conductor behaves as a long coil. (The region $0.45 \lesssim L_q \lesssim 1$ m represents the transition from a small pressure rise to a long coil regime.) Observe that for $L_q \gtrsim 1$ m, this conductor behaves as a long coil. This fact must be considered when attempting to design any experiments in order to model this coil. Many of the scalings obtained from experiments on short coils are not appropriate for the ITER conductor.

6.3 ITER Model Coil

In this section we analyze the ITER Model coil (using both numerical and analytic results) in order to show that for small values of $L_q \lesssim 0.2$ m this conductor falls in the small pressure rise regime. For larger L_q this conductor behaves as a long coil. By properly adjusting the experimental values of L_q in this conductor, it is thus possible to model the quench behavior of the actual ITER conductor. That is, both small pressure rise and long coil regimes may be studied in this experiment by varying L_q in the ranges $L_q \lesssim 0.2$ m and $L_q \gg 0.2$ m.

The characteristic parameters of the ITER model coil are presented in Table 6.5. This coil will be constructed for testing features of the ITER coil discussed in the previous section. We use the MacQuench computer code to study the quench behavior of this conductor. Two cases are presented; (1) $L_q = 2.5$ m, and (2) $L_q = 10$ m. In both cases the magnetic field is uniform with a value $B = 9$ T.

Conductor Length (m)	750
Copper Area (mm ²)	408.1
Nb ₃ Sn Area (mm ²)	148.4
Helium Area, Cable (mm ²)	$A_1 = 342.9$
Helium Area, Spring (mm ²)	$A_2 = 78.6$
Wall Area (mm ²)	121
Hydraulic Diameter, Cable (mm)	$d_1 = 0.588$
Hydraulic Diameter, Spring (mm)	$d_2 = 10$
Wall Inner Perimeter (mm)	117.8
Initial Current (kA)	80
Detection Time (sec)	1.0
Dump Time (sec)	4.0
Inlet Pressure (atm)	5
Outlet Pressure (atm)	5
Inlet Temp. (K)	4.5
Copper RRR	100

Table 6.5: Characteristic Parameters of the ITER Model Coil.

In Fig 6.7 we present the time evolution of the maximum conductor temperature for the two cases. A difference of $\approx 10\%$ is observed between the two scenarios. This difference is due to the more rapid depletion of the helium for the case $L_q = 2.5$ m (see also the discussion in section 6.2 in regard to Fig. 6.6). In Fig. 6.8 we present the time evolution of the conductor and the wall temperatures for the case $L_q = 2.5$ m. The length of the normal region and the maximum pressure for the two cases are presented in Figs. 6.9a and 6.9b, respectively. Observe the decrease in the helium pressure for both cases as time increases. This results from the decrease in the current due to the dump. In Table 6.6 we summarize the important parameters during the quench for both cases.

	$L_q = 2.5$ m	$L_q = 10$ m
T_{max} (K), conductor	147	133
p_{max} (atm)	27	60
$2X_q$ (m)	80	140

Table 6.6: Quench Characteristics of the ITER Model Coil.

In order to analytically study this conductor, note that the model coil is a

long coil during the time scale of interest which we consider to be $t_m = 5$ sec. This is easily observed by first obtaining $d_{eq} = 2.1 \times 10^{-3}$ m. Using $f = 0.07$, $R = 2080$ J/kg-K, $J = 1.96 \times 10^8$ A/m², $\alpha_0 \approx 7.5 \times 10^{-16}$ (see Fig. 4.3 with $A_w/A_c \approx 0.2$ and $B = 9$ T), $c_0 \approx 200$ m/sec, $\rho_0 \approx 130$ kg/m³ and $p_0 = 5$ atm, and considering $L_q = 2.5$ m in Eq. (4.95) we find

$$V_q(t = t_m) = 0.766 \left(\frac{2d_h}{f} \right)^{1/5} \left(\frac{RL_q\alpha_0 J^2}{c_0} \right)^{2/5} \frac{1}{t_m^{1/5}} \approx 4.5 \text{ m/sec} \quad (6.9)$$

Using this value, we find $L^2 V_q f / (24 d_{eq} c_0^2 t_m) \approx 18$, and $R \rho_0 L_q \alpha_0 J^2 / (2 p_0 V_q) = 4.3$. From Fig. 4.5, we thus satisfy the long coil criterion. Similarly, for $L_q = 10$ m we can show that this coil behaves as a long coil.

The maximum pressures occur very early during the quench evolution ($t \lesssim 2$ sec) and we expect the analytic formula to apply during this time period (the current-dump during this period is not significant). From Fig. 6.9a we have

$$\left. \frac{p(L_q = 10)}{p(L_q = 2.5)} \right|_{t=2} = \frac{60}{27} = 2.22 \quad (6.10)$$

From Eq. (5.59) and the discussions presented in section 5.4, recall that the analytic theory predicts the maximum asymptotic pressure to be proportional to $L_q^{3/5}$. Thus, we have

$$\left. \frac{p(L_q = 10)}{p(L_q = 2.5)} \right|_{t=2} = \left(\frac{10}{2.5} \right)^{3/5} = 2.30 \quad (6.11)$$

This is a very good agreement between MacQuench and the analytic theory.

Since Fig. 6.9b constitutes a current-dump scenario, the value of $2X_q$ at the end of the simulation ($t = 30$ sec) given by the analytic theory may not directly apply to this case. For the sake of brevity, however, we use the analytic scaling to compare with the MacQuench simulation presented here. First, from Table 6.6 we have

$$\left. \frac{2X_q(L_q = 10)}{2X_q(L_q = 2.5)} \right|_{t=30} = \frac{140}{80} = 1.75 \quad (6.12)$$

From Eq. (5.58), on the other hand, the analytic theory predicts $2X_q$ to be proportional to $L_q^{2/5}$. Thus, from this equation we have

$$\left. \frac{2X_q(L_q = 10)}{2X_q(L_q = 2.5)} \right|_{t=30} = \left(\frac{10}{2.5} \right)^{2/5} = 1.74 \quad (6.13)$$

Interestingly, the analytic scaling continues to hold even though the current dump is well established. Observe that we have shown this coil to behave as a long coil only for a no-dump situation and for $t = 5$ sec. While, in Eq. (6.13) we use the long coil analytic solution for a much longer period and for a current-dump case. It is not trivial to analytically show whether at $t = 30$ sec and a decreasing J this coil behaves as a long coil. Here, by merely resorting to the outer region profiles obtained from MacQuench we conclude that the diffusion in this region does not fully take place during this scenario and hence the long coil solution continues to hold.

Using the same type of analysis as was done for the ITER conductor we may show that for $L_q \lesssim 0.2$ m, the model coil falls in the small pressure rise regime. For larger L_q this coils behaves as a long coil during the first 5 seconds of a quench event with no current-dump. This coil is thus a good test case for the thermal hydraulic behaviour of the actual ITER coil as long as the experimental value of L_q is varied to cover both the small pressure rise and the long coil regimes.

6.4 Sultan Conductor

In this section we analyze the Sultan coil (using both numerical and analytic results) in order to show that for small values of $L_q \lesssim 0.75$ m this conductor falls in the small pressure rise regime. For larger L_q this conductor behaves as a short coil. This suggests that the small pressure rise regime may be investigated by

using small values of L_q . However, the long coil regime is not experimentally accessible in this conductor.

The Sultan quench experiment is a means for testing certain features of the ITER coil. The parameters that characterize this coil are summarized in Table 6.7. The magnetic field is taken to be uniform at 13 Tesla.

Conductor Length (m)	100
Copper Area (mm ²)	60.3
Nb ₃ Sn Area (mm ²)	40.2
Helium Area, Cable (mm ²)	$A_1 = 55$
Helium Area, Spring (mm ²)	$A_2 = 19.6$
Wall Area (mm ²)	103
Hydraulic Diameter, Cable (mm)	$d_1 = 0.44$
Hydraulic Diameter, Spring (mm)	$d_2 = 5$
Wall Inner Perimeter (mm)	50
Initial Current (kA)	8
Detection Time (sec)	∞
Dump Time (sec)	no dump
Inlet Pressure (atm)	5
Outlet Pressure (atm)	5
Inlet Temp. (K)	4.5
Copper RRR	100

Table 6.7: Characteristic Parameters of the Sultan Experiment.

We have analyzed a quench scenario for this coil at the beginning of this chapter where we also showed that for $L_q = 2$ m this conductor behaves as a short coil. Here we present a quench case where the Sultan experiment falls in the small pressure rise regime. From the analytic theory, we find [Eq. (4.112)]

$$p_1/p_0 = \left(\frac{f\rho_0 L}{4d_h p_0} \right) V_q^2 \approx 1.8 L_q^2 \quad (6.14)$$

where we have used $V_q \approx R\rho_0 L_q \alpha_0 J^2 / 2p_0$. In order to have $p_1/p_0 < 1$ we must therefore have $L_q \lesssim 0.75$ m. That is, for $L_q \lesssim 0.75$ m, this coil behaves in the small pressure rise regime. Using a similar analysis as was presented at the beginning of this chapter, we also note that for $L_q \gtrsim 1$ m, this conductor falls in the short

coil regime. (Again, the region $0.75 \lesssim L_q \lesssim 1$ m represents the transition region from a small pressure rise to a short coil regime.) Thus, for a given quench event this conductor never behaves like a long coil. This fact must be considered when attempting to analyze the data from this experiment and trying to extrapolate this data to the ITER conductor.

We now present a quench study from Quencher, with $L_q = 0.25$ m. In Fig. 6.10a and 6.10b we present the conductor temperature profile and the time evolution of the maximum temperatures, respectively. Observe the difference between this case and Fig. 6.1a. In Fig. 6.11a and 6.11b we present the time evolution of the maximum pressure and $2X_q$, respectively. From Fig. 6.11a, in accord with the analytic predictions, this quench process lies in the small pressure rise regime; $p \approx p_0$ during the quench evolution. In Table 6.8 we summarize the behavior of the Sultan conductor during a quench for the two cases characterized by $L_q = 0.25$ m and $L_q = 2$ m.

	$L_q = 0.25$ m	$L_q = 2$ m
T_{max} (K), conductor	113	110
T_{max} (K), wall	68	70
p_{max} (atm)	12	20
$p(t = 6 \text{ sec})$ (atm)	5.4	8.4
$2X_q(t=6 \text{ sec})$ (m)	11	33

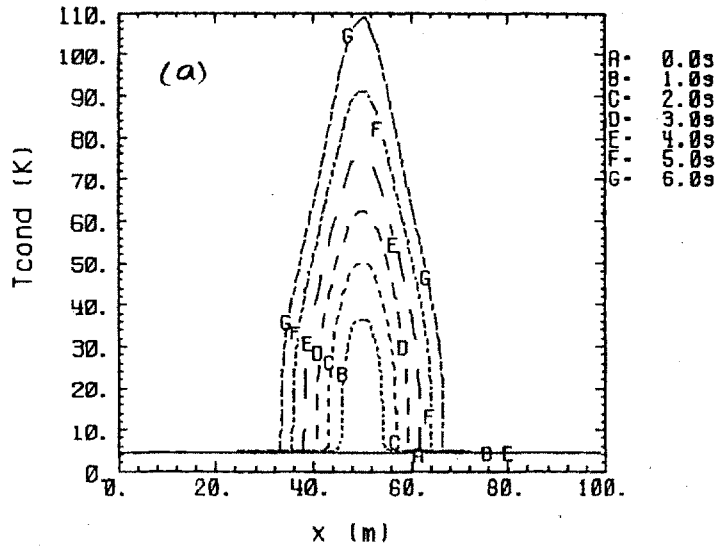
Table 6.8: Quench Characteristics of the Sultan Coil.

Chapter 6 References

- [1] Bottura, L., Zienkiewicz, O. C., *Quench Analysis of Large Superconducting Magnets Parts I and II*. Cryogenics, Vol. 32, No. 7, 1992.
- [2] Wong, R. L., Program CICC Flow and Heat Transfer in Cable-In-Conduit Conductors – Equations & Verification, Lawrence Livermore National Laboratory Internal Report, UCID 21733, May 1989.

Sultan Coil. Lq=2.0m. Small dt
Tcond vs. Position

Tc(max) -109.8 at t- 6.0, x- 49.9
Tc(min) - 4.5 at t- 6.0, x- 31.7



Tc(max) -107.9 at t- 6.0, x- 50.2
Tc(min) - 4.4 at t- 3.8, x- 0.0

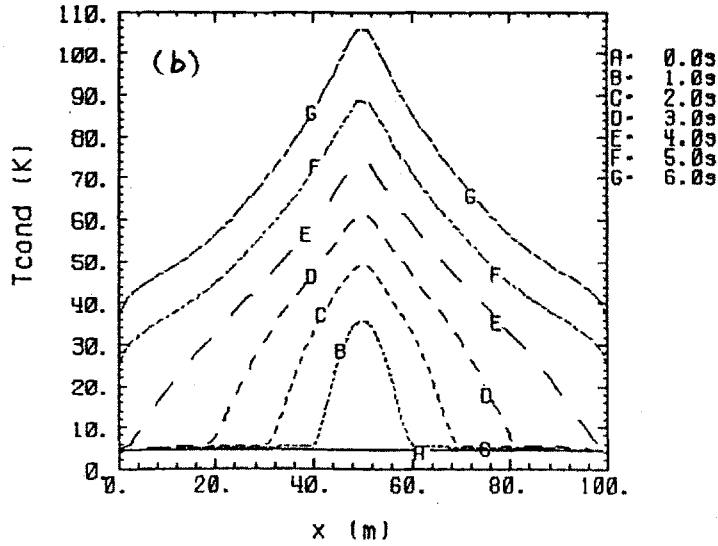


Figure 6.1: Conductor temperature profile during a quench in the Sultan conductor, at various time steps. (a) is a converged numerical study and (b) is a non-converged case.

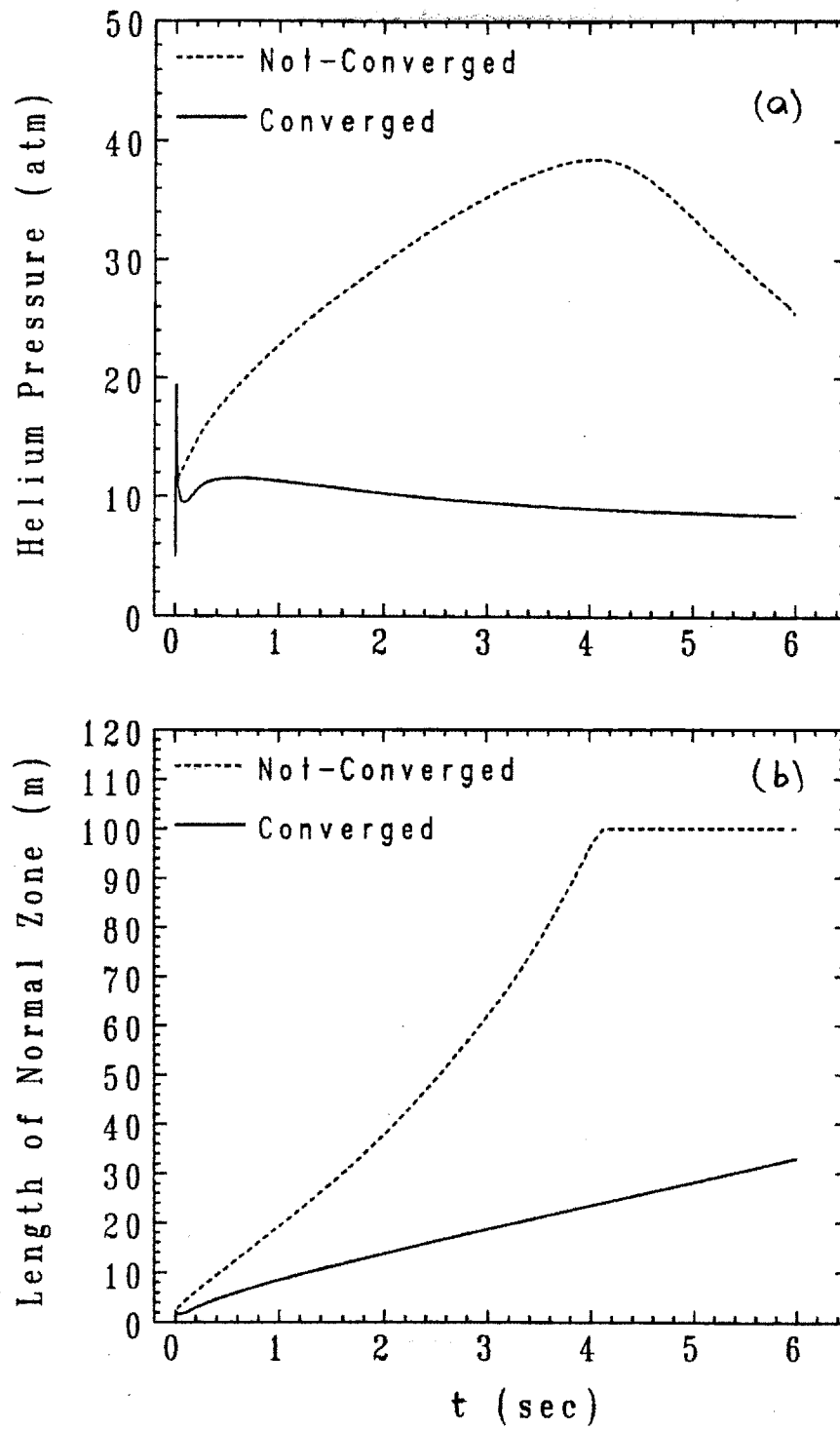


Figure 6.2: (a) Comparison of the maximum helium pressure between a converged and a non-converged numerical study of quench in the Sultan conductor. (b) Comparison of the normal length between the converged and the non-converged numerical studies.

Maximum Conductor Temperature Vs. Time

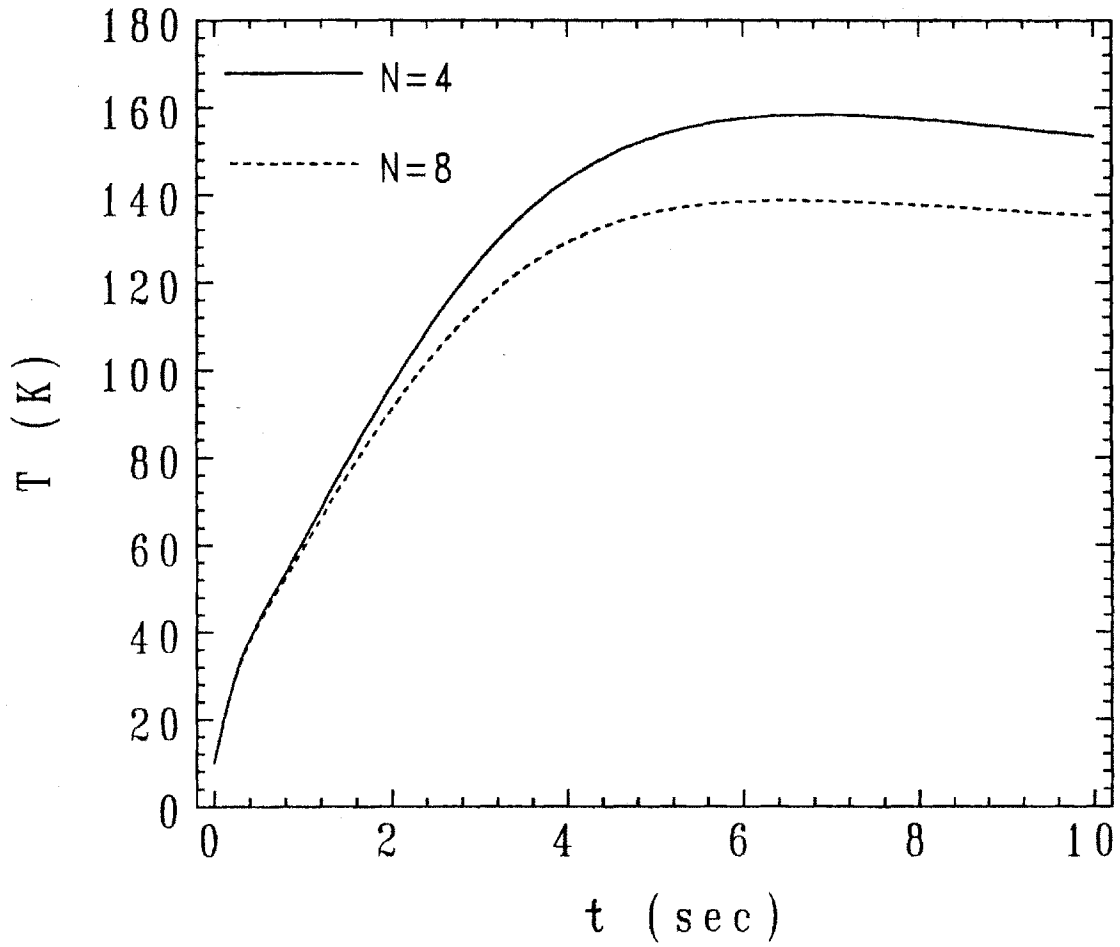


Figure 6.3a: Maximum conductor temperature for the two cases characterized by $N_\ell = 4$ and $N_\ell = 8$.

Maximum Wall Temperature Vs. Time

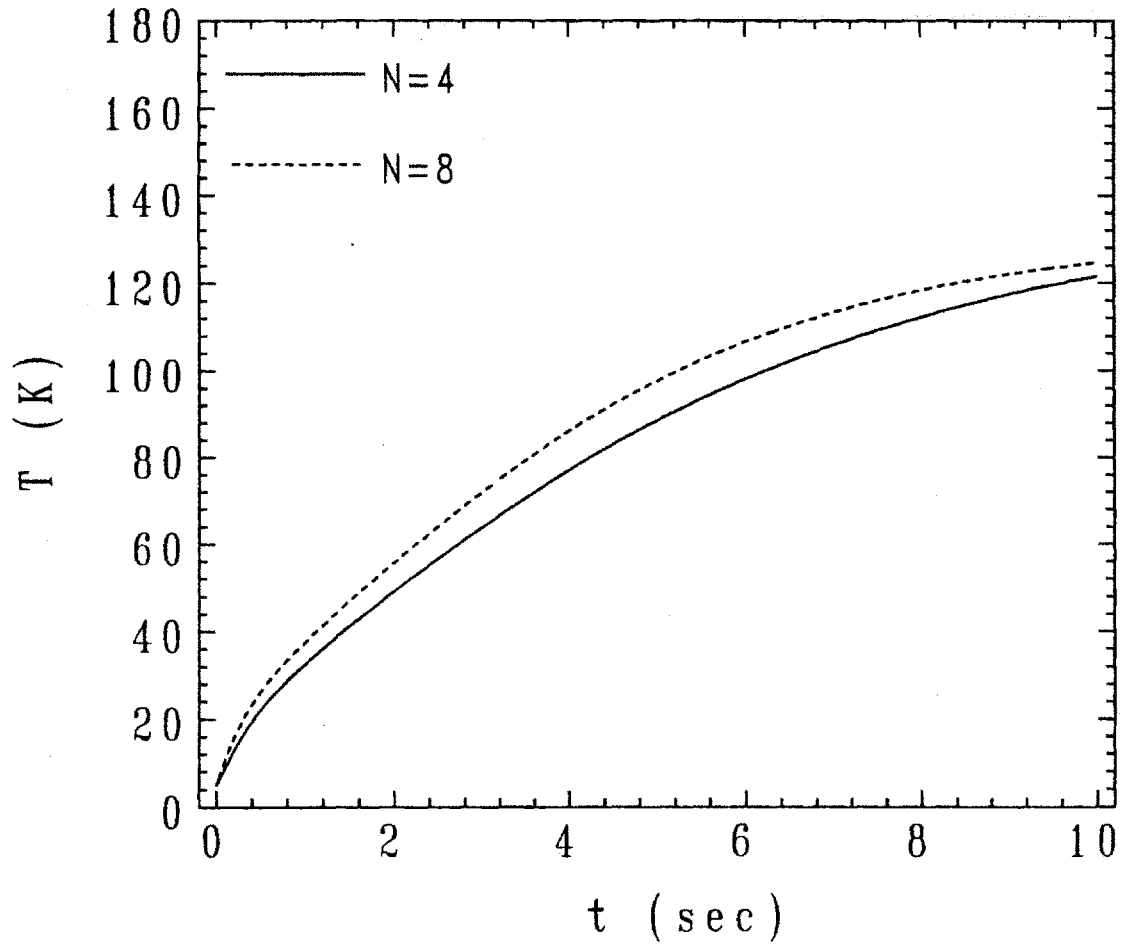
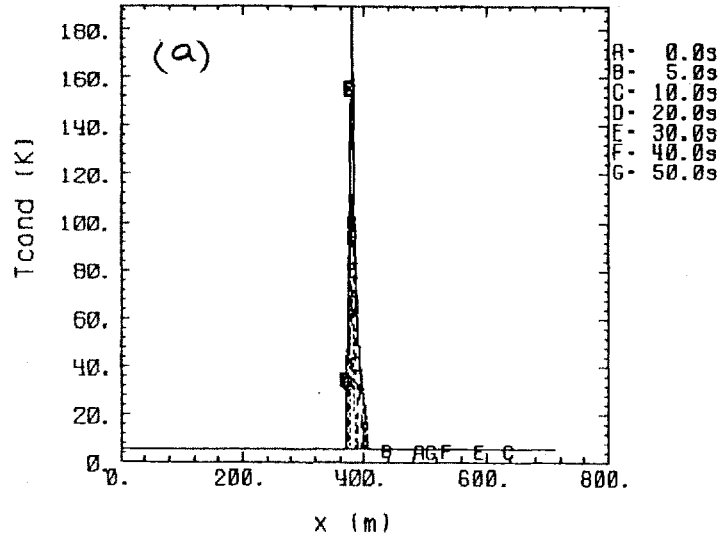


Figure 6.3b: Maximum wall temperature for the two cases characterized by $N_\ell = 4$ and $N_\ell = 8$.

ITER TF HF Coil, $L_q = 20\text{cm}$

Tcond vs. Position

Tc(max) -189.1 at t- 50.0, x- 300.3
Tc(min) - 5.2 at t- 3.2, x- 720.0



ITER TF HF Coil, $L_q = 20\text{m}$

Tcond vs. Position

Tc(max) -166.0 at t- 50.0, x- 300.3
Tc(min) - 5.2 at t- 0.1, x- 720.0

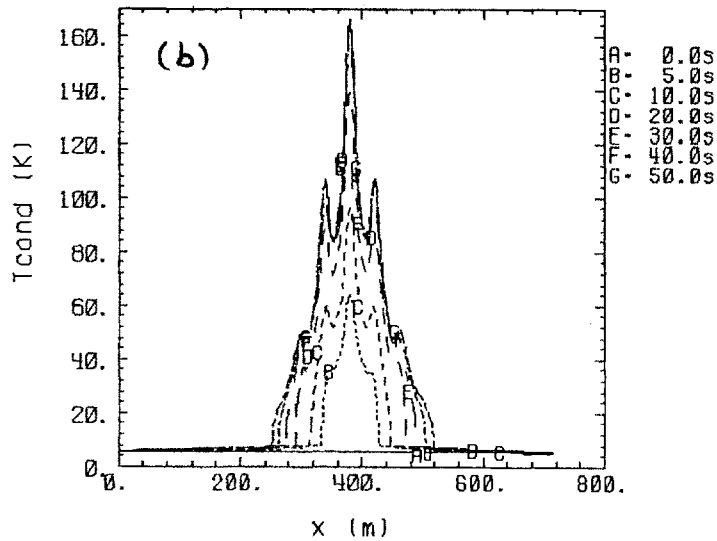
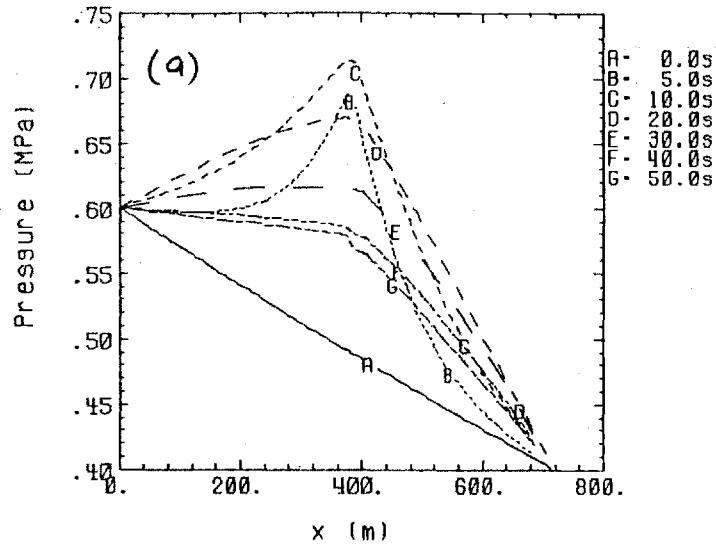


Figure 6.4: Conductor temperature profile at various time steps during a quench in the ITER coil. (a) $L_q = 0.2\text{ m}$ and (b) $L_q = 20\text{ m}$.

ITER TF HF Coil, $L_q = 20\text{cm}$

Pressure vs. Position

$P(\text{max}) = 0.7$ at $t = 0.0$, $x = 380.0$



ITER TF HF Coil, $L_q = 20\text{m}$

Pressure vs. Position

$P(\text{max}) = 4.7$ at $t = 6.2$, $x = 381.0$

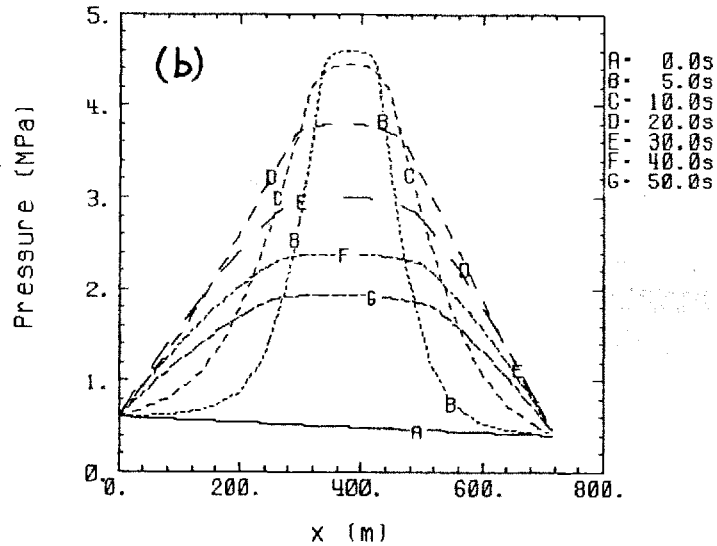
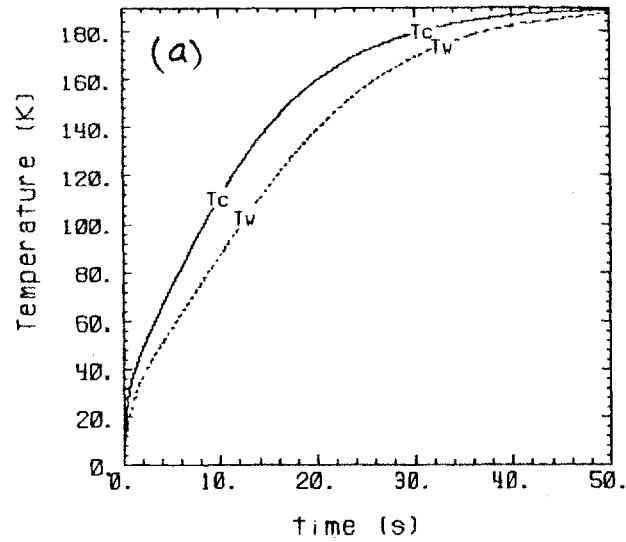


Figure 6.5: Helium pressure profile at various time steps during a quench in the ITER coil. (a) $L_q = 0.2\text{ m}$ and (b) $L_q = 20\text{ m}$.

ITER TF HF Coil, $L_q = 20\text{cm}$

Temperatures vs. Time

$T_c(\text{max}) = 189.1$ at $t = 50.0$, $x = 380.3$
 $T_w(\text{max}) = 187.5$ at $t = 50.0$, $x = 380.3$



ITER TF HF Coil, $L_q = 20\text{m}$

Temperatures vs. Time

$T_c(\text{max}) = 166.0$ at $t = 50.0$, $x = 380.3$
 $T_w(\text{max}) = 164.6$ at $t = 50.0$, $x = 380.3$

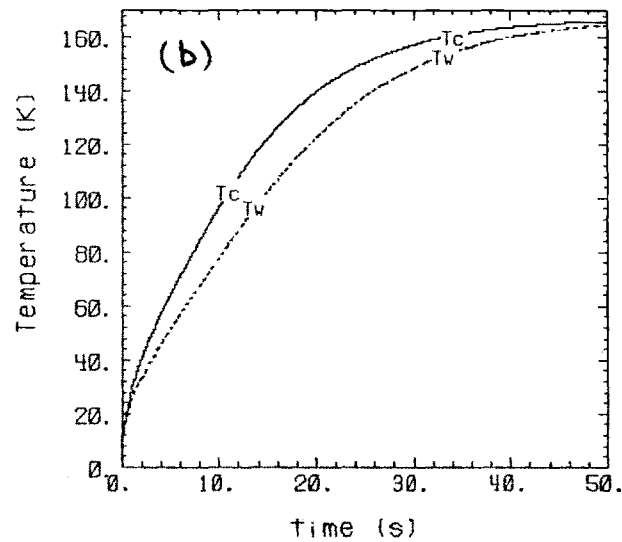


Figure 6.6: Time evolution of the maximum conductor and wall temperatures in the ITER coil. (a) $L_q = 0.2$ m and (b) $L_q = 20$ m.

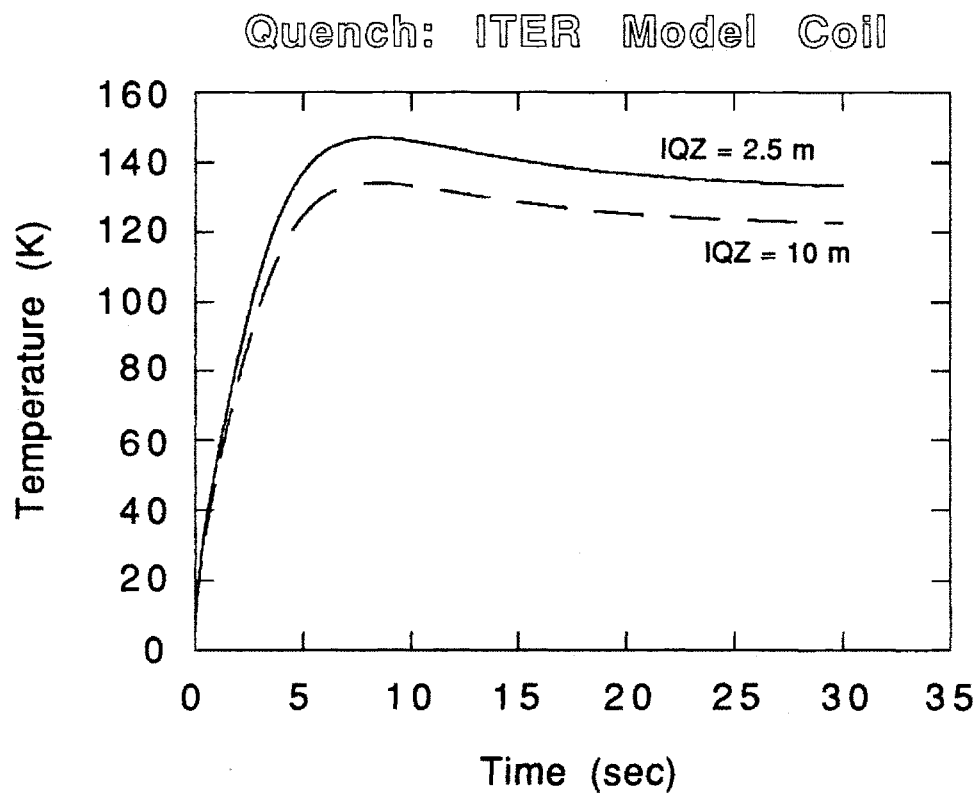


Figure 6.7: Time evolution of the maximum conductor temperature in the ITER model coil for the two cases characterized by $L_q = 2.5$ and 10 m. Note that here IQZ stands for L_q .

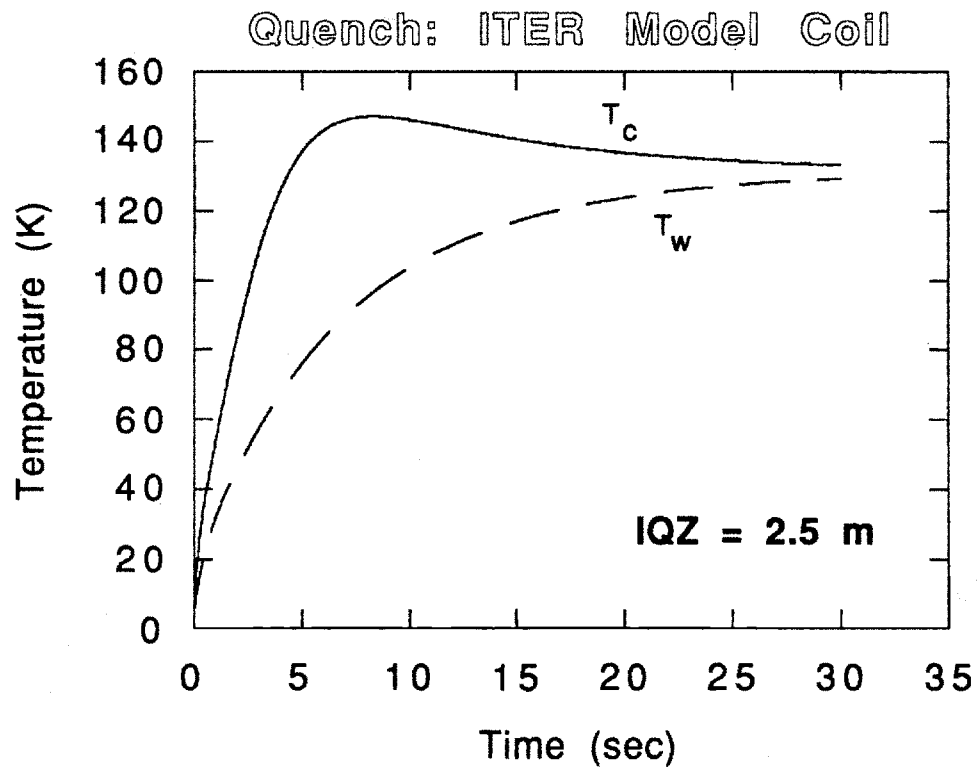


Figure 6.8: Time evolution of the maximum conductor and wall temperatures in the ITER model coil for the case $L_q = 2.5 \text{ m}$.

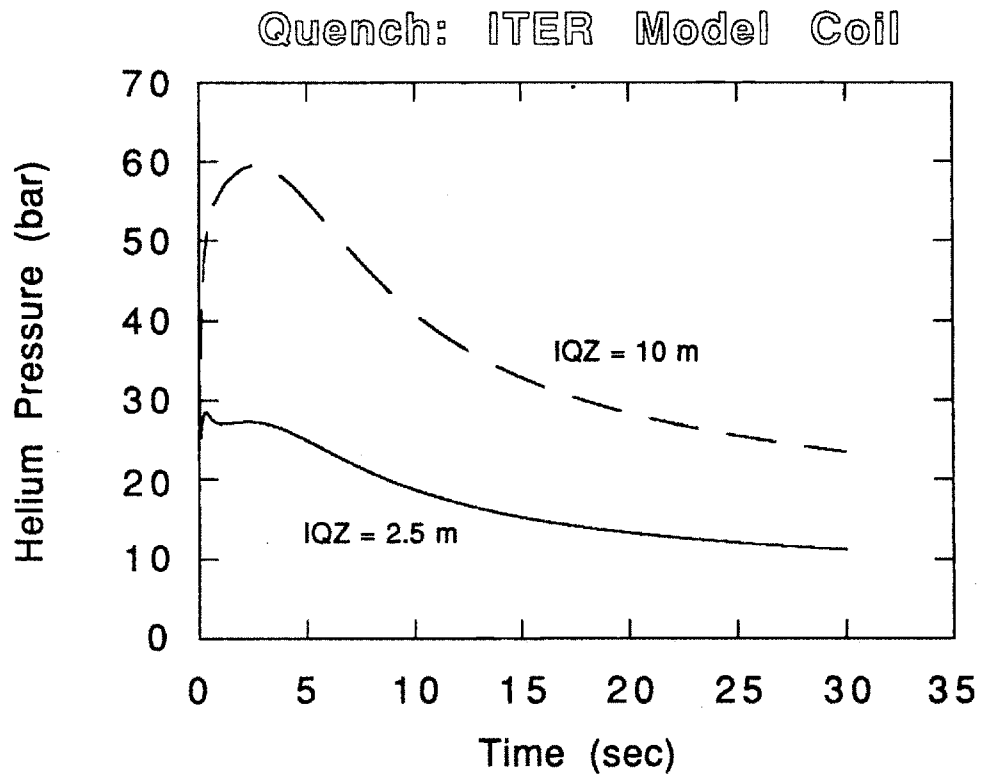


Figure 6.9a: Time evolution of the maximum helium pressure in the ITER model coil for the two cases characterized by $L_q = 2.5$ and 10 m. Note that here IQZ stands for L_q .

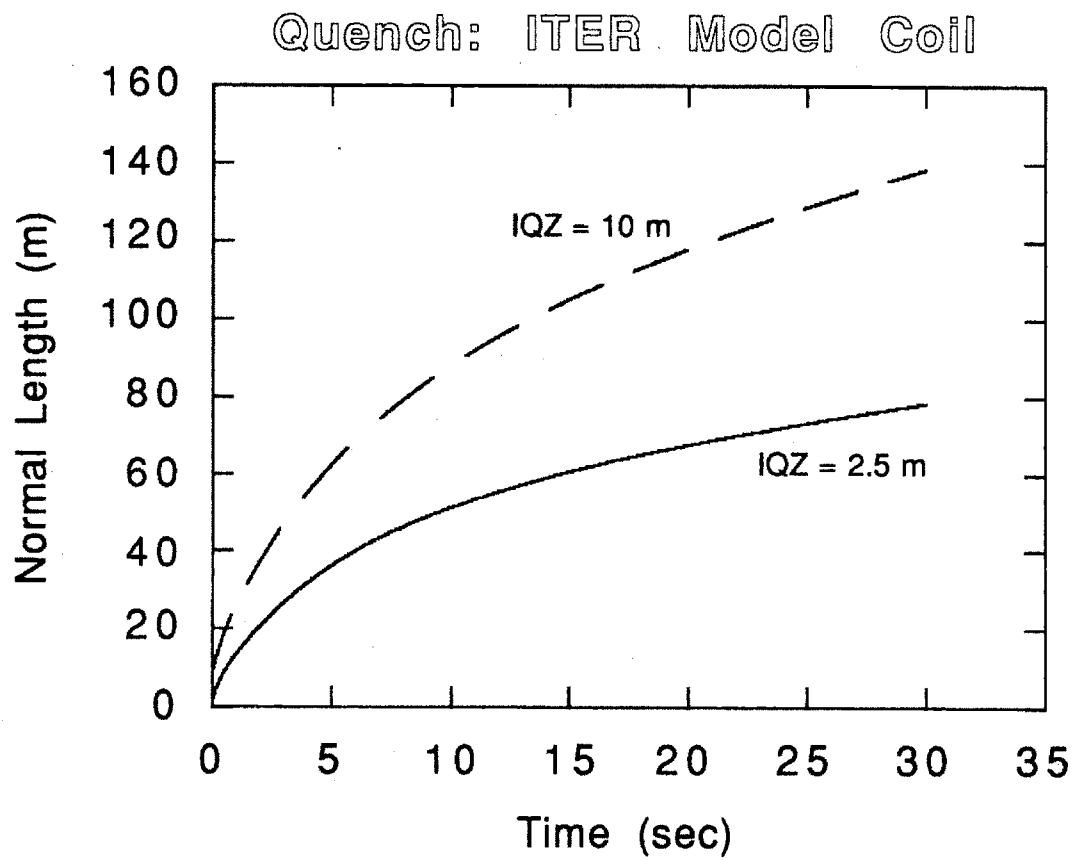


Figure 6.9b: Time evolution of the normal length in the ITER model coil for the two cases characterized by $L_q = 2.5$ and 10 m. Note that here IQZ stands for L_q .

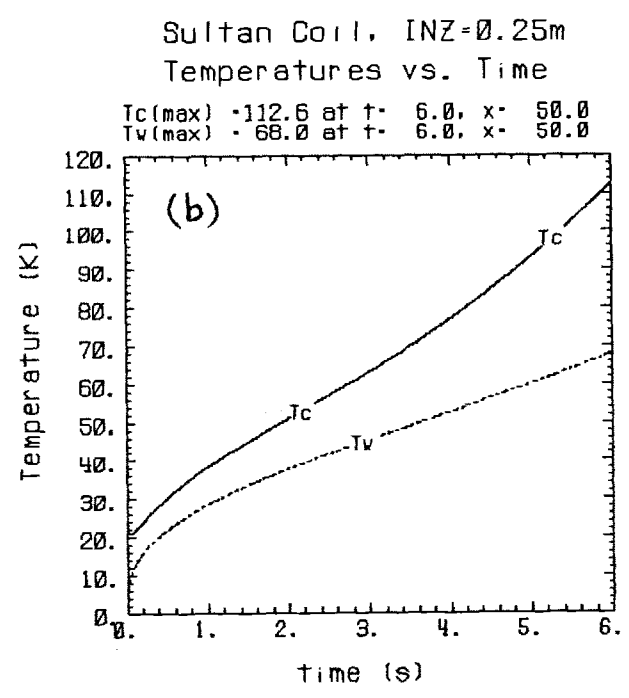
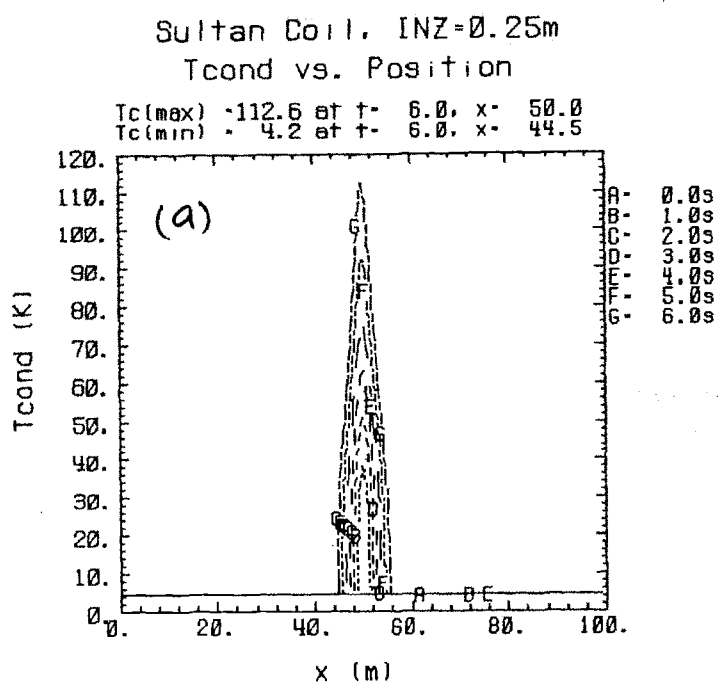
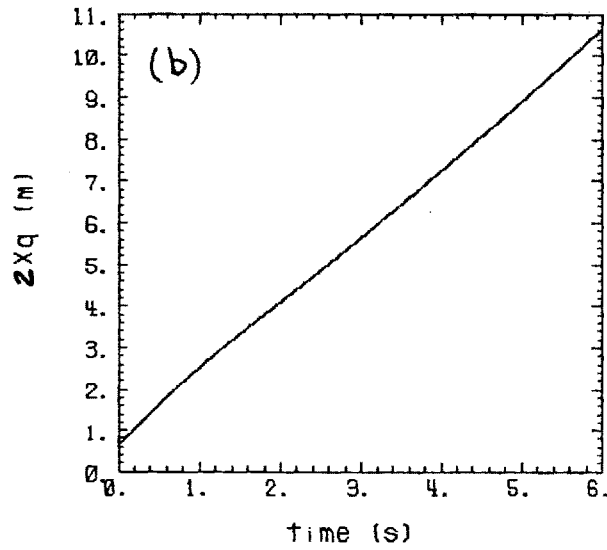


Figure 6.10: (a) Conductor temperature profile at various time steps during a quench in the Sultan coil. (b) Time evolution of the maximum conductor and wall temperatures during a quench event in this coil. In both (a) and (b), we have $L_q = 0.25$ m.

Sultan Coil, INZ=0.25m
 2Xq vs. Time
 Xq(max) = 10.6 at t = 6.0



Sultan Coil, INZ=0.25m
 Pressure vs. Time
 P(max) = 1.2 at t = 0.0, x = 50.0

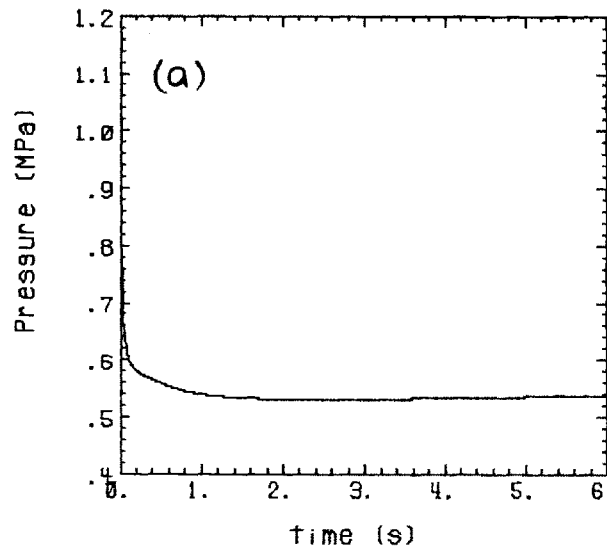


Figure 6.11: (a) Time evolution of the maximum helium pressure during a quench in the Sultan coil. (b) Time evolution of the normal length during a quench in this coil. In both (a) and (b), we have $L_q = 0.25$ m.

Chapter 7

Conclusions

Chapter 7. Conclusions

The problem of quench propagation is of great importance for safety considerations in the design of superconducting magnets. By concentrating on the specific problem of quench, it has been possible to derive a simplified model (for both a CICC and a dual-channel CICC) that is accurate, but avoids most of the numerical difficulties found in more general models. An efficient numerical implementation of the simplified quench model (Quencher) has been presented and shown to be computationally cost efficient. In order to study the behavior of quench for longer periods of time it is desirable to utilize a model such as Quencher because of the prohibitive amount of CPU time required to solve the general models. The results of Quencher have been shown to agree well with those of more general models as well as experimental data.

Further, well justified approximations have resulted in the MacQuench model (for both a CICC and a dual-channel CICC) that is shown to be very accurate and considerably more efficient than the Quencher model. The MacQuench code is suitable for performing quench studies on a personal computer, requiring only several minutes of CPU time. In order to perform parametric studies on new conductor designs it is required to utilize a model such as MacQuench because of the high computational efficiency of this model.

Finally, a set of analytic solutions for the problem of quench propagation in CICC (and a dual-channel CICC) has been presented. These analytic solutions represent the first such results that remain valid for the long time scales of interest during a quench process. Important analytic scalings are verified by direct comparisons with numerical as well as experimental data. The analysis presented in this thesis distinguishes three different regimes of operation for quench events. Each of these regimes is shown to have very distinct quench propagation characteristics. We suggest that to properly interpret any experimental results on quench propagation, it is vital to clearly distinguish the regime of operation of the experiment (e.g. distinction between long and short coils is specially important

in trying to extrapolate experimental test coil results to long coils).

7.1 Future Directions

In this section we point out some future research areas that we believe are important in the area of thermal-hydraulics in a CICC.

1. More comparisons of theory with experimental data. There are a number of experiments being designed to study the quench behavior of a CICC. These experiments provide a great opportunity for further verification of the theory presented in this thesis.
2. Correlations for the heat transfer coefficient in the quench region. Recall that the heat transfer coefficient in the quench region greatly effects certain parameters during a quench in a CICC. The value of this coefficient was obtained by using a Nusselt number of 4. This value corresponds to a steady-state flow of helium in a conduit. However, the quench process is by no means a steady-state scenario. More research is required to either further justify the value of the Nusselt number used or to obtain a more accurate correlation for this quantity during a quench process in a CICC.
3. Analysis of the nature of the boundary layer at the quench front. This boundary layer was only briefly discussed in this thesis. More knowledge about the mathematical structure of this boundary layer may greatly enhance the numerical techniques used to solve the Quencher model. Thus, more efficient numerical codes can result from such studies.
4. Extensive investigation of THQB. The process of Thermal Hydraulic Quench-Back was only briefly discussed in this thesis. The theoretical predictions presented here must be compared to numerical and experimental results. Furthermore, the process of THQB after its initiation remains to be understood.

5. Other relations than the constant pressure conditions used at the boundaries of the conduit need to be investigated. Often times the pressure at an inlet or an outlet may increase due to the finite size of the reservoir that is connected to the conduit.

Each of these areas presents a challenging new aspect of fluid dynamics and heat transfer in Cable-In-Conduit superconducting magnets and perhaps other systems that fall in the same fluid flow-regime.

Appendix A

Simple Application of Multiple Scale Expansion

Appendix A. Simple Application of Multiple Scale Expansion

In this appendix we illustrate the use of the multiple scale expansion by applying the idea to a simple problem. The problem considered here is that of heat conduction in a solid slab that is surrounded by a fluid with constant temperature T_b [1,2]. Figure A.1 depicts the system under consideration. We are interested in the case $d/L \ll 1$, and for this case we derive the 1-D heat equation, in the z -direction that determines the temperature distribution in the slab. A conventional method that is used to derive this 1-D equation [1,2] is to assume that the temperature distribution T in the slab is only a function of z and t . Heat balance on a section of length dz of the slab is then used to arrive at the 1-D equation. In doing this heat balance, the amount of heat leaving the control volume at the surface of the fin ($y = d$ and $y = -d$) is taken to be proportional to $h(T - T_b)$. Here h is the heat transfer coefficient that is used to describe the heat transfer to the fluid surrounding the slab. This procedure leads to the same 1-D equation as that derived in this appendix. The inadequacy of this procedure, however, lies in the fact that for a temperature distribution of the form $T(z, t)$, the heat loss from the surface which is given by $q_y = -\kappa \partial T / \partial y$ (evaluated at $y = d$), is zero since $T = T(z, t)$ is not a function of y . While, in performing the heat balance on the control volume it was assumed that q_y at $y = d$ is proportional to $h(T - T_b)$. Here, we show how this fallacy is resolved.

Since the domain extends from $-\infty \leq x \leq \infty$, the heat equation for the slab is given by

$$\rho C \frac{\partial T}{\partial t} = \kappa \frac{\partial^2 T}{\partial z^2} + \kappa \frac{\partial^2 T}{\partial y^2} + S \quad (\text{A.1})$$

where ρC and κ are the total specific heat and the thermal conductivity of the slab, respectively, and S is the prescribed heat source in the slab. For simplicity we assure that ρC , κ and S are constants. The initial and boundary conditions considered here are given by

$$T(y, z, t) \Big|_{t=0} = T_b \quad (\text{A.1a})$$

$$T(y, z, t) \Big|_{z=0} = T(y, z, t) \Big|_{z=L} = T_b \quad (\text{A.1b})$$

$$\frac{\partial T}{\partial y} \Big|_{y=0} = 0 \quad (\text{A.1c})$$

$$\kappa \frac{\partial T}{\partial y} \Big|_{y=d} = -h(T - T_b) \quad (\text{A.1d})$$

Again, for simplicity we assume that h and T_b are constants. Equation (A.1c) is the symmetry condition applied at $y = 0$, while Eq. (A.1d) is used to describe the heat loss to the surrounding fluid. We wish to consider Eq. (A.1) in the limit $d/L \ll 1$.

It proves useful to write Eq. (A.1) in a dimensionless form. In order to do this we define the following dimensionless parameters; $\hat{z} \equiv z/L$, $\hat{y} \equiv y/d$, $\hat{t} \equiv \kappa t / \rho C L^2$, and $\hat{S} \equiv L^2 S / \kappa$. In terms of these definitions, Eq. (A.1) becomes

$$\frac{\partial T}{\partial \hat{t}} = \frac{\partial^2 T}{\partial \hat{z}^2} + \frac{1}{\epsilon^2} \frac{\partial^2 T}{\partial \hat{y}^2} + \hat{S} \quad (\text{A.2})$$

together with the following normalized initial and boundary conditions

$$T(\hat{y}, \hat{z}, \hat{t}) \Big|_{\hat{t}=0} = T_b \quad (\text{A.2a})$$

$$T(\hat{y}, \hat{z}, \hat{t}) \Big|_{\hat{z}=0} = T(\hat{y}, \hat{z}, \hat{t}) \Big|_{\hat{z}=1} = T_b \quad (\text{A.2b})$$

$$\frac{\partial T}{\partial \hat{y}} \Big|_{\hat{y}=0} = 0 \quad (\text{A.2c})$$

$$\frac{\partial T}{\partial \hat{y}} \Big|_{\hat{y}=1} = -\beta(T - T_b) \quad (\text{A.2d})$$

where $\epsilon \equiv d/L$ and $\beta \equiv hd/\kappa$. It is important to note that for the class of problems under consideration the normalized variables \hat{z} , \hat{y} and \hat{t} are of order one.

The quantity $\beta(T - T_b)$, however, is assumed to be of order ϵ^2 in order for a 1-D description in the z -direction to remain valid. For $\beta(T - T_b) \sim 1$, it is more natural to scale the source term as a $1/\epsilon^2$ term and to consider a 1-D equation in the y -direction. The temperature is not normalized purposely, since in principle we wish to consider the case where $T \gg T_b$ (note that for this case β must be accordingly small such that $\beta(T - T_b) \sim \epsilon^2$). From Eq. (A.2) we observe that the heat flux in the y -direction is multiplied by a large term ($1/\epsilon^2$). In order for this equation to be balanced, the y -component of the heat flux must remain small (of order ϵ^2).

The natural way to exploit the small parameter ϵ that characterizes the problem is to expand the temperature $T(y, z, t)$ in the following perturbation series

$$T(\hat{y}, \hat{z}, \hat{t}) = T_0(\hat{y}, \hat{z}, \hat{t}) + T_2(\hat{y}, \hat{z}, \hat{t}) + \dots \quad (\text{A.3})$$

where $T_2/T_0 \sim \epsilon^2$. Using this expansion in Eq. (A.2) and collecting terms of the order of $1/\epsilon^2$ results in

$$\frac{\partial^2 T_0}{\partial \hat{y}^2} = 0 \quad (\text{A.4})$$

This equation is easily integrated to obtain

$$T_0 = C_1(\hat{z}, \hat{t}) \hat{y} + C_2(\hat{z}, \hat{t}) \quad (\text{A.5})$$

where C_1 and C_2 are as of yet unknown functions of \hat{z} and \hat{t} . Next we consider the leading order terms in Eqs. (A.2a-d) which leads to the initial and boundary conditions for T_0 ;

$$T_0(\hat{y}, \hat{z}, \hat{t}) \Big|_{\hat{t}=0} = T_b \quad (\text{A.6a})$$

$$T_0(\hat{y}, \hat{z}, \hat{t}) \Big|_{\hat{z}=0} = T_0(\hat{y}, \hat{z}, \hat{t}) \Big|_{\hat{z}=1} = T_b \quad (\text{A.6b})$$

$$\left. \frac{\partial T_0}{\partial \hat{y}} \right|_{\hat{y}=0} = 0 \quad (\text{A.6c})$$

$$\left. \frac{\partial T_0}{\partial \hat{y}} \right|_{\hat{y}=1} = 0 \quad (\text{A.6d})$$

Note that Eq. (A.6d) is a consequence of assuming $\beta(T - T_b) \sim \epsilon^2$. Using either Eq. (A.6c) or (A.6d) results in $C_1 = 0$. The zeroth order temperature is thus independent of \hat{y} ;

$$T_0 = T_0(\hat{z}, \hat{t}) \quad (\text{A.7})$$

The equation that determines the \hat{y} -dependence of T_2 is obtained by retaining terms of order ϵ^0 in Eq. (A.2);

$$\frac{\partial T_0}{\partial \hat{t}} = \frac{\partial^2 T_0}{\partial \hat{z}^2} + \hat{S} + \frac{1}{\epsilon^2} \frac{\partial^2 T_2}{\partial \hat{y}^2} \quad (\text{A.8})$$

The initial and boundary conditions for T_2 , in view of Eqs. (A.6a-d), are given by

$$T_2(\hat{y}, \hat{z}, \hat{t}) \Big|_{\hat{t}=0} = 0 \quad (\text{A.8a})$$

$$T_2(\hat{y}, \hat{z}, \hat{t}) \Big|_{\hat{z}=0} = T_2(\hat{y}, \hat{z}, \hat{t}) \Big|_{\hat{z}=1} = 0 \quad (\text{A.8b})$$

$$\left. \frac{\partial T_2}{\partial \hat{y}} \right|_{\hat{y}=0} = 0 \quad (\text{A.8c})$$

$$\left. \frac{\partial T_2}{\partial \hat{y}} \right|_{\hat{y}=1} = -\beta(T_0 - T_b) \quad (\text{A.8d})$$

The analysis of the leading order equation in the perturbation expansion reveals that T_0 is of the form given by Eq. (A.7). The actual dependence of T_0 on \hat{z} and \hat{t} must be determined from Eq. (A.8). This is done by integrating Eq. (A.8) with respect to \hat{y} over the domain $0 \leq \hat{y} \leq 1$. The result is given by

$$\frac{\partial T_0}{\partial \hat{t}} = \frac{\partial^2 T_0}{\partial \hat{z}^2} + \hat{S} + \frac{1}{\epsilon^2} \left. \frac{\partial T_2}{\partial \hat{y}} \right|_{\hat{y}=1} \quad (\text{A.10})$$

Using this relation together with Eq. (A.8d) we obtain the 1-D equation that determines the zeroth order temperature $T_0(z, t)$ in the slab;

$$\frac{\partial T_0}{\partial \hat{t}} = \frac{\partial^2 T_0}{\partial \hat{z}^2} + \hat{S} - \frac{1}{\epsilon^2} \beta(T_0 - T_b) \quad (\text{A.11})$$

or in the original variables

$$\rho C \frac{\partial T_0}{\partial t} = \kappa \frac{\partial^2 T_0}{\partial z^2} + S - \frac{h}{d}(T_0 - T_b) \quad (\text{A.11})$$

The initial and boundary conditions for $T_0(z, t)$ are now given by

$$T_0(z, t) \Big|_{t=0} = T_b \quad (\text{A.11a})$$

$$T_0(z, t) \Big|_{z=0} = T_0(z, t) \Big|_{z=L} = T_b \quad (\text{A.11b})$$

Equation (A.11) is the desired 1-D heat equation for the slab. In order for this equation to be an adequate representation of the physical temperature distribution in the fin, the following two conditions must be satisfied; 1) $\epsilon \ll 1$ and 2) $\beta(T_0 - T_b) \sim \epsilon^2$. It is interesting to note that condition 1 assures that the problem is nearly one dimensional in nature. However, condition 2 determines that, it is the z -direction that we care about.

We may now proceed to obtain T_2 by twice integrating Eq. (A.8) with respect to y , and using Eq. (A.11) to obtain

$$T_2(y, z, t) = -\beta(T_0 - T_b) \frac{\hat{y}^2}{2} = -\frac{hd}{2\kappa} \left(\frac{y}{d}\right)^2 [T_0(z, t) - T_b] \quad (\text{A.12})$$

where we have used the boundary and initial conditions, Eqs. (A.8a-d) to eliminate two integration constants in this process. This is the formal solution for $T_2(y, z, t)$. This solution has a parabolic profile in the y -direction. Note that in order to obtain T_2 , the function $T_0(z, t)$ must exist, and for this reason Eq. (A.11) is termed the "solvability" condition for T_2 . Knowing T_2 it is possible to calculate the heat flux as a function of y .

Appendix A References

- [1] Bird, R. B., Stewart, W. E., Lightfoot, E. N., Transport Phenomena, John Wiley & Sons, New York, 1960.
- [2] Eckert, E. R. G., Drake, Jr., R. M., Analysis of Heat and Mass Transfer, Hemisphere Publishing Corp., New York, 1987.

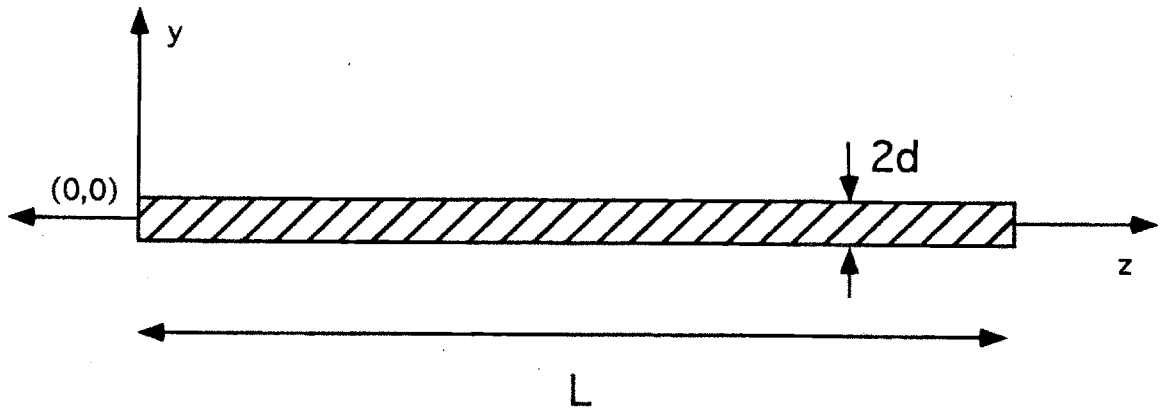


Figure A1: Schematic of the Slab Described by Eq. (A.1).

Appendix B

Consequences of
Neglecting Helium Inertia

Appendix B. Consequences of Neglecting Helium Inertia

In this appendix we consider the consequence of neglecting the inertia in the momentum conservation relation for the helium. Specifically, we discuss the effect of neglecting this term at some distance ($x = L$) away from the quench region ($x = 0$). The main aim of this analysis is to show that when the Mach number of the helium in the conduit remains small, the only consequence of neglecting inertia is that a time delay L/c (where c is the speed of sound in the helium) in observing the “action” is absent in the solution. However, the effect of this time delay is negligible for $t > L/c$.

To begin, consider a conduit of length L with a hydraulic diameter d_h . We analyse a model-problem in which at time $t = 0$ the helium in the conduit is stagnant with a temperature T_0 and density ρ_0 , and where at $t = 0^+$ the helium velocity at $x = 0$ is set to $v = v_0 = \text{constant}$. The effect of setting the velocity equal to v_0 at one end of the conduit is to initiate the flow of helium, such that as $t \rightarrow \infty$ the helium velocity will be non-zero everywhere in the channel. We consider the problem to be adiabatic (constant entropy) which corresponds to the case where no external heat sources are present and the viscous dissipation in the energy conservation relation is neglected. Furthermore, we consider the case where v_0 is small compared to the sound speed c (this is always the case for quench problems). Thus we do not expect large variations in any of the physical quantities. This justifies expanding the helium density and velocity in the following form

$$\rho = \rho_0 + \rho_1(x, t) + \dots \quad (B.1a)$$

$$v = v_1(x, t) + \dots \quad (B.1b)$$

where $\rho_1/\rho_0 \ll 1$ and similarly v_1 is a first order quantity.

In terms of the above expansion, the leading order mass and momentum conservation relations are given by

$$\frac{\partial \rho_1}{\partial t} + \rho_0 \frac{\partial v_1}{\partial x} = 0 \quad (B.2)$$

$$\rho_0 \frac{\partial v_1}{\partial t} = -c_0^2 \frac{\partial \rho_1}{\partial x} - \rho_0 \nu v_1 \quad (B.3)$$

where c_0 is the speed of sound in the background (T_0, ρ_0) conditions. We have eliminated the helium pressure in terms of the helium density by using the constant entropy condition. Note that for simplicity we have also used a different form of the friction force. We assume that the friction force is given by $\rho \nu v$, where ν is a constant (this assumption is necessary in order to obtain exact analytic solutions to the problem). This is similar to what would be obtained in a highly laminar flow of helium in the conduit where $f \propto 1/v$. Such a laminar flow is unrealistic however, since very low velocities of supercritical helium give rise to turbulence (the helium viscosity is very small [1]). Therefore it is more accurate to estimate ν as follows;

$$\nu \approx \frac{f v_0}{2d_h} \quad (B.4)$$

where f is the friction factor assumed to be a constant given by $f = 0.07$, and v_0 is the helium velocity at $x = 0$. Equations (B.2) and (B.3) represent two equations for the unknowns ρ_1 and v_1 .

By simple manipulation of Eqs. (B.2) and (B.3) we may eliminate ρ_1 to obtain a single equation for v_1 . This equation is given by

$$\frac{\partial^2 v_1}{\partial t^2} + \nu \frac{\partial v_1}{\partial t} = c_0^2 \frac{\partial^2 v_1}{\partial x^2} \quad (B.5)$$

The appropriate initial and boundary-conditions for v_1 are given by

$$v_1(x, t = 0) = 0 \quad (B.6a)$$

$$\frac{\partial v_1}{\partial t}(x, t = 0) = 0 \quad (B.6b)$$

$$v_1(x = 0, t) = v_0 \quad (B.6c)$$

$$v_1(x \rightarrow \infty, t) = 0 \quad (B.6d)$$

where for simplicity in Eq. (B.6d) we consider a semi-infinite domain. In order to study the system at some distance L down stream, we simply evaluate the solution at $x = L$. Observe that we are led to seek the solution of a linear partial differential equation. The quantity ρ_1 may be obtained from Eq. (B.2) once v_1 is determined. Even though a series of simplifications have been introduced in arriving at Eq. (B.5), nevertheless, this equation contains all the physics of the helium flow in regions away from the quench zone including inertial effects. In the remainder of this appendix we solve this equation analytically and show how the solution differs from what would be obtained if helium inertia (the first term on the left-hand side of Eq. (B.5)) were to be neglected.

We next consider a normalization of Eq. (B.5). We define $\tau \equiv v_0 t/L$, $\eta \equiv x/L$, and $v \equiv v_1/v_0$ (note that for convenience we have redefined v as the normalized velocity variable). In terms of these definitions we rewrite Eq. (B.5) as follows

$$M^2 \frac{\partial^2 v}{\partial \tau^2} + F \frac{\partial v}{\partial \tau} = \frac{\partial^2 v}{\partial \eta^2} \quad (B.7)$$

where $M \equiv v_0/c_0$ is the Mach number and $F \equiv v_0 L \nu / c_0^2$ represents the friction force. The initial and boundary-conditions in the normalized variables are given by

$$v(\eta, \tau = 0) = \frac{\partial v}{\partial \tau}(\eta, \tau = 0) = 0 \quad (B.8a)$$

$$v(\eta = 0, \tau) = 1 \quad (B.8b)$$

$$v(\eta \rightarrow \infty, \tau) = 0 \quad (B.8c)$$

Equation (B.7) can be solved by Laplace transform methods. After some standard manipulation of Laplace transforms [2] we find

$$v(\eta, \tau) = \left[1 - \int_{\tau}^{\infty} g(\eta, \xi) d\xi \right] H(\tau - M\eta) \quad (B.9)$$

where H is the Heaviside step function ($H(x) = 0$ for $x < 0$ and $H = 1$ for $x > 0$). The function g is given by

$$g(\eta, \tau) = \frac{F\eta}{2M} \frac{I_1 [\epsilon^{-1}(\tau^2 - M^2\eta^2)^{1/2}]}{(\tau^2 - M^2\eta^2)^{1/2}} e^{-\tau/\epsilon} \quad (B.10)$$

where $\epsilon \equiv 2M^2/F$. The function I_1 is the Modified Bessel function of order one.

Before proceeding to further analyze Eq. (B.7) we consider the solution of Eqs. (B.2) and (B.3) in the case where helium inertia is neglected. This corresponds to setting the first term on the left-hand side of Eq. (B.7) to zero. The normalized helium velocity in this case is again easily obtained by Laplace transform methods, and is given by

$$v_f = 1 - \frac{2}{\sqrt{\pi}} \int_0^{\sqrt{\frac{F}{4\tau}}\eta} e^{-\xi^2} d\xi \quad (B.11)$$

We use the subscript f to denote the solution of Eq. (B.7) for the case where inertia is set to zero.

We now make direct comparisons between v and v_f , as given by Eqs. (B.9) and (B.11), respectively. We assume that $L = 100$ m and $d_h = 10^{-3}$ m. These values are typical of a CICC. The quantity v_0 is generally of the order of 1 m/sec, and $c_0 \approx 200$ m/sec. Using these values, we find $F \approx 0.1$. Thus we consider the case $F = 0.1$ and $\eta = 1$ (or $x = L$) to compare Eqs. (B.9) and (B.11) for various values of M . In Fig. B.1a-c we plot $v(\eta = 1, \tau)$ and $v_f(\eta = 1, \tau)$ versus τ (or time) for $M = 0.2, 0.1$ and 0.05 , respectively. Note that during most quench events in a CICC we generally have $M \sim 0.01$, and the case $M = 0.2$ which corresponds to a helium velocity of 40 m/sec is almost never observed. These figures clearly demonstrate that for $\tau > M$ ($t > L/c_0$) the solution v_f closely

approximates v . For $\tau < M$ ($t < L/c_0$) we observe that v_f is finite which is physically impossible since the sound wave has not yet reached the end of the channel. Thus we use the solution v_f with an understanding that for $t < L/c_0$ the actual flow velocity is zero. Note also that the total mass (m) leaving the conduit is very well approximated (for $t > L/c_0$) by the solution v_f , despite the difference observed in the period $0 < t < L/c_0$. The quantity m is proportional to the area under the curve of v versus τ , and as observed in Fig. B.1 this area is approximately the same (for $t > L/c_0$) as calculated by either v or v_f .

In order to further demonstrate the accuracy of v_f , we consider some analytic manipulation of Eq. (B.9). For the case $\eta = 1$, $\tau > M$, and noting that $\epsilon \ll 1$ we may approximate Eq. (B.9) as follows

$$v \approx v_f + \frac{M^2}{F^2} \int_0^{\sqrt{\frac{F}{4\tau}}} h(\xi) d\xi \quad (B.12)$$

where the function h is given by

$$h(\xi) = e^{-\xi^2} (3\xi^2 + 12\xi^4 + 8\xi^6) \quad (B.13)$$

In deriving Eq. (B.12) we have used the asymptotic expansion of $I_1(z)$ for large z [2], together with the appropriate Taylor expansion of some of the other terms. It is clear from this equation that v_f and v differ (for $t > L/c_0$) by terms of the order of M^2/\sqrt{F} ;

$$v = v_f + O\left(\frac{M^2}{\sqrt{F}}\right) \quad (B.14)$$

For $M^2 \ll \sqrt{F}$ friction dominates inertia. Furthermore, Eq. (B.12) states that as time increases v_f becomes increasingly more accurate in approximating v . This is most evident in Fig. B.1a.

Appendix B References

- [1] Van Sciver, S. W., Helium Cryogenics, Plenum Press, New York, 1986, pp. 382-395
- [2] Abramowitz, M., Stegun, I. A., Handbook of Mathematical Functions, Dover Publishing Inc., New York, 1972, pp. 1020-1030.

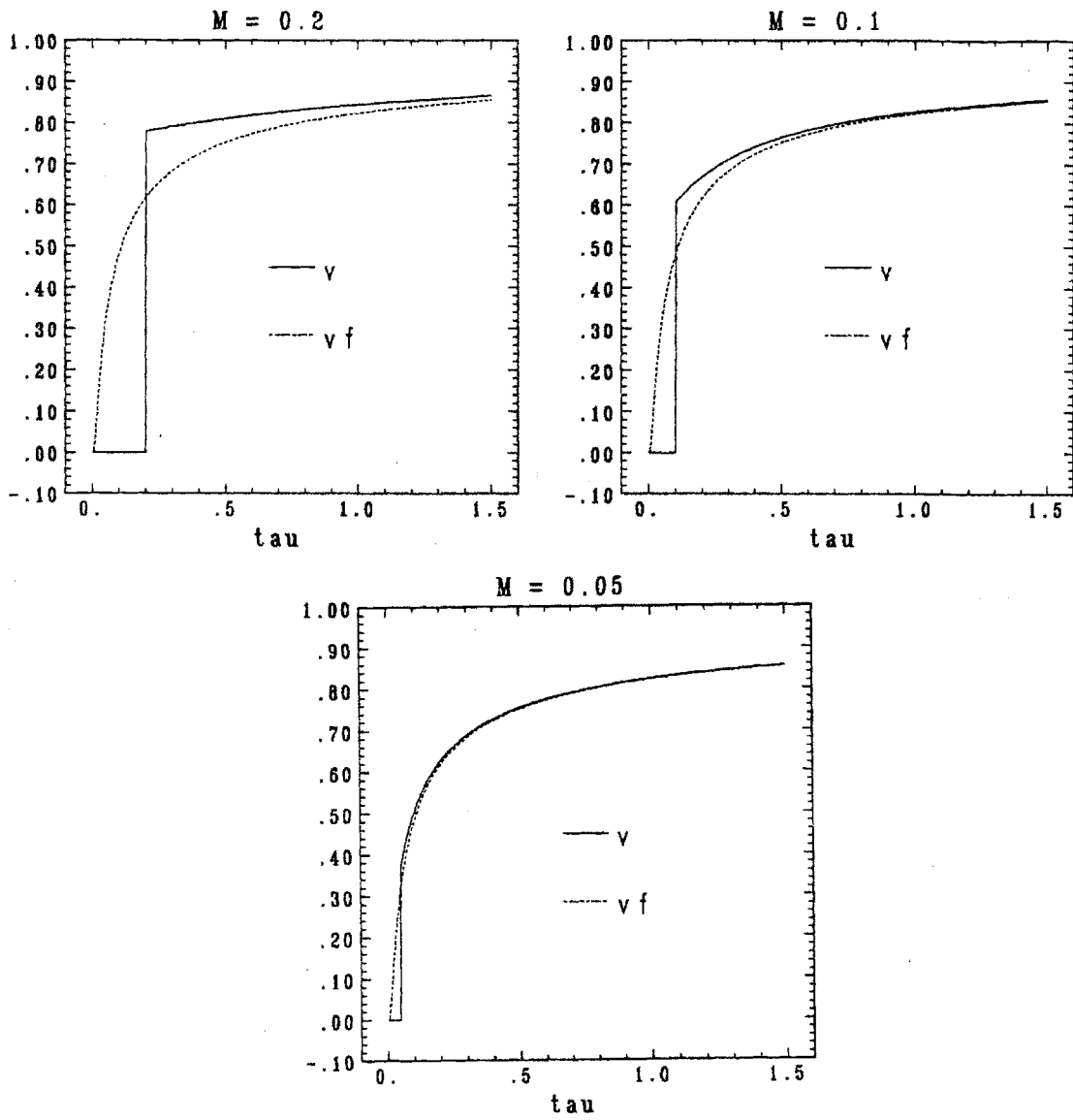


Figure B1: Comparison of Eqs. (B.9) and (B.11), at $x = L$, for Various Values of the Mach Number M .

Appendix C

Discussion of the Boundary Conditions Used in Quencher

Appendix C. Discussion of the BC's Used in Quencher

In this appendix we illustrate how using different boundary conditions affects the solution of a differential equation similar to the energy equation in the Quencher model [see Eq. (2.62)]. Specifically, we attempt to show the advantage of using the outlet boundary condition given by Eq. (2.67d) as opposed to setting $\kappa T' = 0$ at this boundary. We consider a model problem that is easy to solve and also resembles the energy equation for the helium/conductor given by Eq. (2.62). To begin, consider a steady state situation with the following model-equation

$$\frac{\partial y}{\partial x} = \epsilon \frac{\partial^2 y}{\partial x^2} + f(x) \quad (C.1)$$

where the domain is $x = (0, 1)$. The term on the left-hand side of this equation resembles the convective term in Eq. (2.62), while the first term on the right-hand side is equivalent to the conduction term. All heat sources are represented by the function $f(x)$. Just as in Eq. (2.62) we consider the case $\epsilon \ll 1$.

We assume that one physical boundary condition is given at $x = 0$. For Eq. (C.1), this boundary condition is assumed to be $y(x = 0) = 1$. This boundary condition is equivalent to the pressure boundary condition specified for the Quencher model. In Eq. (2.62) the conduction term is important only in a small region (the quench front). Even so, we must keep this term in the equation at all times and over the entire domain of the problem. Doing such, however, requires specifying an additional boundary condition. The process of introducing an additional boundary condition may not be physical for certain problems. Specifically, consider the outflow of helium from the conduit. The helium leaving the conduit, in general is at a higher temperature than the initial background temperature of the system (this is mainly due to compressional and/or frictional heating of the helium in the outer region). Thus, we certainly do not attempt to specify the temperature at the outlet of the conduit, since this would be unphysical. We must resort to other conditions.

One such alternative is to specify the boundary condition $\kappa T'(x = L) = 0$, based on the argument that the amount of heat leaving the system by conduction at the boundary is negligible. Note, however that by using this boundary condition we set $T'(x = L) = 0$. In doing such, we also set the convective heat removal to zero. That is, no heat will leave the system at $x = L$ by either convection or conduction. The arguments leading to $\kappa T'(x = L) \approx 0$ are based on the fact that κ is negligibly small at the outlet of the channel and not that $T'(L) = 0$. Thus, setting $T'(L) = 0$ does indeed make the outlet flux zero, but it also erroneously makes the convection losses zero as well.

To illustrate the consequence of using various boundary conditions we consider two problems, both described by Eq. (C.1) together with the boundary condition $y(x = 0) = 1$. The second boundary condition for case (1) is assumed to be $y'(x = 1) = 0$ and in case (2) we use the condition $y''(x = 1) = 0$. Denoting case (1) by y_1 and similarly using y_2 for case (2), we have

$$y_1(x = 0) = 1 \tag{C.2a}$$

$$\frac{dy_1}{dx}(x = 1) = 0 \tag{C.2b}$$

$$y_2(x = 0) = 1 \tag{C.3a}$$

$$\frac{d^2y_2}{dx^2}(x = 1) = 0 \tag{C.3b}$$

where both y_1 and y_2 are to also satisfy Eq. (C.1). Thus, y_1 resembles the temperature profile in the outer region with the boundary condition $\kappa T'(x = L) = 0$, while y_2 is equivalent to the temperature profile in the outer region with $(\kappa T')'(x = L) = 0$.

Recall that in the outer region the thermal conduction is unimportant and should be neglected although in practice it is maintained for numerical purposes. Denote the solution of Eq. (C.1) for the case $\epsilon = 0$, by y_f . We compare y_1 and y_2 with y_f in order to show the effect of the two boundary conditions given by Eqs. (C.2b) and (C.3b), respectively.

For simplicity, consider the case $f(x) = 2x$. The solutions y_1 and y_2 for this case are easily obtained, and are given by

$$y_1 = 1 + x^2 + 2\epsilon x + 2\epsilon e^{-1/\epsilon} - 2\epsilon e^{(x-1)/\epsilon} - 2\epsilon^2 e^{-1/\epsilon} - 2\epsilon^2 e^{(x-1)/\epsilon} \quad (C.4)$$

$$y_2 = 1 + x^2 + 2\epsilon x - 2\epsilon^2 e^{-1/\epsilon} - 2\epsilon^2 e^{(x-1)/\epsilon} \quad (C.5)$$

Next, consider the solution of Eq. (C.1) with the conduction term set to zero. The resulting equation is given by

$$\frac{\partial y_f}{\partial x} = f(x) \quad (C.6)$$

where we use the subscript f to denote the case with $\epsilon = 0$. The boundary condition for y_f is given by

$$y_f(x = 0) = 1 \quad (C.7)$$

The solution of Eq. (C.6) is given by

$$y_f = 1 + x^2 \quad (C.8)$$

We may now make direct comparisons between y_f , y_1 and y_2 in order to show the consequence of using the various boundary conditions. From Eqs. (C.4), (C.5) and (C.6) we find

$$y_1 = y_f + O(\epsilon) \quad (C.9)$$

$$y_2 = y_f + O(\epsilon) \quad (C.10)$$

Thus, to within order of ϵ , the solutions y_1 and y_2 agree with y_f . That is, regardless of the boundary conditions [see Eqs.(C.2b) and (C.3b)] the solution of Eq. (C.1) approximates the solution of the Eq. (C.6), to within order ϵ .

Next, we compare the gradients of y_1 and y_2 with that of y_f . Again, from Eqs. (C.5) and (C.6) we find

$$\frac{dy_1}{dx} = 2x - 2e^{(x-1)/\epsilon} + 2\epsilon - 2\epsilon e^{(x-1)/\epsilon} \quad (C.11)$$

$$\frac{dy_2}{dx} = 2x + 2\epsilon - 2\epsilon e^{(x-1)/\epsilon} \quad (C.12)$$

Observe that y'_1 and y'_2 are of different orders. Specifically, note that

$$\frac{dy_1}{dx} = \frac{dy_f}{dx} + O(1) \quad (C.13)$$

$$\frac{dy_2}{dx} = \frac{dy_f}{dx} + O(\epsilon) \quad (C.14)$$

Thus, using the $y''(x = 1) = 0$ condition has resulted in a solution y_2 that approximates y_f and it's gradient to within order of ϵ . However, this is not the case with y_1 . The quantity y'_1 forms a boundary layer near the outlet ($x=1$) where it deviates from y'_f by terms of order unity. In Figs. C.1a and C.1b we plot y_1 , y_2 , y_f and the gradient of these quantities, respectively. The value of ϵ used to generate these plots is $\epsilon = 0.01$. From Fig. C.1a it is clearly observed that both y_1 and y_2 are good approximation to y_f . As observed in Fig. C.1b, on the other hand, the quantity y'_2 agrees well with y'_f while y'_1 deviates from the other two curves near $x = 1$. This deviation is a consequence of the boundary condition used to obtain y_1 . It is also worth noting that higher order boundary conditions such as $y'''(1) = 0$ still result in an error of order ϵ in evaluation of $y'(1)$, a consequence of the fact that we are solving a second order ODE.

In conclusion, we have shown that the outlet boundary condition of $(\kappa T)' = 0$ used in Quencher is the most physical condition that may be used. Other conditions such as setting the temperature or the $T' = 0$ result in unphysical boundary layers at the outlet of the conduit.

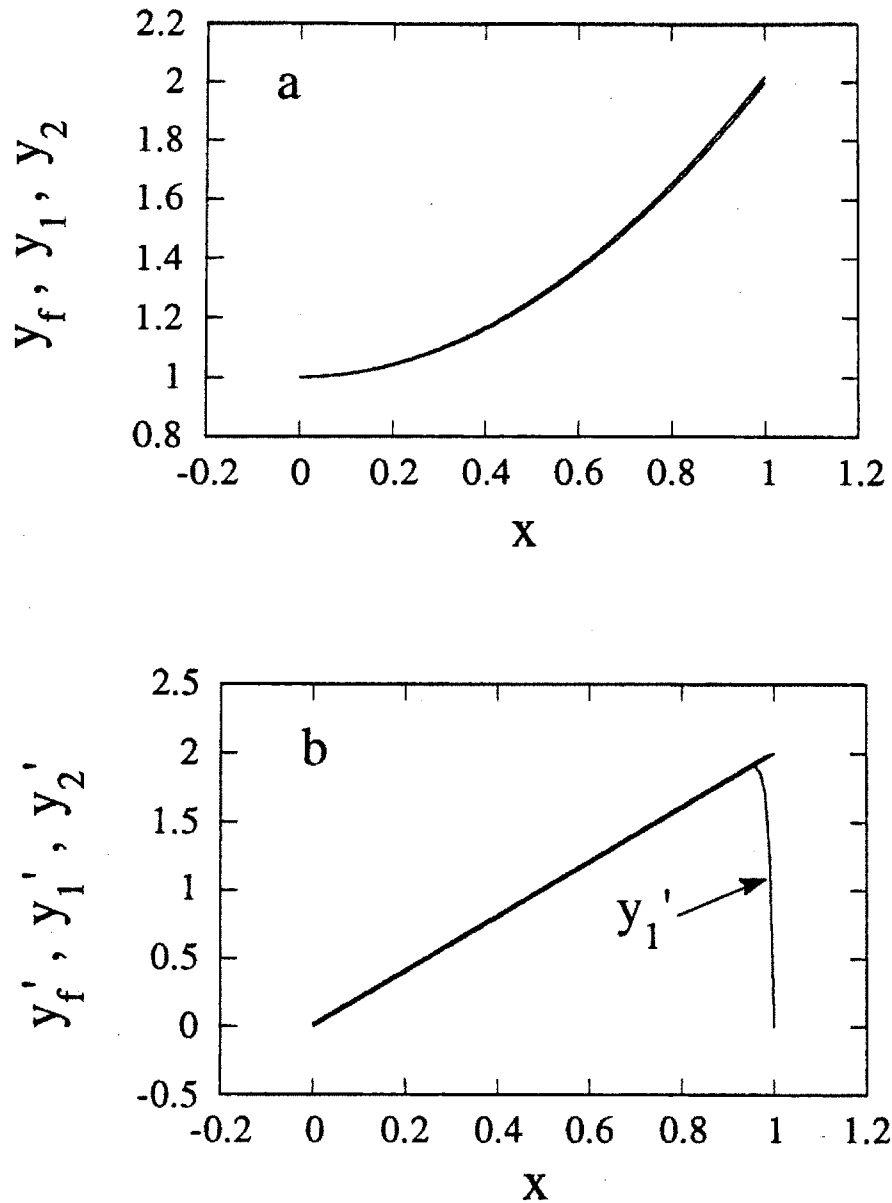


Figure C1: (a) Comparison of y_1, y_2 and y_f as given by Eqs. (C.4), (C.5) and (C.8), respectively. (b) Comparison of the spatial derivative of these quantities.

Appendix D

Thermal Hydraulic Quench-Back in CICC

Appendix D. Thermal Hydraulic Quench-Back in CICC

In this appendix we discuss the process of Thermal Hydraulic Quench-Back (THQB) in Cable-In-Conduit Conductors. This process was first discovered by C. A. Luongo et al. [1] while performing numerical studies of quench in CICC, and has been a subject of active research since then [2,3]. During the THQB process viscous heating, together with the heating due to the compression of the helium may raise the temperature in the outer region above $T = T_{cs}$. When this occurs, Joule heating develops almost instantaneously over large segments of the conductor in the outer region. Hence, a rapid increase of the normal zone is observed. Here, we consider Long coils, Short coils, and the small Δp -regime separately and show that THQB is initiated in each of these regimes by a different mechanism. In long coils the compressional heating in the outer region is mainly responsible for the initiation of THQB, while in short coils the frictional heating is the only mechanism by which this process is initiated. Explicit analytic relations are presented for the onset time of the THQB event. These analytic relations are simple extensions of the theory presented in Chapter 4. We emphasize that the theory of THQB after its initiation is not considered here.

Long Coil

In order to demonstrate the process of THQB in a long coil, consider a CICC of length 200 m. In Fig. D.1a we plot the conductor temperature profile at various time steps during the quench process. Here, after a short period of time THQB is initiated. Note how the boundary layer at the location of the “classical quench” front remains behind, while the actual quench front propagates ahead at a very high rate (~ 50 m/sec). The outer region is rapidly quenching. In Figs. D.1b, D.1c and D.1d we plot the helium pressure, velocity and density profiles, respectively, during this quench event. As quench initiates in the outer region, where $\rho \approx \rho_0$, a very large pressure increase is observed. Since, the pressure in the outer region

is now larger than the quench pressure, a back-flow of helium into the quench region occurs (see Fig. D.1c). The separation of the quench front from $x = X_q$ is further demonstrated in Fig. D.1d. (Note that we now use X_q as the location of the boundary layer that forms the basis of the analytic theory of Chapter 4; this no longer corresponds to the location of the quench front.) From Fig. D.1d, also observe that the density in the quench region starts to increase due to the back-flow of the helium into this region. Comparison of Figs. 4.1a–d and Figs. D.1a–d demonstrate the effect of THQB.

In Figs. D.2a and D.2b we plot the time evolution of the normal length and the maximum helium pressure in the quench region, respectively. Observe, from Fig. D.2a, that at a certain time t_{cr} the process of THQB occurs. From this point a rapid growth of the normal zone is observed. In this figure we also plot the analytic theory of Chapter 4 [see Eq. (4.94)]. The THQB case follows the analytic theory until t_{cr} , after which a large deviation from the analytic theory is observed. In Fig. D.2b we demonstrate how the pressure in the quench region increases very rapidly after $t = t_{cr}$. This increase is due to the back-flow of the helium into the quench region. Recall that the quench pressure is given by $p = R\rho T$, where in both classical and THQB cases, $T \approx \alpha_0 J^2 t$. In the classical regime, however, the density decreases due to the increase of X_q ; $X_q \propto t^{4/5}$ [see Eqs. (4.94) and (4.95)]. The density in this regime behaves as $\rho \propto t^{-4/5}$. Thus, we find that $p \propto t^{1/5}$ during a classical quench. However, this is not the case in the THQB event where the density starts to slowly increase. In this case the pressure behaves as $p \propto t$, nearly following the temperature evolution in this region.

An important characteristic of the THQB event is that the onset time for the initiation of this process is very difficult to obtain numerically. In fact, we have found that the onset time (t_{cr}) becomes longer as the integration time step (Δt) in Quencher is decreased. In many cases, we have not been able to obtain a numerically converged value of t_{cr} . In such cases the numerical solution of the Quencher model appears to be converging both before and after t_{cr} , but the value of t_{cr} itself is difficult to obtain. In Fig. D.3a we present the normal length propa-

gation during a quench that is followed by THQB. Here, we show how decreasing Δt effects the value of t_{cr} while the propagation speed for example appears to have converged (e.g. the slope of X_q versus t curve). In Fig. D.3b we plot t_{cr} versus $1/\Delta t$. Note the slow convergence of t_{cr} as $\Delta t \rightarrow 0$. In the discussions presented below we derive an analytic relation for t_{cr} . From this relation we show the sensitivity of this variable on the various parameters during the quench. We believe that the large variation with certain parameters is responsible for the numerical difficulties involved in obtaining t_{cr} .

Another characteristic of THQB is the following; this process is very similar in nature to what is observed during a quench in a numerically non-converged scenario (see for example Figs. 6.1, 6.2 and also Figs. 3.4a–d). That is, it is difficult to distinguish THQB from a “Numerical Quench-Back” (NQB) event. In both cases a rapid propagation together with large quench pressures are observed. It is not clear whether NQB results from inaccurate low values of t_{cr} or whether this is an entirely different process than a THQB. Further research is required to resolve the two points just discussed. Also the theory of THQB after its initiation is not yet known (i.e. the quench propagation speed after $t = t_{cr}$).

In the analytic solution presented in Chapter 4 we neglected the frictional heating in the outer region. This was done for both long and short coils. In long coils it easily shown that this term is indeed small compared to the compressional heating that occurs in the outer region. Denoting the frictional heating term by Q_{visc} and using Q_{comp} to denote the compressional heating, we have

$$Q_{visc} \equiv \frac{f\rho_0|v|v^2}{2d_h} = -v\frac{\partial p}{\partial x} \quad (D.1)$$

$$Q_{comp} \equiv \rho_0 C_{\beta 0} T_0 \frac{\partial v}{\partial x} \quad (D.2)$$

where $C_{\beta 0} = C_{\beta}(\rho_0, T_0)$. Recall that in the outer region $T = T_0 + T_1$ and similarly $\rho = \rho_0 + \rho_1$. The ratio Q_{visc}/Q_{comp} is given by

$$\frac{Q_{visc}}{Q_{comp}} \sim \frac{v(\partial p/\partial x)}{C_{\beta 0} \rho_0 T_0 (\partial v/\partial x)} \quad (D.3)$$

Noting that $p \sim R\rho T$ and $C_{\beta 0} \sim R$, we find

$$\frac{Q_{visc}}{Q_{comp}} \sim \frac{v(\partial \rho_1/\partial x)}{\rho_0 (\partial v/\partial x)} \sim \frac{\rho_1}{\rho_0} \quad (D.4)$$

Thus, the frictional heating is small compared to the compressional heating, since $\rho_1/\rho_0 \ll 1$ (see Chapter 4).

Observe that in treating the outer region [see Eq. (4.10)] we assumed the right hand side of the energy equation is zero. That is, no heat sources are present in this region. This assumption is valid as long as the temperature in the outer region remains below the current sharing temperature T_{cs} . Once the temperature is above $T = T_{cs}$, quench is initiated in the outer region and the assumptions of Chapter 4 are no longer valid. From the long coil solution, it is easy to obtain the time dependence of the temperature rise T_1 in the outer region. The perturbed density is given by [see Eq. (4.102)]

$$\rho_1 \approx 3\nu_0^2 \frac{\lambda_2^3 t^2}{\left[t^{3/4} + \lambda_2^{3/2} (x - L_q/2)^{3/2} \right]^2} \quad (D.5)$$

where $\lambda_1^2(t) = \rho_0(4V_q/5)/3\nu_0^2$, $\lambda_2(t) = (3\pi/4)^{1/3} \lambda_1$, $\nu_0 = \sqrt{2d_h \rho_0 c_0^2/f}$, and V_q is given by Eq. (4.95). Using this equation together with Eq. (4.74), we find

$$T_1(x, t) = \left[\frac{T_0 C_{\beta 0}}{\rho_0 C_{h0}} \right] \frac{3\nu_0^2 \lambda_2^3 t^2}{\left[t^{3/4} + \lambda_2^{3/2} (x - L_q/2)^{3/2} \right]^2} \quad (D.6)$$

where $C_{h0} \equiv C_h(\rho_0, T_0)$.

Consider the temperature rise just ahead of the quench front, at $x = X_q^+$;

$$\frac{T_1(x = X_q)}{T_0} \approx 3\nu_0^2 \left[\frac{C_{\beta 0}}{\rho_0 C_{h0}} \right] \frac{\lambda_2^3 t^2}{t^{3/2}} = 0.973 \left[\frac{C_{\beta 0}}{\rho_0 C_{h0}} \right] \frac{\rho_0^{3/2} V_q t^{1/2}}{\nu_0} \quad (D.7)$$

Note that in accord with the long coil criteria, we have neglected the second term in the denominator of Eq. (D.5) when considering $x = X_q$. Using Eq. (4.95) to obtain V_q , we find

$$\frac{T_1(x = X_q)}{T_0} \approx 0.653 \left[\frac{C_{\beta 0}}{C_{h 0}} \right] \left(\frac{f}{2d_h c_0^8} \right)^{1/5} (RL_q \alpha_0 J^2)^{3/5} t^{1/5} \quad (D.8)$$

This is a relation for the maximum temperature rise in the outer region during the quench propagation prior to the onset of THQB. The process of THQB is initiated when $T_1(x = X_q) = (T_{cs} - T_0)$. This occurs at time t_{cr} given by

$$t_{cr} = 8.4 \left(\frac{2d_h c_0^8}{f} \right) \left[\frac{1}{RL_q \alpha_0 J^2} \right]^3 \left(\frac{C_{h 0}}{C_{\beta 0}} \frac{T_{cs} - T_0}{T_0} \right)^5 \quad (D.9)$$

Observe the strong dependence of t_{cr} on the temperature margin ($T_{cs} - T_0$), and other quantities. As expected, the value of t_{cr} decreases rapidly with reducing the temperature margin in the outer region. Also, note that t_{cr} decreases with larger L_q , increased Joule Heating ($\alpha_0 J^2$), or larger friction (smaller d_h/f). As discussed above, the strong dependence on these parameters is believed to be responsible for the numerical difficulties involved in obtaining an accurate value of t_{cr} . It is very likely that slight numerical errors in the outer region result in an inaccurate value of t_{cr} , and hence give rise to "Numerical Quench-Back" (NQB).

Short Coil

We found that compressional heating is the dominant mechanism responsible for the initiation of THQB in long coils. In short coils there is no compression of helium occurring in the outer region. From the analytic theory of Chapter 4, we find that T_1 in the outer region is time independent. (Recall that ρ_1 in the outer region is given by the time independent Eq. (4.90), and hence T_1 given by Eq. (4.74) has a similar behavior in space and time.) In obtaining T_1 the frictional heating ($f\rho|v|v^2/2d_h$) was neglected. In long coils, we found that compressional

heating is much larger than this term. In short coils, however, we must consider this term when attempting to analyze THQB. Below, we obtain t_{cr} for short coils by including the frictional heating and by using the analytic relations presented in Chapter 4. We have not numerically analyzed the process of THQB in short coils nearly as extensively as in the long coil case.

In order to obtain an estimate of the temperature rise in the outer region, consider using the analytic theory of Chapter 4 together with the energy equation in the outer region. Recall that in the outer region the dominant contribution to the total specific heat is due to the helium. Also note that in the short coil regime the helium velocity in the outer region is given by $v = V_q$. The quench velocity V_q is given by Eq. (4.86). Keeping the dominant terms in the energy equation for the outer region, we find

$$\rho_0 C_{h0} \frac{\partial T}{\partial t} \approx \frac{f \rho_0}{2d_h} V_q^3 \quad (D.10)$$

where we use T to denote the outer region temperature. From Eq. (4.86), we have

$$V_q = \left(\frac{2d_h R}{fL} L_q \alpha_0 J^2 \right)^{1/3} \quad (D.11)$$

Solving Eq. (D.10), we find the temperature in the outer region is given by

$$T - T_0 \approx \frac{RL_q}{C_{h0}L} \alpha_0 J^2 t \quad (D.12)$$

The onset of THQB occurs at time t_{cr} given by

$$t_{cr} \approx \frac{C_{h0}L}{RL_q} \left(\frac{T_{cs} - T_0}{\alpha_0 J^2} \right) \quad (D.13)$$

Observe that t_{cr} is independent of the friction term f/d_h . This is consequence of a cancelation that is a result of two competing effects; (1) the frictional heating is directly proportional to the term f/d_h , and larger friction tends to increase this term. (2) On the other hand, larger f/d_h will cause reduced helium velocities in

the outer region, and hence a lower value of V_q^3 results in the frictional heating term. Also note that, just as in Eq. (D.9), we find that t_{cr} decreases with larger L_q , increased Joule heating ($\alpha_0 J^2$), and reduced temperature margin in the outer region.

Small Δp Regime

In this section we consider the process of THQB during a quench in the small pressure rise regime. We only consider the case $L^2 < 24d_h c_0^2 t_m / f V_q$. In this case the energy equation in the outer region is identical to Eq. (D.10). Only the quantity V_q is now given by [see Fig. 4.5]

$$V_q \approx \frac{R\rho_0}{2p_0} L_q \alpha_0 J^2 \quad (D.14)$$

Using this relation in Eq. (D.10), we find

$$T - T_0 \approx \frac{f}{2d_h} \left[\frac{R^3 \rho_0^3}{8C_{h0} p_0^3} \right] (L_q \alpha_0 J^2)^3 t \quad (D.15)$$

The onset time of THQB is thus given by

$$t_{cr} \approx \frac{2d_h}{f} \left[\frac{8C_{h0} p_0^3}{R^3 \rho_0^3} \right] \frac{T_{cs} - T_0}{(L_q \alpha_0 J^2)^3} \quad (D.16)$$

Observe that this relation does depend on the friction in the outer region (t_{cr} decreases with higher friction; smaller d_h/f). Again, we observe a decrease in t_{cr} with larger L_q , increased Joule heating ($\alpha_0 J^2$), and reduced temperature margin in the outer region.

An important scaling that is observed in Eq. (D.16), is the dependence of t_{cr} on the ratio p_0/ρ_0 . This dependence suggests that by reducing the operating pressure, while maintaining the same temperature, it is possible to decrease t_{cr} and hence observe THQB at an earlier time. Note that decreasing p_0 also results in a decrease of ρ_0 . However, for supercritical helium the ratio p_0/ρ_0 , at constant

temperature, decreases with reducing pressure. Thus, at $T_0 = 5$ K and $p_0 = 10$ atm for example, we find $p_0/\rho_0 \approx 7000 \text{ m}^2/\text{sec}^2$, while at the same temperature and $p_0 = 5$ atm we find $p_0/\rho_0 \approx 4000 \text{ m}^2/\text{sec}^2$. This reduction in p_0/ρ_0 results in a value of t_{cr} that is approximately 5 times smaller. Recent experiments by T. Ando [4] suggest that the process of THQB has been observed by reducing the operating pressure in the experimental setup that was discussed in both Chapters 3 and 4. Recall that the coil used in this experiment satisfies $L^2 < 24d_h c_0^2 t_m / fV_q$, and due to the small value of L_q , this conductor also satisfies the criterion for the small pressure rise regime (see Chapter 4, section 4.3).

Appendix D References

- [1] Luongo, C. A., et al., *Thermal Hydraulic Simulation of Helium Expulsion From a Cable-In-Conduit Conductor*, IEEE Trans. Magn., Vol. 25, pp. 1589-1595, March 1989.
- [2] Dresner, L., *Theory of Thermal Hydraulic Quenchback in Cable-In-Conduit Superconductors*, Cryogenics, Vol. 31, pp. 557-561, July 1991.
- [3] Lue, J. W., et al., *Investigating Thermal Hydraulic Quenchback in a Cable-In-Conduit Superconductor*, IEEE Trans. Applied Superconductivity, Vol. 31, pp. 338-341, March 1993.
- [4] T. Ando, private communication, 1993.

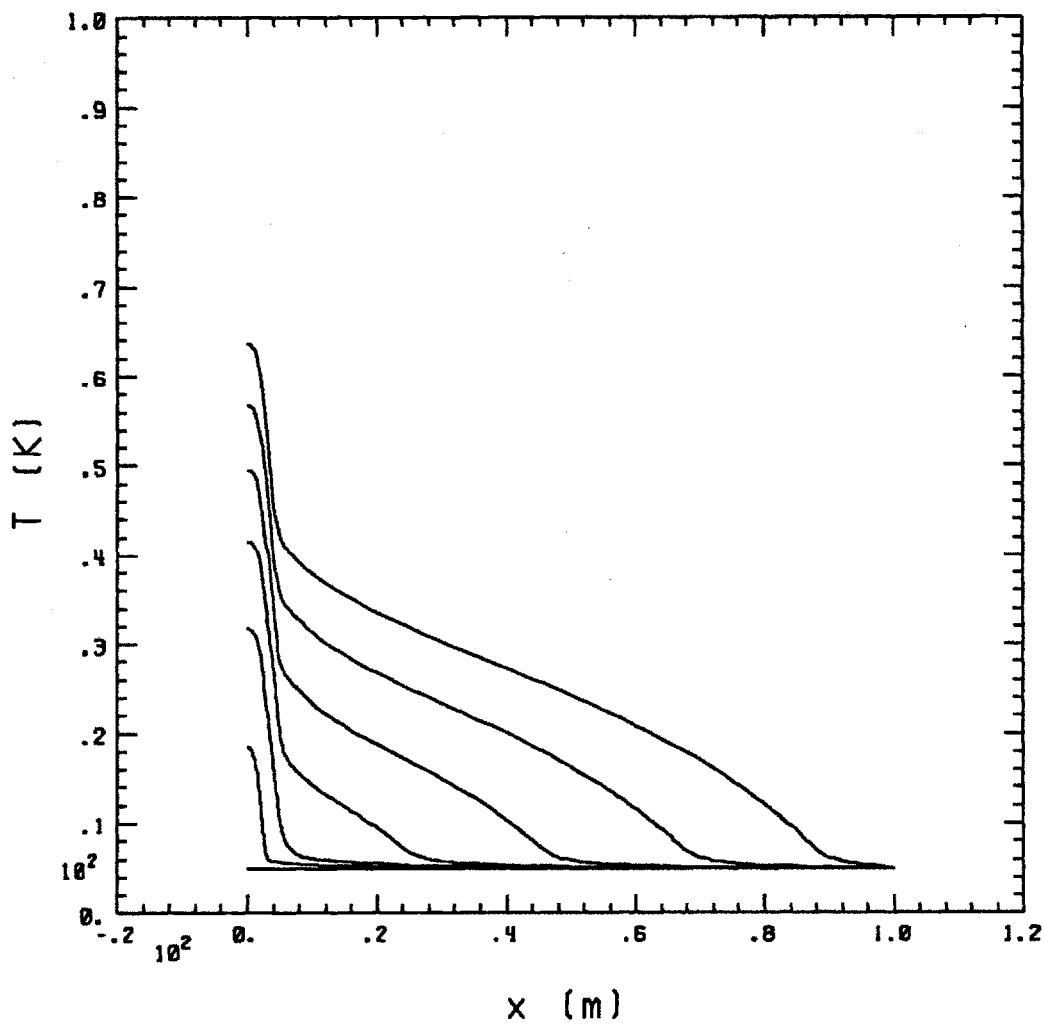


Figure D1a: Temperature distribution during THQB.

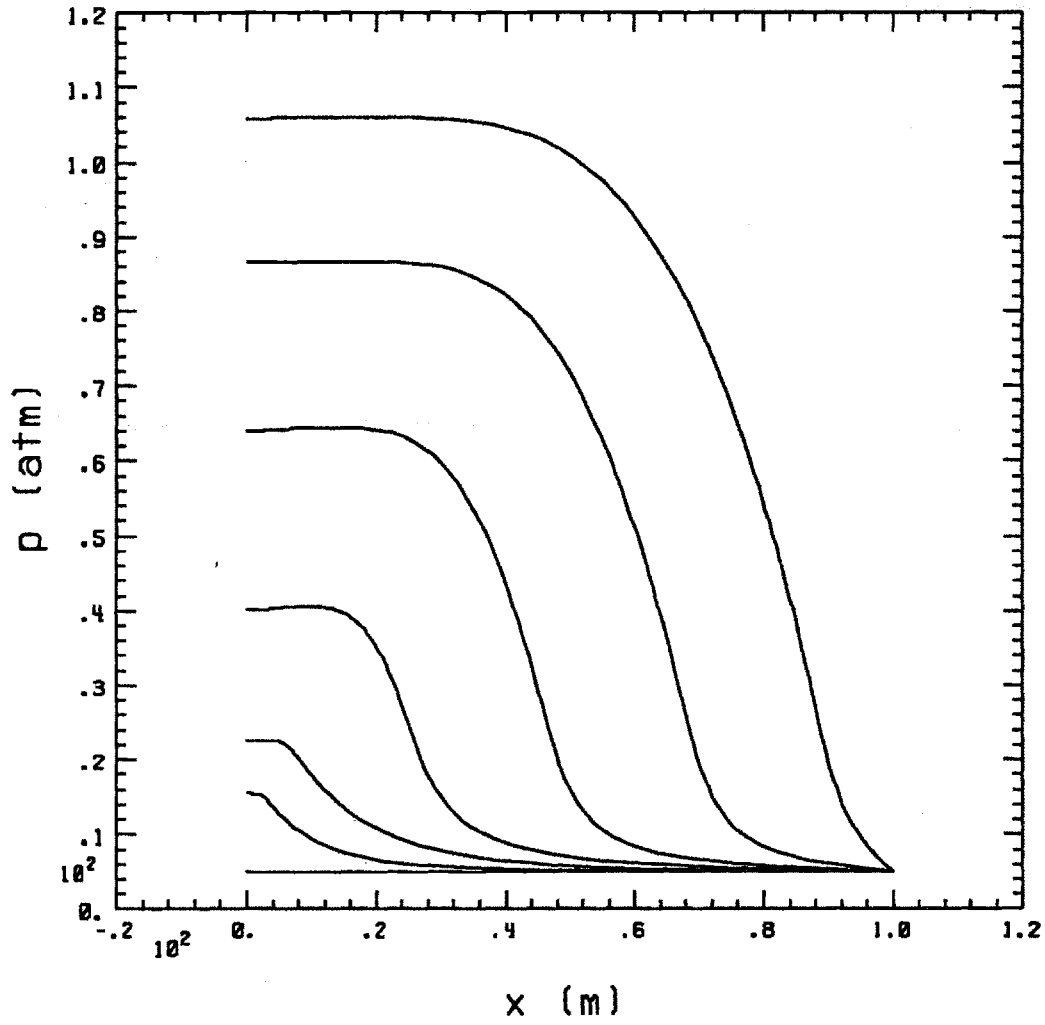


Figure D1b: Helium pressure distribution during THQB.

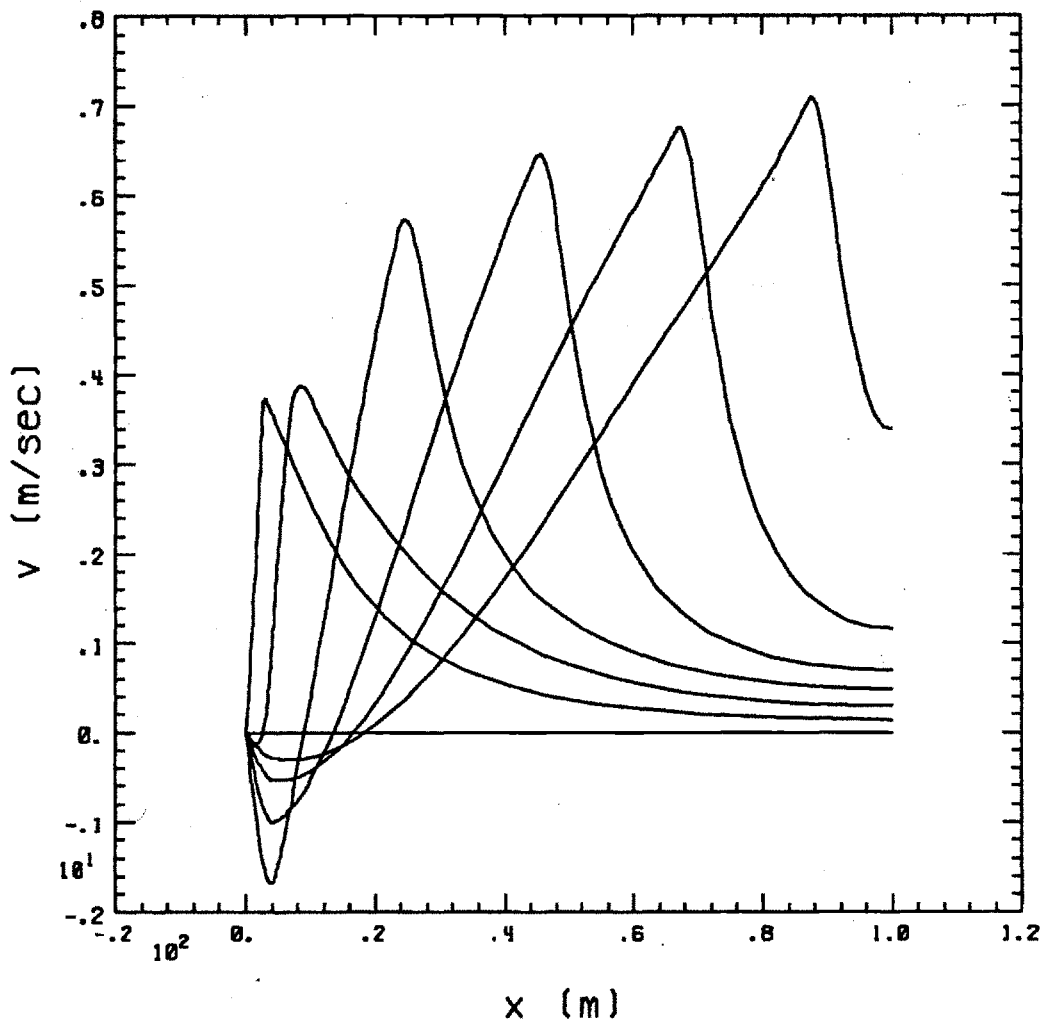


Figure D1c: Helium velocity distribution during THQB.

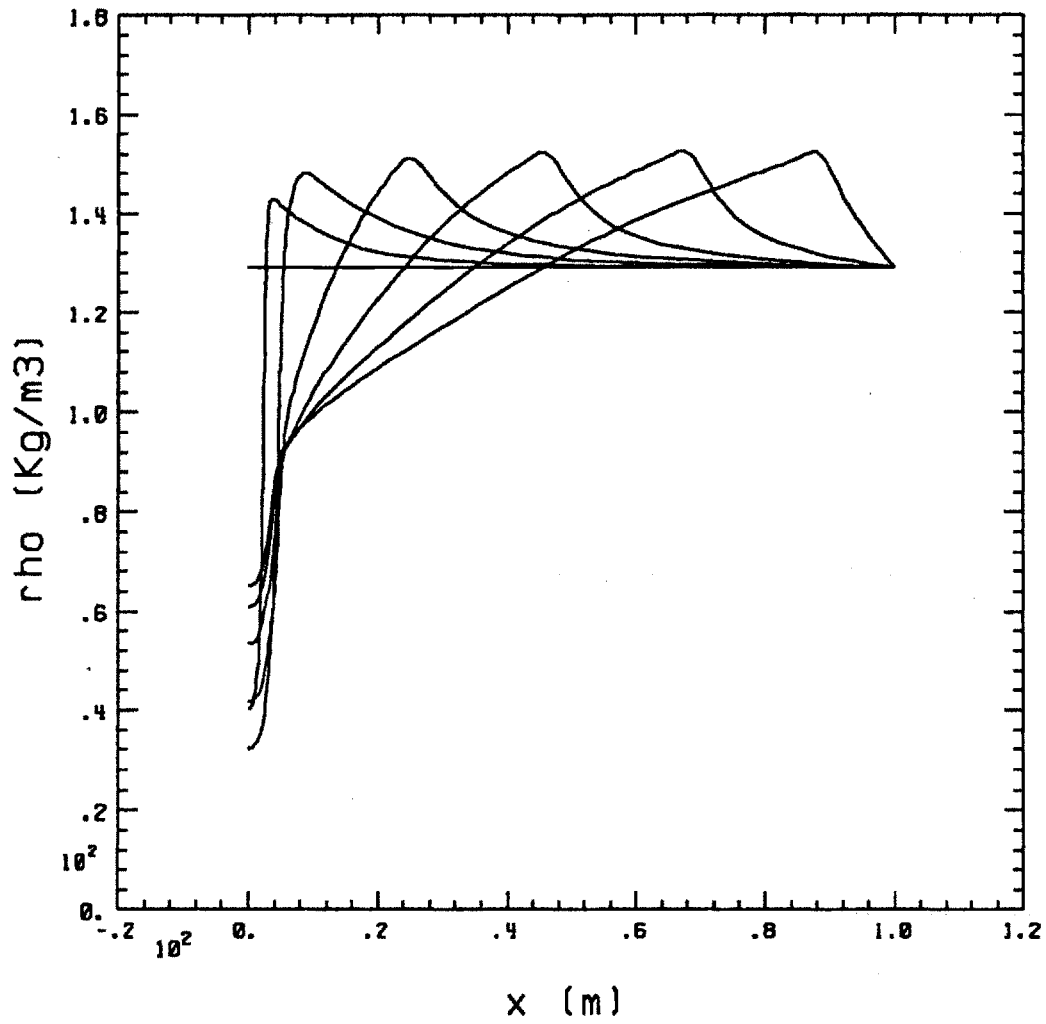


Figure D1d: Helium density distribution during THQB.

Normal Length Vs. time
 $L = 200 \text{ m}$

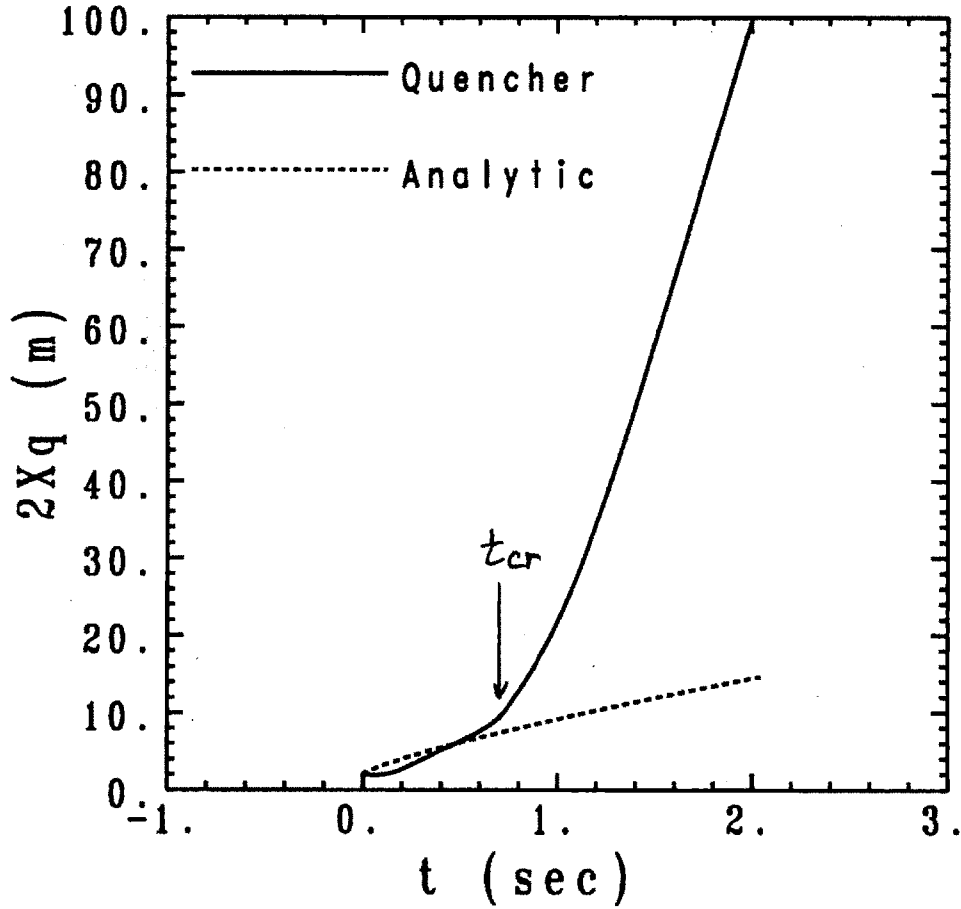


Figure D2a: Normal length evolution during THQB.

Helium Pressure Vs. time
L = 200 m

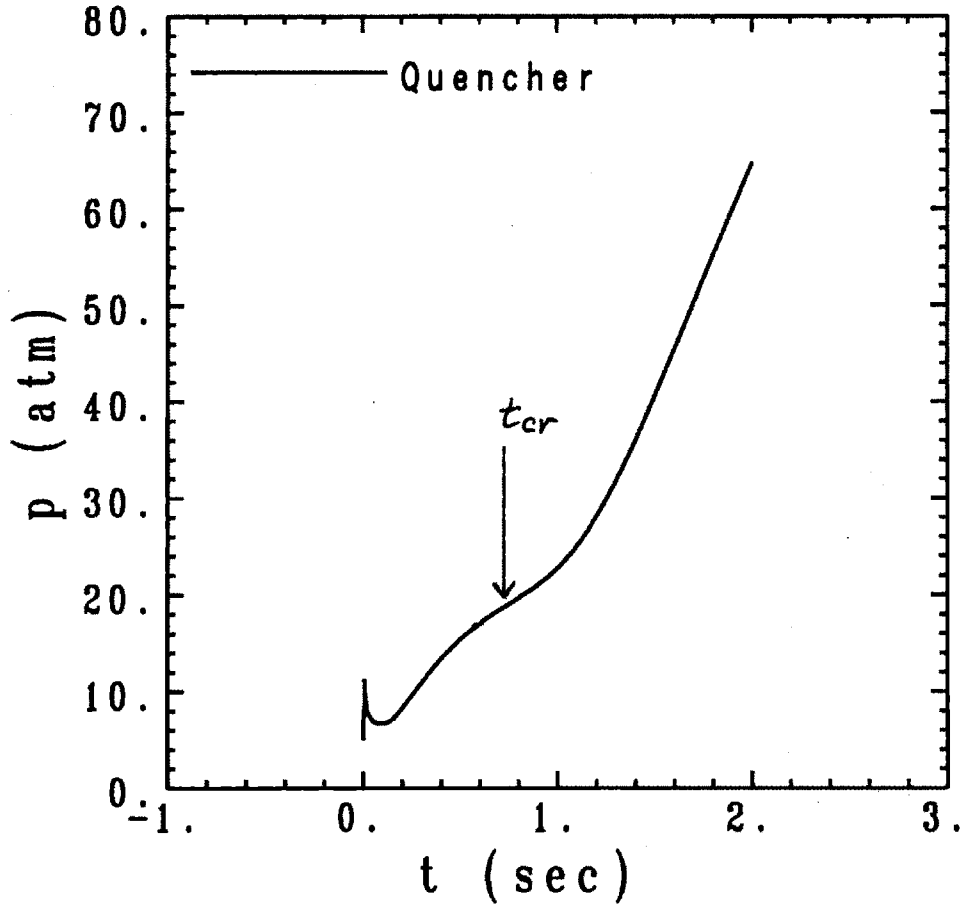


Figure D2b: Maximum helium pressure in the quench region during THQB.

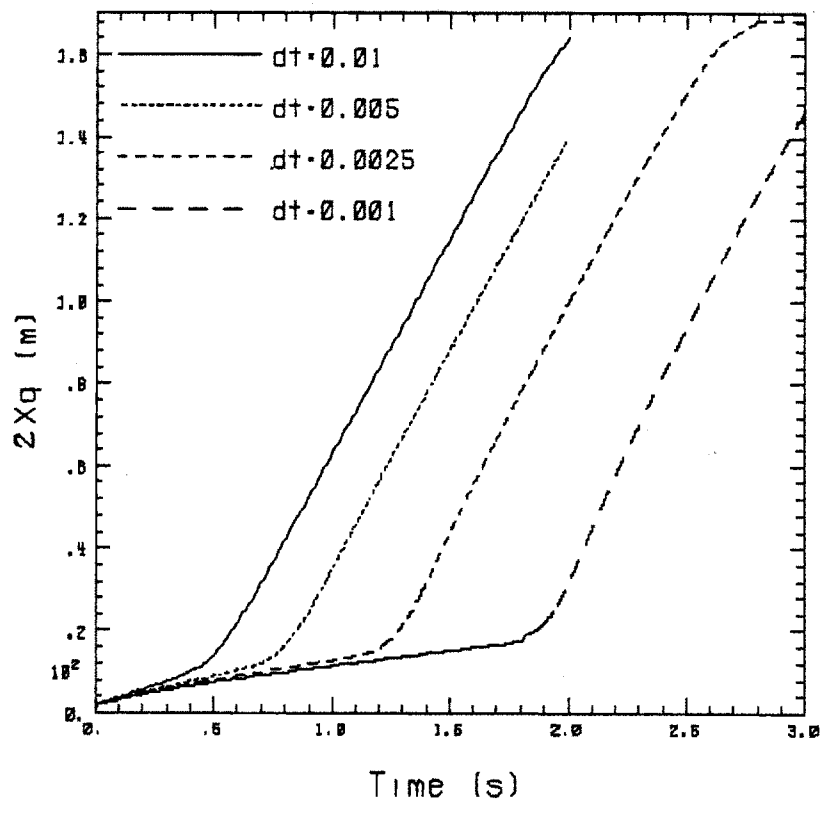


Figure D3a: Normal length evolution during THQB for various Δt .

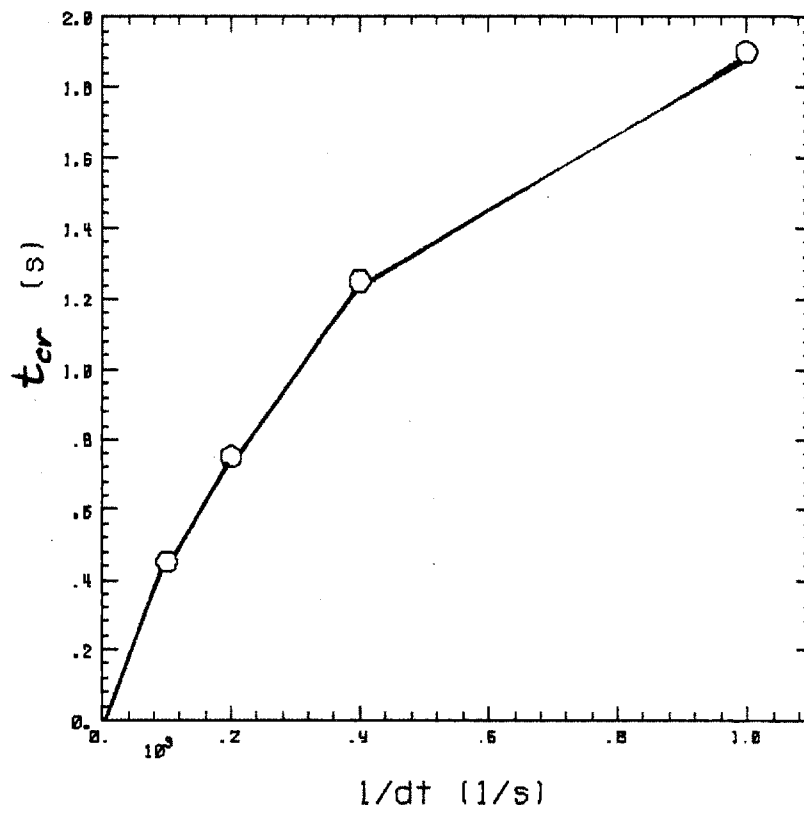


Figure D3b: The THQB onset time t_{cr} versus $1/\Delta t$.